

# **Quantum computation and simulation with trapped ions using dissipation**

Dissertation

zur Erlangung des Doktorgrades an der  
Fakultät für Mathematik, Informatik und Physik  
der Leopold-Franzens-Universität Innsbruck

vorgelegt von

**Philipp Schindler**

durchgeführt am Institut für Experimentalphysik  
unter der Leitung von  
o. Univ. Prof. Dr. R. Blatt

Innsbruck Mai 2013

---

## Abstract

Quantum information processing combines two of the most successful and fascinating ideas of the 20th century - quantum physics and computer science. A quantum computer promises to solve certain problems more efficient than classical computers. But building such a quantum computer is a cumbersome task as the quantum system needs to be manipulated with tremendous accuracy while being well shielded from the classical environment to preserve its quantum nature. An unwanted coupling to the surrounding environment manifests itself in computational errors. This coupling can be suppressed with the aid of quantum error correction schemes that are still a mainly theoretical construct.

These error correcting protocols can only protect the information if they are applied multiple times subsequently. For this, it is necessary to remove the information about previous errors from the quantum system before performing the actual correction. However, this removal of information requires a controlled coupling to the environment which is beyond the standard set of operations available in a quantum computer. In this work, an experimental realization of repetitive quantum error correction in an ion-trap quantum information processor is presented, performing up to three consecutive rounds of correction.

Moreover such an error correction algorithm can also be used to demonstrate a physical connection between information processing and quantum mechanics - computational errors are mapped onto quantum mechanical measurements. Therefore, a quantum error correction protocol is able to undo quantum measurements - a task that seemingly contradicts the foundations of quantum physics. In this work, we show that it is indeed possible to undo a partial measurement on a quantum register using an error correction protocol. After closer inspection it becomes obvious this does not violate the laws of quantum mechanics.

However, the realization of a large-scale quantum computer lies in the far future as current quantum systems do not allow for the required level of control. Nevertheless it seems promising to adapt the techniques developed for quantum information processing to build a quantum simulator. Such a device is able to efficiently reproduce the dynamics of any quantum system - a task that is only possible for small systems on existing classical computers. However, the quantum system of interest may be coupled to a classical environment where many examples for such systems can be found in quantum biology and quantum chemistry. These systems are often embedded in a thermal environment and, analogous to classical physics, show non-reversible, or dissipative, dynamics. Thus, also the quantum simulator should be able to reproduce dissipative dynamics which requires an extension of the usual quantum computing toolbox.

In the context of quantum computing, such a coupling is usually treated as a noise process that defeats the possible gain from using such a device. Interestingly it has been shown that an environment can be engineered that drives the system towards a state that features entanglement and can serve as a resource for quantum information processing. In this thesis, an extended toolbox that goes beyond coherent operations is introduced in our small-scale ion-trap quantum information processor. This is then used to create an entangled state through dissipative dynamics. In the next step a quantum simulation of a dissipative many-body system is performed, demonstrating the hallmark feature of a novel type of quantum phase transitions.

---

## Kurzfassung

Quanteninformationsverarbeitung vereint zwei der erfolgreichsten und faszinierendsten Errungenschaften des 20. Jahrhunderts - Quantenphysik und elektronische Informationsverarbeitung. Ein Quantencomputer könnte gewisse Probleme effizienter lösen als es mit herkömmlichen klassischen Computern möglich ist. Einen solchen zu bauen ist jedoch ein schwieriges Unterfangen, da das Quantensystem sowohl präzise manipuliert als auch vor der klassischen (makroskopischen) Umgebung geschützt werden muss. Eine ungewollte Kopplung mit der klassischen Umgebung führt hierbei zu Rechenfehlern. Es existieren jedoch Methoden zur Quantenfehlerkorrektur, die diese Kopplung unterdrücken.

So eine Fehlerkorrektur muss allerdings wiederholt angewendet werden um die fragile Information schützen zu können. Dies ist nur möglich, wenn die Information über vorangehende Fehler aus dem Quantensystem entfernt wird, was eine kontrollierte Kopplung an die klassische Umgebung nötig macht. Eine entsprechende Kopplung ist nicht in den üblichen Operationen eines Quantencomputers enthalten. Die vorliegende Arbeit beschreibt die Realisierung einer wiederholten Fehlerkorrektur in einem Ionenfallenquantencomputer.

Diese Korrekturmethode kann weiter verwendet werden, um eine Verbindung zwischen Informationsverarbeitung und Quantenphysik aufzuzeigen - Fehler in der Informationsverarbeitung entsprechen quantenmechanischen Messungen. Deswegen ermöglicht es Quantenfehlerkorrektur, eine Messung in einem Quantensystem rückgängig zu machen, was scheinbar den Grundlagen der Quantenmechanik widerspricht. In dieser Arbeit wird gezeigt, dass es tatsächlich möglich ist eine partielle Messung an einem Quantenregister rückgängig zu machen. Bei genauerer Betrachtung wird klar, dass dies in keiner Weise die Gesetze der Quantenmechanik verletzt.

Voraussichtlich wird in den nächsten Jahren kein Quantencomputer entstehen, der schneller als herkömmliche Computer rechnen kann. Dies könnte jedoch mit Quantensimulatoren ermöglicht werden, die auf den Techniken der Quanteninformationsverarbeitung aufbauen. Diese Simulatoren reproduzieren die Dynamik eines beliebigen Quantensystems, was in einem herkömmlichen Computer nur für kleine Systeme möglich ist. Das zu untersuchende Quantensystem kann jedoch an eine klassische Umgebung gekoppelt sein. Beispiele hierfür findet man in der Quantenbiologie und der Quantenchemie. Diese Systeme befinden sich oft in einer warmen (thermodynamischen) Umgebung, die analog zur klassischen Physik einer nichtreversiblen, oder dissipativen, Zeitentwicklung gehorchen. Deswegen sollte auch ein Quantensimulator in der Lage sein, dissipative Zeitentwicklungen nachzustellen. Dies wiederum erfordert eine Erweiterung des üblichen Werkzeugkastens eines Quantencomputers.

Normalerweise wird eine dissipative Zeitentwicklung damit identifiziert, dass ein System seine quantenmechanischen Eigenschaften verliert. Interessanterweise ist es jedoch möglich, eine Kopplung mit der Umgebung zu erzeugen, die das System in Zustände treibt, die quantenmechanische Korrelationen enthalten. So eine dissipative Zeitentwicklung kann dann auch als Ressource für einen Quantencomputer dienen. In dieser Arbeit wird ein Werkzeugkasten demonstriert, der es ermöglicht, verschränkte Zustände mithilfe einer dissipativer Zeitentwicklung zu erzeugen. Dies wird in der Folge dazu verwendet, um ein eindeutiges Kennzeichen eines neuartigen Phasenüberganges im Quantensimulator zu beobachten.

---

# Contents

<b>1. Introduction</b>	<b>1</b>
1.1. Introduction to quantum computation and quantum simulation . . . . .	1
1.2. Basic concepts of quantum information theory . . . . .	5
1.3. Incoherent states and processes in quantum information . . . . .	10
<b>2. A quantum information processor with trapped ions</b>	<b>15</b>
2.1. Introduction to ion traps . . . . .	15
2.2. Publication: A quantum information processor with trapped ions . . . . .	20
2.2.1. Tools for quantum information processing in ion traps . . . . .	20
2.2.2. Experimental setup . . . . .	29
2.2.3. Error sources . . . . .	38
2.2.4. Example algorithms . . . . .	48
2.2.5. Conclusion and Outlook . . . . .	52
<b>3. Experimental quantum error correction</b>	<b>53</b>
3.1. Introduction to quantum error correction . . . . .	53
3.2. Publication: Experimental repetitive quantum error correction . . . . .	59
3.3. Publication: Undoing a quantum measurement . . . . .	65
<b>4. Quantum simulation of open systems</b>	<b>71</b>
4.1. Introduction to open-system quantum simulation . . . . .	71
4.2. Publication: An Open-System Quantum Simulator with Trapped Ions . . . . .	75
4.2.1. Open-System Dynamics & Bell-State Pumping . . . . .	76
4.2.2. Experimental Bell-State Pumping . . . . .	79
4.2.3. Four-Qubit Stabilizer Pumping . . . . .	80
4.2.4. Coherent Four-Particle Interactions . . . . .	82
4.2.5. QND Measurement of Four-Qubit Stabilizer . . . . .	83
4.2.6. Conclusions and Outlook . . . . .	83
4.3. Publication: Quantum Simulation of Dynamical Maps with Trapped Ions . . . . .	87
4.3.1. Competing dissipative and unitary dynamics in a complex spin model . . . . .	91
4.3.2. Experimental realization . . . . .	94
4.3.3. Methods . . . . .	100
<b>5. Summary and outlook</b>	<b>103</b>
<b>A. List of publications</b>	<b>105</b>

<b>B. Supplementary information</b>	<b>107</b>
B.1. A quantum information processor with trapped ions . . . . .	107
B.2. Experimental repetitive quantum error correction . . . . .	111
B.3. An Open-System Quantum Simulator with Trapped Ions . . . . .	117
B.4. Quantum Simulation of Dynamical Maps with Trapped Ions . . . . .	134
<b>Bibliography</b>	<b>169</b>

# 1. Introduction

## 1.1. Introduction to quantum computation and quantum simulation

There is hardly any technical invention that has changed our everyday life over the last decades like computers. The rapid growth of computational power is rooted in an impressive development of their elementary building blocks which started in the 1960s when semiconductor transistors replaced the vacuum tubes in the available computing machines. Of course, a transistor could not be built without a predictive theory of the physics in semiconductor devices. This theory is based upon one of the greatest advances of physics in recent history: quantum physics.

Although quantum physics is required to understand the computer's hardware, any algorithm can be executed on a universal Turing machine which itself can be described by the laws of classical physics. In this sense, the dynamics of any computer, be it a mechanical computing machine used in the 1940's, or a modern supercomputer, are equivalent. Already in the early 1980's it was realized that it might be possible to establish a deeper connection between information and quantum physics: A computer where the information and the algorithms obey the laws of quantum physics. Such a device would represent a revolutionary change in the underlying computational model [1].

It was mainly physicists that began to see the potential of a computing device where the computational model is based on quantum mechanics. In such a device, the information is stored in a register consisting of quantum objects and an algorithm corresponds to the quantum mechanical time evolution of the register. But is a quantum computer more powerful than a classical computer? In order to answer this question, one has to find a way to compare distinct models of computation. In a computer science context, an algorithm is called *efficient*, if the required resources, time and memory, scale polynomially with the system size. Thus, a computational model can be considered more powerful if it is able to solve more problems efficiently. Richard Feynman discussed in 1982 whether a quantum mechanical system can be efficiently simulated on a classical computer, and came to the conclusion that this is not the case [2]. He suggested the use of a quantum computer to solve this problem where his motivation why to use a quantum system to perform this task was simple:

Nature isn't classical, dammit, and if you want to make a simulation of Nature, you'd better make it quantum mechanical, and by golly it's a wonderful problem, because it doesn't look so easy.

To understand why a simulation of quantum mechanical systems cannot be performed efficiently

on a classical computer in general, one needs to analyze the underlying problem. Simulating a quantum system on a classical computer is performed by numerically solving the Schrödinger equation which is a problem whose complexity grows exponentially with the system size. This is due to the fact that the state-space of any quantum system grows exponentially with the system size. On the other hand, a quantum computer has itself an exponentially growing state-space which may be used to simulate any quantum system efficiently.

However, Feynman did not specify the requirements on a quantum system to be used as such a quantum computer. In another groundbreaking work, the theoretical framework of a quantum computer that is capable to perform arbitrary computations was developed by David Deutsch by introducing the quantum Turing machine in 1985 [3]. He suggested that

... such computers could operate at effective computational speeds in excess of Turing-type machines built with the same technology.

At that time, no quantum system was available to host even a small-scale quantum computer and thus the research focused on theoretical aspects of quantum information processing, such as finding efficient algorithms. The most prominent quantum algorithm has been presented by Peter Shor in 1994 to efficiently find the prime factors for any number, where no classical algorithm is known to perform this task efficiently [4]. More importantly, the fact that no efficient algorithm is known to factor an integer is exploited in classical cryptography methods such as the Rivest-Shamir-Adleman (RSA) protocol which is widely used in today's encrypted data transfer [5]. A large-scale quantum computer capable of executing Shor's algorithm would render such an encryption protocol useless.

Since it was evident that a quantum computer would be a useful device, the quest for finding physical implementations was intensified. It soon became a certainty that a real-world quantum computer requires a quantum system which needs to be controlled with tremendous precision while still being well isolated from the environment. In 1995, Peter Zoller and Ignacio Cirac presented a viable route to realize the required quantum operations to build a quantum computer in a system consisting of trapped ions [6]. Five general criteria for any system hosting a quantum computer were formulated by David DiVincenzo in 2000 [7].<sup>1</sup>

1. A scalable physical system with a well characterized quantum register
2. The ability to initialize the quantum register in a simple fiducial state
3. Long relevant coherence times, much longer than the gate operation time
4. A “universal” set of quantum gates
5. A system-specific measurement capability

Since then, multiple groups of physicists have been trying to meet these criteria in various physical systems such as trapped atomic ions, neutral atoms in optical lattices, single photons, superconducting resonators and ensembles of molecules [8–11]. Although impressive proof of concept experiments have been performed, no system has satisfied all criteria at a level to build a quantum computer powerful enough to compete with today's classical computers. The main

---

<sup>1</sup>The wording of the criteria has been adapted to be more understandable.

difficulty in building a large quantum computer lies mainly in the fact that the quantum mechanical system cannot be shielded well enough from the environment resulting in erroneous calculations. In quantum physics this is known as decoherence which is responsible for the fact that we do not experience quantum mechanical effects in macroscopic objects. It is clear, that a realistic system can never be shielded perfectly from the environment and thus at least a small amount of noise will always be present. First, it seemed as if even a small amount of noise would make a large-scale quantum computer impossible, similar to analog classical computers where it is proven that noise forbids arbitrarily long computation. In contrast, for classical digital computers it has been shown that arbitrarily long algorithms can be executed in a noisy implementation faithfully, when error correction techniques are applied [12]. However, it was questionable whether such procedures could be applied to a quantum computer until Andrew Steane and Peter Shor developed an error correction framework for quantum computers in a milestone work in 1996 [13, 14].

With further exploration of the possibilities and requirements to a real-world quantum computer it became clear that for outperforming state-of-the-art classical computers, very large quantum systems would be required. Since such a large quantum computer won't be available in the next few years, the research focused on finding applications for small to medium scale quantum computers [15]. As already mentioned, Richard Feynman stated that a quantum mechanical system cannot be efficiently simulated on a classical computer. This is due to the fact that although in principle the dynamics of any quantum system can be predicted by the Schrödinger equation, it is almost impossible to make precise predictions for a large-scale system because the computational costs grow exponentially. With modern supercomputers it is only possible to store the state of a system consisting of about 40 two-level atoms let alone calculate the dynamics of such a system [16]. Therefore, a quantum simulator that is able to faithfully investigate systems with more than 40 particles would already be a useful device. Simulation problems can be closely related to the physical system building up the quantum computer, making it conceivable that they can be solved relatively easily on a quantum system. Nevertheless, these problems are still hard to solve on a classical computer and thus quantum simulators offer the possibility for a break-even with a classical computer in the near future.

Another major difference between quantum simulation and computation is that for simulations one might also consider quantum systems which are coupled to a classical environment, a setting that is avoided at all costs in traditional quantum computing. Important examples for such systems include quantum chemistry or quantum biology where the classical environment is treated as a thermal bath in analogy to classical thermodynamics [17, 18]. In these systems, the environment introduces noise and drives the system towards a classical state. Analog to classical thermodynamics, the coupling to the environment can only be described by irreversible processes whereas processes that do not couple to the environment are reversible. Algorithms for quantum computers are in general coherent and can thus be described by reversible operations but in contrast, simulating the dynamics of open quantum systems needs to be irreversible as quantum information is lost to the classical environment. This conceptionally distinguishes quantum simulation of open systems from time reversible quantum computing.

Recently, a lot of attention has been devoted to systems where the coupling to the environment is engineered in a way so it does not result in decoherence, but rather builds up quantum co-

herence [19, 20]. Along this line, it has even been shown that it is possible to build a quantum computer without any coherent operation at all [21]. In this work first experiments in this direction are described, where a controlled coupling to the classical environment in combination with coherent quantum operations is used to implement non-reversible processes that generate quantum coherence and can also be used to simulate quantum systems coupled to a classical environment.

This work is based upon a particular physical implementation of a small-scale quantum information processor using trapped atomic ions. The ions are confined in a linear Paul trap, which is able to hold linear strings of ions building up a quantum register [22]. This system has been particularly successful in performing proof-of-concept experiments for both, a quantum computer, and a quantum simulator [23–29]. Such ion trap quantum information processors encode the quantum information in electronic states of single atomic ions that are arranged in a linear string. The motion of the ions in the string is used as a databus to mediate the interaction between different atoms [6].

In particular, this work describes an experimental quantum computer and simulator using  $^{40}\text{Ca}^+$  ions to encode the information in the ground state and a metastable excited state. This thesis is focused on the use of irreversible operations for quantum computation and simulation. In section 1.2 basic concepts of quantum information theory are covered. Section 1.3 extends this analysis to incoherent states and processes followed by a short review of quantum information processing in ion traps in section 2.1. Our particular setup and the extensive toolbox of coherent and incoherent operations are presented in section 2.2. Furthermore, it is shown how the entire toolbox can be used to realize an efficient implementation of the quantum order finding algorithm.

Then, an introduction to quantum error correction techniques and their application is given in section 3.1 and section 3.2 describes the first implementation of a repetitive quantum error correction algorithm. Section 3.3 emphasizes the interesting connection between quantum error correction and the foundations of quantum physics by demonstrating that an error correction protocol can be used to undo a quantum measurement. Subsequently, techniques to simulate open quantum systems are introduced in section 4.1. These techniques are showcased in a universal toolbox for simulation of open quantum systems in section 4.2. Building on this framework, the work presented in section 4.3 realizes the simulation of a complex bosonic many-body system.

## 1.2. Basic concepts of quantum information theory

In the following basic concepts used in quantum information science are introduced, assuming that the reader is familiar with elementary quantum mechanics. For an extensive treatment of this topic the book “Quantum Computation and Quantum Information” is recommended to the interested reader [30]. This section focus now on an idealized quantum computer fulfilling all DiVincenzo criteria [7, 30].

In classical information theory the value of the smallest unit of information (bit) can be in one out of two states, 0 or 1. The quantum mechanical counterpart of the bit is the quantum bit (qubit) which can be represented by a quantum mechanical two-level system with basis states  $|0\rangle$  and  $|1\rangle$ . Due to its quantum nature, the qubit can not only be in one of the two basis states but also in a superposition of the two states which could be interpreted classically as being 0 and 1 simultaneously. The most general state of a single qubit in a system undergoing reversible dynamics can be expressed as

$$|\Psi\rangle = \alpha|0\rangle + \beta|1\rangle$$

where  $\alpha, \beta$  are complex numbers satisfying  $|\alpha|^2 + |\beta|^2 = 1$ . The state can be described by the complex vector  $\vec{c} = (\alpha, \beta)^T$ . It can be interpreted intuitively by a real vector on a unity sphere called the Bloch sphere as shown in figure 1.1. On the Bloch sphere, each state is described by the angles  $\theta$  and  $\phi$  as

$$|\Psi\rangle = \sin\left(\frac{\theta}{2}\right)|0\rangle + \cos\left(\frac{\theta}{2}\right)e^{i\phi}|1\rangle$$

Thus, the basis states represent the poles of the sphere, whereas an equal superposition ( $|\alpha| = |\beta| = 1/\sqrt{2}$ ) is located in the equatorial plane.

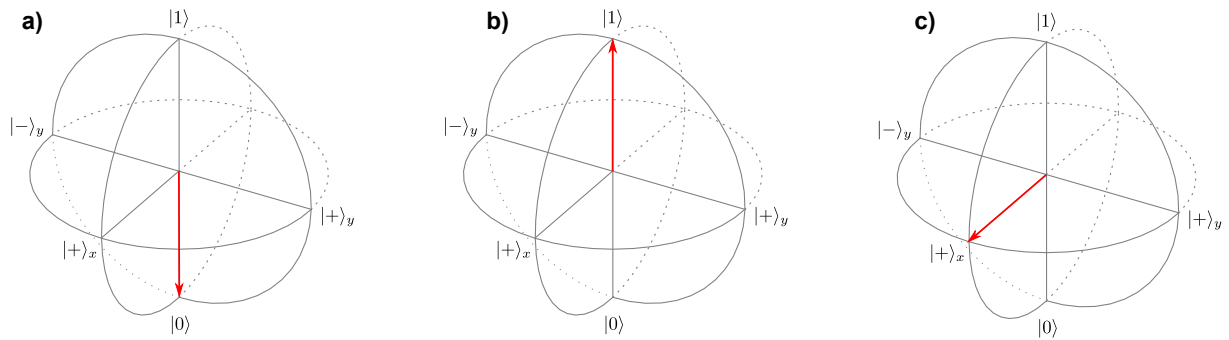


Figure 1.1.: The Bloch sphere representation of a single qubit. a) qubit in state  $|0\rangle$ , b) qubit in state  $|1\rangle$ , c) qubit in state  $|+\rangle_x = 1/\sqrt{2}(|0\rangle + i|1\rangle)$

Reversible operations on a qubit are described by unitary operations  $\hat{U}$  acting on the state vector as

$$\vec{c} \rightarrow \hat{U} \cdot \vec{c}.$$

More specifically, any reversible operation on a two-level system can be expressed by an opera-

tor basis consisting of the three Pauli matrices  $\sigma_{x,y,z}$  and the identity  $\mathcal{I}$

$$\begin{aligned}\sigma_x &= \begin{pmatrix} 0 & 1 \\ 1 & 0 \end{pmatrix} & \sigma_y &= \begin{pmatrix} 0 & i \\ -i & 0 \end{pmatrix} \\ \sigma_z &= \begin{pmatrix} 1 & 0 \\ 0 & -1 \end{pmatrix} & \mathcal{I} &= \begin{pmatrix} 1 & 0 \\ 0 & 1 \end{pmatrix}\end{aligned}$$

acting on the state vector  $\vec{c}$ . The operation can also be visualized by rotations on the Bloch sphere where for example, the operation  $\hat{U} = \exp(-i\theta\sigma_x/2)$  implements a rotation around the x-Axis of the sphere by a rotation angle  $\theta$ .

For useful computation, a quantum register with multiple ( $N$ ) qubits is necessary. Such quantum registers differ from classical registers as they can exhibit correlations that have no counterpart in any classical system. Such correlations are widely known as entanglement where a state is *entangled* if it cannot be written as a product state of its constituents [31]. For a two-qubit entangled state follows

$$|\Psi_{12}\rangle \neq |\Psi_1\rangle \otimes |\Psi_2\rangle .$$

The state of an  $N$ -qubit quantum register can be described by a basis consisting of  $2^N$  vectors. One possible basis are number states where  $|i\rangle_N$  corresponds to the binary representation of  $i$  in an  $N$  qubit register. For example, the state  $|5\rangle_4$  of a four qubit register is  $|0101\rangle$ . This is analogous to a classical register, where the state of each bit in the register is defined by a number  $i$  ranging from 0 to  $2^N - 1$ . But in a quantum register, arbitrary superpositions of all number states are allowed and therefore the most general state of any  $N$ -qubit register can be expressed as

$$|\Psi\rangle_N = \sum_{k=0}^{2^N-1} c_k |k\rangle_N$$

with  $c_k$  being complex numbers satisfying  $\sum_k |c_k|^2 = 1$ . The state of the register is therefore described by the vector  $\vec{c} = (c_0, c_1, \dots, c_{2^N-1})^T$ .

One should note, that if  $|\Psi\rangle_N$  is a superposition of number states, it may be entangled, as it cannot be written as a product state of all constituents. However, not all superpositions of number states are necessarily entangled. Let's consider a two-qubit register and the states  $|\Psi\rangle = 1/\sqrt{2}(|2\rangle_2 + |3\rangle_2)$  and  $|\Phi\rangle = 1/\sqrt{2}(|1\rangle_2 + |2\rangle_2)$ . The state  $|\Psi\rangle$  can be written as a product state of both qubits  $1/\sqrt{2}(|10\rangle + |11\rangle) = 1/\sqrt{2}|1\rangle \otimes (|0\rangle + |1\rangle)$  whereas  $|\Phi\rangle = 1/\sqrt{2}(|10\rangle + |01\rangle)$  is clearly entangled. An extreme example is the equal superposition of all number states ( $c_K = 1/\sqrt{2^N}$ ) which is not an entangled state as it can be written as  $1/\sqrt{2^N}(|0\rangle + |1\rangle)^{\otimes N}$ . Therefore it is not always advantageous to use the number states for representing the state of a quantum register as certain properties such as entanglement cannot be identified easily.

Analogous to a single qubit, reversible operations on a multi-qubit register are described by unitary operations which can be defined by a  $2^N \otimes 2^N$  matrix acting on the state vector  $\vec{c}$

$$\vec{c} \rightarrow \hat{U}_N \cdot \vec{c} .$$

However, describing algorithms by their unitary operation is impractical. In classical information theory, algorithms are often displayed as a circuit built up of elementary logic gates. The

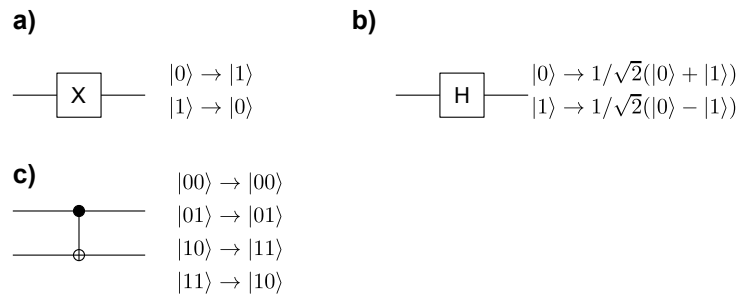


Figure 1.2.: Standard quantum circuit gates. a) Bit-flip operation exchanging the computational basis states. b) Hadamard gate mapping the computational basis state into an equal superposition. c) CNOT operation that performs a bit-flip on the target qubit depending on the state of the control qubit.

quantum mechanical counterpart to these gate sequences is known as the *circuit model* of quantum computation [30]. Analogous to classical computation, it has been shown that every unitary operation can be expressed as a sequence of operations from a finite set of quantum gates. This is crucial for the realization of a quantum computer: If a certain finite set of operations can be implemented it is possible to implement any unitary operation. Such a finite set is known as a *universal set of operations* [30].

A prominent universal set of operations is formed by arbitrary single qubit rotations and controlled NOT (CNOT) operations. The CNOT gate performs a bit-flip on the target qubit if the control qubit is in state  $|1\rangle$  otherwise the target qubit is left unchanged. The circuit representation of the CNOT and other common quantum gates is shown in figure 1.2.

It is easy to understand that performing single-qubit operations on any qubit is certainly not sufficient for universal quantum computing as it is not able to generate entanglement. Any operation that can be decomposed into single-qubit operations is called *local operation* whereas the CNOT operation is an *entangling operation*. The process of generating an entangled state with the aid of a Hadamard and a CNOT operation is performed as follows (see also figure 1.3): (i) The Hadamard creates an equal superposition of the basis states on the first qubit. (ii) The following CNOT operation performs now a bit-flip operation on the second qubit if the first qubit was in state  $|0\rangle$ . The final state of the procedure is one of the maximally entangled two-qubit Bell states. Mathematically, this process is described by<sup>2</sup>:

$$\vec{c}_{final} = \hat{U}_{CNOT} \cdot \hat{U}_{Hadamard} \cdot \vec{c}_{initial}$$

with the initial state being  $|00\rangle$  represented by the vector  $\vec{c}_{initial} = (1, 0, 0, 0)^T$ .

As will be shown in section 2.2, a different set of universal gates might be beneficial for a given physical system. For example in ion trap quantum computers, entangling operations following the ideas of Mølmer and Sørensen have been proven to yield the highest quality [32]. Unlike the CNOT gate, these operations act on the entire register simultaneously. Therefore one needs to find an efficient decomposition of operations for a given quantum circuit. This is a non-trivial problem which scales exponentially with the system size [33].

<sup>2</sup>Please note that the quantum circuit is acting from left to right whereas the matrix multiplication is performed from right to left.

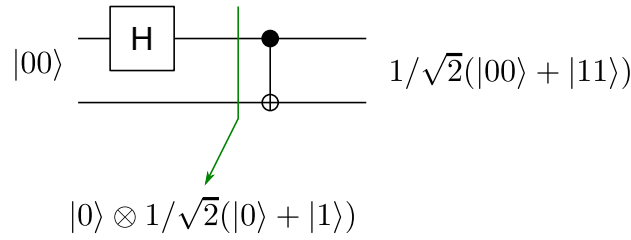


Figure 1.3.: Generating a two qubit entangled state with the aid of a CNOT operation.

At the end of a quantum algorithm it is necessary to learn about the state of the quantum register, which corresponds to performing measurements on the qubits. However, measurements in quantum mechanics, and therefore also in a quantum computer, are an interesting topic in their own right. At this point a brief description of measurements in quantum information processing in general will be presented. In section 3.3 it will be shown that measurements can be used to demonstrate the intriguing connection between the foundations of quantum mechanics and a quantum computer.

In the following *projective* measurements of an observable  $M$  are discussed, where the corresponding measurement operator  $\hat{M}$  is defined by its projectors  $\hat{P}_j$  with eigenvalues  $\lambda_j$  as

$$\hat{M} = \sum_j \lambda_j \hat{P}_j$$

The probability that the outcome  $j$  occurs when performing the measurement  $M$  on a given state  $|\Psi\rangle$  is then given by

$$p(j) = \langle \Psi | \hat{P}_j | \Psi \rangle .$$

Measurements on quantum systems are not only inherently probabilistic, they furthermore affect the state of the system: If a measurement gives the outcome  $j$ , it leaves the system in the corresponding eigenstate of the projector  $\hat{P}_j$ . Multiple initial states may lead to the identical state after the measurement if the same outcome was observed. This means, that in general a measurement is an irreversible process which will be covered in more detail in the next section. One should note that if the system was already in an eigenstate of one of the projectors  $\hat{P}_j$  before the measurement, the measurement will always result in outcome  $j$  and the state of the system is not affected as  $|\Psi\rangle = \hat{P}_j |\Psi\rangle$  holds.

Let's look now on reasonable measurements for a quantum computer. The most straightforward measurement of a single qubit is a projection onto the computational basis states with projectors  $\hat{P}_0 = |0\rangle\langle 0|$  and  $\hat{P}_1 = |1\rangle\langle 1|$ . Therefore, the measurement operator  $\hat{M}$  can be composed as

$$\hat{M} = \sigma_z = (-1)\hat{P}_1 + (+1)\hat{P}_0 .$$

For a multi-qubit register, this can be extended by using the projectors  $P_j = |j\rangle_N\langle j|$  corresponding to the number state  $|j\rangle_N$  as defined before. The measurement operator in the computational basis on the entire register is then defined by

$$\hat{M} = \sum_{j=0}^{2^N-1} \lambda_j \hat{P}_j = \bigotimes_{k=1}^N \sigma_z .$$

Of course measuring a register in the computational basis is not sufficient to gain the full information about its state. This can be achieved by using tomographic techniques which use the fact that a unitary operation  $\hat{U}$  followed by a measurement  $\hat{M}$  can be interpreted as a measurement of the operator  $\hat{N}$  defined as

$$\hat{N} = \hat{U} \cdot \hat{M} \quad (1.1)$$

which can be used to learn about the state  $|\Psi\rangle$  along different directions in the Hilbert space.

### 1.3. Incoherent states and processes in quantum information

The presented concepts of quantum information processing are based on coherent operations that can be completely reversed. In contrast the following section has a focus on irreversible or incoherent processes which arise if the quantum register is coupled to a classical environment. In the literature these processes are predominantly treated as unwanted noise but it is also possible to engineer a coupling to the environment that is able to generate useful quantum coherence as will be shown in section 4.1. An incoherent process acting on a system  $\mathcal{S}$  can be described by a coherent process acting on a larger system consisting of  $\mathcal{S}$  and an environment  $\mathcal{E}$  as sketched in figure 1.4a). The state of the system  $\mathcal{S}$  can then be constructed from the combined state by discarding the state of the environment as shown in figure 1.4b). In order to describe this reduction of the dimension a more general representation of the system's state than the vector formalism used before is required.

The density matrix formalism can describe single quantum states as the state vector formalism, but it is also capable of treating classical ensembles of quantum states. There, a single quantum state  $|\Psi\rangle$  is described by the operator  $\rho = |\Psi\rangle\langle\Psi|$ . Furthermore an ensemble of states is written as

$$\rho = \sum_i c_i |\Psi_i\rangle\langle\Psi_i|$$

with  $\sum c_i = 1$ . This ensemble can be interpreted as a mixture of states  $|\Psi_i\rangle$  each occurring with probability  $c_i$ . A measure whether a given matrix can be written as a quantum state in any possible basis or whether it really is a classical ensemble of states, is the *purity*  $\text{Tr}\rho^2$ . If the purity equals to one, then the density operator corresponds to a single quantum state and is called *pure*. Analogously, it follows that  $\rho$  cannot be written as a single quantum state if  $\text{Tr}\rho^2 < 1$  and is therefore denoted a *mixed* state.

Let's consider now a two-partite state  $|\Psi_{AB}\rangle$  where the combined density matrix  $\rho_{AB} = |\Psi_{AB}\rangle\langle\Psi_{AB}|$  is a pure state. We analyze the state of the system  $A$  if the information from system  $B$  is discarded. This process is described mathematically by a partial trace over the discarded system  $B$  [30]:

$$\rho_A = \text{Tr}_B (|\Psi_{AB}\rangle\langle\Psi_{AB}|) \quad (1.2)$$

It is reasonable that for a state that is *not* entangled ( $\rho_{AB} = \rho_A \otimes \rho_B$ ), the state after the partial trace is  $\rho_A = |\Psi_A\rangle\langle\Psi_A|$  which itself is pure again. For an entangled state this discarding process is not so straightforward but reveals fundamental properties of entanglement [31].

Let's now explain this process on the example of the simple two-qubit entangled state  $|\Psi_{AB}\rangle = 1/\sqrt{2} (|00\rangle + |11\rangle)$ . The density operator of the pure combined state is

$$\rho_{AB} = \frac{1}{2} (|00\rangle\langle 00| + |00\rangle\langle 11| + |11\rangle\langle 00| + |11\rangle\langle 11|) .$$

Now the partial trace over the system  $B$  has to be performed which reduces the elements of the density operator as follows [30]:

$$|a_1 b_1\rangle\langle a_2 b_2| \rightarrow |a_1\rangle\langle a_2| \cdot \langle b_1|b_2\rangle .$$

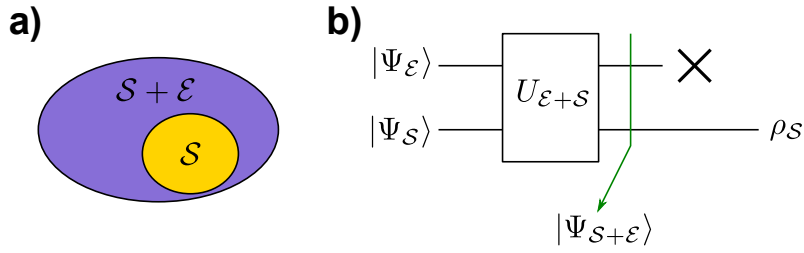


Figure 1.4.: a) Schematic of a system coupled to an environment. b) The time evolution of the system can be calculated by discarding the state of the environment.

Thus, the off-diagonal elements  $|00\rangle\langle 11|$  and  $|11\rangle\langle 00|$  do not contribute to the state  $\rho_A$  after the trace operation as  $\langle 0|1\rangle_B = 0$ . Discarding one qubit out of the state  $|\Psi_{AB}\rangle = 1/\sqrt{2} (|00\rangle + |11\rangle)$  results thus in the state

$$\rho_A = \frac{1}{2} (|0\rangle\langle 0| + |1\rangle\langle 1|) .$$

This state is a mixed state as  $\text{Tr}(\rho_A^2) = 1/2$ . Any pure entangled state is reduced to a classical mixture of states if the information of any subsystem is discarded. This fundamental property of entangled states can be used to describe the decoherence process where a state of the quantum system  $\mathcal{S}$  couples to a classical environment  $\mathcal{E}$ . If the system is entangled with the environment, then the reduced state of the system  $\rho_S$  is a mixed state. One can therefore describe the decoherence process of a quantum superposition being transferred towards a classical state by creating entanglement between the quantum system and a classical environment.

As mentioned above, a process acting on the combined system is described by a unitary operation acting on the combined system. The action of this process on the system  $\mathcal{S}$  is then

$$\rho_S \rightarrow \epsilon(\rho_S) = \text{Tr}_{\mathcal{E}} \left( \hat{U}_{\mathcal{E}+\mathcal{S}} \rho_S \otimes \rho_{\mathcal{E}} \hat{U}_{\mathcal{E}+\mathcal{S}}^\dagger \right) .$$

Describing this process with the full unitary  $\hat{U}_{\mathcal{E}+\mathcal{S}}$  is impractical as the dimensions of the environment are usually very large, often they are even infinite. Therefore, a method is required to describe the action on the system without any knowledge on the environment. In general, this is only feasible for Markov processes, where the environment has no “memory” [30]. With  $|e_o\rangle$  being the initial state of the environment and  $\{|e_k\rangle\}$  being a basis of the environment one can perform the partial trace over the environment

$$\epsilon(\rho) = \sum_k \langle e_k | \hat{U}_{\mathcal{E}+\mathcal{S}} (\rho_S \otimes |e_o\rangle\langle e_o|) \hat{U}_{\mathcal{E}+\mathcal{S}}^\dagger |e_k\rangle$$

One can then calculate the operators  $E_k = \langle e_k | \hat{U}_{\mathcal{E}+\mathcal{S}} |e_o\rangle$  acting on the system only. The entire process is then described by the following *operator sum* representation:

$$\epsilon(\rho) = \sum_k E_k \rho E_k^\dagger \quad (1.3)$$

where the Kraus operators  $E_k$  satisfy the completeness relation  $\sum E_k E_k^\dagger = \mathcal{I}$  [30]. A unitary, and therefore reversible, process acting only on the system  $\mathcal{S}$  can always be described by a single Kraus operator  $E_0 = \hat{U}_{\mathcal{S}}$ .

A simple example for an incoherent process on a single qubit is dephasing. There, the population of the state is not altered but the quantum coherence is destroyed. The process can be described by a random phase-flip that occurs with probability  $p$ . A phase-flip corresponds to applying the operation  $\sigma_z$  and therefore the Kraus operators are

$$E_0 = \sqrt{p} \sigma_z = \sqrt{p} \begin{pmatrix} 1 & 0 \\ 0 & -1 \end{pmatrix} \quad E_1 = \sqrt{1-p} \mathcal{I} = \sqrt{1-p} \begin{pmatrix} 1 & 0 \\ 0 & 1 \end{pmatrix} .$$

Therefore, a single-qubit density matrix  $\rho$  is mapped onto the state

$$\rho_p = \begin{pmatrix} \rho_{11} & (1-2p)\rho_{12} \\ (1-2p)\rho_{21} & \rho_{22} \end{pmatrix}$$

where all off-diagonal elements vanish for a full strength dephasing process with  $p = 0.5$ . Implementations of further incoherent processes are presented in section 4.1.

Any implementation of a quantum computer will show noise and therefore it will never be possible to generate an exactly pure state in the laboratory. Thus it is important to be able to characterize a mixed state, which means reconstructing the density matrix from measured data. A technique that allows one to gain complete knowledge about a density matrix is known as state tomography [34]. Such tomographic protocols require typically a well calibrated set of single-qubit operations.

We will now consider the state tomography of a single qubit to give an intuitive picture of its basic working principle. As described in section 1.2, a pure state of a single qubit can be illustrated by a vector on the surface of the Bloch sphere. This intuitive picture can be easily extended towards mixed states, which are located inside the Bloch sphere. It can be shown that for a pure state, the coordinates of the vector in the Cartesian basis correspond directly to the expectation values of the corresponding Pauli operator  $\sigma_{x,y,z}$ . For example, the projection of the vector on the z-axis is given by its expectation value of  $\sigma_z$ . The expectation value of the operator  $\hat{M}$  for a density matrix  $\rho$  is given by

$$\langle \hat{M} \rangle = \text{Tr}(\hat{M} \cdot \rho)$$

In order to gain information about the quantum state, the expectation values of all three Pauli operators are sufficient to completely describe the state as shown in figure 1.5. Usually, in quantum computers only the expectation value of  $\sigma_z$  can be measured directly, so the other Pauli operators need to be measured indirectly by performing coherent rotations before measuring in the computational basis as shown in equation (1.1).

After measuring all three expectation values, the state can be written as

$$\rho = \frac{1}{2} \left( \mathcal{I} + \vec{n} \cdot \vec{\Sigma} \right)$$

where  $\vec{\Sigma} = (\sigma_x, \sigma_y, \sigma_z)$  is the vector of Pauli matrices and  $\vec{n} = (\langle \sigma_x \rangle, \langle \sigma_y \rangle, \langle \sigma_z \rangle)$  are the expectation values of the Pauli operators.

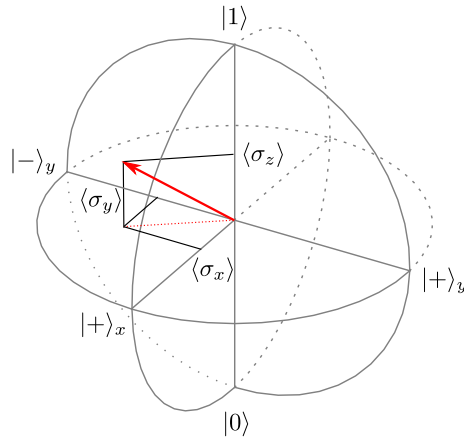


Figure 1.5.: The Bloch sphere representation of a mixed state of a single qubit. The expectation values of the three Pauli matrices  $\langle \sigma_{x,y,z} \rangle$  completely define the state.

This tomography technique can be straightforwardly extended to a multi-qubit system by measuring all permutations of observables

$$\begin{aligned}
 & \sigma_z \otimes \dots \otimes \sigma_z \otimes \sigma_z \\
 & \sigma_z \otimes \dots \otimes \sigma_z \otimes \sigma_x \\
 & \sigma_z \otimes \dots \otimes \sigma_z \otimes \sigma_y \\
 & \sigma_z \otimes \dots \otimes \sigma_x \otimes \sigma_z \\
 & \dots \\
 & \sigma_y \otimes \dots \otimes \sigma_y \otimes \sigma_y \cdot
 \end{aligned}$$

A major drawback of these technique is that the resources needed to perform this tomography scale exponentially with the size of the quantum register as the number of required measurement settings is  $3^N$  [34]. Lately, more efficient techniques have been developed that promise more favorable scaling at the cost of omitting information on the quantum state [35, 36]. These techniques cannot provide full information on any state but they are particularly useful for certain classes of states.

Once the actual generated state  $\rho_{exp}$  has been reconstructed, it has to be compared to the ideal target state  $\rho_{id}$ . The most commonly used measure for comparing two states is the fidelity which can be simply calculated as

$$F = \text{Tr}(\rho_{exp} \cdot \rho_{id})$$

if the target state is a pure state. The fidelity can be interpreted as the probability to generate the desired state. As different problems require different distance measures there exists a huge variety of them [37]. Similar to a density matrix also a quantum process can be fully characterized using quantum process tomography [38]. There, multiple state-tomographies are performed for a set of input states.



## 2. A quantum information processor with trapped ions

### 2.1. Introduction to ion traps

... we never experiment with one electron or atom or molecule. In thought experiments we sometimes assume that we do; this invariably entails ridiculous consequences... we are not experimenting with single particles, any more than we can raise Ichtyosauria in the zoo.

This statement of Erwin Schrödinger in 1952 should not hold for a long time, as it became refuted when the experimental group around Hans Dehmelt stored a single electron in a Penning trap in 1973 [39, 40]. In the meantime, single charged electrons, atoms and molecules are routinely trapped and manipulated due to the advancement of laser-cooling and ion trapping techniques [22].

Trapping a charged particle in all three dimensions is not trivial as Earnshaw's theorem<sup>1</sup> states that a charged particle cannot be confined by static electric and magnetic fields. The quadrupole ion trap, invented by Paul in 1953, is able to sidestep this problem as it uses rapidly varying electric fields to confine charged particles. In such a trap, a quasi-static potential is generated if the oscillations are fast enough so that the particle cannot follow. Since its invention, a constant trap development cycle has begun which was accompanied by the impressive technological progress in laser technology and the discovery of laser-cooling techniques. Today's ion traps deliver us the required precision to routinely perform experiments on a single or a few particles.

A linear Paul trap as sketched in figure 2.1a) consists of four rods and two endcaps. The rods are connected to either ground potential or to an oscillating voltage source. Would the rods be at a constant voltage, their quadrupole field would create a saddle potential in the  $xy$ -plane as shown in figure 2.1b). If a temporally oscillating voltage is applied between the different rods, the potential starts oscillating as sketched in figure 2.1a). If this oscillation is fast enough, a charged particle can be trapped in the  $xy$ -plane of the trap which we denote the radial directions of the trap. For trapping the particle in the axial dimension along the  $z$ -axis, an additional constant repulsive field on the endcaps is sufficient [41].

The motion of a single particle inside the trap can be described by two-distinct types of motion: Micromotion, which is the residual motion of the particle due to the oscillating electrical driving fields and the secular motion which corresponds to the motion of the particle in the harmonic

---

<sup>1</sup>Note that Earnshaw's theorem is an application of the Gauss law.

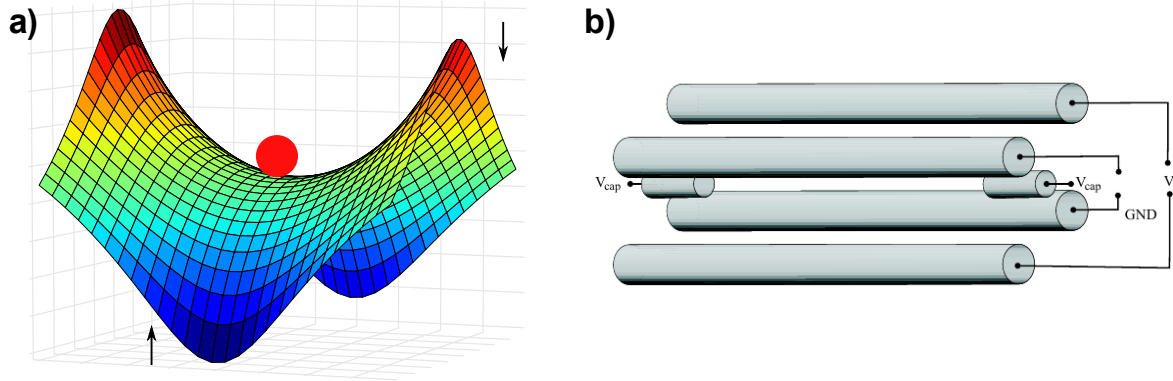


Figure 2.1.: a) Potential generated by a static voltage applied to hyperbolic electrodes. When an oscillating field is applied to the electrodes, the saddle potential oscillates as indicated by the arrows. b) Sketch of a linear Paul trap with four linear rods and two endcaps.

oscillator due to the constant pseudo-potential of the trap. Micromotion can be suppressed by placing the particle in the minimum of the saddle potential generated by the rods. This is accomplished by applying a constant voltage to additional compensation electrodes between the rods. Their field is used to push the equilibrium position of the ion towards the minimum of the potential. In a well designed trap, the amplitude of the micromotion can be suppressed to a level where it does not need to be taken into account to calculate the dynamics of the particles in the trap [41].

The secular motion corresponds to the motion of a particle in a harmonic oscillator and therefore it can be described by normal modes in three dimensions. The parameters are chosen so that the oscillating frequencies in the radial directions are larger than the axial frequency. If the separation of the oscillation frequencies of the axial and radial modes is large enough, it is possible to address the axial mode spectroscopically and thus the system can be modeled as a single mode harmonic oscillator. The axial trapping potential can be stabilized with less effort than the radial potential and thus the secular motion along the  $z$ -axis is preferably used for quantum information processing [41].

The idealized system of an ion trap quantum computer consists of two-level atoms that are coupled to a single mode harmonic oscillator. We will now briefly investigate the interaction of a single two-level ion confined in a single mode harmonic oscillator with an external light field. A more in depth treatment of this subject is given in the PhD thesis of Christian Roos [42]. The Hamiltonian of the ion-trap system without an external field is given by

$$\begin{aligned}
 H_0 &= H_{atom} + H_{trap} \\
 H_{atom} &= \frac{1}{2} \hbar \omega_0 \sigma_z \\
 H_{trap} &= \frac{p^2}{2m} + \frac{1}{2} m \omega_z^2 z^2 = \hbar \omega_z \left( a^\dagger a + \frac{1}{2} \right)
 \end{aligned}$$

where  $\omega_0$  corresponds to the energy difference of the two-level system,  $m$  is the mass of the particle and  $\omega_z$  is the frequency of the secular oscillator mode. It should be noted, that the

state of the two-level system does not couple with the harmonic oscillator in the absence of an external field. This coupling can be introduced by applying a light field onto the atom. The atom-light interaction can be described by the interaction Hamiltonian

$$H_{int} = \frac{\hbar}{2}\Omega(\sigma_+ + \sigma_-)\left(e^{i(kx-\omega t+\phi)} + e^{-i(kx-\omega t+\phi)}\right)$$

where the Rabi frequency  $\Omega$  is determined by the strength of the driving field and the coupling strength of the used transition. This interaction can be written in terms of raising and lowering operators of the harmonic oscillators:

$$H_{int} = \frac{\hbar}{2}\Omega\left(\sigma_+ e^{-i(\eta(a+a^\dagger)+\omega t+\phi)} + \sigma_- e^{i(\eta(a+a^\dagger)+\omega t+\phi)}\right)$$

with the Lamb-Dicke parameter  $\eta = k\sqrt{\frac{\hbar}{2m\omega_z}}$ .

If the Lamb-Dicke parameter is small  $\eta \ll 1$ , it is possible to perform a first order approximation of  $e^{\eta x} \approx 1 + \eta x$  and one can rewrite the Hamiltonian in a frame rotating with the two-level transition frequency  $\omega_o$ . This yields the fundamental interaction Hamiltonian for trapped ion quantum computing:

$$H_{int} = \frac{\hbar}{2}\Omega\sigma_+\left(1 + \eta(a e^{-i\omega_z t+\phi} + a^\dagger e^{i\omega_z t+\phi})\right)e^{i\delta t} + \text{H.c.} \quad (2.1)$$

where  $\delta = \omega_o - \omega$  is the detuning of the driving field from the two-level system transition frequency.

From this Hamiltonian, one can immediately identify three interesting cases namely  $\delta = 0$  and  $\delta = \pm\omega_z$ . For  $\delta = 0$  the harmonic oscillator can be neglected leading to:

$$H_c = \frac{\hbar}{2}\Omega(e^{i\phi}\sigma_+ + e^{-i\phi}\sigma_-) = \Omega\sigma_\phi$$

with  $\sigma_\phi = \sigma_y \sin \phi + \sigma_x \cos \phi$ . Since the motional state of the ion is not changed, this transition is denoted *carrier*. If such a resonant field is applied for a duration  $t$ , the corresponding unitary operation is

$$U(t) = e^{-i\sigma_\phi t}$$

which corresponds to rotations around the rotation axis  $\phi$  in the Bloch sphere. The rotation angle of this operation is determined by the duration when the light field is applied and the rotation axis is given by the phase  $\phi$  of the light field. With this operation it is possible to perform any arbitrary single-qubit operation.

The next interesting case is when the light field is detuned by exactly the axial transition frequency:  $\delta = +\omega_z$ . Then the Hamiltonian is

$$H_+ = \frac{\hbar}{2}\Omega\eta\sqrt{n+1}(e^{i\phi}a^\dagger\sigma_+ + e^{-i\phi}a\sigma_-)$$

which corresponds exactly to the anti-Jaynes-Cummings Hamiltonian known from quantum optics [43]. In an ion-trap system these transitions are called *blue sidebands* and add one phonon to the system when performing a spin-flip as outlined in figure 2.2b).

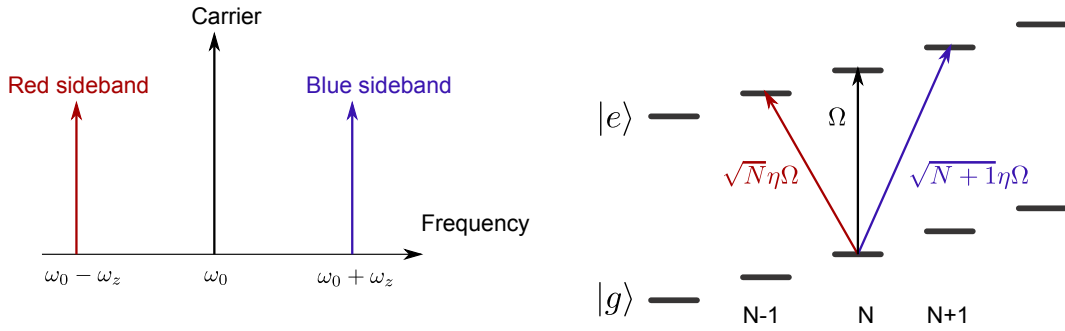


Figure 2.2.: a) Schematic spectrum showing the blue and red sideband transitions. b) Ladder scheme showing the blue and red sideband transitions with the corresponding coupling strengths.

The last case is  $\delta = -\omega_z$  leading to the Hamiltonian:

$$H_- = \frac{\hbar}{2}\Omega\eta\sqrt{n}(e^{i\phi}\sigma_+a + e^{-i\phi}a^\dagger\sigma_-)$$

which corresponds to the Jaynes-Cummings Hamiltonian. Analog to above, this transition is called *red sideband* as it removes a phonon upon a transition from the ground to the excited state. The resulting spectrum including these three transitions and the respective coupling strengths are shown in figure 2.2.

Naturally, a quantum information processor requires more than a single ion inside a trap. Let's consider multiple trapped ions where the axial trap frequency is smaller than the two radial trap frequencies. In such a system, the ions arrange themselves in a linear string along the axial direction [44]. Analog to a classical harmonic oscillator, the movement of the ions can be described by normal modes in three directions. The possible axial modes for a register of two and three ions are shown in figure 2.3. Again, we consider now only the modes in the axial directions and there, the mode corresponding to the smallest frequency is the center-of-mass mode, where all ions move synchronously. This mode is ideally suited as a databus to exchange information between individual ions inside the string as each individual ion can transfer information onto and from the databus with equal coupling strength.

There exist two distinct ways of performing operations on such a register. First, the manipulating light field may act only on a single ion. Mathematically, this can be described by exchanging the single-qubit Pauli matrices with a corresponding matrix describing an operation on the entire register but affecting only on the addressed qubit  $j$ :

$$\sigma_\pm \rightarrow \sigma_\pm^{(j)}$$

In the second approach all ions see the identical light field. It can be shown that considering only the COM mode, the single-particle Hamiltonians as derived above can still be used when the single particle operators are exchanged with a collective operator

$$\sigma_\pm \rightarrow S_\pm = \sum_{j=1}^N \sigma_\pm^{(j)}$$

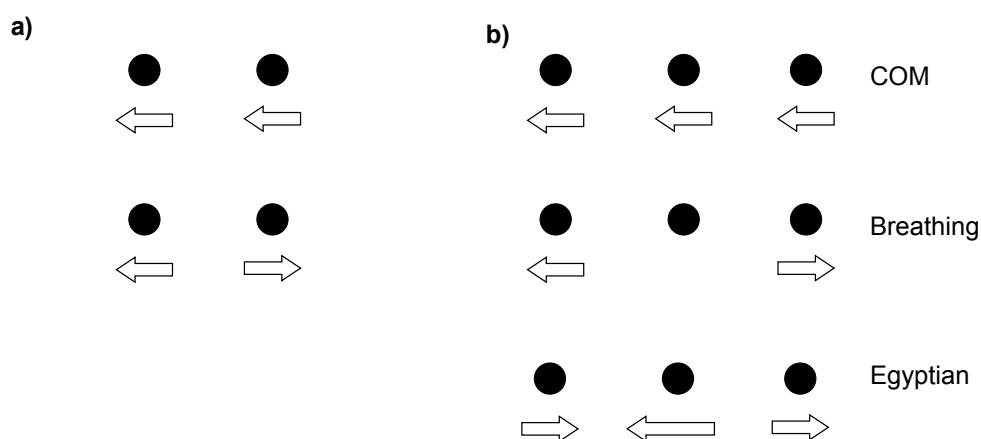


Figure 2.3.: Axial normal modes of a) 2 and b) 3 ions in a Paul trap

where  $\sigma_{\pm}^{(j)}$  is again the operator acting on ion  $j$ .

In the following publication the used ion species and our experimental system will be described extensively. First, the  $^{40}\text{Ca}^+$  ion is introduced and the qubit and detection transitions are described. Then, our universal set of operations is presented which is immediately extended to include incoherent operations. Furthermore, the experimental setup is briefly described, followed by an in detail treatment of the noise sources in our system. Finally, it is shown that our complete toolbox can be exploited to realize an order finding algorithm which lies at the heart of Shor's factoring algorithm.

## 2.2. Publication: A quantum information processor with trapped ions

### A quantum information processor with trapped ions<sup>2</sup>

To be published; Preprint available at arXiv:1308.3096

Philipp Schindler<sup>1</sup>, Daniel Nigg<sup>1</sup>, Thomas Monz<sup>1</sup>, Julio T. Barreiro<sup>1</sup>,  
Esteban Martinez<sup>1</sup>, Shannon X. Wang<sup>3</sup>, Stephan Quint<sup>1</sup>, Matthias F. Brandl<sup>1</sup>  
Volckmar Nebendahl<sup>4</sup>, Christian F. Roos<sup>2</sup>, Michael Chwalla<sup>1,2</sup>, Markus Hennrich<sup>1</sup> and Rainer  
Blatt<sup>1,2</sup>

<sup>1</sup>Institut für Experimentalphysik, University of Innsbruck,  
Technikerstr. 25, A-6020 Innsbruck, Austria,

<sup>2</sup>Institut für Quantenoptik und Quanteninformation  
Österreichische Akademie der Wissenschaften,  
Otto-Hittmair-Platz 1, A-6020 Innsbruck, Austria

<sup>3</sup>Massachusetts Institute of Technology, Center for Ultracold Atoms,  
Department of Physics, 77 Massachusetts Avenue, Cambridge, MA, 02139, USA  
Otto-Hittmair-Platz 1, A-6020 Innsbruck, Austria

<sup>4</sup>Institut für Theoretische Physik, University of Innsbruck,  
Technikerstr. 25, A-6020 Innsbruck, Austria,

Quantum computers hold the promise to solve certain problems exponentially faster than their classical counterparts. Trapped atomic ions are among the physical systems in which building such a device seems viable. In this work we present a small-scale quantum information processor based on a string of  $^{40}\text{Ca}^+$  ions confined in a macroscopic linear Paul trap. We review our set of operations that includes non-coherent operations allowing to realize arbitrary Markovian processes. In order to build a larger quantum information processor it is mandatory to reduce the error rate of the available operations which is only possible if the physics of the noise processes is well understood. We identify the dominant noise sources in our system and discuss their effects on different algorithms. Finally we demonstrate how our entire set of operations can be used to facilitate the implementation of an algorithm by the examples of a quantum Fourier transform and the quantum order finding algorithm.

### 2.2.1. Tools for quantum information processing in ion traps

#### Quantum information processing in ion traps

A quantum computer (QC) promises to solve certain problems exponentially faster than any classical computer. Its development was boosted by the discovery of Shor's algorithm to factorize large numbers and the insight that quantum error correction allows arbitrary long algorithms

---

<sup>2</sup>The author of the present thesis measured and analyzed the data, and wrote the manuscript

even in a noisy environment [4, 13, 14, 45]. These findings initiated major experimental efforts to realize such a quantum computer in different physical systems[8–10]. One of the most promising approaches utilizes single ionized atoms confined in Paul traps. Here, the internal state of each ion represents the smallest unit of quantum information (a qubit). Multiple qubit registers are realized by a linear ion string and the interaction between different ions along the string is mediated by the Coulomb interaction [6, 41, 44]. In this work we present a review of a small scale quantum information processor based on a macroscopic linear Paul trap [46]. The work is structured as follows: The first section summarizes the available coherent and non-coherent operations while in section 2.2.2 the experimental setup is reviewed. In section 2.2.3 the noise sources are characterized and finally, in section 2.2.4 we discuss examples of implemented algorithms using the full set of operations.

### The qubit - $^{40}\text{Ca}^+$

A crucial choice for any QC implementation is the encoding of a qubit in a physical system. In ion trap based QCs, two distinct types of qubits have been explored: (i) Ground-state qubits where the information is encoded in two hyperfine or Zeeman sublevels of the ground state [41], and (ii) Optical qubits where the information is encoded in the ground state and an optically accessible metastable excited state [46]. The two types of qubits require distinct experimental techniques where ground-state qubits are manipulated with either two-photon Raman transitions or by direct microwave excitation [41]. In contrast, operations on optical qubits are performed via a resonant light field provided by a laser [46, 47]. Measuring the state of the qubits in a register is usually performed via the electron shelving method using an auxiliary short-lived state for both qubit types [41]. In the presented setup we use  $^{40}\text{Ca}^+$  ions, which contain both, an optical qubit for state manipulation and a ground-state qubit for a quantum memory. Figure 2.4a) shows a level scheme of the  $^{40}\text{Ca}^+$  ions including all relevant energy levels.

Our standard qubit is encoded in the  $4S_{1/2}$  ground state and the  $3D_{5/2}$  metastable state where the natural lifetime of the  $3D_{5/2}$  state ( $\tau_1 = 1.1s$ ) provides an upper limit to the storage time of the quantum information. The  $4S_{1/2}$  state consists of two Zeeman sublevels ( $m = \pm 1/2$ ) whereas the  $3D_{5/2}$  state has six sublevels ( $m = \pm 1/2, \pm 3/2, \pm 5/2$ ). This leads to ten allowed optical transitions given the constraint that only  $\Delta m = 0, 1, 2$  are possible on a quadrupole transition. The coupling strength on the different transitions can be adjusted by varying the polarization of the light beam and its angle of incidence with respect to the quantization axis set by the direction of the applied magnetic field. Usually we choose the  $4S_{1/2}(m_j = -1/2) = |S\rangle = |1\rangle$  and the  $3D_{5/2}(m_j = -1/2) = |D\rangle = |0\rangle$  as the computational basis states because the transition connecting them is the least sensitive to fluctuations in the magnetic field. Furthermore it is possible to store quantum information in the two Zeeman substates of the  $4S_{1/2}$  ground-state which are not subject to spontaneous decay ( $4S_{1/2}(m_j = -1/2) = |1\rangle_Z$  and  $4S_{1/2}(m_j = +1/2) = |0\rangle_Z$ ).

The projective measurement of the qubit in the computational basis is performed via the  $4S_{1/2} \leftrightarrow 4P_{1/2}$  transition at a wavelength of 397nm. If the qubit is in a superposition of the qubit states, shining in a near resonant laser at the detection transition projects the ion's state either in the  $4S_{1/2}$  or the  $3D_{5/2}$  state. If the ion is projected into the  $4S_{1/2}$  state, a closed cycle transition is

## 2. A quantum information processor with trapped ions

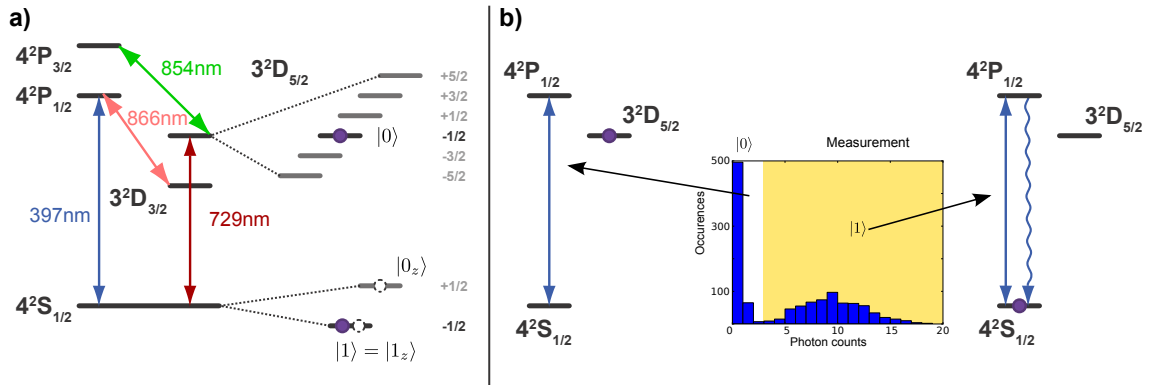


Figure 2.4.: (a) Level scheme of  $^{40}\text{Ca}^+$ . Solid circles indicate the usual optical qubit ( $4S_{1/2}(m_j = -1/2) = |1\rangle$  and  $3D_{5/2}(m_j = -1/2) = |0\rangle$ ). Open circles indicate the ground state qubit that avoids spontaneous decay ( $4S_{1/2}(m_j = -1/2) = |1\rangle_Z$  and  $4S_{1/2}(m_j = +1/2) = |0\rangle_Z$ ). (b) Schematic representation of electron shelving detection. The histogram shows the detected photon counts from projections onto both states during the detection interval. It can be seen that it is possible to distinguish the two different outcomes. The highlighted area illustrates the threshold whether the stat is detected as  $|0\rangle$  or  $|1\rangle$ .

possible and the ion will fluoresce as sketched in figure 2.4(b). It is however still possible that the decay from  $4P_{1/2}$  leads to population being trapped in the  $3D_{3/2}$  state that needs to be pumped back to the  $4P_{1/2}$  with light at 866nm. Fluorescence is then collected with high numerical aperture optics and single-photon counting devices as described in section 2.2.2. If the ion is projected into the  $3D_{5/2}$  state though, it does not interact with the light field and no photons are scattered. Thus the absence or presence of scattered photons can be interpreted as the two possible measurement outcomes which can be clearly distinguished as shown in the histogram in figure 2.4b). In order to measure the probability  $p_{|1\rangle}$  to find the qubit in  $4S_{1/2}$ , this measurement needs to be performed on multiple copies of the same state. In ion-trap QCs these multiple copies are produced by repeating the experimental procedure  $N$  times yielding the probability  $p_{|1\rangle} = n(|1\rangle)/N$  where  $n(|1\rangle)$  is the number of bright outcomes. This procedure has a statistical uncertainty given by the projection noise  $\Delta p_{|1\rangle} = \sqrt{p_{|1\rangle}(1 - p_{|1\rangle})/N}$  [48]. Depending on the required precision, the sequence is therefore executed between 50 and 5000 times.

Preparing the qubit register in a well defined state is a crucial prerequisite of any quantum computer. In our system this means (i) preparing the qubit in one of the two Zeeman levels of the ground state and (ii) cooling the motional state of the ion string in the trap to the ground state. The well established technique of optical pumping is used to prepare each ion in the  $m_j = -1/2$  state of the  $4S_{1/2}$  state [46]. In our setup two distinct methods for optical pumping are available: (i) Polarization dependent optical pumping by a circularly polarized laser beam resonant on the  $4S_{1/2} \leftrightarrow 4P_{1/2}$  transition as shown in figure 2.5a) and (ii) frequency selective optical pumping via the Zeeman substructure of the  $3D_{5/2}$  state as depicted in figure 2.5b). Here, the transfer on the qubit transition at 729nm is frequency selective. Selection rules ensure that depletion the of the  $3D_{5/2}(m_j = -3/2)$  level via the  $4P_{3/2}$  effectively pumps the population into the  $4S_{1/2}(m_j = -1/2)$  state. The second part of the initialization procedure prepares the

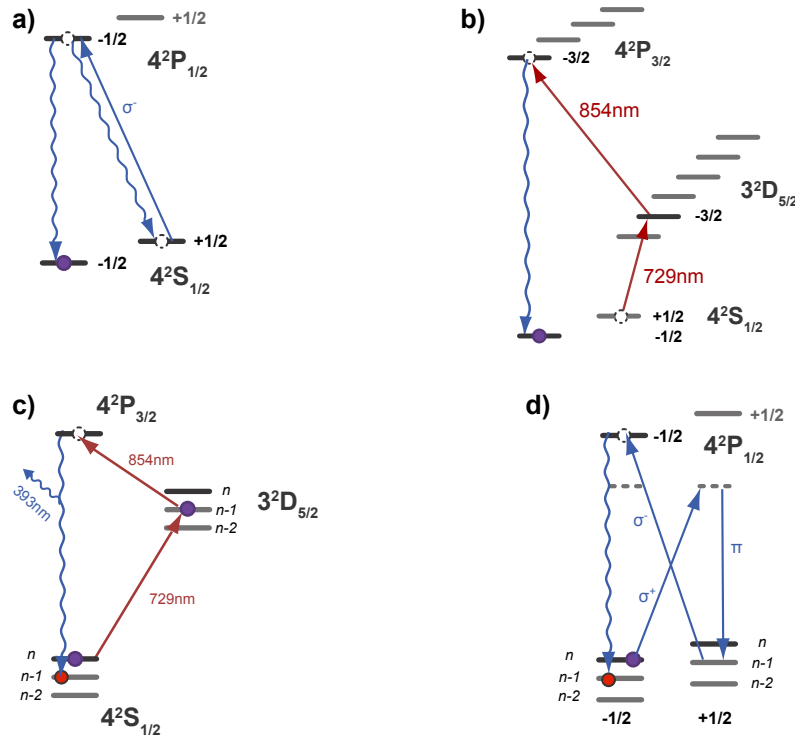


Figure 2.5.: Schematic view of optical pumping which is (a) polarization selective and (b) frequency selective (c) Sideband cooling on the qubit transition. The light resonant with the  $3D_{5/2} \rightarrow 4P_{3/2}$  transition is used to tune the effective linewidth of the excited state leading to an adiabatic elimination of the  $3D_{5/2}$  state. (d) Scheme for sideband cooling utilizing a Raman transition. Here, the  $\sigma^-$  light performs optical pumping which corresponds to the spontaneous decay on the optical transition.

ion string into the motional ground state which requires multiple laser-cooling techniques. We use a two-step process where the first step consists of Doppler cooling on the  $4S_{1/2} \leftrightarrow 4P_{1/2}$  transition that leads to a mean phonon number of  $\langle n \rangle \approx 10$ . The motional ground state is subsequently reached with sideband cooling techniques [49]. In our system, the necessary two-level system can be either realized on the narrow qubit transition [50] or as a Raman process between the two ground states via the  $4P_{1/2}$  level [41, 46]. A crucial parameter, determining the cooling rate, is the linewidth of the actual cooling transition [49]. When cooling on the long-lived optical transition, the excited state lifetime needs to be artificially shortened in order to adjust the effective linewidth of the transition. This is realized by repumping population from the  $3D_{5/2}$  state to the  $4S_{1/2}$  state via the  $4P_{3/2}$  level with light at 854nm, as outlined in figure 2.5c) [49]. The procedure using the Raman transition is outlined in figure 2.5d). Here, the spontaneous decay is replaced by optical pumping as used for state preparation [41, 51]. In principle, this cooling technique allows for faster cooling rates as the coupling strength to the motional mode, described by the Lamb-Dicke parameter, increases for smaller wavelengths. More importantly, it has the advantage that it can be applied within a quantum algorithm without disturbing the quantum state of idling qubits when the population of the  $4S_{1/2}$  state is transferred to a Zeeman substate of the excited state that is outside the computational basis, for example

$3D_{5/2}(m_j = -5/2) = |D'\rangle$  [28].

### The universal set of gates

With a universal set of gates at hand, every unitary operation acting on a quantum register can be implemented [30]. The most prominent example for such a set consists of arbitrary single-qubit operations and the controlled NOT (CNOT) operation. However, depending on the actual physical system, the CNOT operation may be unfavorable to implement and thus it may be preferable to choose a different set of gates. In current ion trap systems, entangling operations based on the ideas of Mølmer and Sørensen have achieved the highest fidelities [27, 32, 52] which, in conjunction with single-qubit operations, form a universal set of gates. In order to implement all necessary operations, we use a wide laser beam that illuminates the entire register uniformly and a second, tightly focused, laser beam to address each ion. Interferometric stability between the two beams would be required, if arbitrary single-qubit operations were performed with this addressed beam in addition to the global MS operations. To circumvent this demanding requirement, the addressed beam is only used for inducing localized phase shifts caused by the AC-Stark effect. Using an off-resonant light field causing AC-Stark shifts has the advantage that the phase of the light field does not affect the operations and thus no interferometric stability is needed. The orientation of the two required laser beams is shown in figure 2.6a).

Applying an off-resonant laser light with Rabi frequency  $\Omega$  and detuning  $\delta$  onto a the  $j$ -th ion modifies its qubit transition frequency by an AC-Stark shift of  $\delta_{AC} = -\frac{\Omega^2}{2\Delta}$ . This energy shift causes rotations around the Z axis of the Bloch sphere and the corresponding operations on ion  $j$  can be expressed as

$$S_z^{(j)}(\theta) = e^{-i\theta\sigma_z^{(j)}/2}$$

where the rotation angle  $\theta = \delta_{AC}t$  is determined by the AC-Stark shift and the pulse duration. As the  $^{40}\text{Ca}^+$  ion is not a two-level system, the effective frequency shift originates from AC-Stark shifts on multiple transitions. We choose the laser frequency detuning from any  $4S_{1/2} \leftrightarrow 3D_{5/2}$  transition to be 20MHz. There, the dominating part of the AC-Stark shift originates from coupling the far off-resonant transitions from  $4S_{1/2}$  to  $4P_{1/2}$  and  $4P_{3/2}$  as well as from  $3D_{5/2}$  to  $4P_{3/2}$  [53].

The second type of non-entangling operations are collective resonant operations using the global beam. They are described by

$$R_\phi(\theta) = e^{-i\theta S_\phi/2}$$

where  $S_\phi = \sum_{i=0}^N (\sigma_x^{(i)} \cos \phi + \sigma_y^{(i)} \sin \phi)$  is the sum over all single-qubit Pauli matrices  $\sigma_{x,y}^{(i)}$  acting on qubit  $i$ . The rotation axis on the Bloch sphere  $\phi$  is determined by the phase of the light field and the rotation angle  $\theta = t/\Omega$  is fixed by the pulse duration  $t$  and the Rabi frequency  $\Omega$ . Together with the single-qubit operations described above this allows us to implement arbitrary non-entangling operations on the entire register.

The entangling MS gate operation completes the universal set of operations. The ideal action of the gate on an N-qubit register is described by

$$MS_\phi(\theta) = e^{-i\theta S_\phi^2/4}.$$

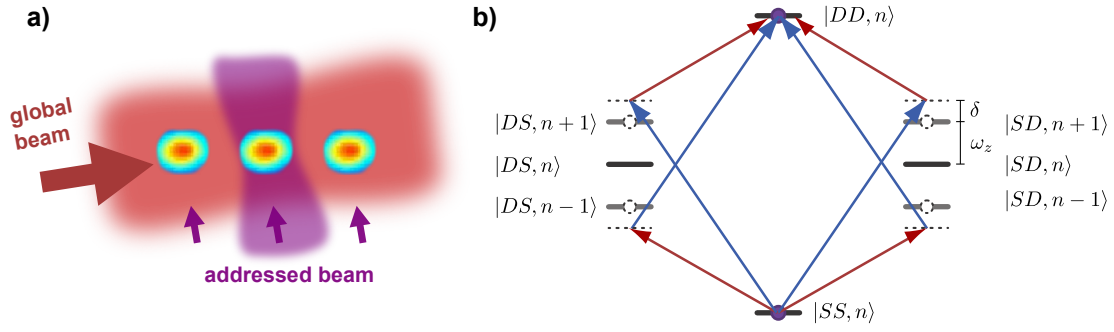


Figure 2.6.: a) Schematic view of the laser beam geometry for qubit manipulation. b) Schematic level scheme of a Mølmer Sørensen type interaction. The bichromatic light field couples the states  $|SS, n\rangle$  with  $|DD, n\rangle$  via the intermediate states  $|SD, n \pm 1\rangle$  and  $|DS, n \pm 1\rangle$  with a detuning  $\delta$ .

For any even number of qubits the operation  $MS_\phi(\pi/2)$  maps the ground state  $|00..0\rangle$  directly onto the maximally entangled GHZ state  $1/\sqrt{2}(|00..0\rangle + e^{i\phi}|11..1\rangle)$ . For an odd number of ions the produced state is still a maximally GHZ-class entangled state which can be transferred to a GHZ state by an additional collective local operation  $R_\phi(\pi/2)$ .

Implementing the MS gate requires the application of a bichromatic light field  $E(t) = E_+(t) + E_-(t)$  with constituents  $E_\pm = E_0 \cos((\omega_0 \pm (w_z + \delta))t)$  where  $\omega_0$  is the qubit transition frequency,  $\omega_z$  denotes the frequency of the motional mode and  $\delta$  is an additional detuning. The level scheme of the MS operation acting on a two-ion register is shown in figure 2.6b). Mølmer and Sørensen showed that if the detuning from the sideband  $\delta$  equals the coupling strength on the sideband  $\eta\Omega$  the operation  $MS(\pi/2)$  is performed when the light field is applied for a duration  $t = 2\pi/\delta$ .

However, implementing MS operations with rotation angles  $\pi/2$  is not sufficient for universal quantum computation. Arbitrary rotation angles  $\theta$  can be implemented with the same detuning  $\delta$  by adjusting the Rabi frequency on the motional sideband to  $\eta\Omega = \delta \theta / (\pi/2)$ . Due to this fixed relation between the rotation angle and the detuning, the gate operation needs to be optimized for each value of  $\theta$ . In practice this optimization is a time-consuming task and thus the gate is optimized only for the smallest occurring angle in the desired algorithm. Gate operations with larger rotation angles are realized by a concatenation of multiple instances of the already optimized operation.

If the physical system would consist of a two-level atom coupled to a harmonic oscillator the AC-Stark introduced by one off-resonant light field would be perfectly compensated by its counterpart in the bichromatic field. However,  $^{40}\text{Ca}^+$  shows a rich level structure where due to the additional Zeeman levels and coupling to the other  $4P$  states an additional AC-Stark shift is introduced [53]. This shift changes the transition frequency between the two qubit states which has the effect that the detuning from the sideband transition  $\delta$  is not equal for both constituents of the bichromatic light field. This would degrade the quality of the operation drastically and thus the shift has to be compensated for which can be achieved by two distinct techniques [54]: (i) The center frequency of the bichromatic light field can be shifted or (ii) the light intensity of the two constituents can be unbalanced to induce a Stark shift on the carrier transition which

compensates the unwanted Stark shift. Depending on the application, one compensation method is favorable over the other. Method (i) makes it easier to optimize the physical parameters to achieve very high gate fidelities but leads to an additional global rotation around  $\sigma_z$  which is tedious to measure and compensate for in a complex algorithm. This can be avoided by method (ii) but the compensation is not independent of the motional state leading to a slightly worse performance [54]. Therefore, we generally choose method (i) if the goal is to solely generate a GHZ state whereas method (ii) is favorable if the gate is part of a complex algorithm.

In general an algorithm requires operations with positive and negative values of the rotation angles for the available operations. For the resonant  $R_\phi(\theta)$  operation both signs of  $\theta$  can be realized by changing the phase of the light field since  $e^{-i(-\theta)S_\phi} = e^{-i\theta S_{(\pi+\phi)}}$  which is not possible for MS operations as  $S_\phi^2 = S_{\phi+\pi}^2$ . The sign of the rotation of the MS operation angle can only be adjusted by choosing the sign of the detuning  $\delta$  [55]. However, performing MS operations with positive and negative detunings results in a more complex setup for generating the required RF signals and also a considerable overhead in calibrating the operation. Therefore it can be favorable to implement negative  $\theta$  by performing  $MS_\phi(\pi - |\theta|)$  which works for any odd number of ions whereas for an even number of ions, an additional  $R_\phi(\pi)$  operation is required [55]. With this approach the quality of operations with negative rotation angles is reduced but the experimental overhead is avoided.

### Optimized sequences of operations

Typically, quantum algorithms are formulated as quantum circuits where the algorithm is build up from the standard set of operations containing single qubit operations and CNOT gates. Implementing such an algorithm is straightforward if the implementation can perform these standard gate operations efficiently. Our set of gates is universal and thus it is possible to build up single qubit and CNOT operations from these gates. However, it might be favorable to decompose the desired algorithm directly into gates from our implementable set as the required sequence of operations might require less resources. This becomes evident when one investigates the operations necessary to generate a four-qubit GHZ state. Here, a single MS gate is able to replace four CNOT gates.

The problem of breaking down an algorithm into an optimized sequence of given gate operations was first solved by the NMR quantum computing community. There, a numerical optimal control algorithm was employed to find the sequence of gate operations that is expected to yield the lowest error rate for a given unitary operation [56]. This algorithm optimizes the coupling strength of the individual parts of the Hamiltonian towards the desired sequence. Unfortunately the NMR algorithm is not directly applicable to our ion trap system as the set of operations differ. In an NMR system the interactions are present at all times, only their respective strengths can be controlled. This allows for an efficient optimization as there is no time order of the individual operations. This is not true for current ion trap quantum computers where only a single operation is applied at a time which makes it necessary to optimize the order of the operations within the sequence in addition to the rotation angles. Furthermore, the same type of operation might appear several times at different positions. Thus we modified the algorithm so that it starts from a long random initial sequence and optimizes the rotation angles of the operation.

This optimization converges towards the desired algorithm, if the required sequence is a subset of this random initial sequence. The key idea of our modification is that rotation angle of operations that are included in the random initial sequence but are not required for the final sequence shrinks during the optimization. If the rotation angle of an operations shrinks below a threshold value, the operation is removed from the sequence as it is superfluous. If the algorithm fails to find a matching sequence, further random operations are inserted into the sequence. A more detailed treatment on the algorithm is given in reference [33]. In general this optimization method is not scalable as the search space increases exponentially with the number of qubits but it is possible to build up an algorithm from optimized gate primitives acting on a few qubits.

Even for complex algorithms on a few qubits, the sequence generated with this optimization method might include too many operations to yield acceptable fidelities when implemented. Then it can be advantageous to split the algorithm in parts that act only on a subset of the register and generate optimized decompositions for these parts. For this task, the physical interactions need to be altered so that they only affect the relevant subset. Multiple techniques for achieving this in ion traps have been proposed, where the best known techniques rely on physically moving and splitting the ion-chains in a complex and miniaturized ion trap [57]. Our approach to this problem is to decouple them spectroscopically by transferring the information of the idling ions into a subspace that does not couple to the resonant laser light. Candidates for such decoupled subspaces are either (i)  $4S_{1/2}(m_j = +1/2)$  with  $3D_{5/2}(m_j = +1/2)$  or alternatively (ii)  $3D_{5/2}(m_j = -5/2) = |D'\rangle$  with  $3D_{5/2}(m_j = -3/2) = |D''\rangle$ . The decoupling technique (ii) is sketched in figure 2.7a). The only remaining action of the manipulation laser on the decoupled qubits is then an AC-Stark shift that acts as a deterministic rotation around the Z-axis. This rotation can be measured and subsequently be compensated for by controlling the phase of the transfer light. When qubits in the set  $U$  are decoupled, the action of the operations can then be described by  $(\prod_{j \in U} 1_j) \otimes U$  where the operation  $U$  is the implemented interaction on the desired subspace. Note that parameters of the MS operations do not change when the number of decoupled qubits is altered thus the gate does not need to be re-optimized.

## Tools beyond coherent operations

In general, any quantum computer requires non-reversible and therefore also non-coherent operations for state initialization and measurements [30]. For example, quantum error correction protocols rely on controlled non-coherent operations within an algorithm to remove information on the error from the system similar to state initialization. Furthermore, the robustness of a quantum state against noise can be analyzed by exposing it to a well defined amount of phase or amplitude damping [58]. Surprisingly, it has been shown theoretically that non-coherent operations can serve as a resource for quantum information [21, 55, 59]. Naturally, these ideas can only be implemented if controlled non-coherent operations are available in the system. Mathematically, these non-reversible operations are described by a trace-preserving completely positive map  $\mathcal{E}(\rho)$  acting on a density matrix rather than unitary operations acting on pure states. The action of such a map is described by  $\mathcal{E}(\rho) = \sum_k E_k^\dagger \rho E_k$  with Kraus operators  $E_k$  fulfilling  $\sum_k E_k^\dagger E_k = 1$  [30].

In our system two different variations of these controlled dissipative processes are available [60]:

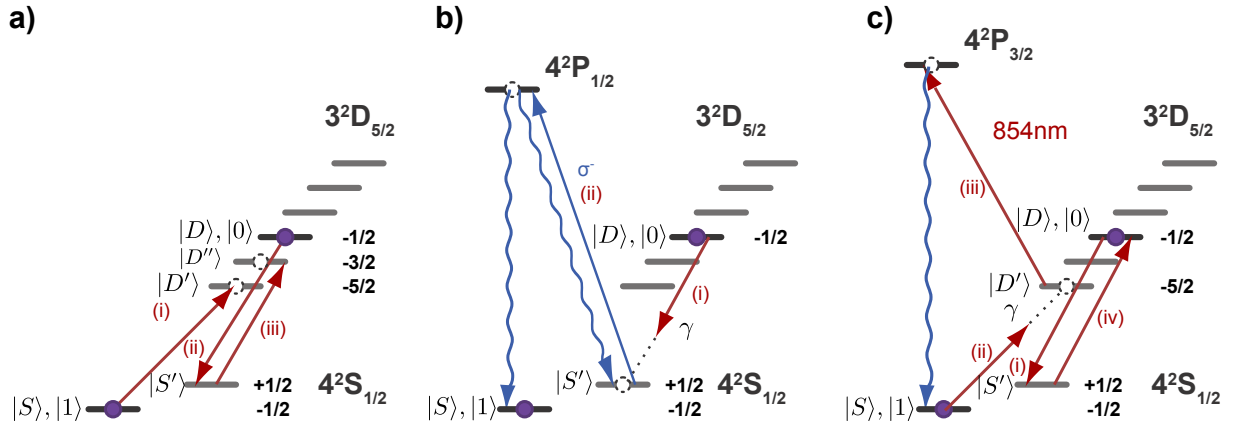


Figure 2.7.: a) The process to decouple individual qubits: (i) The population from  $|S\rangle$  is transferred to  $|D'\rangle$ . (ii) The population from  $|D\rangle$  is transferred to  $|S'\rangle$  and subsequently to (iii)  $|D''\rangle$ . b) Controlled phase damping with strength  $\gamma$  utilizing light at 854nm. (i) Population from  $|D\rangle$  is hidden in the  $|S'\rangle$  state. (ii) The population from  $|S\rangle$  is partially brought to  $|D'\rangle$  and (iii) shining in light at 854 nm depletes the  $3D_{5/2}$  via  $4P_{3/2}$  and finally (iv) the population is brought from  $|S'\rangle$  back to  $|D\rangle$ . (c) Implementing controlled amplitude damping using the 397  $\sigma$  beam. (i) Transferring the population from  $|D\rangle$  to  $|S'\rangle$ . (ii) Optical pumping of  $|S'\rangle$  using light at 397nm.

The archetype of a controlled non-coherent optical process is optical pumping. We can perform optical pumping on individual qubits inside the register with the following sequence as shown in figure 2.7b): (i) Partially transfer the population from  $|D\rangle$  to  $|S'\rangle$  with probability  $\gamma$ , and (ii) optical pumping from  $|S'\rangle$  to  $|S\rangle$  analogous to the qubit initialization. The partial population transfer is performed by a coherent rotation with an angle  $\theta$  on the transition  $4S_{1/2}(m_j = +1/2) \leftrightarrow 3D_{5/2}(m_j = -1/2)$  which leads to  $\gamma = \sin^2(\theta)$ . This reset process can be described as controlled amplitude damping on an individual qubit where the map affecting the qubit is shown in table 2.1. Note that the information in the qubit states is not affected as the optical pumping light couples to neither of the original qubit states. For a full population transfer ( $\gamma = 1$ ) the procedure acts as a deterministic reinitialization of an individual qubit inside a register as required for repetitive quantum error correction [61].

Furthermore an alternative implementation of optical pumping can be used to generate controlled phase damping. This process preserves the populations in the respective qubit states but destroys the coherences between them with probability  $\gamma$ : (i) The information residing in state  $|D\rangle$  of all qubits is protected by transferring it to the  $|S'\rangle = 4S_{1/2}(m_j = +1/2)$  state before the reset step. (ii) On the qubit to be damped, the population from  $|S\rangle$  is partially transferred into the  $|D'\rangle = 3D_{5/2}(m_j = -5/2)$  state with probability  $\gamma$ . Here, the partial population transfer is performed by a coherent rotation on the transition  $4S_{1/2}(m_j = -1/2) \leftrightarrow 3D_{5/2}(m_j = -5/2)$  (iii) Shining light resonant with the  $3D_{5/2} \leftrightarrow 4P_{3/2}$  transition at 854nm onto the ions depletes this level to  $|S\rangle$ . (iv) Transferring  $|S'\rangle$  back to  $|D\rangle$  restores the initial populations, the coherence of the qubit has been destroyed with probability  $\gamma$ . The schematic of this process is shown in figure 2.7c) and the resulting map can be found in table 2.1.

Our system furthermore allows measuring a single qubit without affecting idling qubits in the

Table 2.1.: The extended set of operations in our ion trap QC. This set of operations allows us to implement any possible Markovian process.

Name	Addressed/global	Ideal operation
AC-Stark shift pulses	addressed	$S_z^{(i)}(\theta) = e^{-i\theta/2\sigma_z^{(i)}}$
Collective resonant operations	collective non-entangling	$S_\phi(\theta) = e^{-i\theta/2S_\phi}$
Mølmer-Sørensen	collective entangling	$MS_\phi(\theta) = e^{-i\theta/2S_\phi^2}$
Phase damping	addressed non-coherent	$E_0^p = \begin{vmatrix} 1 & 0 \\ 0 & \sqrt{1-\gamma} \end{vmatrix}$ $E_1^p = \begin{vmatrix} 0 & 0 \\ 0 & \sqrt{\gamma} \end{vmatrix}$
Amplitude damping	addressed non-coherent	$E_0^a = \begin{vmatrix} 1 & 0 \\ 0 & \sqrt{1-\gamma} \end{vmatrix}$ $E_1^a = \begin{vmatrix} 0 & \sqrt{\gamma} \\ 0 & 0 \end{vmatrix}$
Single-qubit measurement	addressed non-coherent	Projection onto $ 0\rangle\langle 0 $ or $ 1\rangle\langle 1 $

same ion string. For this, all spectator ions need to be decoupled from the detection light. This is realized by transferring the population from the  $|S\rangle$  state to the  $|D'\rangle = 3D_{5/2}(m_j = -5/2)$  state. Applying light on the detection transition measures the state of the ion of interest while preserving the quantum information encoded in the hidden qubits. This information can be used to perform conditional quantum operations as needed for teleportation experiments [28] or quantum non-demolition measurements [62].

It should be noted, that the operations forming our implementable set of gates shown in table 2.1 allow the realization of any completely positive map, which corresponds to a Markovian process [19, 20, 62]. The quality of the operations is affected by multiple physical quantities which are discussed in more detail in section 2.2.3. In order to faithfully estimate the resulting fidelity of an implemented algorithm, a complete numerical simulation of the physical system has to be performed. However, a crude estimation can be performed assuming a fidelity of 99.5% for non-entangling operations and  $\{98, 97, 95, 93, 90\}\%$  for the MS operations on a string of  $\{2, 3, 4, 5, 6\}$  ions [23]. The fidelity of the entire algorithm is then estimated by simply multiplying the fidelities of the required operations.

## 2.2.2. Experimental setup

In this section we give an overview of the experimental setup of our ion-trap quantum information processor. First, we describe in detail the ion trap, the optical setup and the laser sources. Then we concentrate on the experiment control system and techniques to infer the state of the qubit register.

### The linear Paul trap

The trap in our experimental system is a macroscopic linear Paul trap with dimensions as shown in figure 2.8[46]. The trap is usually operated at a radial motional frequency of 3MHz and an axial motional frequency of 1MHz. These trapping parameters are slightly adjusted with respect to the number of ions in the string to prevent overlap of the frequencies from different motional modes of all transitions. In order to minimize magnetic field fluctuations, the apparatus is enclosed in a magnetic shield (75x75x125 cm) that attenuates the amplitude of an external

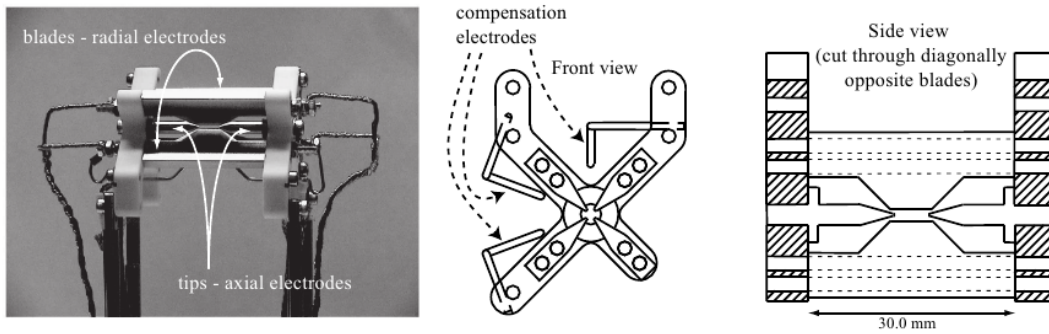


Figure 2.8.: Schematic drawing of the linear Paul trap used in our experiment. The distance between the endcaps is 5mm whereas the distance between the radio-frequency blades is 1.6mm.

magnetic at frequencies above 20 Hz by more than 50dB<sup>3</sup>. The trap exhibits heating rates of 70ms per phonon at an axial trap frequency of 1MHz. Micromotion for a single ion can be compensated with the aid of two compensation electrodes. The remaining micromotion creates sidebands at the trap frequency which can be observed in an ion spectrum on the qubit transition. The strength of the excess micromotion is described by the modulation index  $\beta$  of these sidebands where in our setup a modulation index of  $\beta < 1\%$  is observed [63, 64].

### Optical setup

A quantum information processor with  $^{40}\text{Ca}^+$  requires multiple laser sources, listed in table 2.2, to prepare, manipulate and measure the quantum state of the ions. The ions are generated from a neutral atom beam with a two-step photo-ionization process requiring laser sources at 422nm and 375nm. Manipulating the state of the qubits is done with a Titanium-Sapphire laser at 729nm on the  $4S_{1/2} \leftrightarrow 3D_{5/2}$  qubit transition and its setup as described in reference [65]. Its frequency and amplitude fluctuations affect crucially the performance of the coherent operations as will be discussed in section 2.2.3. The laser has a linewidth of below 20Hz and the relative intensity fluctuations are in the range of 1.5% [65].

The laser sources reside on different optical tables than the vacuum vessel housing the trap, and thus the light is transferred between different tables with optical fibers. The optical access to the trap itself is constrained by the surrounding octagon vacuum vessel which is sketched in figure 2.9 including the available beams with their respective directions. The 397nm light is required for multiple tasks and thus multiple beams are required: one beam for Doppler-cooling and detection, another beam for optical pumping (labeled Pumping  $\sigma$ ), and two beams for Raman sideband-cooling (labeled Raman  $\sigma$ , Raman  $\pi$ ). In particular, the beams used for optical pumping need to be aligned with the magnetic field generated by the coils as indicated in figure 2.9. In practice it is favorable to adjust the orientation of the magnetic field with respect to

<sup>3</sup>Imedco, Proj.Nr.: 3310.68

Transition	Wavelength	Usage	Linewidth
$4S_{1/2} \leftrightarrow 4P_{1/2}$	397nm	Doppler cooling, optical pumping and detection	<1MHz
$4S_{1/2} \leftrightarrow 3D_{5/2}$	729nm	Sideband cooling and qubit manipulation	< 20Hz
$3D_{3/2} \leftrightarrow 4P_{1/2}$	866nm	Repumping for detection	<1MHz
$3D_{5/2} \leftrightarrow 4P_{3/2}$	854nm	Quenching for Sideband cooling and qubit reset	<1MHz
neutral calcium	422nm	Photoionization first stage	-
neutral calcium	375nm	Photoionization second stage	-

Table 2.2.: Laser wavelengths needed for a  $\text{Ca}^+$  ion trap experiment. The lasers are stabilized to a reference cavity with the Pound-Drever-Hall locking technique except for the photoionization lasers which are not actively stabilized.

the light beam since the magnetic field can be adjusted without moving any mechanical part. The beams of the 866nm and 854nm laser are overlapped with the 397nm detection beam in a single-mode photonic crystal fiber.

In order to implement our set of operations, the 729nm light needs to be applied to the ions from two different optical ports: (i) the addressed beam which is a tightly focused beam illuminating only a single ion and (ii) the global beam which is a wide beam that illuminates all ions with an approximately homogeneous light intensity. The angle between the global beam and the axial trap axis is  $22.5^\circ$  which leads to a Lamb-Dicke parameter of  $\eta_{glob} = 6\%$  [66]. The width of the beam is chosen so that the light intensity shows variations of less than 2% over the entire ion string. Considering that the ions are arranged in a linear crystal, it is advantageous to use an elliptical shape for the global beam to achieve higher light intensities at the position of the ions. The elongated axis of the beam has typically a diameter of  $100\mu\text{m}$  which is sufficient for ion strings with up to 8 ions. For larger ion strings, the beam size needs to be enlarged which increases the required time for performing collective operations.

The angle between the addressed beam and the trap axis is  $67.5^\circ$  so that there the Lamb-Dicke parameter is smaller  $\eta_{add} = 2.5\%$ . The addressed beam needs to be able to resolve the individual ions in the string which means that the beam size needs to be smaller than the inter-ion distance of approximately  $5\mu\text{m}$ . This small beam size is realized with the aid of a custom high numerical aperture objective situated in an inverted viewport as sketched in figure 2.10a). Additionally, the beam has to be rapidly switched between the ions which is realized with an electro-optical deflector (EOD). The switching speed depends on the capacitance of the EOD and the output impedance of the driving high voltage amplifier. Figure 2.10b) shows the voltage on the EOD during a switching event between two neighboring ions which demonstrated that a switching event requires approximately  $15\mu\text{s}$ . Experience has shown that a delay between the switching event and the next light pulse of  $30\mu\text{s}$  is sufficient to switch between arbitrary ions in a string of up to 8 ions. Note that the voltage ramp measured at the EOD can only serve as an indicator for the position of the laser beam but does not provide information about the settling time of the laser light phase at the position of the ion. It was observed that the phase of the light field keeps changing for more than  $100\mu\text{s}$  after a switching event. However, this does not affect the qubit operations for our set of operations as the AC-Stark shift does not depend on the phase of the light field as described in section 2.2.1.

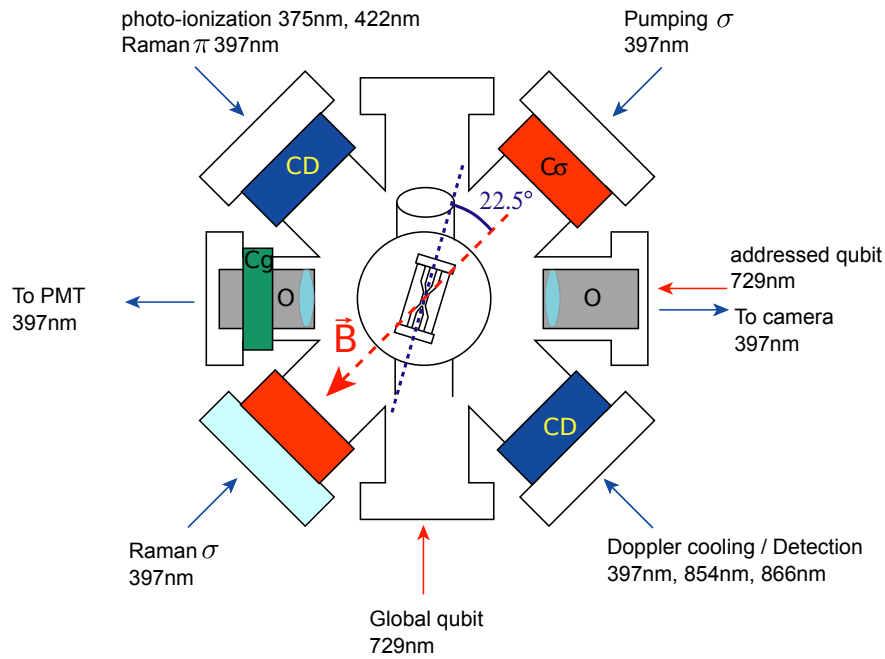


Figure 2.9.: Overview of the alignment of the various laser beams, the coils generating the magnetic field and the trap with respect to the vacuum vessel.

### Experiment control

Any ion-trap quantum information experiment requires precise and agile control of duration, frequency and amplitude of laser beams originating from multiple sources. A typical experimental sequence consists of optical pumping, cooling the center of mass (COM) mode, coherent operations and qubit measurements as shown in figure 2.11a). Usually the required control is achieved by using acousto-optical devices which map the control over intensity and frequency of the light field onto the manipulation of amplitude and frequency of a radio-frequency signal. Thus, versatile and fast radio-frequency (RF) signal generators are a necessity for a high-fidelity quantum information processor. Modern RF signal generators are commonly based on direct digital synthesizers (DDS) enabling switching times on a nanosecond timescale and frequencies between 1 and 400 MHz with sub-Hertz resolution. In our experiment, these DDSs are controlled by a special purpose microcontroller embedded on a field-programmable-gate-array (FPGA) [67]<sup>4</sup>. This FPGA is able to generate digital pulses with a duration from 10ns up to several seconds. In order to allow coherent rotation on different transitions, the control system needs to be able to perform phase-coherent switching between multiple frequencies. The phase stability of the phase-coherent switching has been tested to be  $0.0001(90)^\circ$  [64]. The controller is connected to the experimental control computer via a standard ethernet connection. For quantum algorithms requiring feed-forward operations, such as teleportation, it is necessary to use the outcome of a

<sup>4</sup><http://pulse-programmer.org>

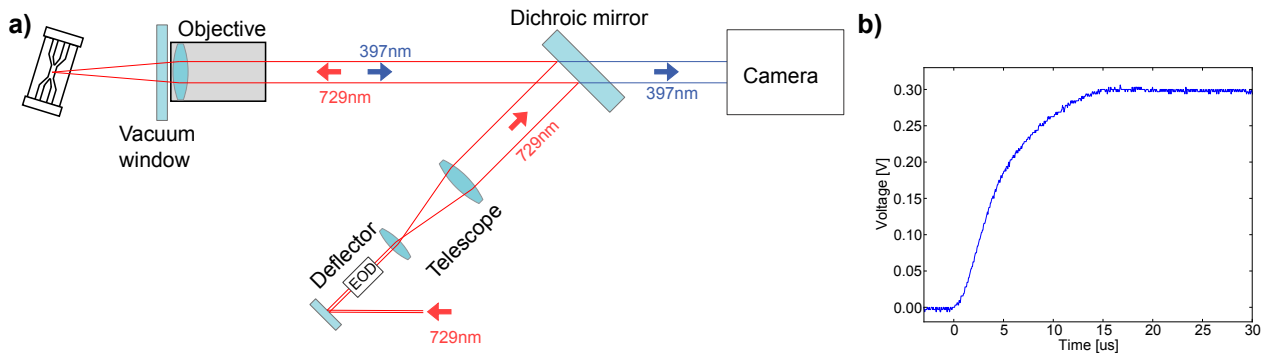


Figure 2.10.: a) Optical setup for the addressing beam setup. b) Time dependence of the voltage on the EOD switching between two neighboring ions. After approximately  $15\mu\text{s}$  the voltage settles and thus the switching process is finished.

Parameter	Type	Required for each ion
Ion position	Voltage	yes
Telescope lens position	Position	no
Rabi frequency	Time	yes
Zeeman splitting	Magnetic field	no
Laser frequency drift	Frequency	no

Table 2.3.: List of automatically calibrated parameters.

measurement within the algorithm to control subsequent operations in the algorithm. This can be realized by analyzing the measurement outcome by counting the PMT signal on dedicated counters and performing the controlled operations in the sequence depending on state of this counters [28]. A schematic view of the control system including this feedback mechanism is shown in figure 2.11b).

The FPGA determining the timing of the experiment is itself controlled by a personal computer running a custom LabView program. This program translates the sequence of operations from a human readable format to binary code that can be executed on the FPGA. In order to minimize the required time for calibrating the system, the parameters shown in table 2.3 are calibrated automatically without any user input. Our set of operations can only be implemented, if the frequency of the manipulation laser is close to the qubit transition frequency. Since the frequency of each individual transition is mainly determined by the center frequency of all transitions shifted by the respective Zeeman shift due to the applied magnetic field, it is sufficient to infer the magnitude of the magnetic field and the frequency difference between the laser and the center frequency. For this, the difference frequencies between the laser and two distinct transitions are measured on the transitions  $4S_{1/2}(m_j = -1/2) \leftrightarrow 3D_{5/2}(m_f = -1/2)$  and  $4S_{1/2}(m_j = -1/2) \leftrightarrow 3D_{5/2}(m_f = -5/2)$  which allows us to determine the long-term drift of the magnetic field and the 729nm reference cavity. Typical values for the magnetic field drift are  $10^{-8} \text{ G/s}$  and for the cavity drift 60 mHz/s which is expected due to aging of the cavity spacer crystal [68].

In order to perform addressed single-qubit operations, the position of the addressed beam with respect to the ion positions needs to be characterized. The position of the beam is controlled

## 2. A quantum information processor with trapped ions

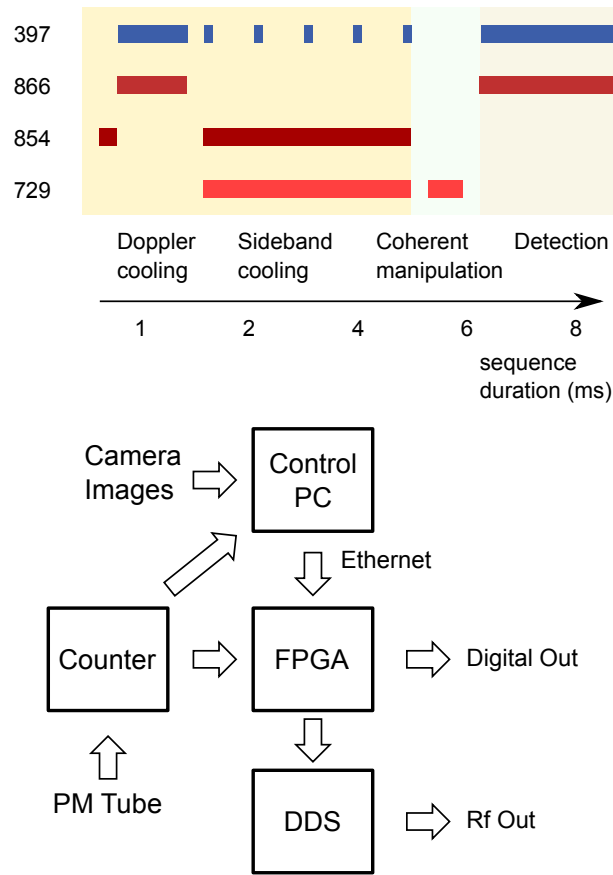


Figure 2.11.: a) Timing sequence of a typical experiment consisting of state initialization, coherent manipulation and measurement. b) Schematic representation of the experiment control hardware. The FPGA is programmed by the experimental control PC and controls the timing of all signals used in the experiment. RF signals for the coherent manipulation are generated by DDS. It is possible to perform conditional operations based on measurement outcomes with external counters that analyze the photon counts from the PMT.

via a motorized lens before the objective, as indicated in figure 2.10a), and the voltage that is applied to the EOD. The calibration routine consists of moving the beam onto the center of the ion string with the motorized lens, followed by finding the EOD voltages for every individual ion. The position of the beam with respect to the ions can be determined to approximately 50nm. In order to perform the desired operations, the Rabi oscillation frequencies on the global beam and the addressed beam need to be measured. On the two global beam the transitions required for the drift compensation need to be covered, whereas on the addressed beam, the oscillation frequencies need to be calibrated for each ion for the AC-Stark operations using Ramsey spectroscopy. In general, the frequencies can be determined with a precision of approximately 1%.

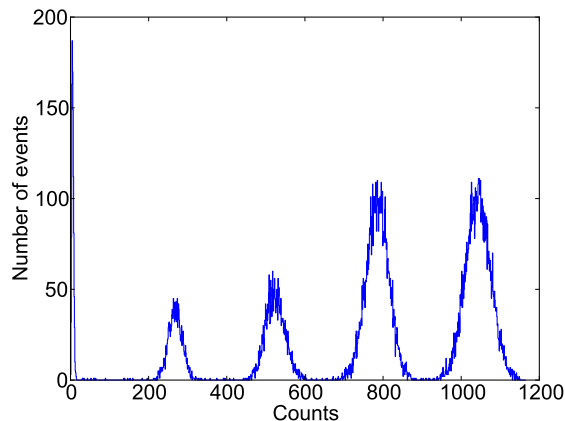


Figure 2.12.: Histogram of counted pulses from the PMT for a 4 ion string. The histogram is derived 21200 measurements with a detection time of 5ms.

### Measuring individual ions within a quantum register

As described in section 2.2.1, measuring the quantum state of the ions is performed by counting single photons on the  $4S_{1/2} \leftrightarrow 4P_{1/2}$  transition. We use high numerical aperture objectives located in an inverted viewport to reduce the distance between the ion and the objective as shown in figure 2.9. Two detection channels are available: one with a photo-multiplier-tube (PMT) and another with an electron multiplying CCD camera. The PMT integrates the photons over its sensitive area and thus cannot infer any spatial information on the ions. The number of detected photon counts depends on the number of bright ions as is indicated in the histogram of PMT counts shown in figure 2.12. By setting appropriate thresholds it is then possible to determine the number of ions found in the  $4S_{1/2} = |0\rangle$  state which is sufficient information to perform permutationally invariant state tomography [35] or to determine the fidelity of a multi-qubit GHZ state [23].

In contrast, the CCD camera is able to resolve the spatial information of the detected light and is thus able to determine the state of each ion in the string separately. It uses the same objective as for generating the addressed 729nm beam where the beam at 729nm and the detected light at 397nm are separated by a dichroic mirror as sketched in figure 2.10a). The analysis of the camera data is performed in five steps: (i) A camera image is taken with an exposure time of 7ms. The value of each pixel corresponds to the number of detected photons. (ii) For further analysis, a limited region of interest (ROI) around the ion's position of the whole camera image is used. For a register of 4 ions the ROI consists of 35x5 pixels but the ROI size needs to be adjusted to the length of the ion string. (iii) The pixel values are summed over the y-axis of the ROI-image to get the brightness information along the ion string. (iv) This brightness distribution is then compared to pre-calculated distributions which are generated from a reference image where all ions are bright. From this reference image, the position and brightness distribution of each ion are determined. The state of the ion string is then inferred by comparing the summed pixel values with the pre-calculated distributions of each possible outcome by calculating the mean squared error  $\chi^2$ . Finally (v) the state with the smallest mean squared error is chosen to be the most

## 2. *A quantum information processor with trapped ions*

---

likely state. Two examples of this analysis procedure are shown in figure 2.13. Note that this method is not scalable as the number of pre-calculated distributions grows exponentially with the number of ions. However recent work on state detection in trapped ion system promises efficient detection schemes [69].

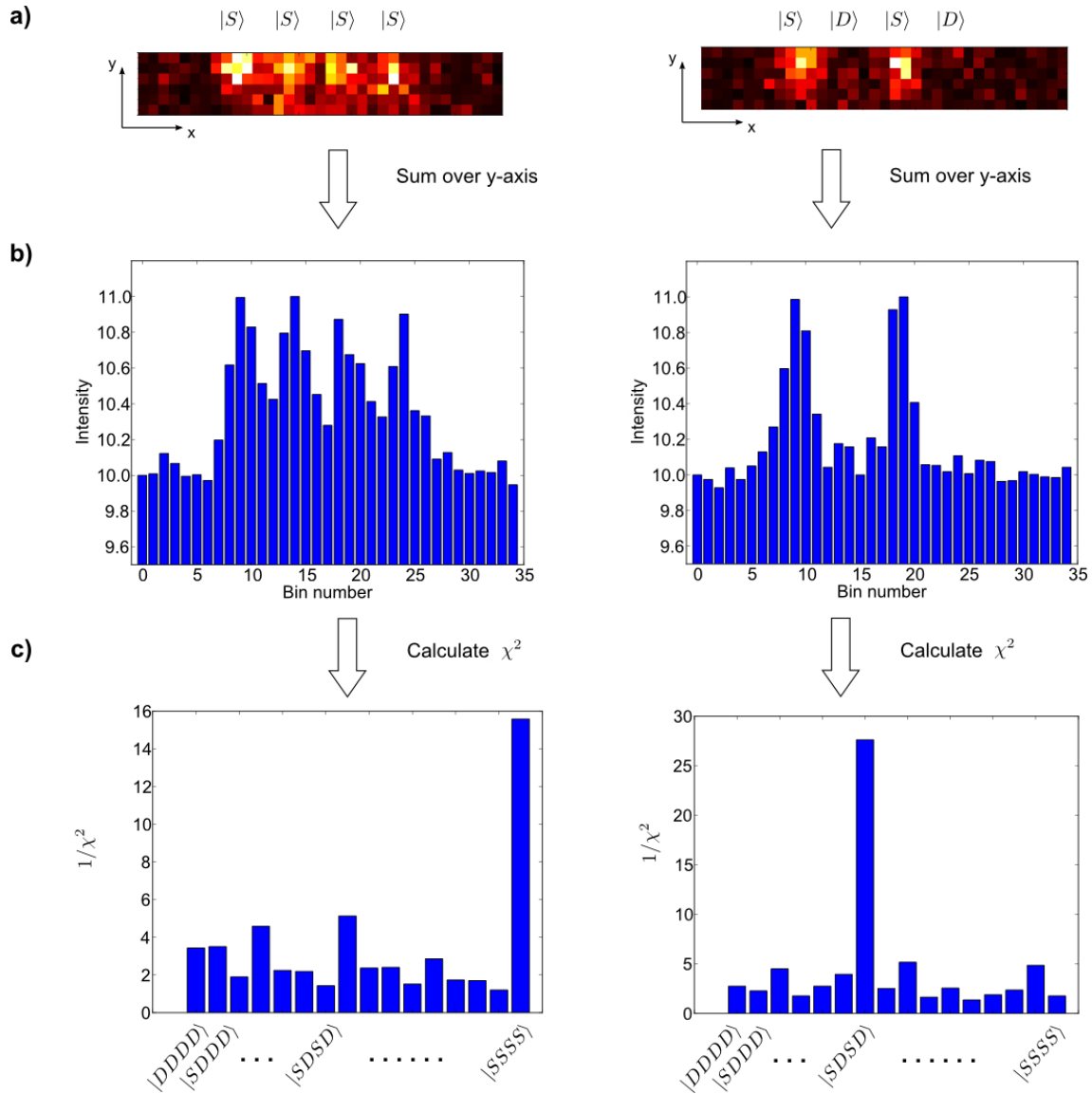


Figure 2.13.: Schematic illustration of the camera detection in a 4 ion register. (a) False color image of the region of interest. (b) Brightness information after summation over the y-axis of the image. (c)  $1/\chi^2$  of the sum with generated data for every possible state. The peak corresponds to the most likely state. In this case index 6 (15), which corresponds to the state  $|SDSD\rangle$  ( $|SSSS\rangle$ ), is the most likely state.

### 2.2.3. Error sources

Any implementation of a quantum computer will be affected by errors which ultimately need to be corrected with quantum error correction techniques. Identifying and characterizing the noise sources are therefore crucial steps towards a large scale quantum information processor. In this analysis we distinguish noise sources, that affect a qubit used as a quantum memory, from additional error sources, that occur when performing operations. For the presented error sources we describe the origin, present a method to characterize the magnitude, and provide typical values for our experimental system.

#### Errors in the qubit memory

In general, errors affecting a qubit memory are described by a combination of phase damping and amplitude damping [30]. In optical qubits, amplitude damping corresponds to decay from the excited to the ground state whereas phase damping destroys the phase of a superposition state but does not alter the population of the qubit. The lifetime of the excited qubit is a fundamental property of the ion species and gives an upper limit to the storage time of a quantum memory encoded in an optical qubit. In the experiment, the lifetime of the excited state can be reduced due to residual light fields depleting the  $3D_{5/2}$  state via another state, or by collisions with background gas particles. This possible error source can be investigated by confirming that the time constant of the exponential decay from the  $3D_{5/2}$  state is close to the natural lifetime of 1.168(7)s [70]. In our setup, we find a lifetime of  $\tau_1 = 1.13(5)$ s [60].

The second noise type, phase damping, is usually investigated with Ramsey spectroscopy which determines the coherence properties of a superposition state [46]. There, the qubit is initially prepared in an equal superposition of the two computational states by a  $R_0(\pi/2)$  rotation. After a certain storage time, a second rotation  $R_\pi(\pi/2)$  is applied that ideally maps the qubit back into the state  $|1\rangle$ . If the phase  $\phi$  of the second pulse  $R_\phi(\pi/2)$  is varied with respect to the first pulse, the probability of being in state  $|1\rangle$  is an oscillation dependent on  $\phi$ . If the coherence of the state is decreased due to phase damping, the second mapping pulse cannot reach the basis states anymore which is observed as a decrease in the amplitude of the oscillation. This loss of contrast corresponds directly to the remaining phase coherence of the superposition which naturally decreases with increasing storage time.

In our system, phase damping is predominantly caused by fluctuations between the frequency of the qubit transition and the driving field. The two main contributions are (i) laser frequency fluctuations and (ii) fluctuations in the magnetic field which translate into fluctuations of the qubit transition frequency. It is then possible to distinguish the contributions by investigating the coherence decay on multiple transitions between different Zeeman substates of the  $4S_{1/2}$  and  $3D_{5/2}$  levels because they show different susceptibility to the magnetic field due to different Lande g factors. In figure 2.14a) the blue rectangles represent the coherence decay on the  $4S_{1/2}(m_j = -1/2) \leftrightarrow 3D_{5/2}(m_j = -1/2)$  transition which is least sensitive to fluctuations in the magnetic field. The green diamonds show the coherence decay for the  $4S_{1/2}(m_j = -1/2) \leftrightarrow 3D_{5/2}(m_j = -5/2)$  which has approximately 5 times higher sensitivity to fluctuations of the magnetic field [64, 71]. Note that both transitions show effectively

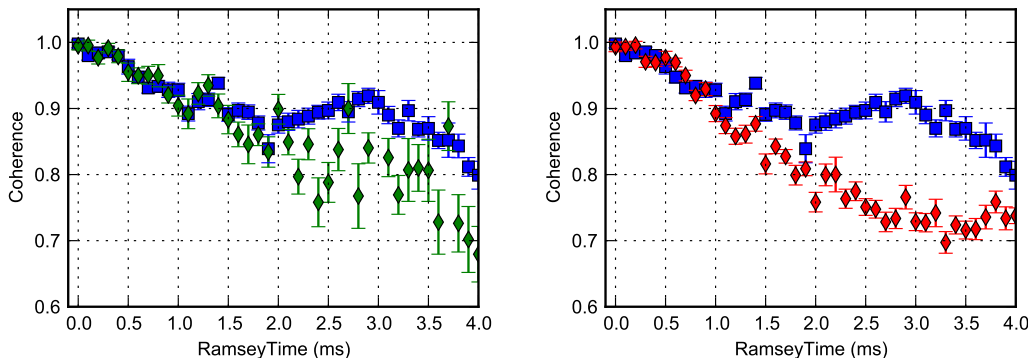


Figure 2.14.: a) Ramsey contrast decay on two transitions with different sensitivity to the magnetic field fluctuations. Blue squares indicate the less sensitive  $4S_{1/2}(m_j = -1/2) \leftrightarrow 3D_{5/2}(m_j = -1/2)$  transition whereas green diamonds correspond to the  $4S_{1/2}(m_j = -1/2) \leftrightarrow 3D_{5/2}(m_j = -5/2)$  transition. b) Ramsey contrast decay on the transition which is least sensitive to magnetic field fluctuations, without (blue squares) and with (red diamonds) spin echo.

the same coherence decay for storage times up to 1ms. This suggests that for typical experiments where the coherent manipulation is shorter than 1ms, the main source for dephasing are laser-frequency fluctuations.

The phase damping process can be theoretically described by a model that applies random phase-flips with a certain probability  $p$  to multiple copies of the same state. The ensemble of all states is then described by a density matrix whose off-diagonal elements are affected by the phase damping as  $\rho_{i,j} \xrightarrow{i \neq j} \rho_{i,j}(1 - 2p)$ . This model of a phase-flip rate is close to the concept of a bit-flip rate used in classical computer science and is therefore widely used in theoretical works on quantum information [30]. However, a physical model for phase damping describes the phase-flip probability as a function of the information storage time. In order to do so, one has to find a noise-model describing temporal correlations of the noise source. The most straightforward noise model assumes temporally uncorrelated noise which leads to an exponential decay of the coherence characterized by the transversal coherence time  $\tau_2$  and therefore to off-diagonal elements  $\rho_{i,j} = \rho_{i,j} e^{-t/\tau_2}$  [41]. This description is used in most quantum computing models where the noise can be fully characterized by the amplitude damping timescale  $\tau_1$  and the phase coherence time  $\tau_2$  [30]. In most physical systems, technical noise is temporally correlated and thus this simple model of uncorrelated phase noise does not apply [23]. In particular the coherence decay in our system deviates notably from an exponential decay as can be seen in figure 2.14a). This effect can be amplified with the aid of a well known method to enhance the storage time of a quantum memory known as the spin echo technique. There, the basis states are swapped at half the storage time which reverses the phase evolution and thus cancels fluctuations provided their timescale is longer than the storage time. However, it is possible that the performance with a single echo is worse than the original register if this condition is not satisfied. This effect is demonstrated in figure 2.14b) where the coherence with spin echo (red diamonds) is worse than without echo (blue squares). There exist more sophisticated methods to enhance the qubit

storage time which are able to take temporal correlations into account. A formal description of this techniques is known as dynamical decoupling which has already been demonstrated in various physical systems[72–78]. For a given noise spectrum an optimal pattern of echo pulses can be determined to maximize the phase coherence. Interestingly, one can use this technique to determine the spectral noise density from multiple coherence decays with varying number of echos [79, 80]. In the following we describe a simple experiment to identify the dominant features of the noise spectrum without using any spin echo technique.

It is possible to infer the noise spectrum from a coherence decay  $C(T)$  without any echo when only a few parameters of the noise spectrum need to be determined. For a given noise spectrum  $A(\omega)$ , the Ramsey contrast decay is given by

$$C(T) = \exp \left\{ - \int_0^\infty d\omega \frac{A(\omega)^2}{\omega^2} \sin^2(\omega T/2) \right\}.$$

which is a special case of the general coherence decay for dynamical decoupling given in reference [80]. Calculating the noise spectrum from a measured coherence decay is not uniquely possible, thus we characterize  $A(\omega)$  assuming a certain spectral shape of the noise and inferring only a few parameters. Our main source of phase noise at relevant timescales smaller than 1ms seems to be the laser frequency noise and thus we model the spectrum accordingly. Typically a laser spectrum is modeled as a Lorentzian line, which we extend with two broad Gaussian peaks, where the first originates from the laser locking electronics centered at 300Hz and the second peak is attributed to the second harmonic of the power line frequency at 100Hz. We model these two contributions with Gaussian peaks  $G_\nu(\omega) = \exp((\omega - \omega_0 - \nu)^2/\sigma^2)$  where  $\sigma = 10\text{Hz}$ . The resulting spectral noise density for our model is then

$$A(\omega) = \alpha \left( \frac{\gamma^2}{\gamma^2 + (\omega - \omega_0)^2} + a_1 G_{300}(\omega - \omega_0) + a_2 G_{100}(\omega - \omega_0) \right).$$

Noise at the fundamental frequency of the power line (50Hz) is not included in the model as it does not contribute to the shape of the coherence decay for waiting times below 10ms. Figure 2.15 shows the fitted coherence decay of the model with parameters  $\alpha = 89\sqrt{\text{Hz}}$ ,  $\gamma = 3 \text{ Hz}$ ,  $a_1 = 0.22$  and  $a_2 = 0.02$ .

When generalizing these results to multi-qubit systems, the spatial correlation of the noise on all qubits needs to be considered. In our system the noise from the laser and magnetic fields are almost identical over the entire register and therefore the phase noise can be modeled affecting the entire register simultaneously. This correlation leads to a faster loss of coherence between states with large total energy difference [23]. On the other hand, this spatial correlation enables decoherence free subspaces (DFS) which are not affected by dephasing. The DFS consists of states where acquiring an equal phase on all qubits leads only to a global phase of the state and thus to no dephasing. For example, a single logical qubit can be encoded in two physical qubits as  $|0_l\rangle = |01\rangle + |10\rangle$  and  $|1_l\rangle = |01\rangle - |10\rangle$  respectively. The two logical states have identical total energy difference and thus form a DFS, where a universal set of operations with two logical qubits has been demonstrated in our system [25]. However, it is not clear how well the concept of a DFS can be extended to larger register sizes, and thus we show the coherence decay of an 8-qubit DFS state of the form  $|00001111\rangle + e^{i\phi}|11110000\rangle$  in figure 2.16. The state is

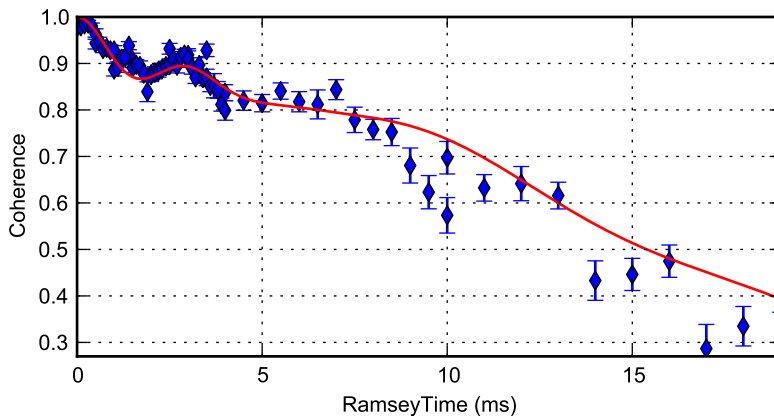


Figure 2.15.: Measured Ramsey contrast decay on the  $4S_{1/2}(m_j = -1/2) \leftrightarrow 3D_{5/2}(m_j = -1/2)$  transition. The solid line shows a modeled Ramsey contrast decay with fitted parameters.

generated by preparing the qubit register in the state  $|00001111\rangle$  and performing a  $MS_{\phi=0}(\pi/2)$  operation. If the DFS is also present for 8 ions, the loss of coherence should correspond to the spontaneous decay of the  $3D_{5/2}$  state resulting in an exponential decay of the coherence with timescale  $\tau = \tau_1/n$  where  $n = 4$  is the number of excited ions. This is illustrated in figure 2.16 showing the measured coherence decay and the expected decay, assuming only spontaneous decay. Furthermore, the spontaneous decay can be eliminated by encoding the qubit in the two substates of the  $4S_{1/2}$  level as introduced in section 2.2.1. The red squares in figure 2.16 show no noticeable decay during a storage time of 200ms where limitations of the experiment control system (and PhD students) prevent investigating longer storage times. The storage time limit of this DFS is then given by fluctuations in the magnetic field gradient and is expected to be in the 30s regime [81].

## Errors in quantum operations

Performing operations on the qubit adds additional noise sources, and thus the error rate of the entire algorithm cannot be described by spontaneous decay and phase damping. We will now describe these sources by their physical causes and categorize them by their occurrence in (i) state initialization, (ii) coherent manipulation and (iii) state detection.

### Initialization

As described in section 2.2.1 the qubit is initialized by means of an optical pumping process towards the  $4S_{1/2}(m = -1/2)$  state using a circularly polarized laser beam aligned parallel to the magnetic field. The possible error sources are (i) imperfect polarization of the pumping light and (ii) misalignment with respect to the magnetic field. The polarization quality is determined by the quality of the polarization optics and the birefringence caused by stress on the window attached to the vacuum vessel. The quantization axis can be aligned by biasing the current in the different magnetic field coils. The error probability of this process can be measured by

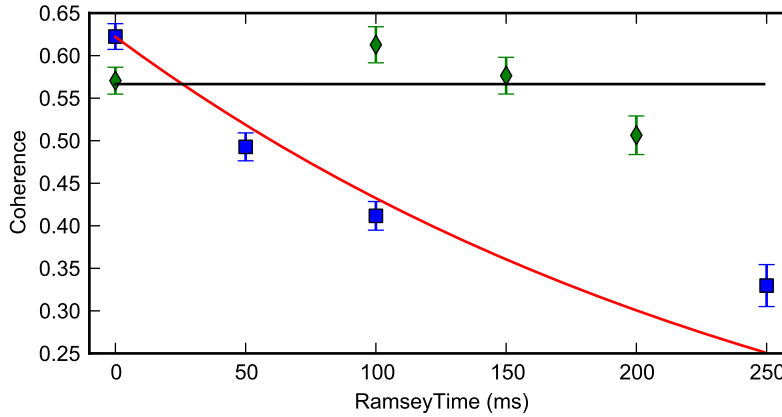


Figure 2.16.: Coherence as a function of the qubit storage time of an 8 qubit DFS state encoded in the optical qubit (blue squares) and the ground-state qubit (green diamonds) eliminating amplitude damping decay. The solid lines represent the expected decay for both qubit types.

transferring the remaining population from the  $4S_{1/2}(m = 1/2)$  to the  $3D_{5/2}$  level and measure it subsequently. If the transfer works perfectly, the population left in the  $4S_{1/2}$  level is due to imperfect optical pumping. Since the transfer is imperfect, the population needs to be shelved multiple times to multiple substates in the  $3D_{5/2}$  manifold. Every shelving pulse is performed with an error rate of less than 1% and thus the error rate of two combined shelving pulses is on the order of  $10^{-4}$ . With this technique, the fidelity of the optical pumping process can be determined accurately. We find a fidelity of the optical pumping process of better than 99.1% [82]. The second optical pumping technique, as introduced in section 2.2.1, is frequency selective on the qubit transition. Thus the direction of the magnetic field with respect to the laser beam can be neglected which leads to a more robust pumping. With this technique we find a pumping fidelity of larger than 99% [83].

The second initialization step prepares the ion in the motional ground state of the harmonic oscillator. We treat the common-mode motion (COM) separate from the other modes as it is used by the entangling MS operations. In order to reach the lowest possible mean phonon number, sideband cooling on the qubit transition as described in section 2.2.1 is performed on the common mode after a Doppler pre-cooling cycle. The final phonon occupation can be determined by various techniques where a suitable method, when the motion is close to the ground state, is to perform Rabi oscillations on the motional sideband. This method uses the fact that the Rabi frequency on the blue sideband for a given phonon number  $n$  is given by  $\Omega_n = \sqrt{n+1} \eta \Omega_0$  where  $\Omega_0$  is the Rabi frequency on the carrier transition. Rabi oscillations for a given phonon distribution are described by

$$p_{|1\rangle} = \sum_n c_n \sin^2(\eta \Omega_0 / 2 \sqrt{n+1} t)$$

where the parameters  $c_n$  can be determined by performing a numerical fit to the measured data assuming a thermal distribution of  $c_n = \langle n \rangle^n / (\langle n \rangle + 1)^{n+1}$  which is completely described by

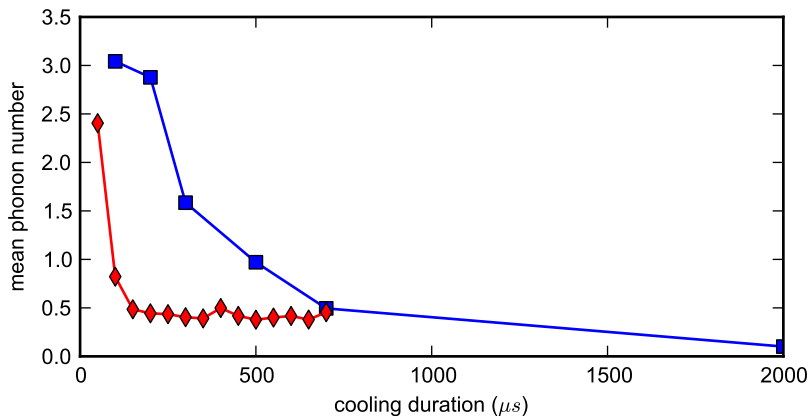


Figure 2.17.: Cooling rates for sideband cooling on the Raman (red diamonds) and the optical (blue squares) transition. Although cooling via the Raman process is faster it leads to a higher steady state phonon number.

the mean phonon number  $\langle n \rangle$ . A typical value for our experiments using sideband cooling on the optical transition is  $\langle n \rangle = 0.05(3)$  after a cooling time of 2ms [50]. In our setup we have also the probability of performing sideband cooling on the Raman transition as introduced in section 2.2.1. This technique is used as an in-sequence recooling technique after a measurement and therefore the cooling time has to be short compared to the qubit coherence time. Therefore, we adjust the cooling parameters to achieve a faster cooling rate at the cost of a higher steady state phonon number of  $\langle n \rangle = 0.5$  after a cooling time of  $200\mu s$ . Figure 2.17 compares the cooling rates of the two distinct cooling techniques.

In first-order Lamb-Dicke approximation ( $\eta \ll 1$ ), the phonon number of the remaining motional modes does not affect the dynamics of the system. But as a second order effect, the occupation of these modes alters the coupling strength of the ion to the light, which causes an effective fluctuation of the Rabi frequency as the phonon number follows a thermal distribution after cooling [41, 84]. These fluctuations are equivalent to intensity fluctuations of the driving laser and cause a damping of the contrast of the Rabi oscillations. This is illustrated in figure 2.18a) which shows Rabi oscillations in a register of three ions where sideband cooling was applied only to the COM mode. In contrast, figure 2.18b) shows the same oscillations where all three axial modes were cooled subsequently and the damping of the oscillations is reduced. An  $N$  ion crystal features  $3N$  modes and thus cooling all modes in a crystal gets increasingly difficult for larger registers. Fortunately, cooling all modes of the crystal is not always necessary as the mean-phonon number decreases with increasing mode energy. Therefore we cool only the three modes corresponding to the lowest energies to effectively suppress this error source for up to 10 ions. In our setup this error source is smaller on the addressed beam than the global beam, as the Lamb-Dicke parameter is smaller as described in section 2.2.2.

### Coherent manipulation

Additional errors occurring during the coherent manipulation of the quantum information are mainly due to (i) laser intensity fluctuations (ii) crosstalk and (iii) the limited coherence of the

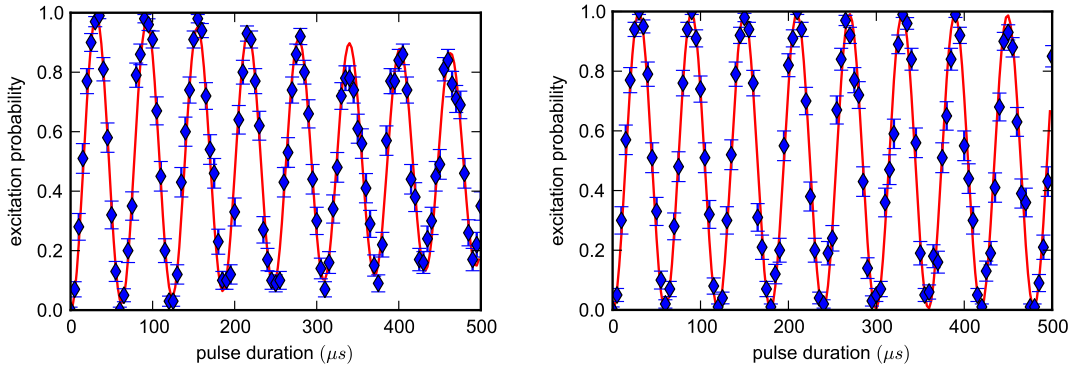


Figure 2.18.: Rabi oscillations illustrating the influence of thermal occupation of the motional modes when a) only the COM mode is cooled and b) all three axial modes are cooled

motional mode.

Intensity fluctuations of the laser light manipulating the ions lead to a fluctuating Rabi frequency and thus decrease the fidelity of the operations. Measuring the fluctuations of the light field with a photo diode indicates that the fluctuations have relevant timescales on the order of seconds to minutes. We assume therefore that the major sources are (i) fluctuations of the coupling efficiency into a single-mode optical fiber, (ii) thermal effects in acousto-optical devices, (iii) polarization drifts in the fiber, which translate into a varying intensity after polarization defining optics, and (iv) beam pointing instability of the laser light with respect to the ion. These intensity fluctuations can be measured directly on the ions by inserting AC-Stark shift operations with varying length into a Ramsey experiment as sketched in figure 2.19a). The AC-Stark shift operations translate intensity fluctuations directly into phase fluctuations and thus the same Ramsey techniques as for characterizing phase-noise can be used to measure them. The timescale of the intensity fluctuations is slow compared to the required time for taking 100 repetitions of the sequence and thus they cause excess fluctuations of the measured excitation probabilities rather than a coherence decay.

These excess fluctuations can be determined by comparing the standard deviation of the measured data with the expected projection noise  $\Delta p^2 = \Delta_{proj}^2 + \Delta_{excess}^2$ . This excess noise in the state probability can be translated into fluctuations of the rotation angle via error propagation. We choose the rotation angle to be  $\theta = N\pi$  with  $N$  being an integer yielding  $\Delta\theta/\theta = \Delta p_{excess}/\pi N$  and perform this analysis up to  $N = 8$ . The measured state probability fluctuations are then analyzed with a linear fit as shown in figure 2.19b). From this, the relative fluctuations of the rotation angles are determined which are directly equivalent to the relative fluctuation of the Rabi frequency  $\Delta\theta/\theta = \Delta\Omega/\Omega$ . For the AC-Stark shift operations the Rabi frequency is directly proportional to the laser intensity yielding  $\Delta\Omega/\Omega = \Delta I/I$ . From the fitted data we can identify the average laser fluctuations to be  $\langle \Delta I/I \rangle_N = 0.41(6)\%$ .

An error source that affects the register when performing addressed single-qubit operations is crosstalk where due to the finite width of the addressing laser, along with the desired ion, also its neighboring ions are affected. This addressing error is characterized by the ratio of the

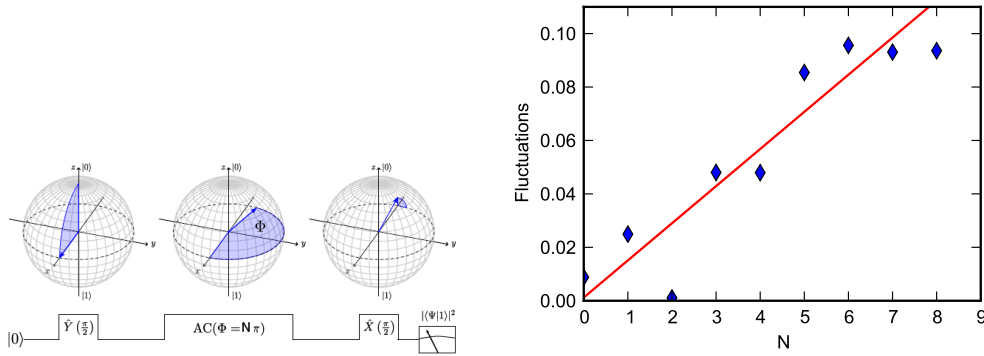


Figure 2.19.: a) Measurement scheme for the slow intensity fluctuations with Ramsey type experiments. Multiple ( $N$ -times) rotations around the z-axis of the Bloch sphere are introduced into a Ramsey experiment translating intensity fluctuations into additional noise on the excitation probability. b) Measured state probability fluctuations  $\Delta p$  for multiple  $N$  where the slope is fitted to be  $0.013(1)$  leading to effective intensity fluctuations of  $\langle \Delta I / I \rangle_N 0.41(6)\%$ .

Rabi frequency of the addressed ion  $i$  to the Rabi frequencies the neighboring ion  $j$ :  $\epsilon_{i,j} = \Omega_i / \Omega_j$ . The addressed operation, when addressing ion  $i$ , can then be described by  $S_z^{(i)}(\theta) = \exp(i\theta \sum_j \sigma_z^{(j)} \epsilon_{i,j})$  where  $\epsilon$  is the addressing matrix describing the crosstalk. The magnitude of the error can then be bounded by the maximum off-diagonal element of this matrix  $\epsilon_{max} = \max_{i \neq j} \epsilon_{i,j}$ . In figure 2.20 an example of excessive crosstalk in a three ion register is shown with  $\epsilon_{max} = 22/121 = 18\%$ . Typically, the maximum crosstalk on the addressed AC-Stark operations is  $\epsilon_{max} < 3\%$  for up to 8 ions where crosstalk between more distant ions is typically smaller than  $10^{-3}$ . Note that this error is coherent, and thus can be undone if the whole addressing matrix is known. Thus, the compensation of the crosstalk can be integrated into the numerical optimization algorithm generating the sequence of operations if the crosstalk is constant over time.

The presented error sources affect both, entangling as well as non-entangling operations. A loss of coherence on the motional mode does not affect non-entangling operations. However, the entangling MS operation require coherences between different motional states which can be decreased by (i) fluctuations of the static voltages defining the trap frequencies and (ii) heating of the ion string. The coherence time of the motional mode can be determined by performing a Ramsey type experiment which is only sensitive to the phase between two different motional states. This is possible by using a superposition of two motional states  $1/\sqrt{2}(|S, 0\rangle + |S, 1\rangle)$  instead of a superposition of the electronic state  $1/\sqrt{2}(|S\rangle + |D\rangle)$  [85]. The motional coherence can then be measured analogous to the qubit storage time and yields an exponential decay with time constant  $\tau_{motional} = 110(20)\text{ms}$ . This coherence time is sufficiently long to allow high fidelity operations [46].

## Measurement

The dominant source of errors in the measurement of the qubit is given by spontaneous decay from the  $3D_{5/2}$  state during the measurement process as well as stray-light. Both errors affect

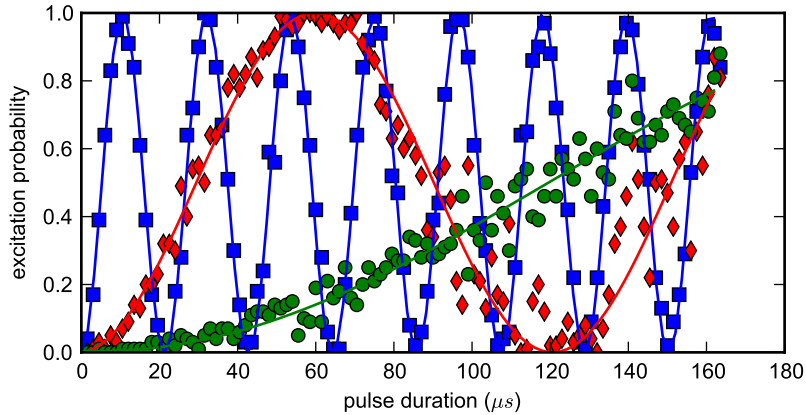


Figure 2.20.: Illustration of the crosstalk between neighboring qubits where the middle ion (blue rectangles) is addressed. The fitted Rabi oscillation periods are  $22\mu s$  for the addressed ion 2,  $121\mu s$  for ion 1 (red diamonds), and  $464\mu s$  for ion 3 (green circles).

the measurement if the qubit is projected into the  $|0\rangle = 3D_{5/2}(m = -1/2)$  state. The stray-light is modeled by a Poissonian distribution with a mean value of typically 1 counts/ms. The decay from the  $3D_{5/2}$  state can also be included which slightly modifies this distributions (for details see reference [42]). For a ion being projected into the  $|1\rangle (4S_{1/2})$  state, the photon distribution corresponds to a simple Poissonian distribution with typically 50 counts/ms. The detection error corresponds then to the overlap of the probability distributions for a bright and a dark ion which can be well below  $10^{-3}$ . The results from the CCD camera detection overlaps with the PMT outcome at a level of better than 99.3% [86].

### Estimating the effect of noise on an algorithm

In order to determine the effect of the individual error sources for a given sequence of operations, a numerical simulation including them has to be performed on a classical computer, which is in general a tedious task - even for a few ions. We developed and use a numerical modeling software named “Trapped Ion Quantum Computing - Simulation Program with Integrated Circuit Emphasis” (TIQC-SPICE) [87]. It follows a Monte Carlo approach which simulates multiple random trajectories of varying parameters [88, 89] where each trajectory yields a pure final state. The ensemble average over all trajectories is then the density operator corresponding to the simulated state of the system.

In the following we investigate two algorithms which show different susceptibility to the individual noise sources. The algorithms will not be explained in detail here as we focus on the effect of the different noise sources on the fidelity of the final state. As a first algorithm we investigate a single timestep of an open-system quantum simulator (details on the algorithm are given in reference [90]). This algorithm acts on two system qubits but requires an additional auxiliary qubit whose state can be neglected. We simulate its sequence of operations, shown in the appendix, table B.1, on a three-ion register using our TIQC-SPICE program where each simulation run consists of a Monte-Carlo simulation with 15 trajectories. The included noise

Error source	Overlap with ideal state
All	77 %
Crosstalk	95%
Dephasing	84 %
Intensity fluctuations	99%
Spectator modes	94%

Table 2.4.: Results for the numerical simulation of a quantum simulation algorithm where smaller overlap means a larger error. In order to identify the dominant error source, the simulation is performed multiple times with only a single active error source. From the results one can infer that dephasing is the dominant source of errors. The errors caused by motional heating, imperfect optical pumping and spontaneous decay are negligible.

Error source	Overlap with ideal state
All	93 %
Crosstalk	95%
Dephasing	98 %
Intensity fluctuations	>99%
Spectator modes	>99%

Table 2.5.: Results of a numerical simulation of a three-qubit QFT algorithm where a smaller overlap means a larger error. Here, the dominant noise source is crosstalk. The errors caused by motional heating, imperfect optical pumping and spontaneous decay are negligible.

sources and their magnitudes are: crosstalk between next neighbors of  $\epsilon_{neighbor} = 3\%$ ; Intensity fluctuations are given by  $\Delta I/I = 2\%$ ; Dephasing is characterized by the coherence time  $\tau_{coh} = 15\text{ms}$  and the correlation time  $\tau_{corr} = 333\mu\text{s}$  as defined in reference [23]. Coupling to spectator modes is modeled by additional intensity fluctuations of 2%. The simulated output state of the two system qubits is then compared with the expected ideal state. The effect for each individual noise source is identified by simulating the sequence multiple times where for each simulation only a single source is affecting the simulation. The simulations for individual error sources indicate that the dominant error source is dephasing as shown in table B.19. This is expected because the duration of the sequence of operations is 2ms which is not short compared to the coherence time of 15ms. Including all noise sources, the simulation predicts a fidelity with the ideal density matrix of 79% whereas the experimentally measured fidelity is 72%. The overlap of the simulated with the measured density matrix is 94%.

The second simulated algorithm is a fully coherent quantum Fourier transform (QFT) which is treated in more detail in section 2.2.4. The sequence of operation as shown in the appendix, table B.2, is simulated with identical parameters as the previous algorithm. The simulation predicts a fidelity of 92.6% with the ideal state whereas an experimentally obtained density matrix leads to an overlap of 81(3)%. The results of the simulation for the individual noise sources are shown in table 2.5 where the biggest contribution is now crosstalk.

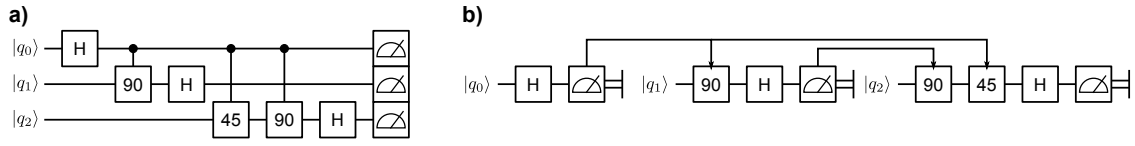


Figure 2.21.: (a) Quantum circuit for a three qubit QFT algorithm. (b) Single-qubit Kitaev version of the QFT. The measurement outcome is stored in a classical memory which controls the subsequent single-qubit rotations.

## 2.2.4. Example algorithms

In the following we provide examples of how the available toolbox can be employed to realize various quantum algorithms where we focus on building blocks for a realization of Shor’s algorithm to factor a large integer numbers [4, 30]. The part of the algorithm that requires a quantum computer is based on an order-finding algorithm which itself requires the quantum Fourier transform (QFT). This quantum analog to the discrete Fourier transform maps a quantum state vector  $|x\rangle = \sum_j x_j |j\rangle$ , into the state  $|y\rangle = \sum_k y_k |k\rangle$  where the vector  $y = (y_1, \dots, y_N) = \mathcal{F}(x)$  is the classical discrete Fourier transform of  $x = (x_1 \dots, x_N)$  [30]. It is straightforward to translate this operation into a quantum circuit (see reference [30]) where an example for three qubits is shown in figure 2.21a). The most straightforward (although not necessarily the most effective) way to implement the QFT is to realize directly the desired unitary using our available operations. With our optimization toolbox as described in section 2.2.1 we are able to find an optimized decomposition of the three-qubit QFT consisting of 18 operations as shown in the appendix, table B.2. The smallest MS operation in the sequence is  $\pi/16$  and thus the MS operations has to be optimized with this rotation angle. A maximally entangling operation is then implemented by applying this operation 8 times subsequently.

We benchmark the QFT by performing a full three-qubit quantum process tomography and find a process fidelity of 72% with the ideal QFT [38]. However, in order to find the best suited measure for the quality of an algorithm, one should consider how the quantum algorithm is embedded in the given problem. The QFT is almost exclusively used as the final building block of larger algorithms and then only the classical information of the final state is needed to determine the algorithm’s performance [91]. The quantum process fidelity is not the optimal measure to benchmark the performance of the QFT as it includes correlations that do not affect the outcome of the algorithm. One would rather choose a measure that utilizes the classical probabilities of the individual output states which can be described by a  $2^N$  vector  $p = (p_1, \dots, P_{2^N})$ . Such a measure is the squared statistical overlap (SSO)  $S(p, q) = (\sum_i \sqrt{p_i q_i})^2$  which is the classical analog to the quantum state fidelity [92]. An alternative suitable measure for the classical information is the statistical distinguishability  $D(p, q) = 1 - 1/2 \sum_i |p_i - q_i|$ , which is related to the quantum trace distance. These benchmarks are applied to a representative set of input states covering all possible periods. In reference [93], a QFT algorithm was benchmarked using 5 input states with different period and thus we use similar input states for comparability, as shown in table 2.6. The classical benchmarks yield on average an SSO of 87% which is considerably higher than the quantum process fidelity of 72%.

Since the QFT is mainly used as the final block in an algorithm, it can be replaced by the

Input state	Period	SSO	Distinguishability
$1/\sqrt{8} ( 111\rangle +  110\rangle + \dots +  000\rangle)$	1	77.1	77.1
$1/\sqrt{4} ( 110\rangle +  100\rangle +  010\rangle +  000\rangle)$	2	78.0	73.3
$1/\sqrt{4} ( 110\rangle +  100\rangle +  011\rangle +  000\rangle)$	3	90.4	86.4
$1/\sqrt{2} ( 011\rangle +  000\rangle)$	4	94.8	87.4
$ 000\rangle$	8	97.3	88.1

Table 2.6.: Results for a fully coherent 3 qubit QFT.

Input state	Period	SSO	Distinguishability
$1/\sqrt{4} ( 000\rangle +  100\rangle +  010\rangle +  110\rangle)$	2	99.5	94.5
$1/\sqrt{2} ( 100\rangle +  000\rangle)$	4	99.6	96.4
$ 000\rangle$	8	99.7	95.6

Table 2.7.: Results for the semiclassical Kitaev single qubit QFT.

semi-classical QFT that exchanges the quantum-controlled rotations by a measurement and a classically controlled rotation [91, 93]. This requires the measurement of each qubit to be performed before the operations that are controlled by this qubit. In figure 2.21 the time order of the measurements corresponds to qubit  $q_0, q_1, q_2$ . A measurement furthermore destroys all quantum coherence on the qubit and thus it is possible to reuse the physical qubit and store the measurement outcome on a classical computer. This allows to perform a semi-classical QFT on a single qubit as sketched in figure 2.21b) which is known as the Kitaev QFT [94]. Note that it is not possible to generate an entangled input state with this version of the QFT and thus the Kitaev QFT is more restricted than the semi-classical QFT. Furthermore, the ability to measure and reset the qubit within the algorithm is required which is possible with our extended set of operations. In ion-trap systems, in-sequence measurements notably disturb the motional state of the ion string and thus it is advisable to make the measurement as short as possible. In this case we chose a measurement duration of  $150\mu s$  which still allows for a detection fidelity of 99% [95]. In order to achieve high fidelity operations after such a measurement it appears necessary to recool the COM mode with the Raman cooling technique as described in section 2.2.1. In the special case of the single-qubit QFT however only local operations are required after a measurement which can furthermore be implemented with the addressed beam. Due to the small Lamb-Dicke parameter, the quality of the single-qubit operations is not notably affected by the thermal occupation of the COM and the spectator modes after the measurements and thus recooling is not required. In table 2.7 the outcome for the single qubit QFT is shown for the non-entangled input states used before, leading to an average SSO of 99.6%. As expected, the single-qubit Kitaev QFT clearly performs better than the fully coherent QFT.

One of the important algorithms that is compatible with the presented Kitaev single-qubit QFT is the order-finding algorithm which is able to determine the order of a permutation operation efficiently [30]. A permutation operation  $\pi(y)$  has order  $k$  if  $k$ -times application of the operations results in the identity:  $\pi(y)^k = y$ . The algorithm splits the available quantum register in two parts: (i) a register where the permutation operation is applied and (ii) a QFT register that is initially prepared in an equal superposition state. The qubits from the QFT register control whether

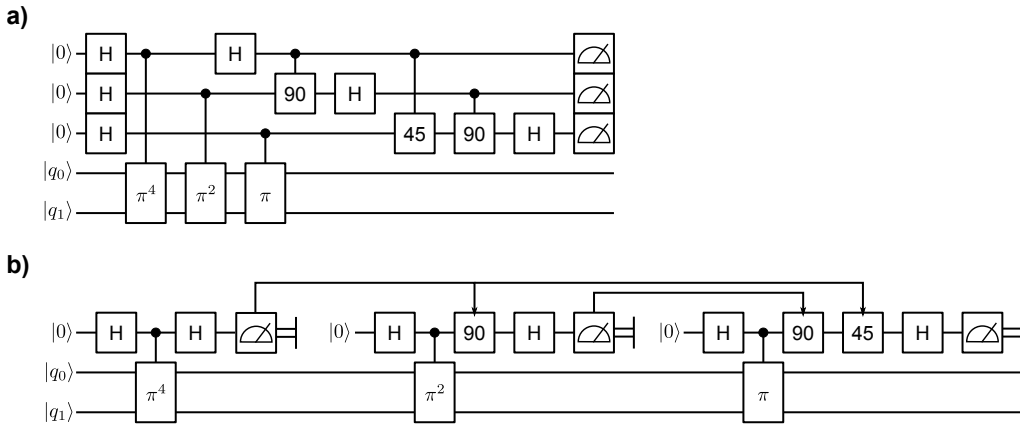


Figure 2.22.: order finding algorithm for a two qubit permutation operation in a) fully coherent and b) Kitaev version.

the permutation operations are applied. This operation is analogous to a CNOT operation where instead of the NOT operation the permutation operation is controlled. The  $k$ -th qubit from the QFT register controls the permutation operations  $\pi(y)^l$  with  $l = 2^k$  as shown in figure 2.22a). With this algorithm it is possible to use the single-qubit QFT to reduce the number of required qubits from 5 to 3 where the resulting quantum circuit is shown in figure 2.22b).

We seek to implement the optimized order-finding algorithm using permutations on two qubits as a proof of concept experiment. The chosen permutations, as shown in table 2.8, span an order from 2 to 4 where it is notable that the order of the permutation can depend on the input state. For example  $\pi_1(y)$  has order one for input states  $y = 0, 2$  and order two for  $y = 1, 3$ , whereas  $\pi_2(y)$  has order two regardless of the input state. The complexity of the algorithm depends on the investigated permutation operation, as the controlled permutation operations require entangling operations. The number of required operations for the individual permutation operations are presented in table 2.8 and the sequences of operations can be found in the appendix. In contrast to the single-ion QFT as presented above, the use of entangling operations after measuring the QFT qubit is required. This makes it necessary to recool the ion string within the sequence, where we employ the Raman recooling technique as described in section 2.2.1. We choose a recooling time of  $800\mu s$  as this proved to provide a good balance between remaining excitation of the COM mode and additional phase damping due to the cooling time [95].

The output of the algorithm is again classical and thus the classical probabilities for measuring the state  $|j\rangle$  are sufficient to infer the quality of the operation. Figure 2.23 shows the classical probabilities of the basis states for all permutation operations where the experimental results (blue bars) are compared with the expected ideal probabilities (red bars) and estimated probabilities from TIQC-SPICE simulations (green bars). Again the implementation is benchmarked with the classical SSO and distinguishability measures as presented in table 2.9 yielding an average SSO of 80.7%. The original problem is finding the correct permutation and therefore one could think of using a classical algorithm to find the most likely order for a given outcome. This algorithm can then serve as a benchmark for the quality of the order-finding. However, finding such an efficient evaluation is beyond the scope of this work.

y	$\pi_1(y)$	$\pi_2(y)$	$\pi_3(y)$	$\pi_4(y)$
0	0	1	0	3
1	3	0	3	0
2	2	3	1	1
3	1	2	2	2
max(order)	2	2	3	4
no of operations $\pi(y)$	11	10	23	24
no of operations $\pi(y)^2$	-	-	17	10

Table 2.8.: Representative permutation operations for order 2 to 4 which were used as examples for the order-finding algorithm. The number of operations for applying the operation once and twice are also shown. The sequence of operation for the controlled permutation operations are presented in the appendix.

Order	Permutation operation	SSO	Distinguishability
1	$\pi_1(0)$	75.3(7)	75.3(7)
2	$\pi_2(0)$	86.4(6)	86.5(6)
3	$\pi_3(1)$	85.9(6)	70.3(8)
4	$\pi_4(0)$	91.6(5)	90.7(6)

Table 2.9.: Results for the semiclassical Kitaev order finding algorithm using the permutation operations defined in table 2.8.

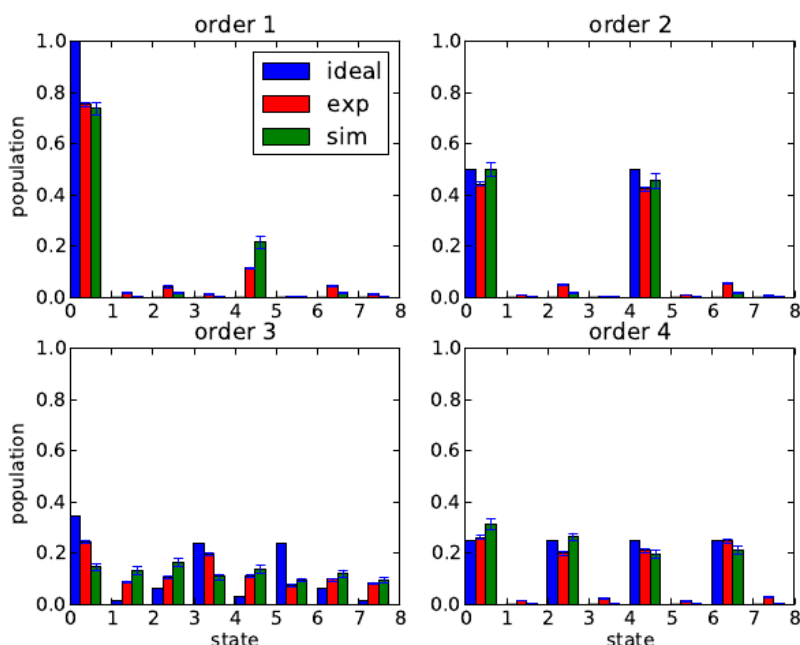


Figure 2.23.: State probabilities for the order finding algorithm for the permutation operations  $\pi_1 \dots \pi_4$ . The ideal probabilities (blue), experimental results (red) and predictions from a classical simulation (green) are shown.

### **2.2.5. Conclusion and Outlook**

In conclusion we have presented a small-scale quantum information processor based on trapped  $^{40}\text{Ca}^+$  ions. A set of operations beyond coherent operations, that is capable to implement arbitrary Markovian processes, has been introduced. The major noise sources of the system acting on a qubit memory and during operations have been analyzed and their influence on different algorithms have been discussed. It has been shown that the dominant source of errors depends on the actual sequence of operations. We used the entire set of operations to realize an efficient implementation of the order-finding algorithm. Here, we have been able to reduce the number of required qubits in the sense that only a single qubit is required for the entire QFT register in the algorithm. We envision, that these techniques will be the building blocks in a scalable implementation of Shor's factoring algorithm. Furthermore we hope that the presented methods for characterizing the noise sources will lead to successful strategies for reducing the error rate in complex algorithms paving the way to fault-tolerant quantum computation.

### **Acknowledgments**

We gratefully acknowledge support by the Austrian Science Fund (FWF), through the SFB FoQus (FWF Project No. F4002-N16), by the European Commission (AQUTE), as well as the Institut für Quantenoptik und Quanteninformation GmbH. This research was funded by the Office of the Director of National Intelligence (ODNI), Intelligence Advanced Research Projects Activity (IARPA), through the Army Research Office grant W911NF-10-1-0284. All statements of fact, opinion or conclusions contained herein are those of the authors and should not be construed as representing the official views or policies of IARPA, the ODNI, or the U.S. Government.

# 3. Experimental quantum error correction

## 3.1. Introduction to quantum error correction

It is obvious that in any physical realization of a quantum computer, the operations cannot be implemented perfectly. Over the course of a complex algorithm, even small errors will amplify and refute any gain from a quantum computer if the errors are ignored. It is well known that classical computing systems can be built fault-tolerant using techniques to detect and correct for failures in parts of the system [12]. However, it was highly disputed whether a fault tolerant quantum computer obeying the laws of quantum mechanics could be built, until the groundbreaking work of Steane and Shor in 1996[13, 14]. They independently proposed quantum error correction (QEC) schemes which allow one to perform arbitrary complex quantum algorithms with non-exponential overhead. These protocols protect the quantum information by encoding the information of a single logical qubit into multiple physical qubits and continuously detecting and correcting occurring errors.

Presenting a full theory of quantum error correction and fault tolerant quantum computing is beyond the scope of this work and thus the interested reader is referred to the tutorial in reference [96]. Instead of presenting a rigorous treatment of QEC protocols I will illustrate the differences between classical and quantum error correction by simple examples.

A familiar example for a classical error correction procedure is the three bit repetition code that copies the information of a single logical bit  $[0_l, 1_l]$  onto a register of three bits:

$$[0_l, 1_l] \rightarrow [000, 111]$$

The set of valid states of the encoded register is then  $\{000, 111\}$ . Errors in a classical computer occur in form of bit-flips described by  $0 \rightarrow 1$  and  $1 \rightarrow 0$ . Assuming a bit-flip on the first qubit of the encoded state changes the register to  $[001, 110]$  moving the state out of the allowed set of states. In a classical computer one can now easily measure all three bits and perform a majority vote to gain information on the error but also on the most likely encoded value. The error can be easily corrected by performing a NOT operation on the distorted qubit if only a single bit-flip occurred on the entire register. If more than a single bit-flips on the physical bits occur, the majority vote will result in a bit-flip of the encoded information and thus the correction fails.

Naturally, QEC techniques share fundamental ideas with error correction in classical computers as they encode the information redundantly in a larger system. Performing error correction in a quantum system adds further difficulties because the laws of quantum mechanics set following

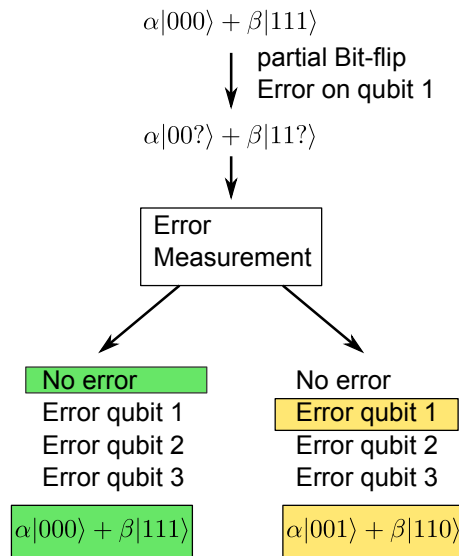


Figure 3.1.: Illustration of the discretization of a partial bit-flip by an error measurement in a three qubit QEC protocol.

constraints:

1. The information of a qubit cannot be copied to another qubit.
2. Errors on a qubit are continuous.
3. The measurement of a qubit irreversibly affects its state.

Let's try to transfer the three-bit classical error correction algorithm to a quantum computer satisfying the mentioned constraints. The most general state of the qubit to be encoded (the system qubit) is  $|\Psi_s\rangle = \alpha|0\rangle_s + \beta|1\rangle_s$  but here, contrary to the classical algorithm, it is impossible to copy this state onto the two remaining qubits. This problem can be overcome by generating an entangled state of the form

$$|\Psi\rangle = \alpha|000\rangle + \beta|111\rangle$$

that allows one to perform a majority vote.

The next obstacle for QEC is that errors in a quantum system are continuous. It should be noted here, that any error can be decomposed in a partial phase-flip and a partial bit-flip. A phase-flip (bit-flip) corresponds to an incoherent rotation around the z-axis (x-axis) on the Bloch sphere. Thus any arbitrary error can be described by these two types of flips in the same way as any coherent operation on a qubit can be decomposed into rotations around the x-axis and z-axis of the Bloch spheres. We will now concentrate on bit-flips only, the generalization onto both types of errors will be done later. First, it is outlined how a collective measurement can be used to discretize a partial bit-flip. It is well known in quantum physics that any measurement affects the state of the system as it leaves the system in a state that is compatible with the outcome of a measurement. For example, a measurement in the computational basis on a qubit projects the system onto the state  $|0\rangle$  or  $|1\rangle$  depending on the outcome. Thus, one can think of a collective measurements on the entire register that asks only if a certain type of error happened or not.

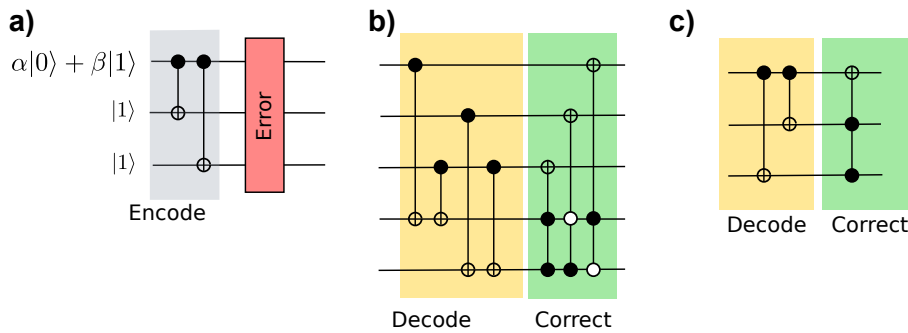


Figure 3.2.: a) Encoding of a qubit in the three-qubit repetition code. b) Decoding and correction without additional ancilla qubits. c) Decoding and correction without leaving the protected subspace

Such a measurement projects the register always into a state where no error happened at all, or where the error happened with full strength which discretizes a partial error. An example for this in a three-qubit repetition code is shown in figure 3.1: The error measurement is performed on the encoded state and has four possible outcomes: No Error or a single qubit bit-flip on a known qubit. After this measurement, the system is projected into an eigenstate of its outcome which corresponds either to the original state or to the state undergoing a full bit-flip. Therefore it is clear that this procedure discretizes a partial error.

One last and crucial difference between classical and quantum error correction is also related to measuring the error syndrome. As discussed above, a measurement always affects the state of the register. In order to protect the encoded quantum information, the measurement for detecting the error has to be designed such, that it cannot gain any information on the state of the logical qubit at the same time as it gets full information about which error happened. As mentioned in section 1.2 it is possible to perform an effective arbitrary measurement by applying unitary operations followed by a measurement in the computational basis. Thus, a measurement is required that maps the information about the errors into the computational basis of additional auxiliary qubits.

Now the quantum circuit that is required to implement a simple proof of concept QEC protocol is discussed. Analogous to classical error correction, the system qubit is encoded into the register as:

$$\alpha|0\rangle + \beta|1\rangle \otimes |00\rangle \rightarrow \alpha|000\rangle + \beta|111\rangle.$$

Similar to the process to create an entangled state with a CNOT operation as described in section 1.2 and shown in figure 1.3, encoding a single qubit into the three qubit repetition code can be performed with the aid of two CNOT operations as shown in figure 3.2a). It is important to note here, that this code only protects against either bit-flips or phase-flips and cannot be used to correct for arbitrary errors. However, it is possible to concatenate two three-qubit repetition codes, where the first instance corrects for phase-flips and the second for bit-flips. In this extension, a single logical qubit is then encoded in nine physical qubits as shown in figure 3.3 [30].

In the classical case, the error syndrome can be simply obtained by measuring all three qubits and performing a majority vote. But as mentioned above, in the quantum case a collective

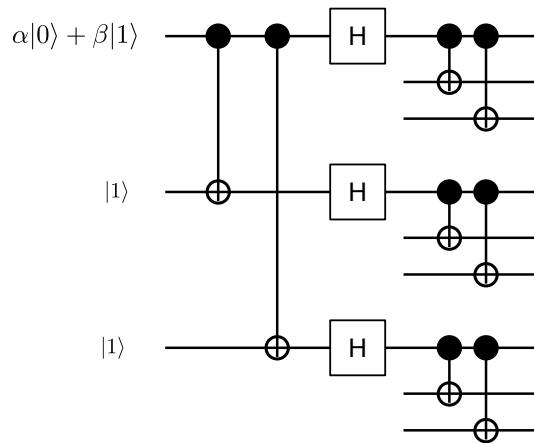


Figure 3.3.: Error correction scheme for a single qubit protecting against arbitrary errors.

State	Detected error	Syndrome state
$\alpha 000\rangle + \beta 111\rangle$	No error	$ 00\rangle$
$\alpha 001\rangle + \beta 110\rangle$	Bit-flip on qubit 1	$ 10\rangle$
$\alpha 010\rangle + \beta 101\rangle$	Bit-flip on qubit 2	$ 01\rangle$
$\alpha 100\rangle + \beta 011\rangle$	Bit-flip on qubit 3	$ 11\rangle$

Table 3.1.: The detectable errors and the corresponding states.

measurement on the system has to be performed to gain information about the possible error. For the three-qubit code, four possibilities exist: No error, or a bit-flip on one of the three qubits. This information can be stored in two qubits and thus one can obtain information on the error (the error syndrome) by mapping it onto two auxiliary qubits as illustrated in figure 3.2b) [30]. The actual value of the syndrome qubits are shown in table 3.1. A bit flip on qubit 3 is indicated by the ancilla qubits being in state  $|11\rangle$  and can be corrected by performing a double controlled NOT operation<sup>1</sup> on the third qubit. Qubit 2 and 3 can be corrected with analogous operations that are performing the NOT operation if the ancilla qubits are in state  $|10\rangle$  and  $|01\rangle$ . Figure 3.2b) shows the full en- and decoding circuit where closed (open) circles correspond to a apply the NOT operation if the corresponding qubit is in state  $|1\rangle$  ( $|0\rangle$ ). This procedure preserves the register in a protected state even after the correction but has the drawback that it requires two additional qubits to gain knowledge about the occurred error.

There exists an alternative correction procedure that leaves the system in an unprotected state after the correction but is still able to correct for an occurring error on the system qubit as shown in figure 3.2c) [30]. Once, the error syndrome is known, the correction of the error can be performed by coherent operations. It should be noted though, that the error syndrome can be represented by classical information and therefore it also possible to perform a measurement of the error syndrome in the computational basis and correct the error with subsequent classically controlled single-qubit rotations as shown in reference [93].

In order to realize a fault-tolerant quantum computer, the errors need to be corrected continuously.

<sup>1</sup>This operation is known as a Toffoli gate.

It has been shown, that it is sufficient to perform the QEC protocols repeatedly, which corresponds to a discrete correction of the occurring errors [96]. In the QEC protocol explained above, the information about the error resides in the auxiliary qubits after the correction. In order to repeat the correction with the same auxiliary qubits, this information has to be removed from the system. This is a prime example of non-coherent operations being required inside an algorithm. From a thermodynamic point of view, the errors can be described by adding entropy to the system, which has to be removed via resetting the auxiliary qubits [97]. A toy model for this error correction process is then a thermodynamic machine, where errors on the register correspond to a heating due to coupling to a hot environment. The QEC procedure couples the register to zero-temperature auxiliary qubits. This allows one to hold the machine at a low temperature which corresponds to the desired low error rate as shown in figure 3.4. The QEC protocol maps the entropy introduced by the noise onto the ancilla qubits. This entropy needs to be removed from the system with an irreversible process. On the qubits, this entropy transfer corresponds to re-initializing them into a well defined state.

From the comparison between quantum and classical error correction it became clear that many differences between the two protocols are rooted in the peculiarities of measurements on a quantum system. Furthermore, errors in a quantum register can be described as measurements in different bases and thus the connection between quantum measurements and error correction becomes even more obvious. Thus, QEC protocols have the ability to *undo* (or reverse) measurements, which seemingly contradicts the foundations of quantum mechanics stating that measurements are irreversible processes [98]. This confusion can be solved if one keeps in mind that the QEC protocol is only able to correct for errors that occur on parts of the register. Therefore it is only possible to reverse measurements that act partially on the register which is not forbidden by the no-cloning theorem. A measurement in the computational basis corresponds to a phase-flip error and thus a three-qubit repetition code protecting against phase-flip errors is able to undo a measurement on a single-qubit in the register.

In the following publication, the first realization of three rounds of QEC were presented. For this experiment, a technique to reset a single qubit in a larger register was developed. In a following experiment, it was shown that the three-qubit repetition code protecting against phase-flips is able to reverse a partial measurement of a qubit register. In order to perform this measurement reversal, it is necessary to be able to perform entangling operations after the measurement on a single qubit. Measurements in ion-trap systems disturb the state of the motional mode significantly and thus the ion-string needs to be recooled before applying subsequent entangling operations. Therefore we introduced an in-sequence recoiling technique based on a Raman transition (for details see section 2.2)

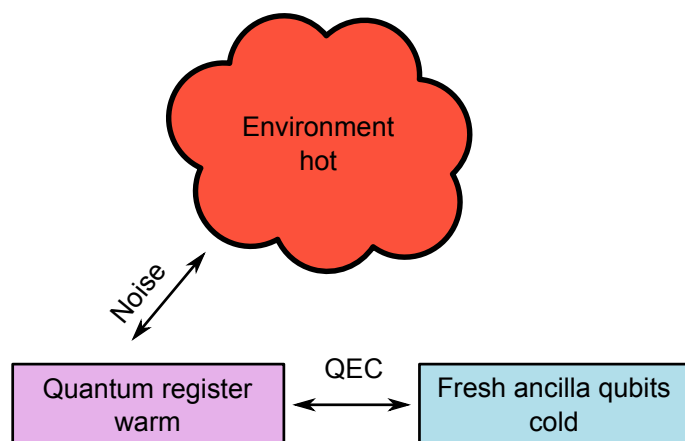


Figure 3.4.: Thermodynamic analogon to a continuously applied QEC protocol.

## 3.2. Publication: Experimental repetitive quantum error correction

### Experimental repetitive quantum error correction<sup>2</sup>

Science **332**, 1059 (2011)

Philipp Schindler<sup>1</sup>, Julio T. Barreiro<sup>1</sup>, Thomas Monz<sup>1</sup>, Volckmar Nebendahl<sup>2</sup>,  
Daniel Nigg<sup>1</sup>, Michael Chwalla<sup>1,3</sup>, Markus Hennrich<sup>1\*</sup>, Rainer Blatt<sup>1,3</sup>

<sup>1</sup>Institut für Experimentalphysik, University of Innsbruck,  
Technikerstr. 25, A-6020 Innsbruck, Austria,

<sup>2</sup>Institut für Theoretische Physik, University of Innsbruck,  
Technikerstr. 25, A-6020 Innsbruck, Austria,

<sup>3</sup>Institut für Quantenoptik und Quanteninformation  
Österreichische Akademie der Wissenschaften,  
Otto-Hittmair-Platz 1, A-6020 Innsbruck, Austria

The computational potential of a quantum processor can only be unleashed if errors during a quantum computation can be controlled and corrected for. Quantum error correction works if imperfections of quantum gate operations and measurements are below a certain threshold and corrections can be applied repeatedly. We implement multiple quantum error correction cycles for phase-flip errors on qubits encoded with trapped ions. Errors are corrected by a quantum-feedback algorithm employing high-fidelity gate operations and a reset technique for the auxiliary qubits. Up to three consecutive correction cycles are realized and the behavior of the algorithm for different noise environments is analyzed.

Information in a quantum computer is extremely vulnerable to noise induced by the environment and thus needs to be protected with quantum error correction (QEC) techniques. Pioneering theoretical work in this field has shown that all errors can be corrected for if imperfections of the quantum operations and measurements are below a certain (error) threshold and the correction can be applied repeatedly [13, 99, 100]. Such error thresholds depend on details of the physical system and quantifying them requires a careful analysis of the system-specific errors, the encoding and decoding procedure and their respective implementation [30]. It is currently accepted that gate error probabilities ranging from  $10^{-4}$  -  $10^{-5}$  are tolerable [101], which seem to be in reach with technical improvements in conjunction with dynamical control techniques [102]. In addition, a fault-tolerant operation requires highly efficient, repeatable algorithms to minimize the computational overhead. So far, all experimental implementations [103–108] are limited to a single correction cycle, where the only experimental implementation in a scalable system [106] relies on projective measurements and classical feedback. Because high-fidelity measurements take time and potentially disturb the qubit system, it can be advantageous to use a measurement-free QEC algorithm based on implicit quantum feedback [30, 103]. Also, in contrast to previous expectations [7], these measurement-free protocols lead to error thresholds comparable to their measurement-based counterparts [109].

---

<sup>2</sup>The author of the present thesis measured and analyzed the data and wrote the manuscript

### 3. Experimental quantum error correction

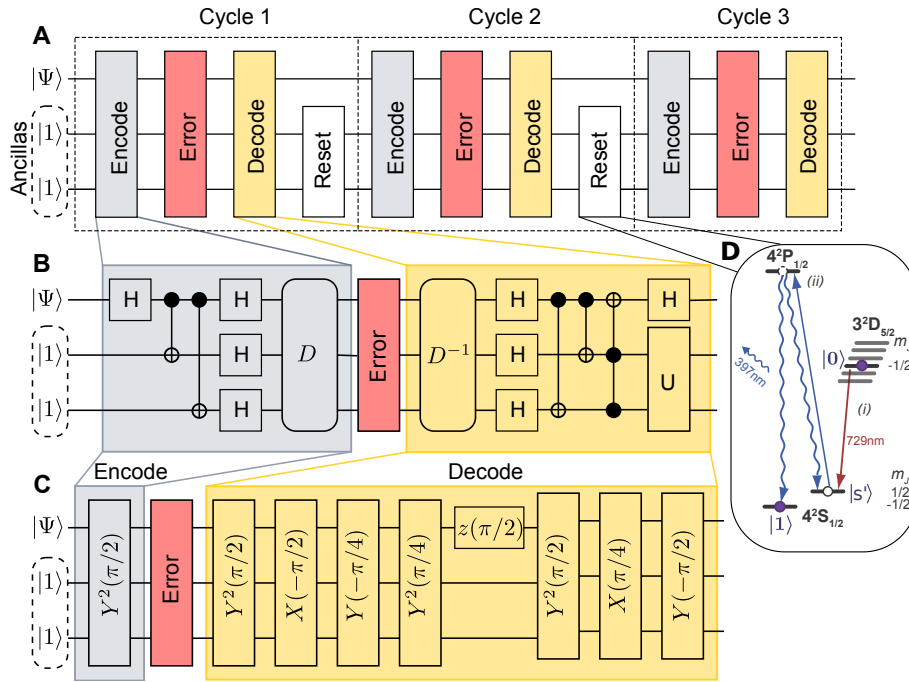


Figure 3.5.: (A) Schematic view of three subsequent error-correction cycles. (B) Quantum circuit for the implemented phase-flip error-correction code. The operations  $D$ ,  $D^{-1}$ , and  $U$  are described in the text. The operations  $H$  are Hadamard gates. (C) Optimized pulse sequence implementing a single error correction cycle; the operations are described in the text. (D) Schematic of the reset procedure. The computational qubit is marked by filled dots. The reset procedure consists of (i) shelving the population from  $|0\rangle$  to  $|s'\rangle = 4S_{1/2}(m = +1/2)$  and (ii) optical pumping to  $|1\rangle$  (straight blue arrow).

We demonstrate repeated QEC with a system of trapped  $^{40}\text{Ca}^+$  ions as qubits, and multiple repetitions of the algorithm are enabled by a toolbox consisting of high-fidelity quantum operations [23, 27], an optimized pulse sequence [33], and a qubit-reset technique that has a negligible effect on the system of qubits. The performance of the implementation is assessed with quantum process tomography in the presence of phase-flip errors and its behavior is analyzed for different environments that show correlated and uncorrelated phase-noise. Our approach is based on the three-qubit repetition code capable of detecting and correcting phase-flip errors on a single qubit [13, 30]. This algorithm protects against phase-noise which is the dominant error source in our ion-trap quantum computer causing gate errors as well as decoherence.

As indicated in figure 3.5a), each QEC cycle consists of (i) encoding the system qubit  $\{|0\rangle, |1\rangle\}$  and two auxiliary qubits (ancillas) into an entangled state, (ii) error incidence, (iii) detecting and correcting the error, and (iv) resetting the ancillas. Initially, the qubit to be protected is in the state  $|\Psi\rangle = \alpha|+\rangle + \beta|-\rangle$ , where  $|\pm\rangle = 1/\sqrt{2}(|0\rangle \pm |1\rangle)$ , and the two ancilla qubits are both prepared in the state  $|1\rangle$ . In the encoding stage, they are mapped into the entangled state  $\alpha|+++ \rangle + \beta|--- \rangle$ . Next, a single-qubit phase-flip error may change  $|\pm\rangle$  to  $|\mp\rangle$ . In the decoding and correction stage, the error is identified by a majority vote and the system qubit is

corrected accordingly. It should be noted that this protocol maps the information in and out of the protected state between QEC cycles. Each cycle is concluded by resetting the ancilla qubits while preserving the information on the system qubit.

The textbook implementation of a single cycle of this QEC procedure would consist of a circuit employing four controlled-NOT (CNOT) and one controlled controlled-NOT (Toffoli) gate operations [30] (see figure 3.5b). While the process fidelities of available CNOT (92%) [110] and Toffoli (80%) [26] implementations could possibly be improved, it seems more promising to pursue an approach based on global Mølmer-Sørensen (MS) entangling gate operations (99%) [27, 32]. These operations provide a universal set of gates in combination with individually addressed Stark-shift gates and collective single-qubit rotations [33, 46]. Moreover, the optimization procedure of Ref. [33] allows us to rigorously simplify the pulse sequence for a complete algorithm based on this set of gates. Two additional refinements lead to the algorithm used for the optimization (figure 3.5b). First, the space of optimized solutions is increased by adding an arbitrary unitary operation  $U$  acting only on the ancillas before resetting them. Second, the encoding stage can be simplified by adding an operation  $D$  and its inverse  $D^{-1}$  that commutes with any phase error. As a result, the encoding stage consists of a single entangling operation, and the decoding stage can be implemented with a total of eight pulses with only three entangling operations (figure 3.5c). Formally, this encoding implements a stabilizer code with the generators  $G = \{\sigma_y^{(1)} \sigma_z^{(2)} \sigma_y^{(3)}, \sigma_y^{(1)} \sigma_y^{(2)} \sigma_z^{(3)}\}$  which are a tensor product of the Pauli operators  $\sigma_{x,y,z}^{(i)}$  acting on qubit  $i$  [30].

The QEC protocol is realized in an experimental system consisting of a string of three  $^{40}\text{Ca}^+$  ions confined in a macroscopic linear Paul trap. Each ion represents a qubit in the  $|1\rangle = 4S_{1/2}(m = -1/2)$  and  $|0\rangle = 3D_{5/2}(m = -1/2)$  states. The state of the qubits is then manipulated by a series of laser pulses resonant with the qubit transition. Our universal set of gates consists of (i) collective local operations  $X(\Theta), Y(\Theta) = \exp(-i\Theta/2 S_{x,y})$ , (ii) single-qubit operations  $Z_k(\Theta) = \exp(-i\Theta/2 \sigma_z^{(k)})$ , and (iii) collective entangling Mølmer-Sørensen [23, 27, 32] operations  $Y^2(\Theta) = \exp(-i\Theta/4 S_y^2)$ , with  $S_{x,y} = \sum_{k=1}^3 \sigma_{x,y}^{(k)}$ . The collective operations are realized with a wide beam exciting all ions simultaneously and the single-qubit operations are performed with a tightly focused beam affecting only individual ions. An experimental cycle consists of cooling the ion string to the motional ground state, applying the manipulating laser pulses, and measuring the population of the qubit states. This procedure is repeated up to 1000 times to obtain the final quantum state of the qubits.

An important tool, critical to the repeated application of the QEC protocol, is the proper reset of the ancilla qubits which is carried out with an optical-pumping technique (figure 3.5d). For the reset procedure, the population of the ancilla qubits in state  $|0\rangle$  is first transferred into the state  $|S'\rangle = 4S_{1/2}(m = +1/2)$  using the addressed beam. This population in  $|S'\rangle$  is then excited to the  $4P_{1/2}(m = -1/2)$  level by a circularly-polarized laser beam at a wavelength of 397 nm. Finally, the population from the  $4P_{1/2}$  level spontaneously decays to the  $4S_{1/2}$  level (population loss into  $3D_{3/2}$  level is avoided by a repump laser resonant with the  $3D_{3/2} - 4P_{1/2}$  transition). The electronic state of the system qubit is not affected by the wide pumping laser because it couples only to the ancillas' population in  $|S'\rangle$ . The effect on the motional state of the ion string was calculated with a multi-level numerical simulation from which we estimate a heating rate of 0.015 phonons per reset step for our experimental parameters. Because the protocol uses only

### 3. Experimental quantum error correction

Number of QEC cycles	no error $F_{none}$	optimized no error $F_{opt}$	single-qubit errors $F_{single}$	optimized single-qubit errors $F_{sopt}$
0	97(2)	97(2)	-	-
1	87.5(2)	90.1(2)	89.1(2)	90.1(2)
2	77.7(4)	79.8(4)	76.3(2)	80.1(2)
3	68.3(5)	72.9(5)	68.3(3)	70.2(3)

Table 3.2.: Process fidelity for a single uncorrected qubit as well as for one, two, and three error correction cycles.  $F_{none}$  is the process fidelity without inducing any errors.  $F_{single}$  is obtained by averaging over all single-qubit errors.  $F_{opt}$  and  $F_{sopt}$  are the respective process fidelities where constant operations are neglected. The statistical errors are derived from propagated statistics in the measured expectation values.

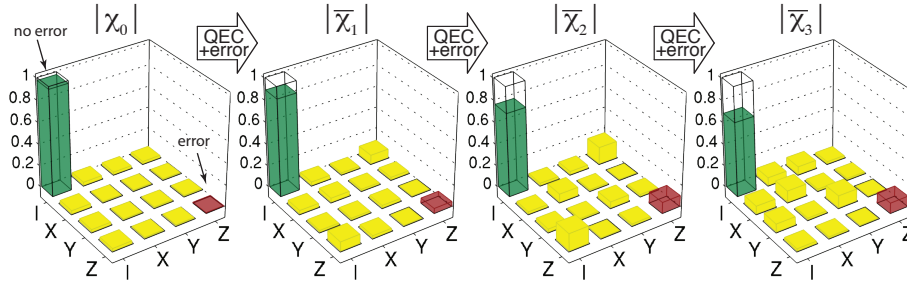


Figure 3.6.: Mean single-qubit process matrices  $\bar{\chi}_n$  (absolute value) for  $n$  QEC cycles with single-qubit errors. Transparent bars show the identity process matrix and the red bar denotes a phase-flip error. These process matrices were reconstructed from a data set averaged over all possible single-qubit errors (see text).

entangling operations of the Mølmer-Sørensen type, which are insensitive to the ion motion in first order, the reset has a negligible effect on the QEC protocol.

The operational quality of the QEC protocol can be assessed by exposing it to correctable errors, i.e. single-qubit phase-flip errors. Ideally, the encoded qubit experiences an identity operation. Experimentally, the implemented process is characterized with quantum process tomography [28, 38] which yields a process matrix  $\chi$ . The performance of the implementation is given by the overlap of the identity process  $\chi_{id}$  with the implemented process, also known as the process fidelity  $F_{proc} = \text{Tr}(\chi \cdot \chi_{id})$ . The achieved process fidelities for up to three repetitions (without inducing any errors)  $F_{none}$  are shown in table 3.2. The process fidelity, however, does not distinguish between constant operational errors (that could be undone in principle) and decoherence (irreversible processes). A measure which is only sensitive to errors due to decoherence is the optimized process fidelity  $F_{opt}$  as displayed in Table 1. It is defined as the maximum fidelity that could be obtained if an additional fixed single-qubit rotation was perfectly implemented on the output state (see supplementary material in section B.2).

The error-correcting capability of the implementation is assessed by applying in each cycle either no-error or a single-qubit phase-flip  $Z_i(\pi)$  on ion  $i$  (1 being the system ion and 2,3 being

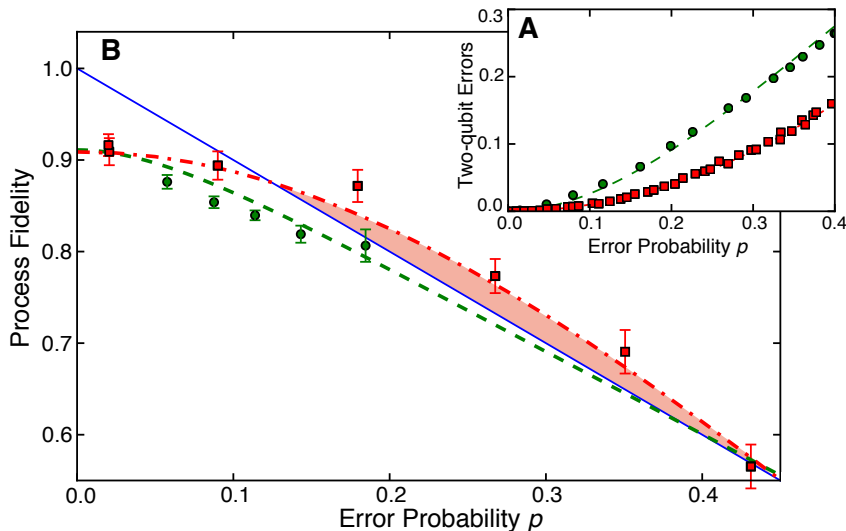


Figure 3.7.: (A) Probability of simultaneous two-qubit phase-flips as a function of the single-qubit phase flip probabilities for uncorrelated (square) and correlated (circle) noise measured by a Ramsey type experiment. (B) Process fidelity of the QEC algorithm in the presence of correlated (circle) and uncorrelated (square) phase noise as a function of the single-qubit phase flip probability. The theory is shown for an unencoded qubit (solid line), a corrected qubit in presence of correlated (dashed line) and uncorrelated noise (dashdotted line).

the 1<sup>st</sup> and 2<sup>nd</sup> ancilla) followed by a process tomography for all combinations. As these single-qubit errors are corrected by the algorithm, the ideal process is again the identity process. The mean process matrix  $\bar{\chi}$  is then reconstructed from the data obtained by averaging over all measured expectation values, as shown for zero to three correction cycles in figure 3.6. The results shown in Table 1 demonstrate that the optimized process fidelities with single-qubit errors,  $F_{\text{sopt}}$ , and without an induced error,  $F_{\text{opt}}$ , are the same for one, two, and three correction cycles. From this data we infer that the QEC protocol corrects single-qubit errors perfectly within our statistical uncertainty. The infidelities of the implementation are mainly caused by imperfections in the entangling gates as discussed in section B.2).

In addition to characterizing the implemented process in the presence of correctable errors we investigate the algorithm's behavior in a dephasing environment where also uncorrectable errors occur. For single qubits, a dephasing process can be described by a phase-flip probability  $p$  which reduces the off-diagonal elements of the density matrix by a factor of  $1 - 2p$  (for complete dephasing  $p = 0.5$ ). In a system of multiple qubits, the probability of simultaneous  $n$ -qubit phase-flips, which cannot be corrected by the three-qubit QEC protocol, depends on the correlations between the qubits (see supplementary material in section B.2). We analyze the behavior of the QEC algorithm in the presence of the two most prominent noise types, namely uncorrelated and correlated phase-noise, where the qubits are affected by independent or one and the same noise source, respectively. In our system, the inherent phase-noise is correlated as it orig-

inates predominantly from fluctuations in the magnetic-field strength and the laser frequency which are both equal on all qubits [23]. A controlled amount of this noise can be simply applied by inserting a waiting time between the encoding and the decoding stage. The second noise type, uncorrelated phase-noise, can be engineered by performing a weak qubit projection [30], which is realized by a short laser pulse on the detection transition once the qubit is encoded (see supplementary material in section B.2). We characterized the phase noise by Ramsey type experiments, which translate phase-flips into bit-flips. The presence of the respective noise type can then be verified by the probability of simultaneous  $n$ -qubit bit-flips (figure 3.7a).

For both uncorrelated and correlated phase noise, our error correction algorithm performs as depicted in figure 3.7b. As uncorrectable two- and three-qubit phase-flips occur more frequently in the presence of correlated noise (figure 3.7b) the QEC implementation yields lower fidelities. It should be noted though, that correlated phase-noise can be completely eliminated by encoding the qubits in decoherence-free subspaces [105, 111, 112] at the expense of a further increased complexity. For uncorrelated phase noise no decoherence-free subspaces exist, and therefore only quantum error correction can protect the qubit. In our implementation, a protected qubit shows less noise than an unencoded qubit for an error probability  $p$  larger than 0.15 (figure 3.7b). In the investigation with uncorrelated noise, the weak projection collapses each qubit with a small probability into the computational basis. Our data thus indicates that the algorithm can recover the quantum information from this single-qubit state collapse.

Our results demonstrate an implementation of a repeatable error correction algorithm in a system of three trapped-ion qubits. Using global-entangling and local-qubit operations in an optimized pulse sequence allows for very short and efficient QEC cycles. For uncorrelated errors, a (single-cycle) corrected qubit performs better than an uncorrected qubit for a range of error probabilities. The algorithm can be extended to a five-qubit implementation, where the qubit stays protected during error correction [33]. Though technically challenging, such an implementation in conjunction with DFS encoding appears as a viable route towards quantum error correction for trapped ions.

### 3.3. Publication: Undoing a quantum measurement

#### Undoing a quantum measurement<sup>3</sup>

Phys. Rev. Lett. **110**, 070403 (2013)

Philipp Schindler<sup>1</sup>, Thomas Monz<sup>1</sup>, Daniel Nigg<sup>1</sup>, Julio T. Barreiro<sup>1</sup>, Esteban A. Martinez<sup>1</sup>,  
Matthias F. Brandl<sup>1</sup>, Michael Chwalla<sup>1,2</sup>, Markus Hennrich<sup>1</sup>, Rainer Blatt<sup>1,2</sup>

<sup>1</sup>Institut für Experimentalphysik, University of Innsbruck,  
Technikerstr. 25, A-6020 Innsbruck, Austria,

<sup>2</sup>Institut für Quantenoptik und Quanteninformation  
Österreichische Akademie der Wissenschaften,  
Otto-Hittmair-Platz 1, A-6020 Innsbruck, Austria

In general, a quantum measurement yields an undetermined answer and alters the system to be consistent with the measurement result. This process maps multiple initial states into a single state and thus cannot be reversed. This has important implications in quantum information processing, where errors can be interpreted as measurements. Therefore, it seems that it is impossible to correct errors in a quantum information processor, but protocols exist that are capable of eliminating them if they affect only part of the system. In this work we present the deterministic reversal of a fully projective measurement on a single particle, enabled by a quantum error-correction protocol that distributes the information over three particles.

Measurements on a quantum system irreversibly project the system onto a measurement eigenstate regardless of the state of the system. Copying an unknown quantum state is thus impossible because learning about a state without destroying it is prohibited by the no-cloning theorem[98]. At first, this seems to be a roadblock for correcting errors in quantum information processors. However, the quantum information can be encoded redundantly in multiple particles and subsequently used by quantum error correction (QEC) techniques [13, 14, 103, 106–108]. When one interprets errors as measurements, it becomes clear that such protocols are able to reverse a partial measurement on the system. In experimental realizations of error correction procedures, the effect of the measurement is implicitly reversed but its outcome remains unknown. Previous realizations of measurement reversal with known outcomes have been performed in the context of weak measurements where the measurement and its reversal are probabilistic processes[113–116]. We will show that it is possible to deterministically reverse measurements on a single particle.

We consider a system of three two-level atoms where each can be described as a qubit with the basis states  $|0\rangle, |1\rangle$ . An arbitrary pure single-qubit quantum state is given by  $|\psi\rangle = \alpha|0\rangle + \beta|1\rangle$  with  $|\alpha|^2 + |\beta|^2 = 1$  and  $\alpha, \beta \in \mathbb{C}$ . In the used error-correction protocol, the information of a single (system) qubit is distributed over three qubits by storing the information redundantly

---

<sup>3</sup>The author of the present thesis designed the experiment, measured and analyzed the data and wrote the manuscript

### 3. Experimental quantum error correction

---

in the state  $\alpha|000\rangle + \beta|111\rangle$ . This encoding is able to correct a single bit-flip by performing a majority vote and is known as the repetition code [30].

A measurement in the computational basis states  $|0\rangle, |1\rangle$  causes a projection onto the  $\sigma_z$  axis of the Bloch sphere and can be interpreted as an incoherent phase flip. Thus, any protocol correcting against phase-flips is sufficient to reverse measurements in the computational basis. The repetition code can be modified to protect against such phase-flip errors by a simple basis change from  $|0\rangle, |1\rangle$  to  $|\pm\rangle = 1/\sqrt{2}(|0\rangle \pm |1\rangle)$ . After this basis change each individual qubit is in an equal superposition of  $|0\rangle$  and  $|1\rangle$  and therefore it is impossible to gain any information about the encoded quantum information by measuring a single qubit along  $\sigma_z$ . Because the repetition code relies on a majority vote on the three-qubit register the measurement can be only perfectly corrected for if it acts on a single qubit as outlined in the schematic circuit shown in Fig. 3.8(a).

This process protects the information on the system qubit, leaving it in the same state as prior to the encoding. A complete reversal of the measurement brings the register back to the state it had immediately before the measurement. Therefore one needs to re-encode the register into the protected state. This is not directly possible because the ancilla qubits carry information about the measurement outcome. Therefore the auxiliary qubits have to be re-initialized prior to re-encoding as outlined in Fig. 3.8(a).

The experiment is realized in a linear chain of  $^{40}\text{Ca}^+$  ions confined in a macroscopic linear Paul trap[46]. Each ion encodes a qubit in the  $4S_{1/2}(m = -1/2) = |1\rangle$  and the metastable  $3D_{5/2}(m = -1/2) = |0\rangle$  state. Coherent manipulations of the qubit state are performed by exactly timed laser pulses in resonance with the energy difference between the two levels. A typical experimental sequence consists of (i) initialization of the quantum register, (ii) coherent state manipulation, and (iii) measurement of the register. Initializing the register consists of preparing the electronic state of the ions in a well defined state and cooling the common motional mode of the ions close to the ground state. In our experiment, any coherent operation can be implemented with a universal set of gates consisting of collective spin flips, phase shifts of individual qubits and collective entangling operations [32, 33].

The qubit can be measured in the computational basis by performing electron shelving on the short-lived  $S_{1/2} \leftrightarrow P_{1/2}$  transition as sketched in Fig. 3.9(a). Here, projection onto the state  $|1\rangle$  enables a cycling transition and scatters many photons if the detection light is applied, whereas after projection onto  $|0\rangle$  no population is resonant with the laser light at 397 nm. The outcomes can be distinguished by shining in the laser light long enough to detect multiple photons with a photo-multiplier tube after projecting into  $|1\rangle$ . The absence of photons is then interpreted as outcome  $|0\rangle$ . Although the projection is already performed after scattering a single photon, it is necessary to detect multiple photons for faithful discrimination.

For the reversal scheme as shown in Fig. 3.8(a) only a single ion of the register is measured. This is realized by protecting the other two ions from the detection light by transferring the population from  $|1\rangle$  in the  $m = -5/2$  Zeeman substate of the  $D_{5/2}$  level with the procedure outlined in Fig. 3.9(a) [28]. Then, a projective measurement does not affect the electronic state of the hidden ions which are the remaining carriers of the information. The uncertainty of the measurement on the remaining ion depends on how many photons are detected if the state was projected into  $|1\rangle$ . Given that the number of detected photons follow a Poissonian distribution,

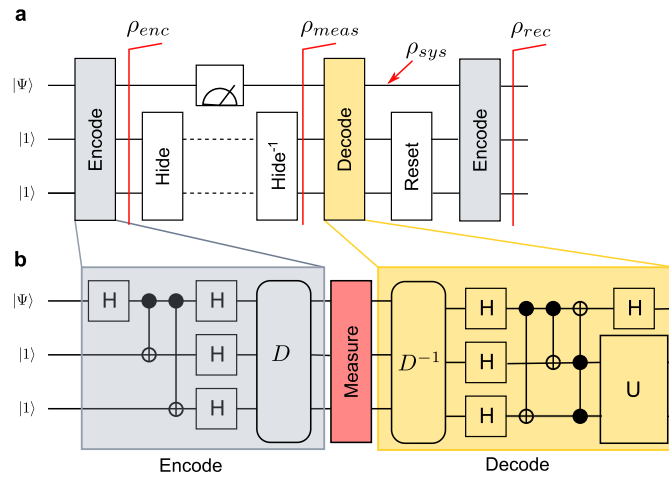


Figure 3.8.: (a) Schematic circuit of undoing a quantum measurement.  $\rho_{enc}$  is the encoded state of the register,  $\rho_{meas}$  is the state after the measurement,  $\rho_{sys}$  is the corrected state of the system qubit after the QEC cycle and  $\rho_{rec}$  is the state of the register after the full correction. (b) Circuit representation of the error correction algorithm.  $D$  is a unitary operation that commutes with phase flips.  $U$  is an arbitrary unitary operation. These operations do not affect the error correction functionality.

the detection uncertainty can be easily calculated via the cumulative distribution function of the Poisson distribution and the measurement durations as shown in columns one to three in table 3.3.

The quality of subsequent coherent operations is significantly lowered by the recoil of the scattered photons heating the motional state of the quantum register. Therefore, recoiling the ion-string close to the ground state is required without disturbing the quantum information in the non-measured qubits. In ion-traps this can be achieved with sympathetic cooling using a second ion species. As trapping and cooling two different ion species requires major experimental effort, we employ a recoiling technique that can be used with a single trapped species. We perform a Raman cooling scheme as shown in Fig. 3.9(b) while the ancilla qubits are still protected.

Encoding and decoding of the register as shown in Fig. 3.8(b) are implemented in our setup as described in Ref.[61]. The encoding is realized with a single entangling operation and the decoding is performed using a numerically optimized decomposition into available operations [33]. In order to facilitate the optimization procedure, the QEC algorithm is slightly modified without affecting its functionality by two additional unitary operations  $D$  and  $U$  as shown in Fig. 3.8(b). The actual implementation can be benchmarked with the aid of quantum state and process tomography [28, 30]. We use a maximum likelihood algorithm to reconstruct the density matrix and perform a non-parametric bootstrap for statistical error analysis [34]. Because the error correction protocol acts as a single qubit quantum channel, it can be characterized by a quantum process tomography on the system qubit (indicated as  $\rho_{sys}$  in Fig 1(a)). This process is characterized by the process matrix  $\chi_{exp}$  and its performance compared to the ideal process  $\chi_{id}$  is given by the process fidelity  $F^{proc} = \text{Tr}(\chi_{id} \cdot \chi_{exp})$ . The process fidelity of a single error correction step without measurement and recoiling was measured to be  $F = 93(2)\%$ . The process

### 3. Experimental quantum error correction

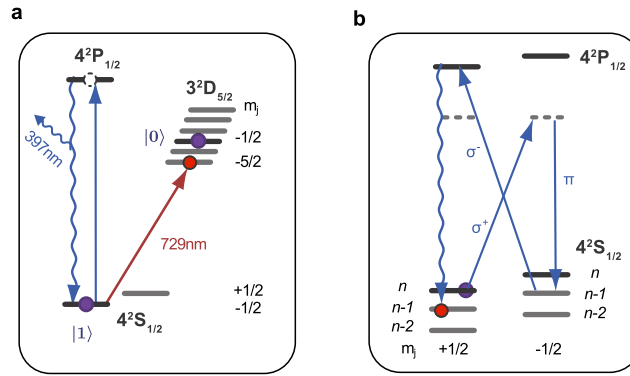


Figure 3.9.: (a) Schematic of the measurement process on the  $S_{1/2} \leftrightarrow P_{1/2}$  transition. The auxiliary qubits are hidden from the measurement by transferring the population to the  $m = -5/2$  substate of the  $D_{5/2}$  level. (b) Schematic of the Raman recoiling procedure. This scheme utilizes two 1.5GHz detuned Raman beams that remove one phonon upon transition from the Zeeman substates  $m = -1/2$  to  $m = +1/2$  and an additional resonant beam that is used to optically pump from  $m = +1/2$  to  $m = -1/2$  via the  $P_{1/2}$  state.

including the measurement can be analyzed by either ignoring the measurement outcome or by investigating the process depending on the outcome as presented in Table 3.3.

The overall performance of the reversal process is determined by the quality of the operations and the loss of coherence during the measurement and the recoiling process. As the quality of the operations is affected by the motional state of the ion-string after recoiling, there is a trade-off between their fidelity and the loss of coherence during measurement and recoiling. It should be noted that the measurement affects the motion only if it is projected into the  $|1\rangle$  state whereas the loss of coherence affects both possible projections. The performance of the algorithm for different measurement and recoiling parameters is shown in Table 3.3. A detection error of less than 0.5% is achieved with a measurement time  $\tau_{meas} = 200\mu s$  and a recoiling time of  $\tau_{recoil} = 800\mu s$  leading to a mean process fidelity of  $F = 84(1)\%$  which exceeds the bound for any classical channel of  $F = 50\%$ . We analyzed the measurement outcome for  $\tau_{meas} = 200\mu s$  and a measurement threshold of three photon counts to show that no information about the encoded quantum information can be gained by measuring a single qubit. The measurement was performed for the initial basis states  $|0\rangle$ ,  $|0\rangle + |1\rangle$ ,  $|0\rangle + i|1\rangle$ ,  $|1\rangle$  and results in probabilities to find the outcome in state  $|0\rangle$  of 48(1)%, 50(1)%, 50(1)%, 50(1)%. This shows that indeed no information about the initial quantum state can be inferred by measuring a single qubit.

The presented procedure is able to protect the quantum information on the system qubit in the presence of a quantum measurement. In order to perform the full measurement reversal, the ancilla qubits have to be reset before applying the same encoding as demonstrated in Ref [61].

As this technique recovers the state of the entire register, the measurement reversal can be directly benchmarked by comparing the state before the measurement and after the reconstruction. A quantum state can be analyzed using quantum state tomography and evaluating the fidelity between two states  $\rho_1, \rho_2$  with the Uhlmann fidelity[117]  $F^{rho}(\rho_1, \rho_2) = (\text{Tr} \sqrt{\sqrt{\rho_1}\rho_2\sqrt{\rho_1}})^2$ .

$\tau_{Raman}$	$\tau_{meas}$	Detection error	$\langle n_{phonon} \rangle$	$F_{mean}^{proc}$	$F_{ 1\rangle}^{proc}$	$F_{ 0\rangle}^{proc}$	$F_{mean}^{rho}$	$F_{ 1\rangle}^{rho}$	$F_{ 0\rangle}^{rho}$
800	100	4 %	0.17	86(3)	82(3)	90(2)	89(1)	87(1)	91(2)
800	200	< 0.5 %	0.24	85(2)	87(3)	90(3)	84(1)	82(1)	85(2)
800	300	< 0.5 %	0.41	81(3)	78(2)	87(3)	84(1)	80(1)	87(2)
800	400	< 0.5 %	0.50	78(3)	71(5)	85(4)	82(1)	76(2)	90(2)

Table 3.3.: Columns 1 to 3: Raman recoiling and measurement duration in  $\mu s$  with corresponding detection error. Column 4: Measured mean phonon number  $\langle n \rangle$  after measurement and recoiling. Columns 5 to 7: Measured process fidelities on the system qubit without re-encoding  $F^{proc}$  in (%) and columns 8 to 10: Overlap of the quantum state after the full reconstruction with the state prior to the measurement  $F^{rho}$  in (%). Lower indices  $F_{mean}$  indicate a mean fidelity while ignoring the measurement outcome.  $F_{|0\rangle}$  and  $F_{|1\rangle}$  indicate fidelities if the measurement outcome was  $|0\rangle$  ( $|D\rangle$ ) and  $|1\rangle$  ( $|S\rangle$ ). Errors correspond to one standard deviation.

The state  $\rho_{enc}$  after encoding shows a fidelity with the ideal state of  $F(\rho_{id}, \rho_{enc}) = 94(1)\%$ . In order to demonstrate the effect of the measurement the states  $\rho_{meas}$  after measuring and recoiling, and  $\rho_{rec}$  after the reconstruction are analyzed with respect to the state  $\rho_{enc}$ . The measured density matrices for these states are shown in Fig. (3.10). The overlap of the state after the measurement  $\rho_{meas}$  with the state  $\rho_{enc}$  is  $F(\rho_{enc}, \rho_{meas}) = 50(2)\%$  as expected from pure dephasing which shows that the measurement acts as dephasing when the outcome is ignored. In contrast, Fig. 3.10 illustrates the evolution of the states with known outcome. The reconstructed state  $\rho_{rec}$  after correction, reset and re-encoding is measured to have an overlap of  $F(\rho_{enc}, \rho_{rec}) = 84(1)\%$  which indicates that the measurement was successfully reversed. The quality of the measurement reversal depends again on the number of scattered photons during the measurement and the recoiling time and the optimum is also  $\tau_{detect} = 200\mu s$ . Fidelities depending on the outcome and for various measurement durations are displayed in table 3.3.

In conclusion we have demonstrated the full reversal of a strong quantum measurement on a single qubit. We further presented an in-sequence recoiling technique that can serve as an alternative to sympathetic two-species cooling. This may simplify the architecture for a future large-scale ion-trap quantum information processor.

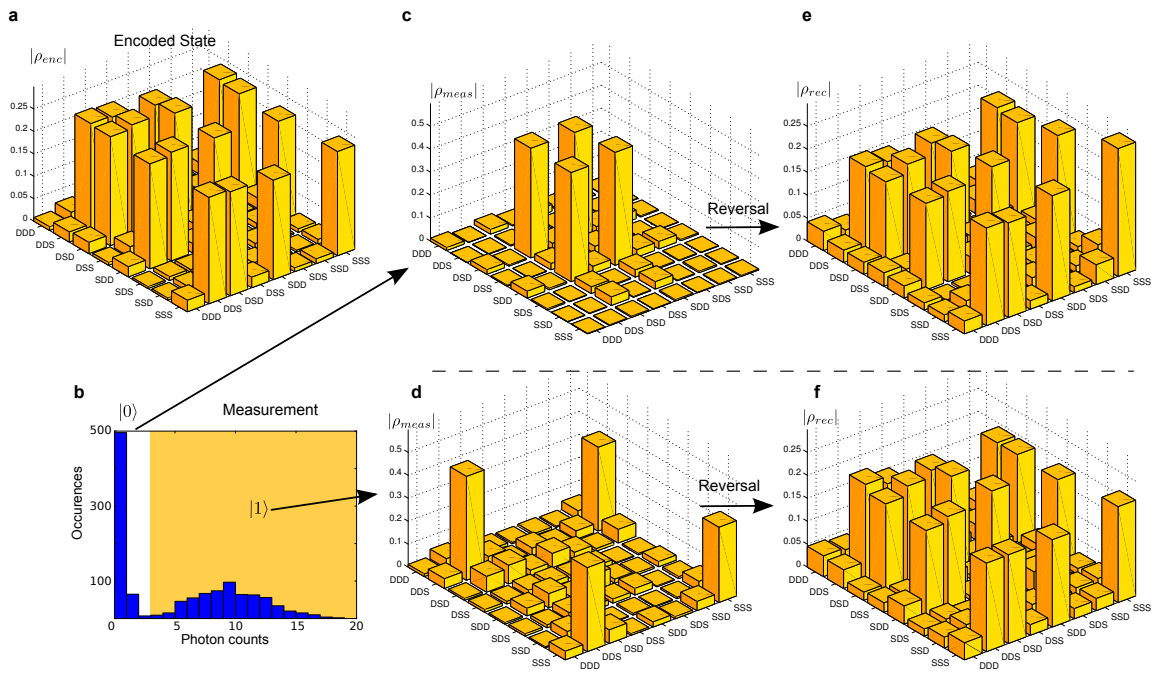


Figure 3.10.: (a) Absolute value of the reconstructed three qubit density matrices before the measurement  $\rho_{enc}$ . (b) Histogram of the measured photon counts for a measurement time of  $200\mu s$ . Absolute value of three qubit density matrices after the measurement  $\rho_{meas}$  for outcome (c)  $|0\rangle$  and (d)  $|1\rangle$ . Density matrices after the measurement reversal  $\rho_{rec}$  for outcome (e)  $|0\rangle$  and (f)  $|1\rangle$ .

# 4. Quantum simulation of open systems

## 4.1. Introduction to open-system quantum simulation

Already in 1982, R. Feynman dreamed of a quantum machine to calculate the dynamics of arbitrary quantum systems [2]. Thus the idea of using a well-controllable quantum system to learn about other quantum systems was already present at the early stages of quantum computing. Presently, two distinct types of quantum simulators are worked on. One is *analog* quantum simulation, or quantum *emulation*, where the system of interest has the same Hamiltonian as the simulator system and the dynamics of the simulator system are therefore equivalent to the dynamics of the systems of interest [16, 118]. The second approach, *digital* quantum simulation, takes a universal set of quantum operations and uses them to simulate any possible quantum system with a discretized time evolution.

These two types of simulators are also found in classical physics. The analog simulator corresponds for example to a wind tunnel where a scaled model of a race-car is tested. The digital simulator could be a classical computer solving the classical equations of motion for a weather forecast. The strengths and weaknesses of both systems are clear: the analog simulator is able to simulate complex systems whereas the digital simulator is more versatile and can be verified easily. The quantum versions of both simulators share the same strengths and weaknesses: The analog quantum simulator is less stringent on the required control of the simulator system. On the other hand it is believed that certifying the simulator for a large quantum system is much more difficult than for a classical system and thus this will be a major challenge for future quantum simulators. This leads immediately to a strong argument in favor of a digital quantum simulator where a universal set of quantum operations is sufficient to perform any possible simulation. Moreover, one can use the quantum error correction framework to make the simulator inherently faithful [119] with the obvious drawback of their substantial overhead.

The following part will focus on digital quantum simulators. These simulators discretize the time and implement the time evolution in fine grained time-steps. This naturally leads to an approximation of the continuous time dynamics of the system of interest. It was shown by Seth Lloyd, that this decomposition into discrete time-steps can be performed efficiently for any closed quantum system of interest [15]. In this case *efficient* means, that the number of required gate operations grows polynomially with the size of the system of interest for any fixed approximation error. The discretization is performed by the *Trotter-Suzuki* approximation [120]. For example, a quantum register may simulate a one dimensional bosonic system as sketched in figure 4.1. There, each lattice site corresponds to a single qubit where the state  $|1\rangle$  ( $|0\rangle$ ) of

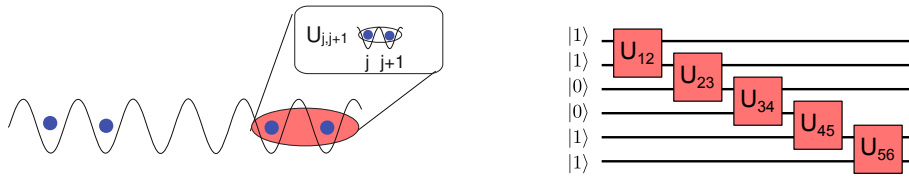


Figure 4.1.: Digital simulation of a bosonic system with next-neighbor interaction. The state  $|1\rangle$  ( $|0\rangle$ ) of the simulator system corresponds to an occupied (empty) lattice site. A single stroboscopic time-step corresponds to performing the unitary corresponding to a next neighbor interaction on all pairs of qubits.

the simulator system corresponds to an occupied (empty) lattice site. Bosonic interactions are mapped onto two-qubit gate operations. In a single stroboscopic time-step of the spin system the interactions between all sites need to be applied.

However, many interesting systems need to be described by open quantum systems that couple to an environment which are not straightforward to simulate with a toolbox consisting only of coherent operations. Prominent examples for such open quantum systems can be found in quantum biology and quantum chemistry, where quantum effects in a very noisy environment are investigated [17, 18]. In these systems, the coupling to the environment results in noise driving the system towards a classical state, but lately systems have been identified where this dissipative coupling to an environment can be used as a resource [19, 20]. An example is a bosonic system, where long-range order can be built up from purely dissipative dynamics. In this system, a novel type of phase transition has been studied theoretically [59, 121].

In the following, a digital quantum simulator is presented that is able to realize the dynamics of any Markovian open quantum system. Such a simulation can be realized in two distinct ways: One can either use a larger simulator system undergoing only coherent dynamics similar to the description of an incoherent process as unitary process of the system and the environment as shown in section 1.3. Alternatively, one can simulate the environment using a single qubit with a controlled coupling to the environment, the coupling of the simulated system to the environment is then implemented by performing entangling operations between the system and the auxiliary qubit. The qubit reset technique as already used for the repetitive quantum error correction in section 3.1 can be interpreted as such a controllable coupling to the environment. As mentioned in section 1.3, any irreversible quantum process can be described by a dynamical map

$$\rho \rightarrow \epsilon(\rho) = \sum_j E_j \rho E_j^\dagger.$$

Such dynamical maps are directly implemented in the simulator and each map corresponds to a discrete time-step of the system of interest. This is then the open-system analogon to the Trotter approximation simulating a time-continuous master equation as will be shown in sections 4.2 and 4.3.

In the following the concept of the open system simulator is demonstrated by the example of a spontaneous decay in a two level scheme as an example of such a dynamical map. If the decay

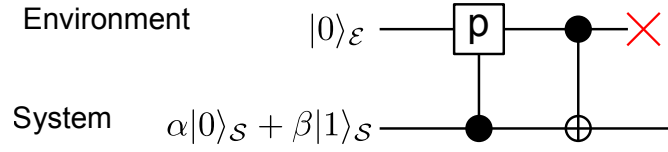


Figure 4.2.: Quantum Circuit to simulate a spontaneous decay on a single qubit.

occurs with probability  $p$  the Kraus operators  $E_j$  are

$$\begin{aligned} E_0 &= \sqrt{p} \begin{pmatrix} 0 & 1 \\ 0 & 0 \end{pmatrix} \\ E_1 &= \begin{pmatrix} 1 & 0 \\ 0 & \sqrt{1-p} \end{pmatrix} \end{aligned} \quad (4.1)$$

For decay probability  $p = 1$  any input state is mapped to the ground state  $\rho = |0\rangle\langle 0|$  which is called the *fixed point* of the map. For any intermediate decay probability, the population in the excited state  $|1\rangle$  is partially transferred to the ground state. The most general output state is then

$$\epsilon(\rho) = p \begin{pmatrix} 0 & 0 \\ 0 & \rho_{11} \end{pmatrix} + \begin{pmatrix} (1-p)\rho_{11} & \sqrt{1-p}\rho_{12} \\ \sqrt{1-p}\rho_{21} & \rho_{22} \end{pmatrix}$$

which is a mixed state. For simulating this process on a quantum computer we will now look at a two-qubit system where a single qubit represents the environment. As a first example the deterministic decay process ( $p = 1$ ) is covered. For this, the information whether the system qubit is in state  $|1\rangle$  or  $|0\rangle$  is mapped onto the auxiliary qubit with the aid of a CNOT operation:

$$(\alpha|0\rangle_S + \beta|1\rangle_S) \otimes |0\rangle_E \rightarrow \alpha|00\rangle + \beta|11\rangle .$$

Then, another CNOT where the control and target qubits are swapped is performed leaving the system in the state

$$\alpha|00\rangle + \beta|11\rangle \rightarrow \alpha|00\rangle + \beta|01\rangle .$$

In the next step the information of the auxiliary qubit is discarded which corresponds to a partial trace over its system as outlined in section 1.3. Now the auxiliary and the system qubit are not entangled and thus the final state is the pure state  $|0\rangle$  as expected.

The more interesting case is certainly a probabilistic decay process ( $p < 1$ ). In the interest of simplicity, I will assume a pure input state  $|\Psi\rangle = \alpha|0\rangle + \beta|1\rangle$ . In the first step, the CNOT operation does not perform a full bit-flip anymore but the flip is performed only with probability  $p$ . This operation corresponds to a controlled rotation around the x-axis on the Bloch sphere with rotation angle  $\theta = \arcsin \sqrt{p}$

$$|\Psi\rangle_S \otimes |0\rangle_E \rightarrow \alpha|00\rangle + \beta \left( \sqrt{p}|11\rangle + \sqrt{1-p}|10\rangle \right) .$$

The second step is now performed analogous to the deterministic decay by performing a deterministic CNOT with the auxiliary qubit as control

$$\alpha|00\rangle + \beta \left( \sqrt{p}|11\rangle + \sqrt{1-p}|10\rangle \right) \rightarrow \alpha|00\rangle + \beta \left( \sqrt{p}|01\rangle + \sqrt{1-p}|10\rangle \right) .$$

In the next step, the information of the auxiliary qubit is discarded. The partial trace leads to the following density matrix:

$$\begin{pmatrix} (1-p)|\beta|^2 & \sqrt{1-p}\alpha\beta^* \\ \sqrt{1-p}\alpha^*\beta & |\alpha|^2 + p|\beta|^2 \end{pmatrix}.$$

This state is equal to the target state as shown in equation (4.1). A quantum circuit for this procedure is shown in figure 4.2 consisting of a probabilistic CNOT operation, a deterministic CNOT and the final reset of the environment qubit.

This example demonstrated how a simple *single-body* dynamical map can be implemented using coherent operations and a qubit reset. The realization of *many-body* dynamical maps is analog to this procedure where the system consists of multiple qubits. Such many body dynamical maps are an interesting subject on their own right. Their unique dark-state or fixed point can be any multi-qubit state may it be entangled or not. This means it is possible to design a map that shows a dark state with long-range many-body correlations allowing us to explore new many-body physics. Such states may also be used as a resource for quantum computation[19, 20].

In the following publication, a toolbox for a universal open system simulator is demonstrated. First, a many-body dissipative map is demonstrated simulating a process that has a maximally entangled state as its unique dark state. Furthermore, a framework is developed to implement any arbitrary dynamical map. In the second publication, this toolbox is then used to simulate a many body bosonic system. The dynamics of this system is governed by composite dynamical maps build up from quasi-local elementary maps [59, 121] leading to a dark state showing long-range coherence. In a bosonic picture, this dark state corresponds to a superfluid state where the particles are delocalized. In our simulation, we explore the dynamics that arises when these composite maps are complemented by coherent operations that are incompatible with the dark state. As the coherent operations are incompatible with the dark state, their competition with the dissipative dynamics will lead to the destruction of the phase coherence. This resembles the hallmark feature of a theoretically predicted non-equilibrium many-body quantum phase transition.

During the analysis of the data obtained by the boson simulation process, it became clear that an error reduction technique is required to achieve faithful simulation results. The problem arises as the erroneous operations in our simulator do not preserve the simulated boson number. Therefore we developed a novel error detection and error reduction scheme based on quantum feedback techniques stabilizing the boson number. This opens the question whether a full QEC protocol is required for a special purpose digital simulator or if a simplified error reduction protocol with less overhead is sufficient.

## 4.2. Publication: An Open-System Quantum Simulator with Trapped Ions

### An Open-System Quantum Simulator with Trapped Ions<sup>1</sup>

Nature **470**, 486 (2011)

Julio T. Barreiro<sup>\*,1</sup>, Markus Müller<sup>\*,2,3</sup>, Philipp Schindler<sup>1</sup>, Daniel Nigg<sup>1</sup>, Thomas Monz<sup>1</sup>, Michael Chwalla<sup>1,2</sup>, Markus Hennrich<sup>1</sup>, Christian F. Roos<sup>1,2</sup>, Peter Zoller<sup>2,3</sup> and Rainer Blatt<sup>1,2</sup>

<sup>1</sup>Institut für Experimentalphysik, Universität Innsbruck,  
Technikerstrasse 25, 6020 Innsbruck, Austria

<sup>2</sup>Institut für Quantenoptik und Quanteninformation,  
Österreichische Akademie der Wissenschaften,  
Technikerstrasse 21A, 6020 Innsbruck, Austria

<sup>3</sup>Institut für Theoretische Physik,  
Universität Innsbruck, Technikerstrasse 25, 6020 Innsbruck, Austria

\* These authors contributed equally to this work.

The control of quantum systems is of fundamental scientific interest and promises powerful applications and technologies. Impressive progress has been achieved in isolating the systems from the environment and coherently controlling their dynamics, as demonstrated by the creation and manipulation of entanglement in various physical systems. However, for open quantum systems, engineering the dynamics of many particles by a controlled coupling to an environment remains largely unexplored. Here we report the first realization of a toolbox for simulating an open quantum system using up to five qubits. Using a quantum computing architecture with trapped ions, we combine multi-qubit gates with optical pumping to implement coherent operations and dissipative processes. We illustrate this engineering by the dissipative preparation of entangled states, the simulation of coherent many-body spin interactions and the quantum non-demolition measurement of multi-qubit observables. By adding controlled dissipation to coherent operations, this work offers novel prospects for open-system quantum simulation and computation.

Every quantum system is inevitably coupled to its surrounding environment. Significant progress has been made in isolating systems from their environment and coherently controlling the dynamics of several qubits [122–125]. These achievements have enabled the realization of high-fidelity quantum gates, the implementation of small-scale quantum computing and communication devices as well as the measurement-based probabilistic preparation of entangled states, in atomic [126, 127], photonic [128], NMR [129] and solid-state setups [9, 130, 131]. In particular, successful demonstrations of quantum simulators [2, 15], which allow one to mimic and study the dynamics of complex quantum systems, have been reported [132].

In contrast, controlling the more general dynamics of open systems amounts to engineering both the Hamiltonian time evolution of the system as well as the coupling to the environment. In pre-

---

<sup>1</sup>The author of the present thesis measured and analyzed the data.

vious works [58, 133–135], controlled decoherence has been used to systematically study its detrimental effects on many-body or multi-qubit open systems. The ability to design dissipation can, however, be a useful resource, as in the context of the preparation of a desired entangled state from an arbitrary initial state [59, 136, 137], and, closely related, dissipative quantum computation [21] and quantum memories [138]. It also enables the preparation and manipulation of many-body states and quantum phases [59], and provides an enhanced sensitivity in precision measurements [139]. In particular, by combining suitably chosen coherent and dissipative operations, one can engineer the system-environment coupling, thus generalizing the concept of Hamiltonian quantum simulation to open quantum systems [15, 19].

Here we provide the first experimental demonstration of a toolbox of coherent and dissipative *multi-qubit* manipulations to control the dynamics of open systems. In a string of trapped ions, each ion encoding a qubit, we subdivide the qubits into “system” and “environment”. The system-environment coupling is then engineered through the universal set of quantum operations available in ion-trap quantum computers [140, 141], whereas the environment ion is coupled to the dissipative bath of vacuum modes of the radiation field via optical pumping. Following Ref. [21] (see also [142]) these quantum resources provide a complete toolbox to engineer general Markovian open-system dynamics in our multi-qubit system [19, 143].

We first illustrate this engineering by dissipatively preparing a Bell state in a 2+1 ion system, such that an initially fully mixed state is pumped into a given Bell state. Similarly, with 4+1 ions, we also dissipatively prepare a 4-qubit GHZ-state, which can be regarded as a minimal instance of Kitaev’s toric code [144]. Besides the dissipative elements, we show coherent  $n$ -body interactions by implementing the fundamental building block for 4-spin interactions. In addition, we demonstrate a readout of  $n$ -particle observables in a non-destructive way with a quantum-nondemolition (QND) measurement of a 4-qubit stabilizer operator. We conclude by outlining future perspectives and implications of the present work in quantum information processing and simulation, as well as open-system quantum control scenarios including feedback [19].

### 4.2.1. Open-System Dynamics & Bell-State Pumping

The dynamics of an open quantum system  $S$  coupled to an environment  $E$  can be described by the unitary transformation  $\rho_{SE} \mapsto U\rho_{SE}U^\dagger$ , with  $\rho_{SE}$  the joint density matrix of the composite system  $S + E$ . Thus, the reduced density operator of the system will evolve as  $\rho_S = \text{Tr}_E(U\rho_{SE}U^\dagger)$ . The time evolution of the system can also be described by a completely positive Kraus map

$$\rho_S \mapsto \mathcal{E}(\rho_S) = \sum_k E_k \rho_S E_k^\dagger \quad (4.2)$$

with  $E_k$  operation elements satisfying  $\sum_k E_k^\dagger E_k = 1$ , and initially uncorrelated system and environment [30]. If the system is decoupled from the environment, the general map (4.2) reduces to  $\rho_S \mapsto U_S \rho_S U_S^\dagger$ , with  $U_S$  the unitary time evolution operator acting only on the system.

Control of both coherent and dissipative dynamics is then achieved by finding corresponding sequences of maps (4.2) specified by sets of operation elements  $\{E_k\}$  and engineering these sequences in the laboratory. In particular, for the example of dissipative quantum-state preparation,

pumping to an entangled state  $|\psi\rangle$  reduces to implementing appropriate sequences of dissipative maps. These maps are chosen to drive the system to the desired target state irrespective of its initial state. The resulting dynamics have then the pure state  $|\psi\rangle$  as the unique attractor,  $\rho_S \mapsto |\psi\rangle\langle\psi|$ . In quantum optics and atomic physics, the techniques of optical pumping and laser cooling are successfully used for the dissipative preparation of quantum states, although on a *single-particle* level. The engineering of dissipative maps for the preparation of entangled states can be seen as a generalization of this concept of pumping and cooling in driven dissipative systems to a *many-particle* context. To be concrete, we focus on dissipative preparation of stabilizer states, which represent a large family of entangled states, including graph states and error-correcting codes [145].

We start by outlining the concept of Kraus map engineering for the simplest non-trivial example of “pumping” a system of two qubits into a Bell state. The Hilbert space of two qubits is spanned by the four Bell states defined as  $|\Phi^\pm\rangle = \frac{1}{\sqrt{2}}(|00\rangle \pm |11\rangle)$  and  $|\Psi^\pm\rangle = \frac{1}{\sqrt{2}}(|01\rangle \pm |10\rangle)$ . Here,  $|0\rangle$  and  $|1\rangle$  denote the computational basis of each qubit, and we use the short-hand notation  $|00\rangle = |0\rangle_1|0\rangle_2$ , for example. These maximally entangled states are stabilizer states: the Bell state  $|\Phi^+\rangle$ , for instance, is said to be *stabilized* by the two stabilizer operators  $Z_1Z_2$  and  $X_1X_2$ , where  $X$  and  $Z$  denote the usual Pauli matrices, as it is the only two-qubit state being an eigenstate of eigenvalue +1 of these two commuting observables, i.e.  $Z_1Z_2|\Phi^+\rangle = |\Phi^+\rangle$  and  $X_1X_2|\Phi^+\rangle = |\Phi^+\rangle$ . In fact, each of the four Bell states is uniquely determined as an eigenstate with eigenvalues  $\pm 1$  with respect to  $Z_1Z_2$  and  $X_1X_2$ . The key idea of pumping is that we can achieve dissipative dynamics which pump the system into a particular Bell state, for example  $\rho_S \mapsto |\Psi^-\rangle\langle\Psi^-|$ , by constructing two dissipative maps, under which the two qubits are irreversibly transferred from the +1 into the -1 eigenspaces of  $Z_1Z_2$  and  $X_1X_2$ .

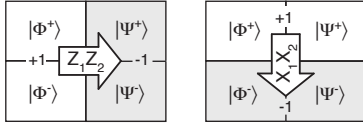
The dissipative maps are engineered with the aid of an ancilla “environment” qubit [19, 146] and a quantum circuit of coherent and dissipative operations. The form and decomposition of these maps into basic operations are discussed in Box 1. The pumping dynamics are determined by the probability of pumping from the +1 into the -1 stabilizer eigenspaces, which can be directly controlled by varying the parameters in the employed gate operations. For pumping with unit probability ( $p = 1$ ), the two qubits reach the target Bell state — regardless of their initial state — after only one pumping cycle, i.e., by a single application of each of the two maps. In contrast, when the pumping probability is small ( $p \ll 1$ ), the process can be regarded as the infinitesimal limit of the general map (4.2). In this case, the system dynamics under a repeated application of the pumping cycle are described by a master equation [147]

$$\begin{aligned} \dot{\rho}_S = & -i[H_S, \rho_S] \\ & + \sum_k \left( c_k \rho_S c_k^\dagger - \frac{1}{2} c_k^\dagger c_k \rho_S - \rho_S \frac{1}{2} c_k^\dagger c_k \right). \end{aligned} \quad (4.3)$$

Here,  $H_S$  is a system Hamiltonian, and  $c_k$  are Lindblad operators reflecting the system-environment coupling. For the purely dissipative maps discussed here,  $H_S = 0$ . Quantum jumps from the +1 into the -1 eigenspace of  $Z_1Z_2$  and  $X_1X_2$  are mediated by a set of *two-qubit* Lindblad operators (see box 1 for details); here the system reaches the target Bell state asymptotically after many pumping cycles.

**Box 1: Engineering dissipative open-system dynamics**

Dissipative dynamics which pump two qubits from an arbitrary initial state into the Bell state  $|\Psi^-\rangle$  are realized by two maps that generate pumping from the +1 into the -1 eigenspaces of the stabilizer operators  $Z_1Z_2$  and  $X_1X_2$ :



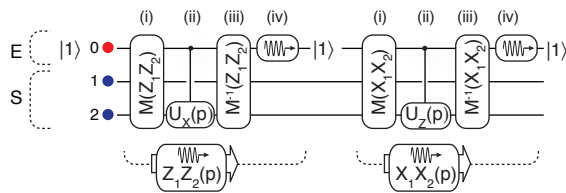
For  $Z_1Z_2$ , the dissipative map pumping into the -1 eigenspace is  $\rho_S \mapsto \mathcal{E}(\rho_S) = E_1\rho_S E_1^\dagger + E_2\rho_S E_2^\dagger$  with

$$E_1 = \sqrt{p} X_2 \frac{1}{2} (1 + Z_1 Z_2),$$

$$E_2 = \frac{1}{2} (1 - Z_1 Z_2) + \sqrt{1-p} \frac{1}{2} (1 + Z_1 Z_2).$$

The map's action as a uni-directional pumping process can be seen as follows. Since the operation element  $E_1$  contains the projector  $\frac{1}{2}(1 + Z_1Z_2)$  onto the +1 eigenspace of  $Z_1Z_2$ , the spin flip  $X_2$  can then convert +1 into -1 eigenstates of  $Z_1Z_2$ , e.g.,  $|\Phi^+\rangle \mapsto |\Psi^+\rangle$ . In contrast, the -1 eigenspace of  $Z_1Z_2$  is left invariant. In the limit  $p \ll 1$ , the repeated application of this map reduces the process to a master equation with Lindblad operator  $c = \frac{1}{2}X_2(1 - Z_1Z_2)$ .

We implement the two dissipative maps by quantum circuits of three unitary operations (i)-(iii) and a dissipative step (iv). Both maps act on the two system qubits  $S$  and an ancilla which plays the role of the environment  $E$ :



Pumping  $Z_1Z_2$  proceeds as follows:

- (i) Information about whether the system is in the +1 or -1 eigenspace of  $Z_1Z_2$  is mapped by  $M(Z_1Z_2)$  onto the logical states  $|0\rangle$  and  $|1\rangle$  of the ancilla (initially in  $|1\rangle$ ).
- (ii) A controlled gate  $C(p)$  converts +1 into -1 eigenstates by flipping the state of the second qubit with probability  $p$ , where

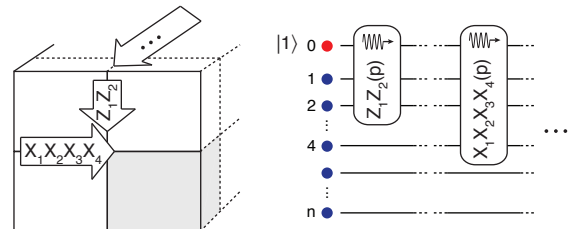
$$C(p) = |0\rangle\langle 0|_0 \otimes U_{X_2}(p) + |1\rangle\langle 1|_0 \otimes \mathbb{1},$$

with  $U_{X_2}(p) = \exp(i\alpha X_2)$  and  $\alpha$  controlling the pumping probability  $p = \sin^2 \alpha$ .

- (iii) The initial mapping is inverted by  $M^{-1}(Z_1Z_2)$ . At this stage, in general, the ancilla and system qubits are entangled.
- (iv) The ancilla is dissipatively reset to  $|1\rangle$ , which carries away entropy to “cool” the two system qubits.

The second map for pumping into the -1 eigenspace of  $X_1X_2$  is obtained from interchanging the roles of  $X$  and  $Z$  above.

The engineering of dissipative maps can be readily generalized to systems of more qubits. As an example, dissipative preparation of  $n$ -qubit stabilizer states can be realized by a sequence of  $n$  dissipative maps (e.g. for  $Z_1Z_2$  and  $X_1X_2X_3X_4$  pumping), which are implemented in analogy to the quantum circuits for Bell state pumping discussed above:



### 4.2.2. Experimental Bell-State Pumping

The dissipative preparation of  $n$ -particle entangled states is realized in a system of  $n+1$   $^{40}\text{Ca}^+$  ions confined to a string by a linear Paul trap and cooled to the ground state of the axial centre-of-mass mode [46]. For each ion, the internal electronic Zeeman levels  $D_{5/2}(m = -1/2)$  and  $S_{1/2}(m = -1/2)$  encode the logical states  $|0\rangle$  and  $|1\rangle$  of a qubit. For coherent operations, a laser at a wavelength of 729 nm excites the quadrupole transition connecting the qubit states ( $S_{1/2} \leftrightarrow D_{5/2}$ ). A broad beam of this laser couples to all ions (see Fig. 4.3a) and realizes the collective single-qubit gate  $U_X(\theta) = \exp(-i\frac{\theta}{2} \sum_i X_i)$  as well as a Mølmer-Sørensen [148] (MS) entangling operation  $U_{X^2}(\theta) = \exp(-i\frac{\theta}{4} (\sum_i X_i)^2)$  when using a bichromatic light field. Shifting the optical phase of the drive field by  $\pi/2$  exchanges  $X_i$  by  $Y_i$  in these operations. As a figure of merit of our entangling operation, we can prepare 3 (5) qubits in a GHZ state with 98% (95%) fidelity [23]. These collective operations form a universal set of gates when used in conjunction with single-qubit rotations  $U_{Z_i}(\theta) = \exp(-i\frac{\theta}{2} Z_i)$ , which are realized by an off-resonant laser beam that can be adjusted to focus on any ion.

For engineering dissipation, the key element of the mapping steps, shown as (i) and (iii) in Box 1, is a single MS operation. The two-qubit gate, step (ii), is realized by a combination of collective and single-qubit operations. The dissipative mechanism, step (iv), is here carried out on the ancilla qubit by a reinitialization into  $|1\rangle$ , as shown in Fig. 4.3b. Another dissipative process [61] can be used to prepare the system qubits in a completely mixed state by the transfer  $|0\rangle \rightarrow (|0\rangle + |S'\rangle)/\sqrt{2}$  followed by optical pumping of  $|S'\rangle$  into  $|1\rangle$ , where  $|S'\rangle$  is the electronic level  $S_{1/2}(m = 1/2)$ .

Qubit read-out is accomplished by fluorescence detection on the  $S_{1/2} \leftrightarrow P_{1/2}$  transition. The ancilla qubit can be measured without affecting the system qubits by applying hiding pulses that shelve the system qubits in the  $D_{5/2}$  state manifold during fluorescence detection [149].

We use these tools to implement up to three Bell-state pumping cycles on a string of 2+1 ions. Starting with the two system qubits in a completely mixed state, we pump towards the Bell state  $|\Psi^-\rangle$ . Each pumping cycle is accomplished with a sequence of 8 entangling operations, 4 collective unitaries and 6 single-qubit operations; see the Supplementary Information section B.3. The pumping dynamics are probed by quantum state tomography of the system qubits after every half cycle. The reconstructed states are then used to map the evolution of the Bell-state populations.

In a first experiment, we set the pumping probability at  $p = 1$  to observe deterministic pumping, and we obtain the Bell-state populations shown in Fig. 4.4a. As expected, the system reaches the target state after the first pumping cycle. Regardless of experimental imperfections, the target state population is preserved under the repeated application of further pumping cycles and reaches up to 91(1)% after 1.5 cycles (ideally 100%). In a second experiment towards the simulation of master-equation dynamics, the probability is set at  $p = 0.5$  to probe probabilistic pumping dynamics. The target state is then approached asymptotically (Fig. 4.4b). After pumping the system for 3 cycles with  $p = 0.5$ , up to 73(1)% of the initially mixed population pumps into the target state (ideally 88%). To achieve Bell-state pumping in the limit of  $p \ll 1$ , the gate fidelities need to be raised closer to one because close to the stationary state of the dynamics, the

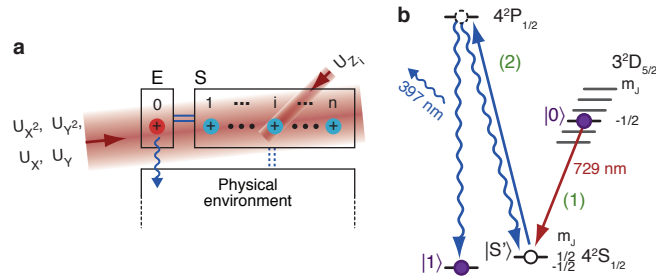


Figure 4.3.: **Experimental tools for the simulation of open quantum systems with ions.** **a**, The coherent component is realized by collective ( $U_X, U_Y, U_{X^2}, U_{Y^2}$ ) and single-qubit operations ( $U_{Z_i}$ ) on a string of  $^{40}\text{Ca}^+$  ions which consists of the environment qubit (ion 0) and the system qubits (ions 1 through  $n$ ). Coherent operations on S and E, combined with a controllable dissipative mechanism involving spontaneous emission of a photon from the environment ion, allow one to tailor the coupling of the system qubits to an artificial environment. This should be contrasted to the residual, detrimental coupling of the system (and environment) ions to their physical environment. **b**, The dissipative mechanism on the ancilla qubit is realized in the two steps shown on the Zeeman-split  $^{40}\text{Ca}^+$  levels by (1) a coherent transfer of the population from  $|0\rangle$  to  $|S'\rangle$  and (2) an optical pumping to  $|1\rangle$  after a transfer to the  $4^2P_{1/2}$  state by a circularly-polarised laser at 397 nm.

pumping rate  $p$  for populating the target state competes directly with loss processes at a rate  $\epsilon$ . Such losses are associated with gate errors and lead to a steady state infidelity scaling as  $\propto \epsilon/p$ , see Supplementary Information (section B.3) for further details.

In order to completely characterize the Bell-state pumping process, we also perform a quantum process tomography [30]. As an example, the reconstructed process matrix for  $p = 1$  after 1.5 cycles (Fig. 4.4c) has a Jamiolkowski process fidelity [37] of 87.0(7)% with the ideal dissipative process  $\rho_S \mapsto |\Psi^-\rangle\langle\Psi^-|$  which maps an arbitrary state of the system into the Bell state  $|\Psi^-\rangle$ .

### 4.2.3. Four-Qubit Stabilizer Pumping

The engineering of the system-environment coupling, as demonstrated by Bell-state pumping above, can be readily extended to larger  $n$ -qubit open quantum systems. We illustrate such an engineering experimentally with the dissipative preparation of a four-qubit Greenberger-Horne-Zeilinger (GHZ) state  $(|0000\rangle + |1111\rangle)/\sqrt{2}$ . This state is uniquely characterized as the simultaneous eigenstate of the four stabilizers  $Z_1Z_2, Z_2Z_3, Z_3Z_4$  and  $X_1X_2X_3X_4$ , all with eigenvalue +1 (see Fig. 4.5a). Therefore, the pumping dynamics into the GHZ state are realized by four consecutive dissipative steps, each pumping the system into the +1 eigenspaces of the four stabilizers. In a system of 4+1 ions, we implement such pumping dynamics in analogy with the Bell-state pumping sequence. Here, however, the circuit decomposition of one pumping cycle involves 16 five-ion entangling operations, 20 collective unitaries and 34 single-qubit operations;

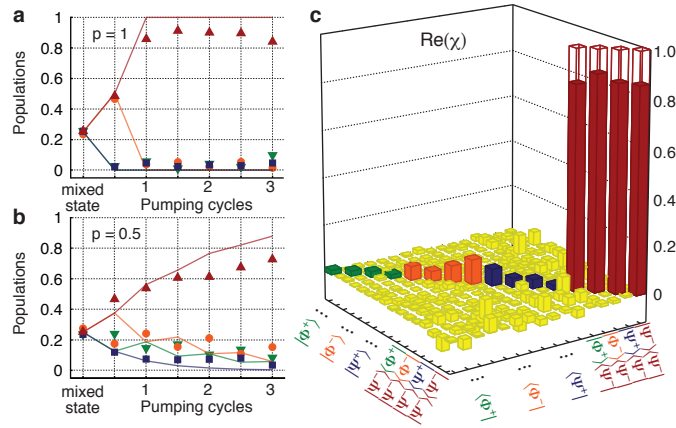


Figure 4.4.: **Experimental signatures of Bell-state pumping.** Evolution of the Bell-state populations  $|\Phi^+\rangle$  (down triangles),  $|\Phi^-\rangle$  (circles),  $|\Psi^+\rangle$  (squares) and  $|\Psi^-\rangle$  (up triangles) of an initially mixed state under a pumping process with probability **a**,  $p = 1$  or deterministic and **b**,  $p = 0.5$ . Error bars, not shown, are smaller than 2% ( $1\sigma$ ). **c**, Reconstructed process matrix  $\chi$  (real part), displayed in the Bell-state basis, describing the deterministic pumping of the two ions after one and a half cycles. The ideal process mapping any input state into the state  $|\Psi^-\rangle$  has as non-zero elements only the four transparent bars shown. The imaginary elements of  $\chi$ , ideally all zero, have an average magnitude of 0.004 and a maximum of 0.03. The uncertainties in the elements of process matrix are smaller than 0.01 ( $1\sigma$ ).

further details in the Supplementary Information section B.3.

In order to observe this deterministic pumping process into the GHZ state, we begin by preparing the system ions in a completely mixed state. The evolution of the state of the system after each pumping step is characterized by quantum state tomography. The reconstructed density matrices shown in Fig. 4.5b for the initial and subsequent states arising in each step have a fidelity, or state overlap [117], with the expected states of  $\{79(2), 89(1), 79.7(7), 70.0(7), 55.8(4)\}\%$  (the final state is genuinely multi-partite entangled [150]); see Supplementary Information (section B.3) for further details. The pumping dynamics is clearly reflected by the measured expectation values of the stabilizers  $Z_i Z_j$  ( $ij = 12, 23, 34, 14$ ) and  $X_1 X_2 X_3 X_4$  at each step, as shown in Fig. 4.5c.

Although the simulation of a master equation requires small pumping probabilities, as an exploratory study, we implement up to five consecutive  $X_1 X_2 X_3 X_4$ -stabilizer pumping steps with two probabilities  $p = 1$  and 0.5, for the initial state  $|1111\rangle$ . The measured expectation values of all relevant stabilizers for pumping with  $p = 1$  are shown in Fig. 4.5d. After the first step, the stabilizer  $X_1 X_2 X_3 X_4$  reaches an expectation value of  $-0.68(1)$ ; after the second step and up to the fifth step, it is preserved at  $-0.72(1)$  regardless of experimental imperfections.

For  $X_1 X_2 X_3 X_4$ -stabilizer pumping with  $p = 0.5$ , the four-qubit expectation value increases at each step and asymptotically approaches  $-0.54(1)$  (ideally  $-1$ , fit shown in Fig. 4.5d). A state tomography after each pumping step yields fidelities with the expected GHZ-state of  $\{53(1), 50(1), 49(1), 44(1), 41(1)\}\%$ . From the reconstructed density matrices we determine that the

states generated after one to three cycles are genuinely multi-partite entangled [150].

#### 4.2.4. Coherent Four-Particle Interactions

The coupling of the system to an ancilla particle, as used above for the engineering of dissipative dynamics, can also be harnessed to mediate effective coherent  $n$ -body interactions between the system qubits [30, 146]. The demonstration of a toolbox for open-system quantum simulation is thus complemented by adding unitary maps  $\rho_S \mapsto U_S \rho_S U_S^\dagger$  to the dissipative elements described above. Here,  $U_S = \exp(-i\tau H_S)$  is the unitary time evolution operator for a time step  $\tau$ , which is generated by a system Hamiltonian  $H_S$ . In contrast to the recent achievements [151, 152] of small-scale analog quantum simulators based on trapped ions, where two-body spin Hamiltonians have been engineered directly [153], here we pursue a gate-based implementation following the concept of Lloyd’s digital quantum simulator [15], where the time evolution is decomposed into a sequence of coherent (and dissipative) steps.

In particular, the available gate operations enable a simulation of  $n$ -body spin interactions which we illustrate by implementing time dynamics of a four-body Hamiltonian  $H_S = -gX_1X_2X_3X_4$ . This example is motivated by the efforts to experimentally realize Kitaev’s toric code Hamiltonian [144], which is a sum of commuting four-qubit stabilizer operators representing four-body spin interactions. This paradigmatic model belongs to a whole class of spin systems, which have been discussed in the context of topological quantum computing and quantum phases exhibiting topological order [154].

The elementary unitary operation  $U_S$  can be realized by the circuit shown in Fig. 4.6a: (i) As in the stabilizer pumping above, an operation  $M(X_1X_2X_3X_4)$ , here realized by an entangling MS gate  $U_{X^2}(\pi/2)$ , coherently maps the information about whether the four system spins are in the  $+1(-1)$  eigenspace of  $X_1X_2X_3X_4$  onto the internal states  $|0\rangle$  and  $|1\rangle$  of the ancilla qubit. (ii) Due to this mapping, effectively all  $+1(-1)$  eigenstates acquire a phase  $\beta/2(-\beta/2)$  by a subsequent single-qubit rotation  $U_Z(\beta)$  on the ancilla ion. The simulation time step  $\tau$  is related to the phase by  $\beta = 2g\tau$ . (iii) After the initial mapping is inverted by a second MS gate  $U_{X^2}(\pi/2)$ , the ancilla qubit returns to its initial state and decouples from the four system qubits, which in turn have evolved according to  $U_S$ . This compact sequence makes the simulation of  $n$ -body interactions *experimentally efficient*. Here, the use of global MS gates conveniently bundles the effect of several operations [55], which arise in alternative circuit decompositions based on two-qubit gates [30].

In an experiment carried out with 4+1 ions, we apply  $U_S$  for different values of  $\tau$  to the system ions initially prepared in  $|1111\rangle$ . We observe coherent oscillations in the subspace spanned by  $|0000\rangle$  and  $|1111\rangle$ , as shown in Fig. 4.6b. We characterize our implementation of  $U_S$  by comparing the expected and measured states, determined by quantum state tomography, for each value of  $\tau$ . The fidelity between the expected and measured states is on average 85(2)%.

### 4.2.5. QND Measurement of Four-Qubit Stabilizer

Our toolbox for quantum simulation of open systems is extended by the possibility of reading out  $n$ -body observables in a nondestructive way, which is also an essential ingredient in quantum error correction protocols. Here, we illustrate this for a 4-qubit stabilizer operator  $X_1 X_2 X_3 X_4$ . As above, we first coherently map the information about whether the system spins are in the  $+1$  ( $-1$ ) eigenspace of the stabilizer operator onto the logical states  $|0\rangle$  and  $|1\rangle$  of the ancilla qubit. In contrast to the engineering of coherent and dissipative maps above, where this step was followed by single- and two-qubit gate operations, here we proceed instead by measuring the ancilla qubit.

Thus, depending on the measurement outcome for the ancilla, the system qubits are projected onto the corresponding eigenspace of the stabilizer:  $\rho_S \mapsto P_+ \rho_S P_+ / N_+$  ( $P_- \rho_S P_- / N_-$ ) for finding the ancilla in  $|0\rangle$  ( $|1\rangle$ ) with the normalization factor  $N_{\pm} = \text{Tr}(P_{\pm} \rho_S P_{\pm})$ . Here,  $P_{\pm} = \frac{1}{2}(1 \pm X_1 X_2 X_3 X_4)$  denote the projectors onto the  $\pm 1$  eigenspaces of the stabilizer operator. Note that our measurement is QND in the sense that (superposition) states within one of the two eigenspaces are not affected by the measurement.

In the experiment with 4+1 ions, we prepare different four-qubit system input states (tomographically characterized in additional experiments), carry out the QND measurement and tomographically determine the resulting system output states.

To characterize how well the measurement device prepares a definite state, we use as input  $|1111\rangle$ , which is a non-eigenstate of the stabilizer. In this case, when the ancilla qubit is found in  $|0\rangle$  or  $|1\rangle$  the system qubits are prepared in the state  $(|0000\rangle \pm |1111\rangle) / \sqrt{2}$  by the QND measurement. Experimentally we observe this behaviour with a quantum state preparation (QSP) fidelity [155] of  $F_{\text{QSP}} = 73(1)\%$ . On the other hand, for a stabilizer eigenstate, the QND measurement preserves the stabilizer expectation value. Experimentally, for the input state  $(|0011\rangle - |1100\rangle) / \sqrt{2}$ , we observe a QND fidelity [155] of  $F_{\text{QND}} = 96.9(6)\%$ . For more details see the Supplementary Information section B.3.

### 4.2.6. Conclusions and Outlook

In the present work we have demonstrated engineering of dissipative Kraus maps for Bell-state and four-qubit stabilizer pumping. These particular examples exploited the available quantum resources by coupling the system qubits to an ancilla by a universal set of entangling operations. The engineered environment was here represented by an ancilla ion undergoing optical pumping by dissipative coupling to the vacuum modes of the radiation field. These experiments, where the ancilla remains unobserved, represent an *open-loop* dynamics. Such scenarios were recently discussed in the context of an open-system quantum simulator for spin models, including lattice gauge theories, realized with Rydberg atoms in optical lattices. In fact, according to Ref. [142], four-qubit stabilizer pumping together with four-spin interactions demonstrates the basic ingredients for the simulation of spin dynamics and ground-state cooling for the example of Kitaev's toric code Hamiltonian [144] on a single four-spin plaquette.

For a closed system only a small number of Hamiltonians as generators are required to generate all possible unitary time evolutions. In the context of qubits this is given by a finite set of single

qubit operations together with an entangling CNOT gate. In contrast, as noted in Ref. [19, 143], using a single ancilla qubit the most general Markovian open-system dynamics cannot be obtained with a finite set of non-unitary open-loop transformations. However, such a universal dynamical control can be achieved through repeated application of coherent control operations and measurement of the auxiliary qubit, followed by classical feedback operations onto the system. We note that our demonstration of a multi-qubit QND measurement provides, in combination with our previously demonstrated feedback techniques [156], the basic ingredient for the realization of such *closed-loop* dynamics.

Our experimental demonstration of a toolbox of elementary building blocks in a system of trapped ions should be seen as a conceptual step towards the realization of an open quantum system simulator with applications in various fields [132], including condensed-matter physics and quantum chemistry, possibly in modelling quantum effects in biology [157], and in quantum computation driven by dissipation [21].

Although the present experiments were performed with a linear ion-trap quantum computer architecture, the ongoing development of two-dimensional trap arrays promises scalable implementations of spin-models simulators. In addition, gate-based simulation approaches can incorporate quantum error correction protocols, which may prove essential for fault-tolerant quantum simulation. The demonstrated concepts can also be readily adapted to other physical platforms ranging from optical, atomic and molecular systems to solid-state devices.

**Acknowledgments** We would like to thank K. Hammerer, I. Chuang, and O. Gühne for discussions and T. Northup for critically reading the manuscript. We gratefully acknowledge support by the Austrian Science Fund (FOQUS), the European Commission (AQUTE), the Institut für Quanteninformation GmbH, and a Marie Curie International Incoming Fellowship within the 7th European Community Framework Programme.

**Author Contributions** M.M. and J.T.B. developed the research, based on theoretical ideas proposed originally by P.Z.; J.T.B., P.S. and D.N. carried out the experiment; J.T.B., P.S. and T.M. analysed the data; P.S., J.T.B., D.N., T.M., M.C., M.H. and R.B. contributed to the experimental setup; M.M., J.T.B. and P.Z. wrote the manuscript, with revisions provided by C.F.R.; all authors contributed to the discussion of the results and manuscript.

**Author Information** Reprints and permissions information is available at [www.nature.com/reprints](http://www.nature.com/reprints). The authors declare no competing financial interests. Correspondence and requests for materials should be addressed to P.Z. (Peter.Zoller@uibk.ac.at) and R.B. (Rainer.Blatt@uibk.ac.at).

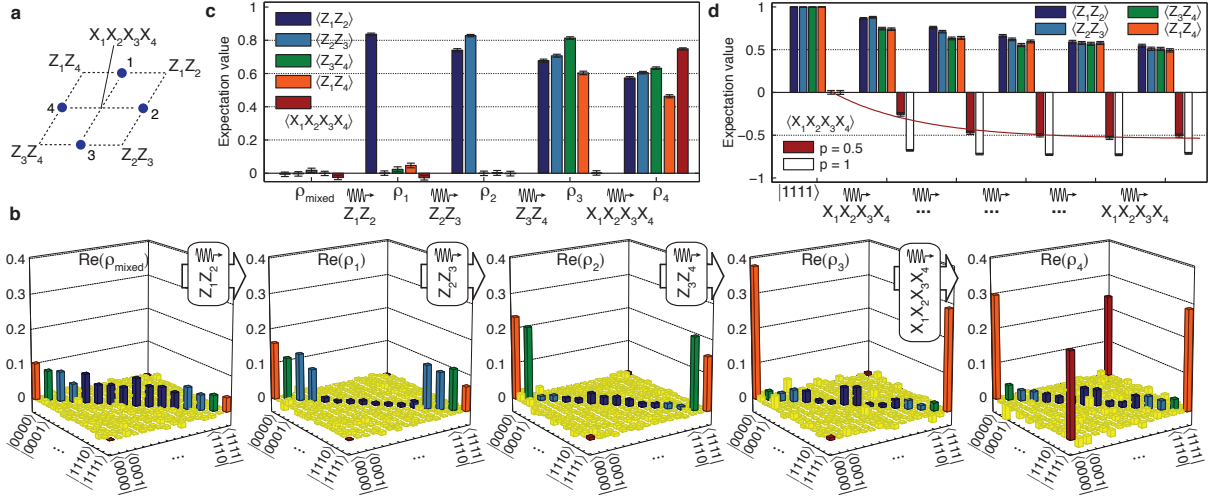


Figure 4.5.: **Experimental signatures of four-qubit stabilizer pumping.** **a**, Schematic of the four system qubits to be pumped into the GHZ state  $(|0000\rangle + |1111\rangle)/\sqrt{2}$ , which is uniquely characterized as the simultaneous eigenstate with eigenvalue +1 of the shown stabilizers. **b**, Reconstructed density matrices (real part) of the initial mixed state  $\rho_{\text{mixed}}$  and subsequent states  $\rho_{1,2,3,4}$  after sequentially pumping the stabilizers  $Z_1Z_2$ ,  $Z_2Z_3$ ,  $Z_3Z_4$  and  $X_1X_2X_3X_4$ . Populations in the initial mixed state with qubits  $i$  and  $j$  antiparallel, or in the -1 eigenspace of the  $Z_iZ_j$  stabilizer, disappear after pumping this stabilizer into the +1 eigenspace. For example, populations in dark blue disappear after  $Z_1Z_2$ -stabilizer pumping. A final pumping of the stabilizer  $X_1X_2X_3X_4$  builds up the coherence between  $|0000\rangle$  and  $|1111\rangle$ , shown as red bars in the density matrix of  $\rho_4$ . **c**, Measured expectation values of the relevant stabilizers; ideally, non-zero expectation values have a value of +1. **d**, Evolution of the measured expectation values of the relevant stabilizers for repetitively pumping an initial state  $|1111\rangle$  with probability  $p = 0.5$  into the -1 eigenspace of the stabilizer  $X_1X_2X_3X_4$ . The incremental pumping is evident by the red line fitted to the pumped stabilizer expectation value. The evolution of the expectation value  $\langle X_1X_2X_3X_4 \rangle$  for deterministic pumping ( $p = 1$ ) is also shown. The observed decay of  $\langle Z_iZ_j \rangle$  is due to imperfections and detrimental to the pumping process (see Supplementary Information). Error bars in **c** and **d**,  $\pm 1\sigma$ .

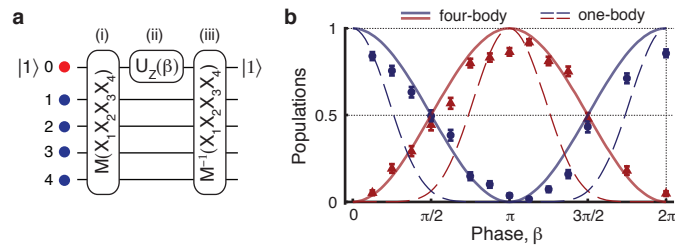


Figure 4.6.: **Coherent simulation of 4-body spin interactions.** **a**, The elementary building block for the simulation of coherent evolution  $U_S = \exp(-i\tau H_S)$  corresponding to the four-body Hamiltonian  $H_S = -gX_1X_2X_3X_4$  ( $\beta = 2g\tau$ ). **b**, Experimentally measured populations in state  $|0000\rangle$  (up triangles) and  $|1111\rangle$  (circles) as a function of  $\beta$  for a single application of  $U_S$  to the initial state  $|1111\rangle$  of the four system qubits (error bars,  $\pm 1\sigma$ ). The solid lines show the ideal behavior. For comparison, the dashes lines indicate these populations for simultaneous single-qubit (one-body) oscillations, each driven by the rotation  $\exp(-i\frac{\beta}{2}X_i)$ .

## 4.3. Publication: Quantum Simulation of Dynamical Maps with Trapped Ions

### Quantum Simulation of Dynamical Maps with Trapped Ions<sup>2</sup>

Accepted for publication in Nature physics

Preprint available at arXiv:1212.2418

P. Schindler<sup>\*1</sup>, M. Müller<sup>\*2</sup>, D. Nigg<sup>1</sup>, J. T. Barreiro<sup>1</sup>, E. A. Martinez<sup>1</sup>, M. Hennrich<sup>1</sup>  
T. Monz<sup>1</sup>, S. Diehl<sup>3,4</sup>, P. Zoller<sup>3,4</sup>, R. Blatt<sup>1,4</sup>

<sup>1</sup>Institut für Experimentalphysik, University of Innsbruck,  
Technikerstr. 25, A-6020 Innsbruck, Austria,

<sup>2</sup>Departamento de Física Teórica I, Universidad Complutense,  
Avenida Complutense s/n, 28040 Madrid, Spain

<sup>3</sup>Institut für Theoretische Physik, University of Innsbruck,  
Technikerstr. 25, A-6020 Innsbruck, Austria,

<sup>4</sup>Institut für Quantenoptik und Quanteninformation  
Österreichische Akademie der Wissenschaften,  
Otto-Hittmair-Platz 1, A-6020 Innsbruck, Austria

\* These authors contributed equally to this work

Dynamical maps describe general transformations of the state of a physical system - their iteration interpreted as generating a discrete time evolution. Prime examples include classical nonlinear systems undergoing transitions to chaos. Quantum mechanical counterparts show intriguing phenomena such as dynamical localization on the single particle level. Here we extend the concept of dynamical maps to a many-particle context, where the time evolution involves both coherent and dissipative elements: we experimentally explore the stroboscopic dynamics of a complex many-body spin model with a universal trapped ion quantum simulator. We generate long-range phase coherence of spin by an iteration of purely dissipative quantum maps and demonstrate the characteristics of competition between combined coherent and dissipative non-equilibrium evolution - the hallmark of a novel dynamical phase transition. In order to do so, we employ a new spectroscopic decoupling technique facilitating the simulation of complex many-body systems in an ion trap quantum information processing architecture.

Obtaining full control of the dynamics of many-particle quantum systems represents a fundamental scientific and technological challenge. Impressive experimental progress on various physical platforms has been made [9, 118, 122, 126, 128, 130, 131, 158–162], complemented with the development of a detailed quantum control theory [19, 20, 112, 143]. Controlling the *coherent* dynamics of systems well-isolated from the environment enables, for example, quantum computation in the circuit model [30]. But this also allows for digital coherent quantum simulation with time evolution realized by sequences of small Trotter steps [15], as demonstrated in recent experiments [24, 163]. On the other hand, engineering the coupling of a system

---

<sup>2</sup>The author of the present thesis designed the experiment, measured and analyzed the data and wrote the manuscript

to its environment – and thus its resulting *dissipative* dynamics – introduces new scenarios of dissipative quantum state preparation [62, 136, 137, 164, 165], dissipative variants of quantum computing and memories [21, 138, 166] and non-equilibrium many-body physics [59, 142, 167]. The experimental combination of both coherent and dissipative evolution allows us to explore the dynamics of novel classes of non-equilibrium many-body quantum systems.

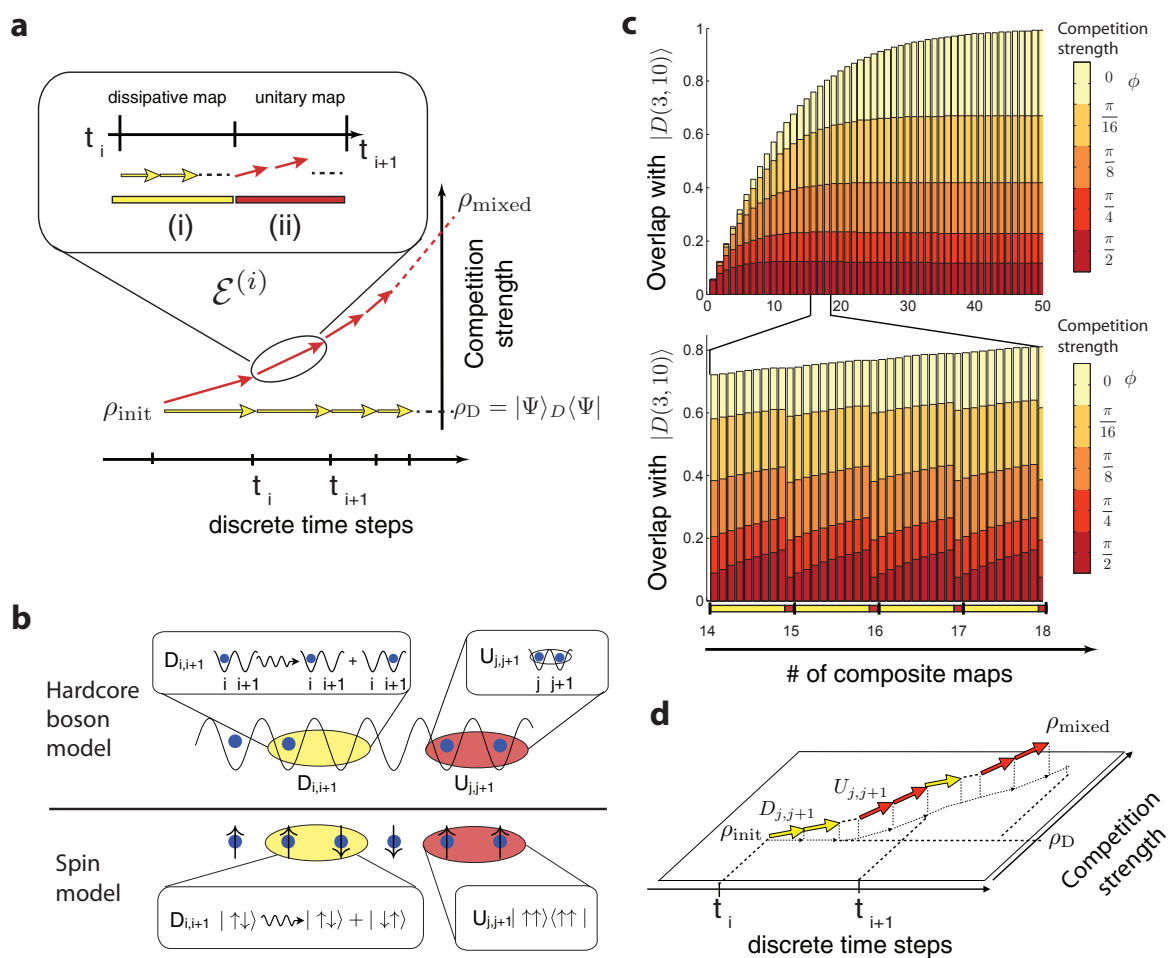
The dynamics of these systems is often considered as continuous in time, described by many-body Lindblad master equations, cf. e.g. [168]. This may be conceived as a special instance of a more general setting, where a discrete time evolution of a system’s reduced density matrix is generated by concatenated dynamical maps. So far, the concept of dynamical maps has proven useful for the description of periodically driven classical nonlinear systems [169], and their quantum mechanical counterparts, such as the kicked rotor, providing one of the paradigmatic models of quantum chaos [170–172]. Remarkable experiments have been performed with periodically driven systems of cold atoms, which have demonstrated some of the basic phenomena of quantum chaos such as dynamical localization [173–176]. At present all these studies are on the level of single particle physics.

Below we present a first experimental study of many-particle open-system dynamical maps for complex spin models (representing hardcore bosons), implemented in a linear ion-trap quantum computing architecture using up to five ions. The dynamical maps are realized by a digital simulation strategy, contrasting analog Hamiltonian quantum simulation with trapped ions [151–153, 177, 178]. Our study of new physical phenomena, involving the competition between coherent and dissipative multi-particle dynamics, is enabled by recent progress in performing high-fidelity quantum operations in systems of trapped ions. This allows us not only to engineer (program) complex individual dynamical maps, but provides the high fidelities required to iterate dynamical maps in a meaningful way to follow the time evolution for multiple iterated maps, and thus to observe for the first time the novel physics associated with the competition between coherent and dissipative dynamics.

In particular, we demonstrate the purely dissipative creation of quantum mechanical long-range phase order. Furthermore, we implement a competition between coherent and dissipative many-particle dynamics by alternating sequences of unitary and non-unitary maps outlined in Fig. 4.3a, and observe the destruction of phase coherence as a result. This reflects the hallmark feature of a strong coupling non-equilibrium phase transition predicted in a closely related driven-dissipative model of bosons [121]. In the actual implementation of the simulation, the engineered dissipative and coherent dynamics compete with undesired dissipative processes mainly caused by imperfect gate operations. We address this generic, though so far widely disregarded aspect, by carefully assessing the experimental errors. As a step towards solving this problem, we develop a novel and efficient special purpose error reduction technique.

Figure 4.7 (following page): **Competing dissipative and Hamiltonian dynamical maps in the spin or hardcore boson model.** **a**, Dynamical maps, acting on the reduced density matrix  $\rho$  of an open many-body quantum system, can be composed of elementary (i) dissipative and (ii) unitary maps. The dissipative maps considered here drive the system into a pure, long-range ordered many-body “dark” state  $\rho_D = |\psi\rangle_D \langle\psi|$ . The addition of suitable Hamiltonian maps leads to a *competition* of dissipative and coherent dynamics, in such a way that for strong enough coherent interactions, a phase transition into a mixed, disordered state results in large systems. **b**, Analogy of spins and hardcore bosons, in turn equivalent to bosons in the limit of low lattice filling (cf. Methods): In the considered open-system spin-1/2 (hardcore boson) lattice model, spin excitations  $|\uparrow\rangle$  ( $|\downarrow\rangle$ ) can be identified with occupied (empty) lattice sites. Quasi-local dissipative maps  $D_{i,i+1}$  acting on neighboring pairs of spins lead to delocalization of spin excitations (hardcore bosons) over pairs of lattice sites. Competing coherent dynamics is realized by unitary maps corresponding to interactions of spin excitations (hardcore bosons) located on neighboring lattice sites  $U_{j,j+1}$ . **c**, Numerically simulated dynamics for an open-boundary chain of  $N = 10$  spins, starting in an initial state containing  $m = 3$  spin excitations (hardcore bosons) (see appendix section B.4.2). Time evolution is realized by sequentially applying composite maps consisting of (i) dissipative and (ii) coherent elementary dynamical maps, as shown in a. For vanishing Hamiltonian interactions, perfect long-range order (as measured by the overlap fidelity with the Dicke state  $|D(m, N)\rangle$ ) is built up by the sequential application of dissipative maps (white), whereas increasing competing interactions (from yellow to red) lead to a decrease in the dissipatively created long-range order. The lower part of the figure shows a zoom into the composite maps 14 to 18, resolving that each of them is built up from 9 two-spin elementary dissipative maps, followed by 9 two-spin coherent maps, the latter which can be realized by a single, global unitary map in our setting. **d**, Illustration of the generic effect of experimental errors affecting the quantum simulation. The sketched plane corresponds to the simulation subspace with a given, ideally conserved hardcore boson (spin excitation) number  $m$ . Experimental errors in the implementation of dynamical maps lead to population leakage of the system out of the desired subspace.

#### 4. Quantum simulation of open systems



### 4.3.1. Competing dissipative and unitary dynamics in a complex spin model

Two competing, non-commuting contributions to a Hamiltonian give rise to a quantum phase transition, if the respective ground states of each contribution separately favor states with different symmetries [179]. The transition takes place at a critical value of the dimensionless ratio  $g$  of the two competing energy scales. A non-equilibrium analog can be achieved in open many-body quantum systems, where coherent Hamiltonian and dissipative dynamics compete with each other: The role of the ground state is played by the stationary state of the combined evolution, and the dimensionless ratio  $g$  is provided by a Hamiltonian energy scale vs. a dissipative rate. Such a situation has been addressed previously theoretically in the context of driven-dissipative dynamics of atomic bosons on a lattice [121]: A dissipative dynamics can be devised to drive the system from an arbitrary initial state with density matrix  $\rho_{\text{in}}$  into a Bose-Einstein condensate with long-range phase coherence as the unique, pure “dark” state  $|\psi\rangle_D$  of the dissipative evolution, i.e.  $\rho_{\text{in}} \rightarrow \rho_D = |\psi\rangle_D \langle \psi|$  for long enough waiting time. Supplementing this dynamics with a Hamiltonian representing local interactions, being incompatible with the dissipative tendency to delocalize the bosons, gives rise to a strong coupling dynamical phase transition. It shares features of a quantum phase transition in that it is driven by the competition of non-commuting quantum mechanical operators, and a classical one in that the ordered phase terminates in a strongly mixed state.

In our experiment, we consider analogous open-system dynamics of a quantum spin-1/2 – or hardcore boson – model, realized with trapped ions. A schematic overview of the relation of the ionic spin- and the atomic boson model is given in Fig. 4.3b, whereas a more detailed description is provided in Methods and (see appendix section B.4.2). The discrete time evolution is generated by sequences of dynamical or Kraus maps  $\mathcal{E}^{(l)}$  acting on the system’s reduced density matrix  $\rho$  as illustrated in Fig. 4.3a, with time steps  $t_\ell \rightarrow t_{\ell+1}$  represented by

$$\rho(t_\ell) \mapsto \rho(t_{\ell+1}) = \mathcal{E}^{(l)}[\rho(t_\ell)] = \sum_{k=1}^K E_k^{(l)} \rho(t_\ell) E_k^{(l)\dagger}. \quad (4.4)$$

The set of Kraus operators  $\{E_k^{(l)}\}$  satisfies  $\sum_{k=1}^K E_k^{(l)\dagger} E_k^{(l)} = 1$  [30]. While the familiar sequences of unitary maps are obtained for a single Kraus operator  $K = 1$ , dissipative dynamics corresponds to multiple Kraus operators  $K > 1$ . In particular, the continuous time evolution of a Lindblad master equation is recovered in the limit of infinitesimal time steps, cf. Methods. The dissipative dynamics studied in our spin model is governed by dynamical maps according to two-body Kraus operators acting on pairs of neighboring spins  $i, i + 1$ :

$$E_{i,1} = c_i, \quad E_{i,2} = 1 - c_i^\dagger c_i. \quad (4.5)$$

The elementary operators generating the dynamics are given by

$$c_i = (\sigma_i^+ + \sigma_{i+1}^+)(\sigma_i^- - \sigma_{i+1}^-), \quad (4.6)$$

where  $\sigma_i^\pm = (\sigma_i^x \pm i\sigma_i^y)/2$  are spin-1/2 raising and lowering operators acting on spin  $i$ . In the continuous time limit, the operators  $c_i$  correspond precisely to Lindblad quantum jump operators and generate a dissipative evolution described by a quantum master equation, cf. Methods.

The operators act bi-locally on pairs of spins, as visualized in Fig. 4.3b: Physically, they map any antisymmetric component in the wave function on a pair of sites into the symmetric one, or – in the language of hardcore bosons – symmetrically delocalize particles over pairs of neighboring sites. Since this process takes place on each pair of neighboring sites, eventually only the symmetric superposition of spin excitations over the whole array persists as the stationary state of the evolution: Iteration of the dissipative dynamical map attracts the system towards a unique dynamical fixed point, or dark state, characterized by  $\rho(t_{\ell+1}) = \rho(t_\ell) \equiv \rho_D$ , resulting from the property  $c_i \rho_D = 0$  for all  $i$  separately. More specifically, for  $m$  spin excitations initially present in the array of  $N$  spins, this pure dark state is given by the Dicke state

$$|\psi\rangle_D = |D(m, N)\rangle \sim \left( \sum_{i=1}^N \sigma_i^+ \right)^m |\downarrow\rangle^{\otimes N} \quad (4.7)$$

with  $m$  collective spin excitations. The delocalization of the spin excitations over the whole array gives rise to the creation of entanglement and quantum mechanical off-diagonal long range order, witnessed, e.g., by the single-particle correlations  $\langle \sigma_i^+ \sigma_j^- \rangle \neq 0$  for  $|i - j| \rightarrow \infty$  (see appendix section B.4.3).

In our interacting lattice spin system, competing unitary dynamics can be achieved by the stroboscopic realization of coherent maps  $\rho(t_\ell) \mapsto \rho(t_{\ell+1}) = U \rho(t_\ell) U^\dagger$  with  $U = \exp(-i\phi H)$  according to the dimensionless spin Hamiltonian

$$H = \sum_i |\uparrow\rangle\langle\uparrow|_i \otimes |\uparrow\rangle\langle\uparrow|_{i+1} = \sum_i (1 + \sigma_i^z)(1 + \sigma_{i+1}^z)/4. \quad (4.8)$$

The bi-local terms of the Hamiltonian describe interactions of spin excitations or hardcore bosons located on neighboring sites (see Fig. 4.3a). The competition between dissipative and unitary dynamics arises since the dissipative dark states  $\rho_D$  are not eigenstates of the Hamiltonian, which is diagonal in Fock space and thus leads to a dephasing of the dissipatively induced off-diagonal order. The strength of the competition between the Hamiltonian and dissipative dynamics is determined by the parameter  $\phi \in [0, \pi]$  and plays a role analogous to a dimensionless ratio of energy scales in a quantum phase transition, or of an energy scale and a dissipative rate in the above scenario (see Methods). Clearly, for small system sizes, the sharp transition found in the thermodynamic limit is replaced by a smooth crossover as indicated in the numerical simulations in Fig. 4.3c.

Whereas under ideal dynamical coherent and dissipative maps, the total spin excitation (or hardcore boson) number  $m$  is a conserved quantity, the presence of experimental errors leads to a population leakage out of the initial subspace with  $m_0$  excitations (see Fig. 4.3d). Thus, even under the repeated application of almost ideal dissipative dynamical maps the system of  $N$  sites is ultimately driven into the steady state

$$\rho = \frac{1}{2^N} \sum_{m=0}^N \binom{N}{m} |D(m, N)\rangle\langle D(m, N)|. \quad (4.9)$$

This steady state, representing an incoherent mixture of Dicke states, each appearing according to its microcanonical statistical weight, is independent of the initial state and excitation number

$m_0$ , and an expected mean filling of  $\langle m \rangle / N = 1/2$  (see appendix section B.4.3). This generic effect imposes a major obstacle of a controlled study of systems at small and high excitation number (hardcore boson) densities, and motivates us to develop and implement a quantum-feedback error correction to counteract this effect.

We note that many of the theoretical aspects of the long time evolution of dynamical maps in many particle physics, such as the question of dynamical phase transitions are presently unexplored. In addition, the present experimental study emphasizes the importance of understanding the role of imperfections in this dynamics.

### 4.3.2. Experimental realization

The simulation is performed with  $^{40}\text{Ca}^+$  ions, confined to a string by a macroscopic linear Paul trap (see appendix section B.4.1). Each ion hosts a qubit or spin-1/2, which is encoded in the  $4S_{1/2}(m = -1/2) = |1\rangle \equiv |\uparrow\rangle$  and the  $3D_{5/2}(m = -1/2) = |0\rangle \equiv |\downarrow\rangle$  states. The backbone of this digital quantum simulator setup is a universal set of high-fidelity operations, which are realized by exactly timed laser pulses resonant with the qubit transition (see appendix section B.4.1). The entangling gate operations [148] act on the entire ion string, but the elementary dissipative maps  $D_{i,i+1}$  act on only two of the  $N$  system spins (Fig. 4.8a). We achieve operations on subsets of ions via decoupling all ions *not* involved in the elementary map, by shelving their population into additional storage states (Fig. 4.8b). In these electronic states, these ions are effectively “inactive” as they do not interact with the globally applied laser beams. This novel spectroscopic decoupling technique is experimentally simpler than physically moving the ions with respect to the laser beam [57]. This technique has the potential to simplify the architecture of ion traps used for quantum simulation and quantum computing.

To observe the complex dynamics of the open interacting spin system, we combine these experimental techniques (i) to generate long-range phase coherence of spins by an iteration of purely dissipative maps, (ii) to combine these dissipative dynamics with competing coherent maps, (iii) and finally to implement quantum non-demolition (QND) readout and quantum-feedback protocols for error detection and stabilization.

(i) The basis of the composite maps is a single elementary dissipative map  $D_{i,i+1}$  that is implemented by a quantum circuit of coherent gate operations and addressed optical pumping (see Fig. 4.8c), acting on the two currently active ions  $i, i + 1$  and an ancillary qubit, which is used to engineer the coupling to the environment [19, 62, 143]. The circuit decomposition of the three-qubit unitary underlying a single elementary dissipative map, is obtained from an optimal control algorithm (see appendix section B.4.1), resulting in a sequence of 17 operations containing 4 entangling gates. We have characterized a single elementary dissipative map by quantum process tomography on the two system qubits leading to a mean state fidelity of 68(1)%, which approximately corresponds to an average fidelity of over 98% per gate operation (see appendix section B.4.2). Due to the considerable complexity of the gate sequence, errors occur in different bases and are expected to average out and give rise to depolarizing noise without any preferred direction. Therefore, the actual implemented dynamics can be modeled as a combination of the ideal, tailored dissipative map and the depolarizing noise channel. Detailed numerical simulations show that the error is mainly caused by laser frequency and magnetic field fluctuations (see appendix section B.4.3).

We repeatedly apply such elementary maps  $D_{i,i+1}$ , interspersed with decoupling pulses to coherently transfer ions in and out from the storage states, to build up the composite dissipative map in a modular way, Fig. 4.8a. Using 3+1 ions, we studied pumping towards Dicke states in a three-spin chain with open boundary conditions, where we applied up to three simulation timesteps, each consisting of the two elementary maps  $D_{1,2}$  and  $D_{2,3}$ . The results displayed in Fig. 4.9a show a clear experimental signature of dissipatively induced delocalization of the spin excitations during the application of the first two elementary dissipative maps, before experimental imperfections become dominant for longer sequences.

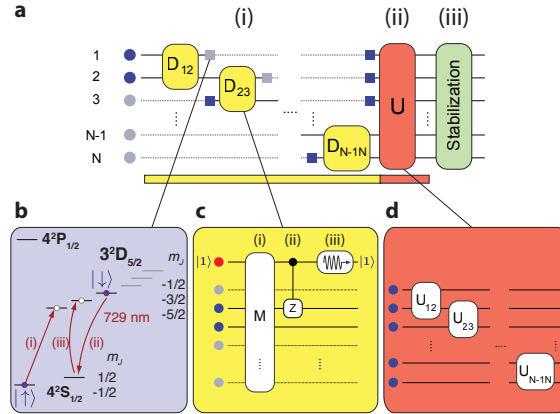


Figure 4.8.: **Experimental procedure to implement open-system dynamical maps.** **a**, Schematic overview of the experimental implementation of a composite dynamical map consisting of (i) multiple elementary dissipative maps, (ii) coherent competition, and (iii) error detection and correction. Decoupled ions are represented as gray bullets and decoupling (re-coupling) operations as gray (blue) squares. **b**, Scheme for decoupling ions from the interaction with the manipulating light fields: (i) shelve population from  $4S_{1/2}(m = -1/2) = |\uparrow\rangle$  to  $3D_{5/2}(m = -5/2)$ , (ii) transfer the population from  $3D_{5/2}(m = -1/2) = |\downarrow\rangle$  to  $4S_{1/2}(m = +1/2)$ , and subsequently to (iii)  $3D_{5/2}(m = -3/2)$ . **c**, A single dissipative element is realized using two system spins and one ancilla qubit ( $|0\rangle \equiv |\downarrow\rangle, |1\rangle \equiv |\uparrow\rangle$ ) by (i) mapping the information whether the system is in the symmetric or antisymmetric subspace onto the logical states  $|1\rangle$  or  $|0\rangle$  of the ancilla, respectively; (ii) mapping the antisymmetric onto the symmetric state using a controlled phase flip conditioned by the state of the ancilla qubit; and finally (iii) reinitialization of the ancilla qubit via optical pumping using the  $4^2P_{1/2}$  state (see appendix section B.4.1). **d**, Schematic view of the competing interaction consisting of quasi-local unitary maps  $U_{j,j+1}$ .

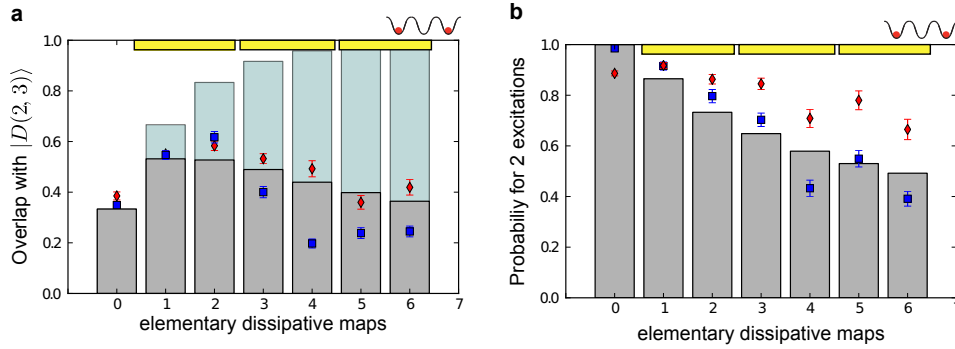


Figure 4.9.: **Experimental results of dissipatively induced delocalization through composite dynamical maps with 3+1 ions.** The results from an ideal model are shown in light-blue bars whereas those from a model including depolarization noise are indicated by dark-grey bars. Blue rectangles indicate the experimentally observed dynamics without any correction scheme whereas red diamonds include a post-selective error detection scheme (error bars,  $1\sigma$ ). **a**, Dissipative pumping into a three-spin Dicke state: Starting in an initial product state with two localized spin excitations  $|\uparrow\downarrow\uparrow\rangle$ , the application of the first two elementary dissipative maps leads to an increase in the delocalization of the two excitations over the spin chain, which is reflected by an increasing state overlap fidelity with the three-spin Dicke state  $|D(2, 3)\rangle$ . However, after applying a second and a third composite dissipative map, a decrease in the state overlap fidelity sets in and becomes dominant for long sequences of dynamical maps. **b**, The presence of depolarizing noise results in population leakage out of the initial subspace with  $m = 2$  spin excitations. This effect is evident in the decay of the probability of finding the three-spin system in the  $m = 2$  excitations subspace as a function of the number of applied elementary dissipative maps. A single composite dissipative map is indicated by a yellow bar.

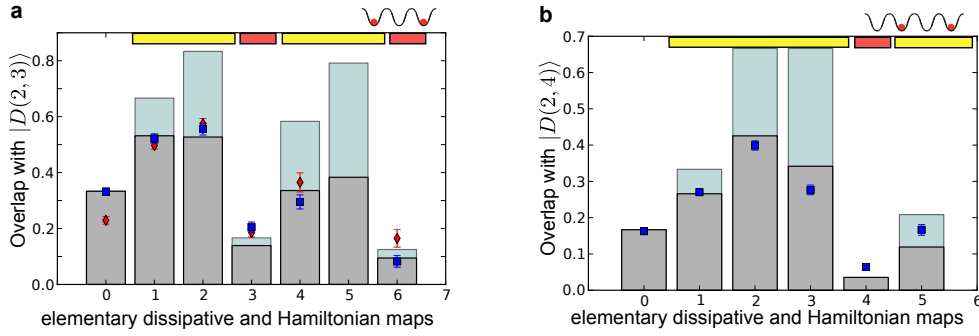


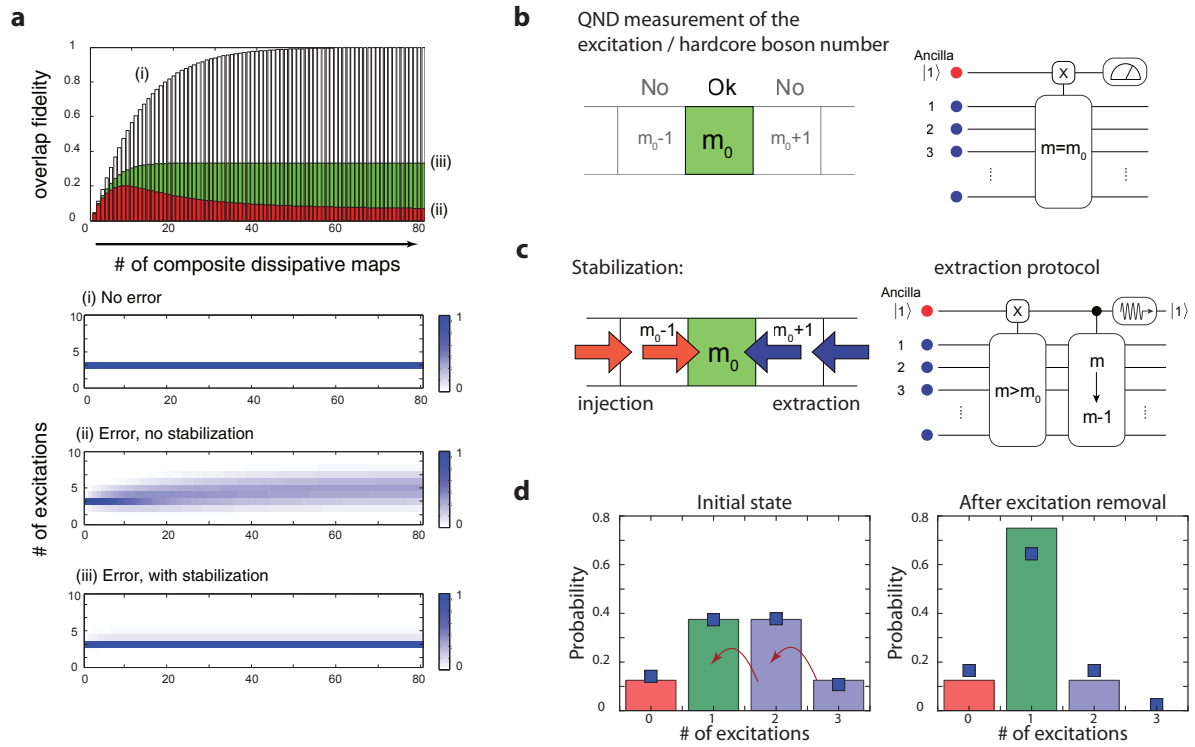
Figure 4.10.: **Experimental results for competing dissipative and coherent dynamics with 3+1 and 4+1 ions.** As in Fig. 4.9, the results from an ideal model are shown in light-blue bars whereas those from a model including depolarization noise are indicated by dark-grey bars. Blue rectangles indicate the experimentally observed dynamics without any correction scheme whereas red diamonds include a post-selective error detection scheme (error bars,  $1\sigma$ ). The application of dissipative (coherent) maps is indicated by yellow (red) bars. Competing dissipative and coherent dynamics for  $m = 2$  excitations in chains of **a**,  $N = 3$  and **b**,  $N = 4$  spins: the spin chains are first driven towards the Dicke-type dark state by the two and three elementary dissipative maps for a system of 3 and 4 spins. The subsequent application of the non-compatible unitary dynamical maps leads to a strong decrease of the overlap with the respective Dicke states, before subsequent elementary dissipative maps again start to pump the system back towards the Dicke states.

(ii) To investigate the competition between dissipative and competing Hamiltonian dynamics, we added elementary unitary maps according to nearest-neighbor spin-spin interactions to the composite dynamical maps (see appendix section B.4.2). Note that due to the commutativity of the two-spin elementary unitary maps, the composite, globally acting unitary map can be realized by a single unitary sequence (Fig. 4.8d). The results displayed in Fig. 4.10 for experiments with 3+1 and 4+1 ions show a clear fingerprint of incompatible Hamiltonian dynamics, which competes with the dissipative maps driving the spin chains towards the Dicke states. Further measurements with varying excitation number and competition strength are discussed (see appendix section B.4.7).

(iii) To reduce the detrimental effect of the experimental imperfections and thus to enable the implementation of longer sequences of dynamical maps, we developed and implemented two counter-strategies (see Fig. 4.3.2 for details). In a first approach we applied a quantum non-demolition (QND) measurement of the spin excitation number at the end of the sequence of dynamical maps, which allowed us to detect and discard experimental runs with a final erroneous excitation number and thereby improve the overall simulation accuracy. This global measurement is QND in the sense that only information about the total number of excitations, but not on their individual spatial locations along the chain is acquired; thus the simulation subspace is not disturbed (see appendix section B.4.5). The results shown in Fig. 4.9 and Fig. 4.10 confirm that the errors in the spin excitation number are strongly suppressed and a reasonable overlap with

the ideal evolution can be maintained for more simulation time steps.

Figure 4.11 (following page): **Experimental error detection and reduction techniques.** **a**, Numerical simulation of the time evolution consisting of composite dynamical maps building up long-range order quantified by overlap fidelity with the Dicke state  $|D(m, N)\rangle$ , starting in an initial state containing  $m = 3$  spin excitations on an open-boundary chain of  $N = 10$  spins. The simulation was performed for (i) ideal operations without experimental imperfections, (ii) a model including experimental errors, (iii) a model including errors but with the stabilization scheme. The lower part depicts the expected excitation distribution of the time evolution demonstrating that the stabilization keeps the system in the correct excitation subspace. **b**, Schematic idea and quantum circuit for a post-selective QND measurement of the total spin excitation number: First the information whether the  $N$  system spins are (not) in the subspace with  $m$  spin excitations or not is mapped coherently onto the logical state  $|1\rangle$  ( $|0\rangle$ ) of an ancillary qubit. A subsequent projective measurement of the latter indicates the presence of an erroneous excitation number, in which case the experimental run is discarded. **c**, Active QND feedback scheme to stabilize the spin system in a desired excitation number subspace by actively extracting (injecting) spin excitations in case errors in previous dynamical maps have led to a larger (smaller) excitation number than present initially. The information whether more excitations than the desired value are present in the system (or not) is coherently mapped onto the state  $|1\rangle$  ( $|0\rangle$ ) of the ancilla qubit. A non-unitary controlled-operation, only active for the ancilla qubit in  $|1\rangle$ , then extracts in a minimally destructive way one spin excitation from the system and automatically stops once this is achieved. **d**, Experimental demonstration of the stabilization protocol for  $m_0 = 1$  using 3+1 ions by applying the excitation removal to an initial state consisting of an equal superposition of all computational states,  $|\psi_0\rangle = 1/\sqrt{8}(|\downarrow\rangle + |\uparrow\rangle)^{\otimes 3}$ . Here, a single spin excitation should be removed if two or more excitations are present in the system (blue bars). Thus, pumping from the  $m = 3$  into the  $m = 2$  and from the  $m = 2$  into the  $m = 1$  subspace is expected, whereas population initially present in the  $m = 0$  and  $m = 1$  subspaces should be left untouched. The correct populations after the application of the excitation removal protocol are confirmed by the measured data (blue rectangles) which are close to the ideally expected behavior (colored bars). Data error bars are smaller than the markers.



Complementary to this post-selective method, we introduced a more powerful, active QND feedback scheme, which bears similarities to quantum feedback protocols as realized with photons in a cavity [180]. The key idea is to actively stabilize the spin system during the sequence of dynamical maps in a subspace with a particular spin excitation (or hardcore boson) number. In order to be able to perform this stabilization with a single ancilla qubit, we break the stabilization process into two independent parts, where the first part removes one excitation if there are too many excitations in the system, and the second part adds one excitation if needed. Similarly to the post-selective technique presented above, first the information whether there are too many (few) excitations in the system is coherently mapped onto the ancilla qubit. Depending on the state of the ancilla qubit, a single excitation is removed from (injected into) the system by a quantum feedback protocol. This extraction (injection) is in general an ambiguous process, as the excitation can be removed (injected) on multiple sites. We use a scheme that tries to perform the removal (injection) subsequently on each site and stops once it was successful. Using only a single ancilla qubit, this process cannot be performed efficiently as a unitary process, therefore we developed a technique making use of the resetting and decoupling techniques described above (see appendix section B.4.6).

We demonstrate the excitation removal for a chain of 3+1 spins, initially prepared in an equal superposition of all basis states, as shown in Fig. 4.9c. At the current level of experimental accuracy, the implementation of this stabilization scheme cannot improve the performance when used in the full simulation sequence (see appendix section B.4.6). We emphasize, however, that our approach relies only on a single ancillary qubit, regardless of the system size. More generally, such customized error detection and reduction strategies will incur a substantially reduced resource overhead as compared with full-fledged quantum error correction protocols. We showcased a novel error management technique consisting of theoretical modeling of the errors, as well as designing system specific error reduction techniques. For the simulation of large systems it will be imperative to develop and understand sophisticated error models. Furthermore, we expect our experimental observations on the interplay of engineered and detrimental dissipation to stimulate theoretical research on the fundamental issue of robustness of (dynamical) many-body phenomena in open quantum systems in the presence of noise - similar to the persistence of quantum phases at finite as compared to zero temperature in Hamiltonian systems.

### 4.3.3. Methods

**Dynamical maps vs. quantum master equation.** The dissipative Kraus maps specified in equation (4.5) are obtained as a special case of the operators  $E_{i,1} = \sin \theta c_i$ ,  $E_{i,2} = 1 + (\cos \theta - 1)c_i^\dagger c_i$ , for  $\theta = \pi/2$ . This limit corresponds to a deterministic action of the Kraus map (see appendix section B.4.2), in this case generating truly stroboscopic dynamics. Instead, in the limit  $\theta \rightarrow 0$ , we approximate  $E_{i,1} \approx \theta c_i$ ,  $E_{i,2} \approx 1 - \frac{1}{2}\theta^2 c_i^\dagger c_i$ . In this limit, the sequence of dynamical maps reduces to the continuous time evolution described by a quantum master equation entirely generated by a dissipative Liouville operator,  $\mathcal{L}[\rho] = \sum_i \left( c_i \rho c_i^\dagger - \frac{1}{2} \{c_i^\dagger c_i, \rho\} \right)$  [30]. Similarly, the Hamiltonian Kraus map can be expanded,  $\exp(-i\phi H) \approx 1 - i\phi H$  for  $\phi \rightarrow 0$ . The dynamics in this continuum limit is then described by the quantum master equation  $\partial_t \rho = -i[UH, \rho] + \kappa \mathcal{L}[\rho]$ , with the dimensionful energy scale  $U$  ( $U dt = \phi$ ) and dissipative rate  $\kappa$  ( $\kappa dt = \theta^2$ ).

Here,  $dt$  is the physical time required for the implementation of one Kraus map in the digital simulation. The dimensionless ratio describing the competition  $g = U/\kappa = \phi/\theta^2$  remains well-defined in this limit. We finally note that a temporal coarse graining implemented by averaging over a sequence of elementary maps with even larger discrete mapping steps gives rise to a quasi-continuous evolution, as shown numerically in Fig. 4.3c. In a large system, the quasilocal operations can be coarse grained also over space. The result is an effective quasi-continuous master equation dynamics for the density operator.

**Atomic boson vs. ionic spin model.** The dissipative spin operators  $c_i$  of equation (4.6) are constructed in complete analogy to the case of bosons, which has been proposed theoretically in [59]: Formally, and as further detailed in (see appendix section B.4.2), they obtain by replacing the spin raising (lowering) operators  $\sigma_i^+$  ( $\sigma_i^-$ ) by bosonic creation (annihilation) operators  $a_i^\dagger$  ( $a_i$ ) of atoms confined to an optical lattice. In that case, the dark state is given by  $m$  symmetrically delocalized particles on  $N$  lattice sites, i.e.  $|\psi\rangle_D = (m!)^{-1/2} \left( \sum_{i=1}^N a_i^\dagger \right)^m |0\rangle^{\otimes N}$  – the Dicke dark states of the spin model are replaced by a fixed number Bose-Einstein condensate (the bosonic vacuum state is defined by  $a_i|0\rangle^{\otimes N} = 0$  for all  $i$ ). Using the Holstein-Primakoff representation of spin 1/2 operators in terms of bosons,  $\sigma_i^\pm = a_i^\dagger \sqrt{1 - \hat{n}_i}$  ( $\hat{n}_i = a_i^\dagger a_i$ ), it is seen that the dissipative spin operators reduce to their bosonic counterpart in the limit of small average occupation  $\bar{n} = \langle \hat{n}_i \rangle \ll 1$ , where the square root can be safely replaced by one.

### Acknowledgments

We gratefully acknowledge support by the Austrian Science Fund (FWF), through the SFB FoQus (FWF Project No. F4002-N16 and F4016-N16) and the START grant Y 581-N16 (S. D.), by the European Commission (AQUTE), as well as the Institut für Quantenoptik und Quanteninformation GmbH. This research was funded by the Office of the Director of National Intelligence (ODNI), Intelligence Advanced Research Projects Activity (IARPA), through the Army Research Office grant W911NF-10-1-0284. All statements of fact, opinion or conclusions contained herein are those of the authors and should not be construed as representing the official views or policies of IARPA, the ODNI, or the U.S. Government. M. M. acknowledges support by the CAM research consortium QUITMAD S2009-ESP-1594, European Commission PICC: FP7 2007-2013, Grant No. 249958, and the Spanish MICINN grant FIS2009-10061.

### Author contributions

M.M., P.S., J.T.B. and S.D. developed the research, based on theoretical ideas conceived with P.Z.; P.S. and D.N. performed the experiments; P.S. and T.M. analysed the data; P.S., J.T.B., D.N., T.M., E.A.M., M.H. and R.B. contributed to the experimental set-up; P.S., M.M. and S.D. wrote the manuscript, with revisions provided by J.T.B., P.Z. and R.B.; all authors contributed to the discussion of the results and manuscript.



## 5. Summary and outlook

This work summarized several proof of concept experiments towards a quantum information processor beyond coherent operations. First a toolbox beyond a universal set of operations was developed to implement both, coherent and incoherent, dynamics on a register of qubits.

This toolbox was used to implement the first experimental realization of repetitive quantum error correction. This is an important milestone towards a quantum computer because it requires high quality coherent operations in addition to a technique to remove entropy from the system. The three qubit error correction algorithm represents furthermore an ideal benchmark for different implementations of a quantum computer. Recently, the same algorithm has been implemented in a quantum information processor based on superconducting qubits with comparable fidelity [181]. The implementation of multiple rounds of quantum error correction procedures has not been repeated in any other physical system and thus our work emphasizes the feasibility of a trapped ion quantum computer.

Another addition to our toolbox is the in-sequence recooling technique which allows us to perform measurements during an algorithm. This technique enabled the reversal of a quantum measurement with the aid of the quantum error correction protocol. We have also demonstrated that these techniques are useful tools towards a scalable and efficient implementation of an order finding algorithm in an ion trap following the ideas of Kitaev. There, measurements during the algorithm are used to perform the required quantum Fourier transform semiclassically and this reduces the number of required qubits considerably.

Besides quantum computing, well controllable quantum systems can also be used for the simulation of quantum system which has gained a lot of interest lately. In our lab, a universal coherent quantum simulator has been demonstrated recently [24]. The concept of simulating quantum systems was then extended towards open systems, where in a first proof of concept experiment, a complete toolbox to simulate any arbitrary Markovian system was realized. For the first time, a dissipative process with an entangled state as its unique dark state was realized. This toolbox was then used to simulate the complex dissipative dynamics of a many-body bosonic system in an ion trap. In particular, the hallmark features of competition between coherent and dissipative many-body dynamics have been observed. For a large system, this competition should yield a novel non-equilibrium phase transition which shares features of both classical and quantum phase transitions.

Future ion trap quantum simulators will certainly try to increase the system size in analog quantum emulators to a level where classical computers cannot reproduce the results. These achievements will be likely criticized as they are not believed to be faithful, which means that the effect of the experimental errors on the simulation results cannot be quantified reliably. Therefore, error detection and reduction procedures will be required, but the overhead of full quantum error

correction protocols will be likely too large so that these techniques are not able to improve the actual simulation. Therefore it is necessary to develop error reduction methods with significantly less overhead. We took a first step in this direction for the boson simulation where we developed an error reduction scheme that requires only a single auxiliary qubit independent of the system size. This scheme can be interpreted as a feedback loop that keeps the system inside the simulation subspace. Although we were not able to show an improvement in the actual simulation, the required quality of operations for an improvement is in the reach of today's technology.

Anyway, a fault tolerant quantum computer needs to be the long-term goal of our efforts in experimental quantum information processing. I envision, that further experimental analysis of quantum error correction techniques will converge with the process of developing more efficient error correction algorithms. Ideally, this will lead to a feedback process where the next generation of quantum computer hardware is being designed to yield optimal results for the refined error correction procedures.

# A. List of publications

1. “Quantum simulation of open-system dynamical maps with trapped ions”, **P. Schindler**, M. Müller, D. Nigg, J. T. Barreiro, E. A. Martinez, M. Hennrich, T. Monz, S. Diehl, P. Zoller, R. Blatt, Nature Physics, in press (2013) arXiv:1212.2418
  2. “Undoing a Quantum Measurement”, **P. Schindler**, T. Monz, D. Nigg, J. T. Barreiro, E. A. Martinez, M. F. Brandl, M. Chwalla, M. Hennrich, and R. Blatt, Phys. Rev. Lett. 110, 070403 (2013)
  3. “Experimental repetitive quantum error correction”, **P. Schindler**, J. T. Barreiro, T. Monz, V. Nebendahl, D. Nigg, M. Chwalla, M. Hennrich, and R. Blatt, Science 332, 1059-1061 (2011)
- 
4. “Certifying Systematic Errors in Quantum Experiments”, T. Moroder, M. Kleinmann, **P. Schindler**, T. Monz, O. Gühne, and R. Blatt, Phys. Rev. Lett. 110, 180401 (2013)
  5. “Atom-atom entanglement by single-photon detection”, L. Slodicka, G. Hetet, N. Röck, **P. Schindler**, M. Hennrich, R. Blatt, Phys. Rev. Lett. 110, 083603 (2013)
  6. “Experimental Characterization of quantum dynamics through many-body interactions”, D. Nigg, J. T. Barreiro, **P. Schindler**, M. Mohseni, T. Monz, M. Chwalla, M. Hennrich, and R. Blatt, Phys. Rev. Lett. 110, 060403 (2013)
  7. “Tunable ion-photon entanglement in an optical cavity”, A. Stute, B. Casabone, **P. Schindler**, T. Monz, P. O. Schmidt, B. Brandstätter, T. E. Northup, and R. Blatt, Nature 485, 482 (2012)
  8. “Interferometric thermometry of a single sub-Doppler-cooled atom”, L. Slodicka, G. Hetet, N. Röck, S. Gerber, **P. Schindler**, M. Kumph, M. Hennrich, and R. Blatt, Phys. Rev. A 85, 043401 (2012).
  9. “Universal digital quantum simulation with trapped ions”, B. Lanyon, C. Hempel, D. Nigg, M. Müller, R. Gerritsma, F. Zähringer, **P. Schindler**, J. T. Barreiro, M. Rambach, G. Kirchmair, M. Hennrich, P. Zoller, R. Blatt, C. F. Roos, Science 334, 57 (2011).
  10. “14-qubit entanglement: creation and coherence”, T. Monz, **P. Schindler**, J. T. Barreiro, M. Chwalla, D. Nigg, W. A. Coish, M. Harlander, W. Hänsel, M. Hennrich, and R. Blatt , Phys. Rev. Lett. 106 , 130506 (2011)
  11. “An open-system quantum simulator with trapped ions”, J. T. Barreiro, M. Müller, **P. Schindler**, D. Nigg, T. Monz, M. Chwalla, M. Hennrich, C. F. Roos, P. Zoller, and R. Blatt, Nature 470, 486 (2011)

12. “Experimental multiparticle entanglement dynamics induced by decoherence”, J. T. Barreiro,  
**P. Schindler**, O. Gühne, T. Monz, M. Chwalla, C. F. Roos, M. Hennrich, and R. Blatt, Nature Physics 6, 943 (2010)
13. “Absolute frequency measurement of the  $^{40}\text{Ca}^+ 4s^2S_{1/2} - 3d^2D_{5/2}$  clock transition”, M. Chwalla, J. Benhelm, K. Kim, G. Kirchmair, T. Monz, M. Riebe, **P. Schindler**, A. S. Villar, W. Hänsel, C. F. Roos, R. Blatt, M. Abgrall, G. Santarelli, G. D. Rovera, and Ph. Laurent, Phys. Rev. Lett. 102, 023002 (2009)
14. “Realization of universal ion-trap quantum computation with decoherence-free qubits”, T. Monz, K. Kim, A. S. Villar, **P. Schindler**, M. Chwalla, M. Riebe, C. F. Roos, H. Häffner, W. Hänsel, M. Hennrich, and R. Blatt, Phys. Rev. Lett. 103, 200503 (2009)
15. “Realization of the quantum Toffoli gate with trapped ions”, T. Monz, K. Kim, W. Hänsel, M. Riebe, A. S. Villar, **P. Schindler**, M. Chwalla, M. Hennrich, and R. Blatt, Phys. Rev. Lett. 102, 040501 (2009)
16. “Deterministic entanglement swapping with an ion trap quantum computer”, M. Riebe, T. Monz, A. S. Villar, **P. Schindler**, M. Chwalla, M. Hennrich, and R. Blatt, Nature Physics 4, 839 (2008)
17. “Precision spectroscopy with two correlated atoms”, M. Chwalla, K. Kim, T. Monz, **P. Schindler**, M. Riebe, C. F. Roos, and R. Blatt, Appl. Phys. B 89, 483 (2007)
18. “Process tomography of ion trap quantum gates”, M. Riebe, K. Kim, **P. Schindler**, T. Monz, P. O. Schmidt, T. K. Körber, W. Hänsel, H. Häffner, C. F. Roos, and R. Blatt, Phys. Rev. Lett. 97, 220407 (2006)

## B. Supplementary information

### B.1. A quantum information processor with trapped ions

In the following, tables containing the sequences operations for the presented algorithms are shown.

Number	Pulse	Number	Pulse
1	$S_z^{(1)}(1.5\pi)$	11	$MS_{1.5\pi}(0.5\pi)$
2	$R_\pi(1.5\pi)$	12	$S_z^{(3)}(1.75\pi, 2)$
3	$MS_\pi(0.25)$	13	$MS_{2.25\pi}(0.5\pi)$
4	$S_z^{(2)}(\pi)$	14	$R_{1.75\pi}(0.5\pi)$
5	$MS_\pi(0.875\pi)$	15	$R_{2.25\pi}(0.5\pi)$
6	$S_z^{(3)}(\pi)$	16	$MS_{2.25\pi}(0.25\pi)$
7	$MS_\pi(0.125\pi)$	17	$S_z^{(3)}(1.5\pi)$
8	$S_z^{(3)}(\pi)$	18	$S_z^{(2)}(1.0\pi)$
9	$R_{0.5\pi}(0.5\pi)$	19	$R_{2.25\pi}(0.5\pi)$
10	$S_z^{(3)}(0.5\pi)$		

Table B.1.: Sequence of operations for the algorithm used for an open system quantum simulator [90].

Number	Pulse	Number	Pulse
1	$R_\pi(\pi/2)$	10	$R_{\pi/2}(3\pi/16)$
2	$S_z^{(2)}(\pi)$	11	$S_z^{(2)}(3\pi/2)$
3	$S_z^{(3)}(\pi/2)$	12	$R_{\pi/2}(\pi/4)$
4	$MS_{\pi/2}(\pi/8)$	13	$MS_{\pi/2}(\pi/8)$
5	$S_z^{(3)}(\pi)$	14	$S_z^{(3)}(\pi)$
6	$MS_{\pi/2}(\pi/16)$	15	$MS_{\pi/2}(\pi/8)$
7	$R_{-\pi/2}(\pi/2)$	16	$S_z^{(1)}(\pi/2)$
8	$S_z^{(2)}(\pi)$	17	$S_z^{(2)}(\pi)$
9	$MS_{\pi/2}(3\pi/16)$	18	$R_\pi(\pi/2)$

Table B.2.: Sequence of operations for the fully coherent QFT operation on three qubits.

Number	Pulse	Number	Pulse
1	$R_{\pi/2}(\pi/2)$	7	$MS_0(\pi/4)$
2	$S_z^{(3)}(7\pi/4)$	8	$S_z^{(3)}(3\pi/2)$
3	$MS_0(\pi/2)$	9	$MS_0(\pi/2)$
4	$R_{\pi}(\pi/2)$	10	$R_{-\pi}(\pi/2)$
5	$S_z^{(3)}(\pi/2)$	11	$R_{-\pi/2}(\pi/2)$
6	$R_{\pi}(\pi/4)$		

Table B.3.: Sequence of the controlled  $\pi_1(y)$  permutation operation.

Number	Pulse	Number	Pulse
1	$R_{\pi}(\pi/2)$	5	$MS_0(\pi/4)$
2	$S_z^{(1)}(3\pi/2)$	6	$S_z^{(1)}(3\pi/2)$
3	$MS_0(\pi/2)$	7	$R_{\pi}(\pi/2)$
4	$R_{\pi}(\pi/2)$	8	$S_z^{(2)}(\pi)$

Table B.4.: Sequence of the controlled  $\pi_2(y)$  permutation operation.

Number	Pulse	Number	Pulse
1	$S_z^{(3)}(\pi/2)$	13	$S_z^{(2)}(\pi/2)$
2	$R_{\pi}(3\pi/2)$	14	$S_z^{(3)}(3\pi/2)$
3	$S_z^{(3)}(\pi/2)$	15	$MS_0(3\pi/4)$
4	$MS_0(\pi/4)$	16	$R_{-\pi/2}(0.196\pi)$
5	$R_{-\pi}(5\pi/2)$	17	$S_z^{(2)}(2\pi/3)$
6	$S_z^{(1)}(3\pi/2)$	18	$R_{\pi/2}(0.196\pi)$
7	$R_{\pi}(\pi/2)$	19	$R_{\pi}(\pi/4)$
8	$R_{\pi/2}(\pi/4)$	20	$MS_0(\pi/2)$
9	$S_z^{(2)}(\pi)$	21	$S_z^{(2)}(7\pi/4)$
10	$R_{\pi/2}(\pi/4)$	22	$R_{\pi/2}(\pi/2)$
11	$MS_0(\pi/2)$	23	$S_z^{(1)}(\pi/2)$
12	$S_z^{(1)}(\pi)$		

Table B.5.: Sequence of the controlled  $\pi_3(y)$  permutation operation.

Number	Pulse	Number	Pulse
1	$R_{\pi/2}(\pi/2)$	10	$S_z^{(2)}(3\pi/2)$
2	$S_z^{(2)}(\pi/4)$	11	$MS_0(\pi/2)$
3	$R_{-\pi}(\pi/2)$	12	$S_z^{(3)}(3\pi/2)$
4	$MS_0(\pi/2)$	13	$R_{\pi}(\pi/4)$
5	$S_z^{(2)}(3\pi/2)$	14	$MS_0(\pi/4)$
6	$MS_0(3\pi/4)$	15	$S_z^{(1)}(3\pi/2)$
7	$R_{\pi}(\pi/4)$	16	$S_z^{(2)}(3\pi/2)$
8	$S_z^{(3)}(\pi/4)$	17	$R_{-\pi}(\pi/2)$
9	$R_{\pi}(\pi/2)$		

Table B.6.: Sequence of the controlled  $\pi_3^2(y)$  permutation operation.

Number	Pulse	Number	Pulse
1	$R_{-\pi}(\pi/2)$	13	$R_{-\pi/2}(0.196\pi)$
2	$R_{\pi/2}(\pi)$	14	$S_z^{(1)}(4\pi/3)$
3	$S_z^{(1)}(3\pi/2)$	15	$S_z^{(3)}(1.905\pi)$
4	$MS_0(7\pi/8)$	16	$R_{\pi/2}(0.196\pi)$
5	$S_z^{(3)}(\pi)$	17	$R_{-\pi}(\pi/4)$
6	$MS_0(\pi/8)$	18	$R_{-\pi/2}(\pi/2)$
7	$R_{\pi/2}(\pi/2)$	19	$MS_0(\pi/2)$
8	$R_{-\pi}(3\pi/2)$	20	$S_z^{(2)}(\pi/3)$
9	$S_z^{(1)}(3\pi/2)$	21	$MS_0(\pi/2)$
10	$S_z^{(2)}(\pi/2)$	22	$S_z^{(3)}(1.905\pi)$
11	$MS_0(3\pi/4)$	23	$R_{\pi/2}(\pi/2)$
12	$S_z^{(3)}(1.33\pi)$	24	$S_z^{(3)}(7\pi/4)$

Table B.7.: Sequence of the controlled  $\pi_4(y)$  permutation operation.

Number	Pulse	Number	Pulse
1	$R_\pi(\pi/2)$	6	$R_\pi(\pi/4)$
2	$S_z^{(1)}(3\pi/2)$	7	$MS_0(\pi/4)$
3	$MS_0(\pi/4)$	8	$S_z^{(1)}(3\pi/2)$
4	$R_\pi(\pi/4)$	9	$R_\pi(\pi/2)$
5	$S_z^{(2)}(\pi)$	10	$S_z^{(2)}(\pi)$
1	$R_{-\pi}(\pi/2)$	13	$R_{-\pi/2}(0.196\pi)$
2	$R_{\pi/2}(\pi)$	14	$S_z^{(1)}(4\pi/3)$
3	$S_z^{(1)}(3\pi/2)$	15	$S_z^{(3)}(1.905\pi)$
4	$MS_0(7\pi/8)$	16	$R_{\pi/2}(0.196\pi)$
5	$S_z^{(3)}(\pi)$	17	$R_{-\pi}(\pi/4)$
6	$MS_0(\pi/8)$	18	$R_{-\pi/2}(\pi/2)$
7	$R_{\pi/2}(\pi/2)$	19	$MS_0(\pi/2)$
8	$R_{-\pi}(3\pi/2)$	20	$S_z^{(2)}(\pi/3)$
9	$S_z^{(1)}(3\pi/2)$	21	$MS_0(\pi/2)$
10	$S_z^{(2)}(\pi/2)$	22	$S_z^{(3)}(1.905\pi)$
11	$MS_0(3\pi/4)$	23	$R_{\pi/2}(\pi/2)$
12	$S_z^{(3)}(1.33\pi)$	24	$S_z^{(3)}(7\pi/4)$

Table B.8.: Sequence of the controlled  $\pi_4^2(y)$  permutation operation.

## B.2. Experimental repetitive quantum error correction

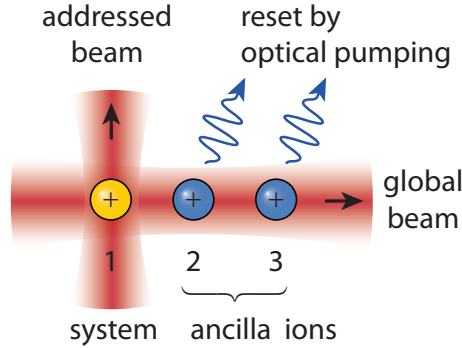


Figure B.1.: Schematic of the experimental setup. The ion string contains one system qubit (ion 1) and two ancillas (ions 2 and 3). In the QEC protocol quantum operations are performed by addressed and global laser pulses. After each QEC cycle the ancilla ions are reset by an optical pumping technique.

### B.2.1. Process fidelity

Any quantum process acting on a state  $\rho$  can be described by a completely positive map  $\mathcal{E}(\rho)$ . For our three-qubit QEC algorithm it is sufficient to characterize the process experienced by the system qubit. This process is expressed in an operator sum representation

$$\mathcal{E}(\rho) = \sum_{m,n=1}^4 \chi_{mn} A_m \rho A_n^\dagger,$$

where the basis is formed by the single-qubit Pauli operators and the identity operator:  $\{A_i\} = \{\mathbb{1}, \sigma_x, \sigma_y, \sigma_z\}$ . The process is then completely described by the process matrix  $\chi$ , which can be reconstructed from measured data with the help of a maximum likelihood method (4,16).

The reconstructed process matrix is then compared to the ideal process to evaluate the quality of the implementation. In the case of the QEC algorithm, the ideal process corresponds to the identity ( $\mathbb{1}\rho\mathbb{1}$ ) for the correctable single-qubit errors and  $\sigma_z$  ( $\sigma_z\rho\sigma_z$ ) for the uncorrectable two- and three-qubit errors (the majority voting detects the wrong state and effectively induces a phase flip (4)). A measure of the quality of the implementation is the process fidelity  $F_{\text{proc}}$  which can be directly calculated from the  $\chi$  matrix as  $F_{\text{proc}} = \text{Tr}(\chi \chi_{\text{id}})$ .

This measure does not distinguish between constant operational errors (the wrong operation is performed) and irreversible decoherence, and is thus not an ideal test for the algorithm. A benchmark measure which is only susceptible to decoherence but still closely related to the process fidelity can be generated by maximizing the overlap of the measured process and the ideal process with the help of unitary single-qubit operations. Applying this unitary with angles

$\theta_{x,y,z}$  around the  $x, y, z$  axis leads to a rotated process matrix

$$\chi^{\theta_x, \theta_y, \theta_z} = \left( \prod_{j=\{x,y,z\}} e^{i\theta_j \Sigma_j} \right) \chi \left( \prod_{j=\{x,y,z\}} e^{i\theta_j \Sigma_j} \right)^\dagger.$$

where  $\Sigma_j$  are maps corresponding to the rotation axes. The optimization procedure maximizes then the process fidelity:  $F_{\text{opt}} = \text{Tr}(\chi_{\text{id}} \chi^{\theta_x, \theta_y, \theta_z})$ .

## B.2.2. Gate errors and infidelities

As discussed above, the performance of any quantum process is faithfully given by the process fidelity. In general, a full quantum process tomography (QPT) is necessary to determine this quantity. For the QPT to produce meaningful results, the quality of the operations which are needed for the tomography need to be considerable higher than the quality of the process under investigation. We believe that the fidelity of our single-qubit operations is  $F_{\text{local}} \approx 99\%$ . For the entangling gate we determine the fidelity of a generated entangled state only. The fidelity of the generated Greenberger-Horne-Zeilinger (GHZ) state is  $F_{\text{MS}} \approx 97\%$  (16). Numerical simulations indicate that infidelities are mainly caused by phase-fluctuations due to laser-frequency and magnetic-field fluctuations. One can then naively determine the expected fidelity of the QEC algorithm by multiplying these state fidelities for each implemented operation:

$$F_{\text{QEC}} = F_{\text{MS}}^4 \cdot F_{\text{local}}^5 \approx 84\%$$

The process fidelity of the implemented algorithm is higher than this expected value. This may be because we are not using the full three-qubit Hilbert space but rather a smaller subspace that is restricted to the information of a single qubit.

## B.2.3. QEC and different noise models

In general, phase noise describes a kind of noise that destroys the coherence of a quantum state, but does not change its populations. The amount of phase noise on a single qubit can be described by the phase-flip probability  $p$  that reduces the off-diagonal elements of the density matrix by  $1 - 2p$ . For a completely dephasing process, the phase-flip probability is  $p = 0.5$ .

The noise of a multi-qubit system can be described by considering the correlations between the qubits. If the probabilities  $p_n$  for  $n$  simultaneous phase flips are known for a given noise model, it is straightforward to analyze the performance of the implemented QEC algorithm for this model. The simplest error model includes uncorrelated noise on all qubits. For the three-qubit QEC the probabilities  $p_n$  are then

$$\begin{aligned} p_0 &= (1 - p)^3 \\ p_1 &= 3p(1 - p)^2 \\ p_2 &= 3p^2(1 - p) \\ p_3 &= p^3 \end{aligned}$$

similar to the analysis in Ref. (10) and in chapter 10.3. of Ref. (4). As the QEC algorithm can correct up to one phase flip, the probability of implementing an identity operation is equal to the probability that no error or a single error occurs  $p_{\mathbb{1}} = p_0 + p_1$ . For two and three simultaneous phase flips the majority vote identifies the wrong state so that after the correction cycle the qubit experiences a phase flip. Such uncorrectable errors occur with probability  $p_z = p_2 + p_3$ .

The noise model used above assumes uncorrelated noise on all qubits. On the other hand many systems, including our experimental setup, show correlated noise on all qubits (16). This error model leads to an increased probability for two- and three-qubit errors for a given single-qubit error probability.

This correlated noise process cannot be expressed by phase-flip probabilities  $p_n$  independent of the input states. Therefore it is not possible to reconstruct the performance of the algorithm analogous to the uncorrelated case. Instead, one has to simulate the whole algorithm including correlated noise. This simulation is split into the three steps: i) encoding, ii) error incidence, and iii) decoding. First, the input state  $\rho_{in} = |\psi_{in}\rangle\langle\psi_{in}|$  with  $|\psi_{in}\rangle = (\alpha|0\rangle_q + \beta|1\rangle_q) \otimes |1\rangle_{a1} \otimes |1\rangle_{a2}$  ( $q$  being the system qubit,  $a1$  and  $a2$  the ancillas) is mapped by the unitary operation  $U_{enc}$  (as in figure 3.5c) to the encoded state

$$\rho_{enc} = U_{enc}\rho_{in}U_{enc}^\dagger.$$

Then the correlated noise acts as

$$\rho_{corr} = \int_{\phi=-\infty}^{\infty} \mathcal{N}(\phi, \mathbb{P}) U_{corr}(\phi) \rho_{enc} U_{corr}(\phi)^\dagger d\phi$$

where  $\rho_{corr}$  is the erroneous state,  $U_{corr}(\phi) = e^{i\phi S_z}$  is a global phase rotation with angle  $\phi$  and  $\mathcal{N}(\phi, \mathbb{P})$  is the noise density. Finally, after the decoding stage (with unitary operation  $U_{dec}$  as in figure 3.5c) the decoded state reads

$$\rho_{dec} = U_{dec} \rho_{corr} U_{dec}^\dagger.$$

As we reset the ancilla qubits after the correction cycle, we can neglect their states. Mathematically this can be formulated by tracing over both auxiliary qubits so that we reach the final output state

$$\rho_f = Tr_{2,3}(\rho_{dec}).$$

The full process from the input state  $\rho_i = Tr_{2,3}(\rho_{in})$  to the output state  $\rho_f$  can then be written as

$$\rho_f = (1 - p_z) \cdot \mathbb{1}\rho_i\mathbb{1} + p_z \cdot \sigma_z\rho_i\sigma_z,$$

where  $(1 - p_z)$  is the probability that only correctable errors occur (no error or single-qubit phase-flip errors) while  $p_z$  corresponds to the probability for uncorrectable errors (two- or three-qubit phase flips) in the algorithm. The fidelity of the quantum error correction algorithm is then the overlap with the identity process,  $F = 1 - p_z$ .

A detailed analysis requires to choose a noise density  $\mathcal{N}(\phi, \mathbb{P})$ , for example the cases of Lorentzian ( $\mathcal{N}_L(\phi, \mathbb{P}) = \frac{\mathbb{P}}{\pi} \frac{1}{\mathbb{P}^2 + \phi^2}$ ) and Gaussian ( $\mathcal{N}_G(\phi, \mathbb{P}) = \frac{1}{\sqrt{\pi\mathbb{P}}} e^{-\phi^2/\mathbb{P}^2}$ ) noise distributions. Generally, the fidelity of the QEC algorithm  $F = 1 - p_z(\mathbb{P})$  will depend on the parameter  $\mathbb{P}$  which defines the magnitude of the respective noise. A more accessible parameter is the single-qubit phase-flip

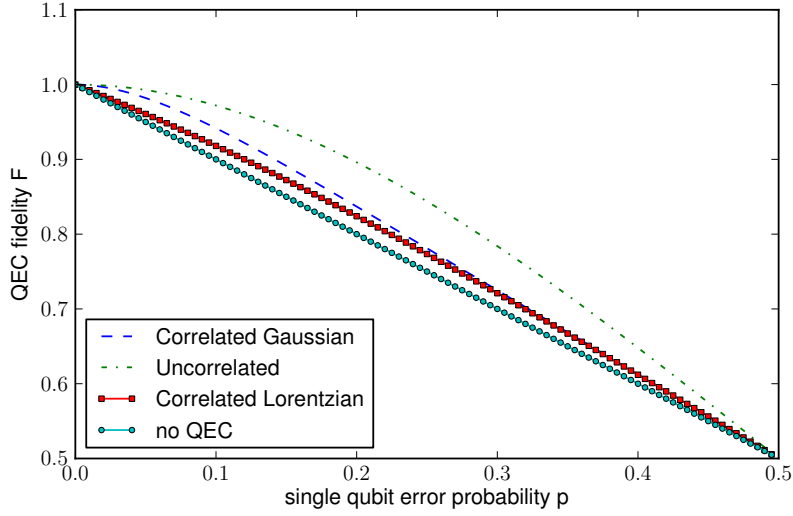


Figure B.2.: Simulated fidelity of a single QEC cycle in the presence of different noise models.

probability  $p$  which is independent of the type of noise and can be directly characterized in the experiment. This probability  $p$  can be defined for the respective noise types by

$$\epsilon_{single}(\rho_i) = (1 - p) \cdot \mathbb{1}\rho_i\mathbb{1} + p \cdot \sigma_z \rho_i \sigma_z = \int_{\phi=-\infty}^{\infty} \mathcal{N}(\phi, \mathbb{P}) U_{\text{corr}}(\phi) \rho_i U_{\text{corr}}(\phi)^\dagger$$

This equation gives a direct relation between  $p$  and  $\mathbb{P}$  which can then be used to eliminate  $\mathbb{P}$ . For correlated Lorentzian noise we then obtain the process fidelity

$$F_{\text{corr, Lorentz}} = 1 - \frac{3}{4}p - \frac{3}{4}p^2 + \frac{1}{2}p^3,$$

and for correlated Gaussian noise

$$F_{\text{corr, Gauss}} = 1 - 9p^2 + 42p^3 - 126p^4 + 252p^5 - 336p^6 + 288p^7 - 144p^8 + 32p^9.$$

In figure B.2 we show the expected fidelity of a perfect QEC cycle in the presence of uncorrelated and, correlated noise with a Lorentzian density as well as correlated noise with a Gaussian density. It is remarkable that for small phase-flip probabilities  $p$ , the fidelity decays linearly with  $p$  for correlated Lorentzian noise, whereas it decays quadratically with  $p$  for correlated Gaussian noise.

## B.2.4. Implementing noise

The main noise source in our experimental system is correlated phase noise. Thus the system can be exposed to a controlled amount of this noise by adding a waiting time between the encoding and the decoding stage. We perform a Ramsey type experiment where the second

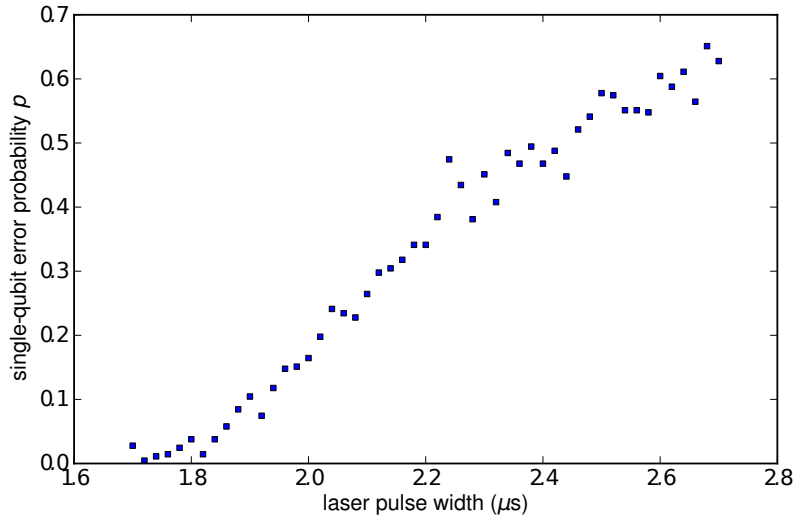


Figure B.3.: Single-qubit phase-flip probability  $p$  as a function of laser pulse duration to induce uncorrelated phase noise.

pulse has an opposite phase to the first pulse (corresponding to the pulses  $X(\pi/2)$  and  $X(-\pi/2)$  separated by a waiting time). A phase flip is then directly mapped into a bit flip which can be easily measured. The single-qubit phase-flip probability  $p$  is then directly determined via the single-qubit excitations and the correlated phase-flip probabilities correspond to their respective bit-flip counterparts. As the noise level in our system fluctuates slowly over time, a frequent recalibration of the delay time is necessary.

Realizing uncorrelated phase noise requires a different approach. It can be shown that projecting a state with probability  $p'$  can be interpreted as phase damping with probability  $p = p'/2$  (4). We realize this measurement by exciting the  $3D_{1/2} \leftrightarrow 4P_{1/2}$  transition with a short ( $\approx 5\mu\text{s}$ ) pulse resonant with this transition. To avoid population loss to the state  $|S'\rangle = 4S_{1/2}(m = +1/2)$  which is outside the computational subspace, an additional optical pumping step is necessary. This technique introduces an additional AC Stark shift, which could in principle be measured and compensated for. In figure B.3 we show the single-qubit error probability as a function of the excitation duration. It can be seen that a delay time of around  $1.6\mu\text{s}$  is introduced by electronic and optical components.

### B.2.5. Determining noise correlations

It was shown above that the scaling of the fidelity of the QEC implementation changes dramatically with different noise densities. We determined the noise in our experimental setup by directly measuring  $p_n(p)$  in a two-qubit system. We use a Ramsey type experiment to measure the correlations of the phase flip probabilities. As noted above, the single-qubit phase-flip probability  $p$  is then directly determined via the single-qubit excitations whereas the correlated phase-flip probabilities  $p_n$  can be determined via the simultaneous  $n$ -qubit excitations. In figure B.4 we

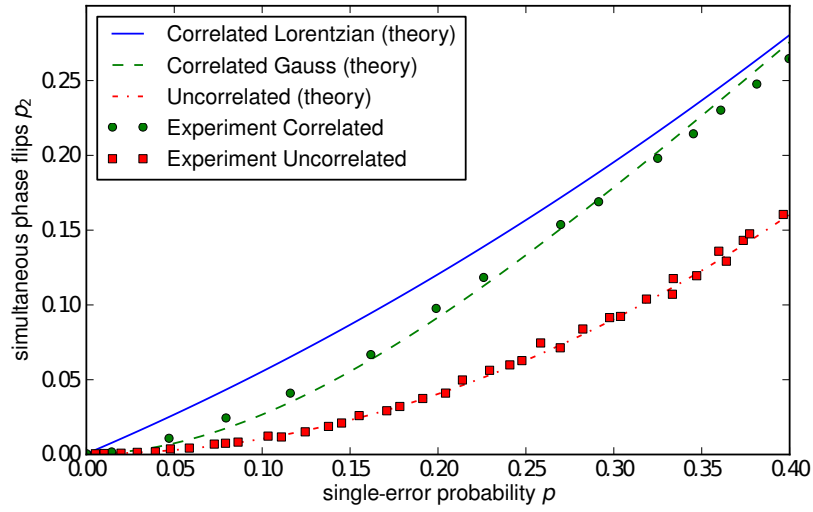


Figure B.4.: Probability of two simultaneous phase flips as a function of single-qubit flip probability  $p$  for different noise sources.

show  $p_2(p)$  for a two qubit system which allows us to confirm the presence of Gaussian correlated noise. With the same analysis we prove that we are able to engineer uncorrelated phase noise with the aid of a weak projection.

## B.3. An Open-System Quantum Simulator with Trapped Ions

### B.3.1. Bell-state pumping

#### Implemented Kraus maps

The Bell state  $|\Psi^-\rangle$  is not only uniquely determined as the simultaneous eigenstate with eigenvalue -1 of the two stabilizer operators  $X_1X_2$  and  $Z_1Z_2$  (as mentioned in the text), but also by  $X_1X_2$  and  $Y_1Y_2$ . In the experiment, we implemented pumping into  $|\Psi^-\rangle$  by engineering the two Kraus maps  $\rho_S \mapsto E_1\rho_S E_1^\dagger + E_2\rho_S E_2^\dagger$  and  $\rho_S \mapsto E'_1\rho_S E'_1{}^\dagger + E'_2\rho_S E'_2{}^\dagger$ , where

$$E_1 = \sqrt{p} Y_1 \frac{1}{2} (1 + X_1 X_2), \quad (\text{B.1})$$

$$E_2 = \frac{1}{2} (1 - X_1 X_2) + \sqrt{1-p} \frac{1}{2} (1 + X_1 X_2) \quad (\text{B.2})$$

$$E'_1 = \sqrt{p} X_1 \frac{1}{2} (1 + Y_1 Y_2), \quad (\text{B.3})$$

$$E'_2 = \frac{1}{2} (1 - Y_1 Y_2) + \sqrt{1-p} \frac{1}{2} (1 + Y_1 Y_2), \quad (\text{B.4})$$

which generate pumping into the -1 eigenspaces of  $X_1X_2$  and  $Y_1Y_2$  (instead of pumping into the eigenspaces of  $X_1X_2$  and  $Z_1Z_2$  as explained in Box 1 of the main text). The reason for pumping into the eigenspaces of  $X_1X_2$  and  $Y_1Y_2$  is that the mapping and unmapping steps, shown as (i) and (iii) in Box 1, are realized by a single MS gate  $U_{X^2}(\pi/2)$  and  $U_{Y^2}(\pi/2)$ , respectively.

#### Circuit decomposition

The map for pumping into the -1 eigenspace of  $X_1X_2$  can be realized by the unitary

$$U_{X^2(\pi/2)} C(p) U_{X^2(\pi/2)} \quad (\text{B.5})$$

(corresponding to steps (i) - (iii) in Box 1) followed by optical pumping of the ancilla qubit to  $|1\rangle$ . Here, the two-qubit controlled gate is

$$\begin{aligned} C(p) &= |0\rangle\langle 0|_0 \otimes \exp(i\alpha Z_1) + |1\rangle\langle 1|_0 \otimes \mathbb{1} \\ &= \exp\left[\frac{1}{2}(1 + Z_0)i\alpha Z_1\right] \\ &= U_{Z_1}(-\alpha) U_Y(\pi/2) U_{X^2}^{(0,1)}(-\alpha) U_Y(-\pi/2) \end{aligned} \quad (\text{B.6})$$

where  $U_{X^2}^{(0,1)}(-\alpha) = \exp(i(\alpha/2)X_0X_1)$  denotes an MS gate acting only on the ancilla and the first system qubit. This two-qubit MS gate operation was implemented in the experiment by the use of refocusing techniques [33]. In more detail, the gate  $U_{X^2}^{(0,1)}$  was realized by interspersing two of the available three-qubit MS gate operations with single-ion light shifts on the

second system qubit which induces a  $\pi$ -phase shift between the qubit states. Alternatively, this refocusing could be avoided, and the sequences further simplified, by hiding the population of individual ions (here the second system ion) which are not supposed to participate in collective coherent operations in electronic levels decoupled from the driving laser excitation. More details on how to systematically decompose Kraus maps into the experimentally available ion-trap gate operations, in particular the multi-ion MS entangling gate, can be found in [55].

The circuit decompositions for the actual experimental implementation of the two maps are shown in Fig. B.5. They differ from the two quantum operations, which are specified in Eqs. (B.1)-(B.4), by two single-ion rotations. They arise since the circuit has been slightly modified (by changing the phase of one of the global  $Y$ -rotations) at the expense of implementing in addition in each dissipative map a flip operation  $Y_1 Y_2$  on the two system qubits. However, as this additional unitary corresponds to one of the stabilizers into whose -1 eigenspace the pumping is performed, this does not interfere with the pumping dynamics.

Pumping with unit pumping probability  $p = 1$  corresponds to  $\alpha = \pi/2$ , whereas  $p = 0.5$  is realized by setting  $\alpha = \pi/4$ . In the experiment, the "fundamental" MS gate was calibrated to implement  $U_{X^2}(\alpha/2)$ . The fully entangling operation  $U_{X^2}(\pi/2)$  at the beginning and the end of the sequence Fig. B.5a was then implemented by applying the  $U_{X^2}(\alpha/2)$  operation twice (for  $p = 1$ ) or four times (for  $p = 0.5$ ). The fully entangling operations  $U_{Y^2}(\pi/2)$  in Fig. B.5b were implemented by two- and four-fold application of the "fundamental" MS gate with a shifted optical phase of the driving laser (cf. Section 4.2.2 in the main text).

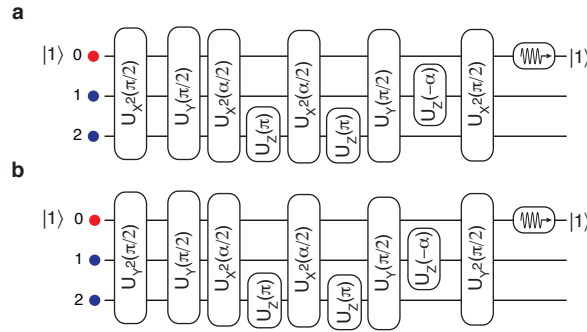


Figure B.5.: **Experimental sequences for Bell-state pumping.** Pumping into the eigenspaces of eigenvalue -1 of  $X_1 X_2$  (circuit **a**), and  $Y_1 Y_2$  (circuit **b**), occurs with a probability  $p$  in each step, where  $\sin^2 \alpha = p$ . The circuit is up to two local rotations equivalent to the quantum operations specified in Eqs. (B.1)-(B.4).

## Towards master equation dynamics

For an implementation of pumping dynamics with small pumping probabilities  $p \ll 1$ , described by a multi-qubit master equation with two-qubit quantum jump operators, several requirements have to be met:

From a practical point of view, to reach the desired target Bell state via pumping with small

pumping probabilities  $p$  requires increased gate fidelities as more time steps are needed to come close to the steady state of the repeated pumping dynamics. This implies that processes, such as e.g. decay of population into decoupled electronic states, which correspond to “leakage” out of the logical Hilbert space, have to be kept small after a larger number of gate operations. More fundamentally, even in the absence of these leakage processes, the errors in the implementation of the dissipative maps eventually hinder the system from coming arbitrarily close to the target state. Loosely speaking, one can think of the ideal dissipative dynamics as describing an infinite set of non-reversible paths along which any initial state is pumped towards the desired target state. Deviations from the ideal path during the preparation due to implementation errors and other disturbances then place the system onto points in Hilbert space, which differ from the ideally expected ones. From there, the system “gets a new chance” and is again attracted towards the target state under subsequent dissipative operations. However, as the system approaches the vicinity of the target state, the errors hinder the system from coming closer and closer to the target state. Here, a balance between pumping towards and repulsion from the target state builds up, which is closely related to the error level and the chosen pumping probability: here the pumping rate  $p$  for populating the target state competes with the loss processes at a rate  $\epsilon$  due to implementation errors. This competition leads to a steady state infidelity scaling as  $\propto \epsilon/p$ .

In the experiment on Bell state pumping into  $|\Psi^-\rangle$  at a pumping rate  $p = 0.5$ , we have carried out up to three and a half pumping cycles and observed that the two system qubits reached a maximum overlap fidelity with the target Bell state of 73(1)% after three pumping cycles.

### Further experimental details

As mentioned in the main text, fully mixed states of two and four qubits were prepared by a dissipative process based on optical pumping. First, every system qubit, initially prepared in  $|0\rangle$ , is coherently transferred to  $(|0\rangle + |S'\rangle)/\sqrt{2}$  via a  $\pi/2$  laser pulse on the quadrupole transition, where  $|S'\rangle$  is the electronic level  $S_{1/2}(m = 1/2)$ . Subsequently, optical pumping of the population in  $|S'\rangle$  into  $|1\rangle$  creates a state where the coherence between the resulting populations in  $|0\rangle$  and  $|1\rangle$  is completely destroyed.

The initial two-qubit mixed state was prepared with a fidelity of  $F=99.6(3)\%$  with respect to the ideal state  $\frac{1}{4}\mathbb{1}_{4\times 4}$ .

Physical process matrices were reconstructed with maximum likelihood techniques [34]. An error analysis was carried out via Monte Carlo simulations over the multinomially distributed measurement outcomes of the state and process tomography. For each process and state, 200 Monte Carlo samples were generated and reconstructed via maximum-likelihood estimation.

### B.3.2. Four-qubit stabilizer pumping

Expectation values of the stabilizer operators  $Z_1Z_2$ ,  $Z_2Z_3$ ,  $Z_3Z_4$  and  $X_1X_2X_3X_4$  were not determined from the reconstructed density matrices of the system qubits. Instead, we performed fluorescence measurements in the  $X$  and  $Z$  basis on 5250 copies of the corresponding quantum

states (for  $p = 0.5$  pumping, 2100 copies were measured). The error bars were then determined from the multinomially distributed raw data.

## Pumping

Pumping into the GHZ state  $(|0000\rangle + |1111\rangle)/\sqrt{2}$  was realized by a pumping cycle where the four system qubits were deterministically pumped into the +1 eigenspaces of the stabilizers  $Z_1Z_2$ ,  $Z_2Z_3$ ,  $Z_3Z_4$  and  $X_1X_2X_3X_4$ .

The ideal dissipative Kraus map describing the first three pumping steps into the +1 eigenspace of  $Z_1Z_2$ ,  $Z_2Z_3$  and  $Z_3Z_4$  read  $\rho_S \mapsto \mathcal{E}_{Z_iZ_j}^{\text{id}}(\rho_S) = E_1\rho_S E_1^\dagger + E_2\rho_S E_2^\dagger$  with

$$E_1 = \frac{1}{2}(1 + Z_iZ_j), \quad (\text{B.7})$$

$$E_2 = \frac{1}{2}X_j(1 - Z_iZ_j), \quad (\text{B.8})$$

for  $(i, j = 12, 23, 34)$ . The Kraus maps are constructed such that the +1 eigenspace of  $Z_iZ_j$  is left invariant, whereas a spin flip  $X_j$  on the second spin (index  $j$ ) converts with unit probability -1 into +1 eigenstates.

The dissipative map for pumping into the +1 eigenspace of, e.g.,  $Z_1Z_2$  could be achieved in complete analogy with Bell state pumping, i.e. by effectively only implementing operations on the ancilla qubit and the system qubits #1 and #2, whereas the system qubits #3 and #4 remain completely unaffected. This could either be achieved through refocusing techniques or by hiding system ions #3 and #4 in electronically decoupled states for the duration of the dissipative circuit.

In the experiment, however, we used a few simplifications that allowed us to simplify the employed circuits. These are schematically shown in Fig. B.6 and listed below:

- For deterministic pumping ( $p = 1$ ), the inverse mapping step (shown in Box 1) is not necessary and has been taken out.
- In the coherent mapping step (shown in Box 1) the information about whether the system ions are in a  $\pm 1$  eigenstate of  $Z_1Z_2$  is mapped onto the logical states of the ancilla qubit. This step ideally only involves the ancilla and the system qubits #1 and #2. One way to achieve this three-qubit operation without affecting the system qubits #3 and #4, is to combine the available five-ion MS gate with appropriately chosen refocusing pulses, i.e. light shift operations on individual ions. Those would have to be chosen such that ions #0, #1 and #2 become decoupled from ions #3 and #4, and furthermore residual interactions between ions #3 and #4 cancel out. However, it turns out that residual interactions between ions #3 and #4 can be tolerated: although not required for the  $Z_1Z_2$ -pumping dynamics, they are not harmful, as they do not alter the expectation values of the other two-qubit stabilizers  $Z_2Z_3$  and  $Z_3Z_4$ . In our experiment the decoupling of ions #0, #1 and #2 from the ions #3 and #4 was achieved by the circuit shown in Fig. B.6b.

The additional interactions in the pumping of the two-qubit stabilizer operators  $Z_iZ_j$  affect the state of the system qubits with respect to the four-qubit stabilizer  $X_1X_2X_3X_4$ .

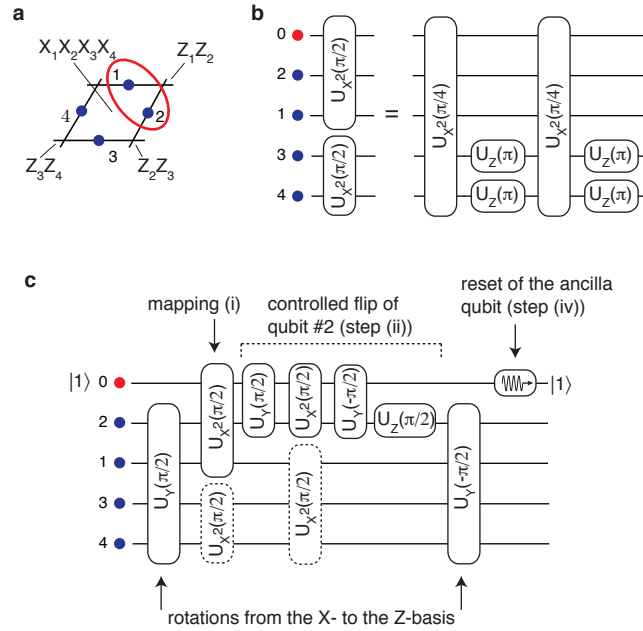


Figure B.6.: **Pumping into the +1 eigenspace of the  $Z_1 Z_2$  stabilizer operator** **a**, Ideally, only the ancilla qubit and the two system qubits #1 and #2 are involved in the circuit. **b**, An entangling gate acting on these three ions can be achieved by a refocusing technique, where ions #3 and #4 decouple from the dynamics. However, the latter ions still become entangled. However, these residual interactions are not harmful to the pumping, as they do not affect the expectation values of the other two-qubit stabilizer operators. **c**, Dashed operations in the quantum circuit indicate such residual entangling operations.

However, this effect is not detrimental to the pumping, provided the pumping into the eigenspace of  $X_1 X_2 X_3 X_4$  is performed as the final step in the pumping cycle.

- In the employed sequence, the number of single-qubit rotations was reduced wherever possible. Essential single-qubit light shift operations, such as those needed for re-focusing operations, were kept.
- Local rotations of the system ions at the end of a pumping step, which would be compensated at the beginning of the subsequent pumping step, were omitted when several dissipative maps were applied in a row. The corresponding gate operations of the sequences are displayed in blue in Steps 1-3.

These simplifications allowed us to significantly reduce the length and complexity of the employed gate sequences for one stabilizer pumping step. As a consequence, the actual Kraus map for pumping into the +1 eigenspace of the stabilizer operator  $Z_1 Z_2$  as implemented in the

## B. Supplementary information

---

experiment is  $\rho_S \mapsto \mathcal{E}_{Z_i Z_j}^{\text{exp}}(\rho_S) = E_1 \rho_S E_1^\dagger + E_2 \rho_S E_2^\dagger$  with

$$E_1 = X_1 X_2 \left( \tilde{A} - Z_1 \tilde{S} \right) X_2 \frac{1}{2} (1 - Z_1 Z_1), \quad (\text{B.9})$$

$$E_2 = \left( X_1 X_2 \tilde{S} + \frac{i}{2} (X_1 Y_2 + Y_1 X_2) \tilde{A} \right) \frac{1}{2} X_2 (1 - Z_1 Z_2), \quad (\text{B.10})$$

where

$$\tilde{S} = X_3 X_4 + Y_3 Y_4 \quad \text{and} \quad \tilde{A} = X_3 Y_4 + Y_3 X_4. \quad (\text{B.11})$$

This quantum operation differs from the ideal Kraus map specified in Eqs. (B.7) and (B.8) by combinations of additional simultaneous  $X$  and  $Y$ -type spin flips on all four system spins. As explained above, these additional terms do not interfere with the  $Z_i Z_j$  pumping dynamics, as any four-spin operator, which is built up by a product of either  $X$  or  $Y$  for each of the four spins commutes with the  $Z$ -type two-body stabilizers, e.g.  $[X_1 X_2 Y_3 Y_4, Z_i Z_j] = 0$ .

The experimental Kraus maps for pumping into the +1 eigenspaces of  $Z_2 Z_3$  and  $Z_3 Z_4$  are obtained from Eqs. (B.9)-(B.11) by applying the corresponding permutation of system spin indices.

The fourth dissipative step, which realizes pumping into the +1 eigenspace of  $X_1 X_2 X_3 X_4$ , is described by the ideal and also experimentally implemented Kraus map  $\rho_S \mapsto \mathcal{E}_{X_1 X_2 X_3 X_4}^{\text{exp}}(\rho_S) = E_1 \rho_S E_1^\dagger + E_2 \rho_S E_2^\dagger$  with

$$E_1 = \frac{1}{2} (1 + X_1 X_2 X_3 X_4), \quad (\text{B.12})$$

$$E_2 = \frac{1}{2} Z_4 (1 - X_1 X_2 X_3 X_4). \quad (\text{B.13})$$

The gate sequences, which have been used in the experiment to implement these Kraus maps are explicitly given below:

Step 1 (pumping into the +1 eigenspace of  $Z_1 Z_2$ ):

$$\begin{aligned} & U_Y(-\pi/2) U_{Z_2}(-\pi/2) \\ & U_X(\pi/2) U_{Z_2}(-\pi/2) U_X(-\pi/2) \\ & U_{Z_1}(\pi) U_{X^2}(\pi/4) U_{Z_2}(\pi) U_{Z_0}(\pi) U_{X^2}(\pi/4) \\ & U_X(-\pi/2) U_{Z_2}(-\pi/2) U_{Z_0}(-\pi/2) U_X(\pi/2) \\ & U_{X^2}(\pi/4) U_{Z_4}(\pi) U_{Z_3}(\pi) U_{X^2}(\pi/4) \\ & U_Y(\pi/2) U_X(-\pi/2) U_{Z_0}(-\pi/2) U_X(\pi/2) \end{aligned}$$

Step 2 (pumping into the +1 eigenspace of  $Z_2 Z_3$ ):

$$\begin{aligned} & U_Y(-\pi/2) U_{Z_3}(-\pi/2) \\ & U_X(\pi/2) U_{Z_3}(-\pi/2) U_X(-\pi/2) \\ & U_{Z_2}(\pi) U_{X^2}(\pi/4) U_{Z_3}(\pi) U_{Z_0}(\pi) U_{X^2}(\pi/4) \\ & U_X(-\pi/2) U_{Z_3}(-\pi/2) U_{Z_0}(-\pi/2) U_X(\pi/2) \\ & U_{X^2}(\pi/4) U_{Z_4}(\pi) U_{Z_1}(\pi) U_{X^2}(\pi/4) \\ & U_Y(\pi/2) U_X(-\pi/2) U_{Z_0}(-\pi/2) U_X(\pi/2) \end{aligned}$$

Step 3 (pumping into the +1 eigenspace of  $Z_3Z_4$ ):

$$\begin{aligned}
 & U_Y(-\pi/2) U_{Z_4}(-\pi/2) \\
 & U_X(\pi/2) U_{Z_4}(-\pi/2) U_X(-\pi/2) \\
 & U_{Z_3}(\pi) U_{X^2}(\pi/4) U_{Z_4}(\pi) U_{Z_0}(\pi) U_{X^2}(\pi/4) \\
 & U_X(-\pi/2) U_{Z_4}(-\pi/2) U_{Z_0}(-\pi/2) U_X(\pi/2) \\
 & U_{X^2}(\pi/4) U_{Z_2}(\pi) U_{Z_1}(\pi) U_{X^2}(\pi/4) \\
 & U_Y(\pi/2) U_X(-\pi/2) U_{Z_0}(-\pi/2) U_X(\pi/2)
 \end{aligned}$$

Step 4 (pumping into the +1 eigenspace of  $X_1X_2X_3X_4$ ):

$$\begin{aligned}
 & U_X(-\pi/2) \\
 & U_{Z_4}(-\pi/2) U_X(\pi/2) U_{Z_4}(-\pi/2) \\
 & U_{X^2}(\pi/4) U_{Z_4}(\pi) U_{Z_0}(\pi) U_{X^2}(\pi/4) \\
 & U_{Z_4}(-\pi/2) U_X(-\pi/2) U_{Z_0}(-\pi/2) U_X(\pi/2) \\
 & U_{X^2}(\pi/4) U_{X^2}(\pi/4)
 \end{aligned}$$

Figure B.14 shows the reconstructed density matrices (real and imaginary parts) for every step of the pumping cycle. The complete circuit decomposition of one pumping cycle involves 16 five-ion entangling operations, 28 (20) collective unitaries and 36 (34) single-qubit operations with (without) optional operations in blue. The reset operation involves further pulses not accounted for above.

### Repeated four-qubit stabilizer pumping

To study the robustness of the dissipative operation, we prepared the initial state  $|1111\rangle$  and subsequently applied repeatedly the dissipative map for pumping into the +1 eigenspace of the four-qubit stabilizer  $X_1X_2X_3X_4$ . We observed that after a single dissipative step a non-zero expectation value of  $X_1X_2X_3X_4$  built up and stayed constant under subsequent applications of this dissipative map. However, due to imperfections in the gate operations, the expectation values of the two-qubit stabilizers decreased, ideally they should not be affected by the  $X_1X_2X_3X_4$ -pumping step (see Fig. B.7). Interestingly, the expectation values of  $Z_1Z_4$  and  $Z_3Z_4$  decayed significantly faster than those for  $Z_1Z_2$  and  $Z_2Z_3$ . This decay can be explained by the fact that in the gate sequence used for pumping into the +1 eigenspace of  $X_1X_2X_3X_4$ , step 4 above, single-ion light-shift operations are applied only to the fourth system qubit and the ancilla. This indicates that errors in the single-qubit gates applied to the fourth system ion accumulate under the repeated application of the dissipative step, and thus affect the stabilizers  $Z_1Z_4$  and  $Z_3Z_4$  which involve this system qubit more strongly than the others. This destructive effect can be minimized by alternating the roles of the system qubits.

Such optimization has been done for the dissipative dynamics shown in Fig. B.8. Here, starting from the initial state  $|1111\rangle$ , repeated pumping into the -1 eigenspace of  $X_1X_2X_3X_4$  has been implemented by the sequence

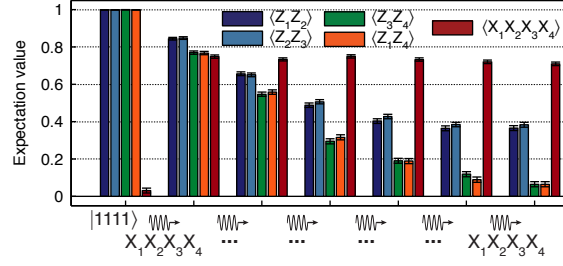


Figure B.7.: **Measured expectation value of stabilizers for repeated pumping without sequence optimization.** The expectation values of  $Z_1Z_4$  and  $Z_3Z_4$  show a significantly faster decay than those for  $Z_1Z_2$  and  $Z_2Z_3$ . In every step of the pumping, most single-ion light-shift operations are applied to the fourth system qubit.

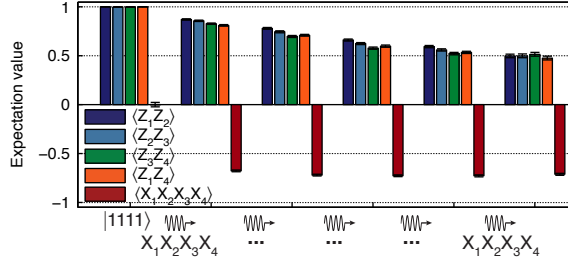


Figure B.8.: **Measured expectation value of stabilizers for repeated pumping with sequence optimization.** All two-qubit stabilizers decay at the same rate during pumping. In step 1,2,3,4, and 5 the single-qubit light-shift operations were applied on the system qubits 4,3,2,1, and 1, respectively.

$$\begin{aligned}
 & U_{X^2}(\pi/8) U_{X^2}(\pi/8) U_{X^2}(\pi/8) U_{X^2}(\pi/8) \\
 & \quad U_X(-\pi/2) \\
 & \quad U_{Z_4}(-\pi/2 \times p) U_X(\pi/2) U_{Z_4}(\pi) \\
 & U_{Y^2}(\pi/4 \times p) U_{Z_0}(\pi) U_{Z_4}(\pi) U_{Y^2}(\pi/4 \times p) \\
 & \quad U_Y(\pi/2) U_{Z_0}(-\pi/2) U_Y(-\pi/2) \\
 & U_{X^2}(\pi/8) U_{X^2}(\pi/8) U_{X^2}(\pi/8) U_{X^2}(\pi/8).
 \end{aligned}$$

Here, we observed that indeed the expectation values of all two-qubit stabilizers decreased at the same pace and at a slightly slower rate (see Fig. B.8). Upon repeating the sequence above 1,2,3,4, and 5 times, we changed the operations shown in red to act on qubits 4,3,2,1, and 1, respectively. The stabilizer expectation values for deterministic pumping, or  $p = 1$ , are shown in Fig. B.8.

## Pushing “anyons” around

In Kitaev’s toric code [144], spins are located on the edges of a two-dimensional square lattice. The Hamiltonian

$$H = -g\left(\sum_p A_p + \sum_v B_v\right) \quad (\text{B.14})$$

is a sum of mutually commuting four-qubit stabilizers  $A_p = \prod_{i \in p} X_i$  and  $B_v = \prod_{i \in v} Z_i$ , which describe four-spin interactions between spins located around plaquettes  $p$  and vertices  $v$  of the lattice. The ground state of the Hamiltonian is the simultaneous +1 eigenstate of all stabilizer operators. The model supports two types of excitations that obey anyonic statistics under exchange (braiding), and they correspond to -1 eigenstates of either plaquette or vertex stabilizers.

For a minimal instance of this model, represented by a single plaquette of four spins located on the edges, the Hamiltonian contains a single four-qubit interaction term  $X_1 X_2 X_3 X_4$  and pairwise two-spin interactions  $Z_i Z_j$  of spins sharing a corner of the plaquette. The ground state as the simultaneous +1 eigenstate of these stabilizers is the GHZ-state  $(|0000\rangle + |1111\rangle)/\sqrt{2}$ . States corresponding to -1 eigenvalues of a two-qubit stabilizer  $Z_i Z_j$  can be interpreted as a configuration with an excitation located at the corner between the two spins  $i$  and  $j$ . Similarly, a four-qubit state with an eigenvalue of -1 with respect to  $X_1 X_2 X_3 X_4$ , would correspond to an anyonic excitation located at the center of the plaquette.

In the experiment we prepared an initial state  $|0111\rangle$  and then performed the pumping cycle of four deterministic pumping steps into the +1 eigenspaces of  $Z_1 Z_2$ ,  $Z_2 Z_3$ ,  $Z_3 Z_4$  and  $X_1 X_2 X_3 X_4$ , using the sequences for Steps 1 to 4 given in section B.3.2. The expectation values of the stabilizer operators for the initial state and the four spins after each pumping step are shown in Fig. B.9. The dissipative dynamics can be visualized as follows: For the initial state with  $\langle Z_1 Z_2 \rangle = -1$  and  $\langle Z_1 Z_4 \rangle = -1$  a pair of excitations is located on the upper left and right corners of the plaquette, whereas  $\langle X_1 X_2 X_3 X_4 \rangle = 0$  implies an anyon of the other type is present at the center of the plaquette with a probability 50%. In the first pumping step, where the first two spins are pumped into the +1 eigenspace of  $Z_1 Z_2$ , the anyon at the upper right corner is dissipatively pushed to the lower right corner of the plaquette. In the third step of pumping into the +1 eigenspace of  $Z_3 Z_4$ , the two excitations located on the upper and lower lefts corners fuse and disappear from the system. In the final step of pumping into the +1 eigenspace of  $X_1 X_2 X_3 X_4$ , the anyon with a probability of 50% at the center of the plaquette is pushed out from the plaquette.

However, we’d like to stress that borrowing concepts from topological spin models, such as anyonic excitations, here is merely a convenient language to phrase and visualize the dissipative dynamics. In the present work with up to five ions, we do *not* explore the physics of topological spin models, since (i) in a minimal system of four spins the concepts developed for larger lattice models become questionable, and more importantly, (ii) during the implemented pumping dynamics the underlying (four-body) Hamiltonian of the model was not present. We rather demonstrate the basic tools which will allow one to explore this physics once larger, two-dimensional systems become available in the laboratory.

We note that photon experiments have reported the observation of correlations compatible with

the manipulations of “anyons” in a setup representing two plaquettes [182, 183]. Such experiments are based on postselection of measurements [as in teleportation by 184], which should be contrasted to our deterministic implementation of open system dynamics to prepare and manipulate the corresponding quantum state [as in deterministic teleportation by 185, 186].

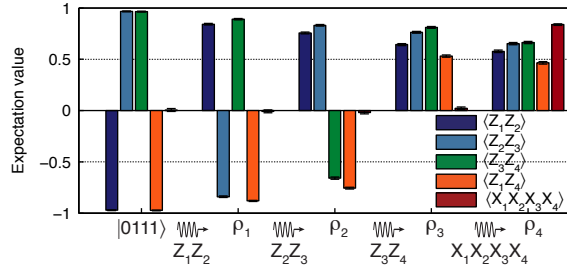


Figure B.9: **Pushing “anyons” around by dissipation.** Measured expectation values of stabilizer operators for pumping dynamics of pumping into the +1 eigenspaces of  $Z_1Z_2$ ,  $Z_2Z_3$ ,  $Z_3Z_4$  and  $X_1X_2X_3X_4$ , starting in the state  $|0111\rangle$ .

### Pumping into “excited” states

Starting from an initially fully mixed state of four qubits, we also implemented pumping into a different GHZ-type state,  $(|0010\rangle - |1101\rangle)/\sqrt{2}$ , by a sequence of four dissipative steps: 1) pumping into the +1 eigenspace of  $Z_1Z_2$ , 2) pumping into the -1 eigenspace of  $Z_2Z_3$ , 3) pumping into the -1 eigenspace of  $Z_3Z_4$  and 4) pumping into the -1 eigenspace of  $X_1X_2X_3X_4$ . In the context of Kitaev’s toric code, this state would correspond to an excited state. However, as above, we point out that the underlying Hamiltonian was not implemented in the pumping dynamics.

The measured expectation values of the stabilizers are shown in Fig. B.10. The final density matrix, as determined from quantum state tomography after the four pumping steps, is shown in Fig. B.11. This pumping cycle was implemented with the same sequences as given for Step 1 to 4 in section B.3.2, with the only difference that the sign of the phase shift operations displayed in red was changed in Steps 2, 3, and 4. This allowed us to invert the pumping direction from the +1 into -1 eigenspaces of  $Z_2Z_3$ ,  $Z_3Z_4$  and  $X_1X_2X_3X_4$ .

### B.3.3. QND measurement of a four-qubit stabilizer

#### Further details

As shown in Fig. B.12, the QND measurement involves a mapping step where the information about whether the system described by an input density matrix  $\rho^{\text{in}}$  is in the +1 / -1 eigenspace of  $A = X_1X_2X_3X_4$  is coherently mapped onto the internal states  $|0\rangle$  and  $|1\rangle$  of the ancilla qubit, which is initially prepared in  $|1\rangle$ . Subsequently the ancilla qubit is measured in its computational basis, leaving the system qubits in a corresponding output state  $\rho^{\text{out}}$ .

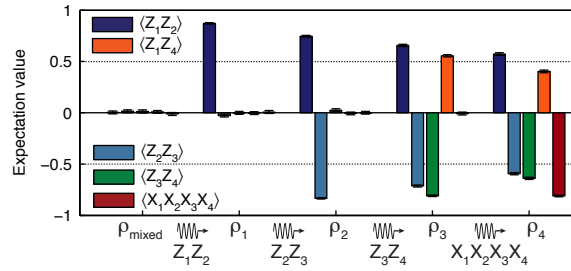


Figure B.10.: **Pumping into an “excited” state.** Measured expectation values of two- and four-qubit stabilizer operators for pumping into the state  $(|0010\rangle - |1101\rangle)/\sqrt{2}$ , starting from an initially four-qubit mixed state.

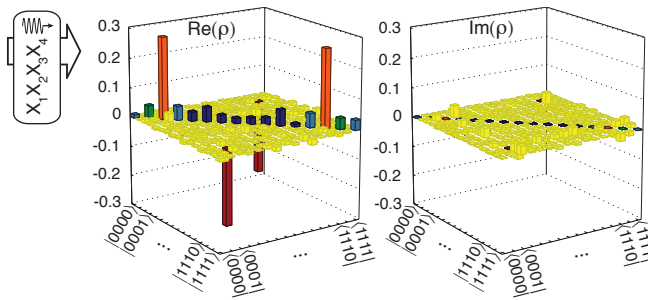


Figure B.11.: **Reconstructed density matrix after the full pumping cycle for dissipative preparation of the state  $(|0010\rangle - |1101\rangle)/\sqrt{2}$ .** This final state has a fidelity of 60(2)% with the expected state. This fidelity was determined from parity and coherence measurements and analysed with bayesian inference techniques as done in [23].

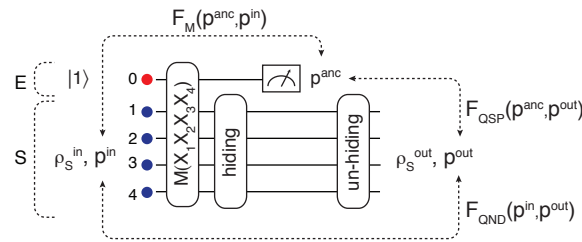


Figure B.12.: **QND measurement of the four-qubit stabilizer operator  $X_1X_2X_3X_4$ .** After the coherent mapping  $M(X_1X_2X_3X_4)$ , the ancilla qubit is measured. This measurement was performed both with and without applying additional pulses to hide the populations of the system qubits in electronically uncoupled states for the duration of the fluorescence measurement on the ancilla.

The coherent mapping  $M(X_1X_2X_3X_4)$  was realized by the sequence

$$\begin{aligned}
 & U_X(\pi/4)U_{Z_0}(\pi)U_X(-\pi/4) \\
 & U_{X^2}(\pi/4)U_{X^2}(\pi/4)U_{Z_0}(-\pi/2)U_{X^2}(\pi/4)U_{X^2}(\pi/4) \\
 & U_Y(-\pi/4)U_{Z_0}(\pi)U_Y(\pi/4)
 \end{aligned}$$

which implements

$$M(X_1X_2X_3X_4) = -\frac{i}{\sqrt{2}}(X_0 + Y_0) \otimes P_+ + \frac{1}{\sqrt{2}}(1 - iZ_0) \otimes P_-, \quad (\text{B.15})$$

with  $P_{\pm} = \frac{1}{2}(1 \pm X_1X_2X_3X_4)$  the projectors onto the  $\pm 1$  eigenspaces of  $X_1X_2X_3X_4$ . Equation (B.25) shows that for the system qubits being in a state belonging to the +1 eigenspace of the stabilizer operator, the ancilla is flipped from  $|1\rangle$  to  $|0\rangle$ , whereas it remains in its initial state  $|1\rangle$  otherwise.

Subsequently, the ancilla as well as the four system qubits were measured. This was done by measuring the five ions simultaneously. Alternatively, we first hid the four system qubits in electronic levels decoupled from the laser excitation, performed the fluorescence measurement of the ancilla qubit, then recovered the state of the system qubits and tomographically measured the state of the four system qubits. The second approach, where the state of the system is not affected by the measurement of the ancilla, is of importance if the information from the ancilla measurement is to be used for feedback operations on the state of the system.

### Quantitative analysis of the performance

To characterize the performance of a QND measurement for a (multi-)qubit system, a set of requirements and corresponding fidelity measures have been discussed in the literature [155].

(1) First of all, the measurement outcomes for the ancilla qubit should agree with those that one would expect from a direct measurement of the observable  $A$  on the input density matrix. This property can be quantified by the *measurement fidelity*,

$$F_M = \left( \sqrt{p_+^{\text{in}} p_{|0\rangle}^{\text{m}}} + \sqrt{p_-^{\text{in}} p_{|1\rangle}^{\text{m}}} \right)^2, \quad (\text{B.16})$$

which measures the correlations of the distribution of measurement outcomes  $p^{\text{m}} = \{p_{|0\rangle}^{\text{m}}, p_{|1\rangle}^{\text{m}}\}$  of the ancilla qubit with the expected distribution  $p^{\text{in}} = \{p_+^{\text{in}}, p_-^{\text{in}}\}$  directly obtained from  $\rho^{\text{in}}$ , where  $p_{\pm}^{\text{in}} = \text{Tr}\{\frac{1}{2}(1 \pm A)\rho^{\text{in}}\}$ .

(2) The QND character, reflected by the fact that the observable  $A$  to be measured should not be disturbed by the measurement itself, becomes manifest in ideally identical probability distributions  $p^{\text{in}}$  and  $p^{\text{out}}$ , which are determined from the input and output density matrices. These correlations are quantified by the *QND fidelity*

$$F_{\text{QND}} = \left( \sqrt{p_+^{\text{in}} p_+^{\text{out}}} + \sqrt{p_-^{\text{in}} p_-^{\text{out}}} \right)^2, \quad (\text{B.17})$$

where  $p_{\pm}^{\text{out}} = \text{Tr}\{\frac{1}{2}(1 \pm A)\rho^{\text{out}}\}$ .

(3) Finally, by measuring the ancilla qubit the system qubits should be projected onto the corresponding eigenspace of the measured observable  $A$ . Thus the quality of the QND measurement

as a quantum state preparation (QSP) device is determined by the correlations between the ancilla measurement outcomes and the corresponding system output density matrices. It can be described by the *QSP fidelity*

$$F_{\text{QSP}} = p_{+}^{\text{m}} p_{|0\rangle,+}^{\text{out}} + p_{-}^{\text{m}} p_{|1\rangle,-}^{\text{out}}, \quad (\text{B.18})$$

where  $p_{|0/1\rangle,\pm}^{\text{out}}$  denotes the conditional probability of finding the system qubits in the +1 (-1) eigenspace of  $A$ , provided the ancilla qubit has been previously measured in  $|0\rangle$  ( $|1\rangle$ ).

The probability distributions for the system input and output states, the ancilla measurement outcome distributions, and the resulting fidelity values are summarized in Tables I to IV. The input states had a fidelity [117] with the ideal states  $(|0000\rangle + |1111\rangle)/\sqrt{2}$ ,  $(|0000\rangle - |1111\rangle)/\sqrt{2}$  and  $(|0011\rangle - |1100\rangle)/\sqrt{2}$  of 75.3(9), 77.3(8), 93.2(4)%.

We observe that we obtain higher values for the measurement and QND fidelities than for the QSP fidelities. The latter is relevant in the context of quantum error correction or closed-loop simulation protocols or more generally whenever the information from the ancilla measurement is used for further processing of the system output state.

With the additional hiding and unhiding pulses before and after the measurement of the ancilla we observe a loss of fidelity of a few percent in the QSP fidelities.

## B. Supplementary information

Table B.9.: QND probability distributions. Obtained from measurements **with** hiding of the system ions during the measurement of the ancilla.

input state	eigen-space	$p_{in}^m$	$p_{out}^m$	$p^{in}$	$p_{m=0}^{in}$	$p_{m=1}^{in}$	$p^{out}$	$p_{m=0}^{out}$	$p_{m=1}^{out}$
0000⟩ +  1111⟩	+1	0.959(1)	0.847(3)	0.817(9)	0.822(9)	0.618(34)	0.689(12)	0.736(12)	0.359(34)
	-1	0.041(1)	0.153(3)	0.183(9)	0.178(9)	0.382(34)	0.311(12)	0.264(12)	0.641(34)
0000⟩ -  1111⟩	+1	0.955(1)	0.169(3)	0.191(10)	0.187(9)	0.328(36)	0.310(11)	0.640(26)	0.242(12)
	-1	0.045(1)	0.831(3)	0.809(10)	0.813(9)	0.672(36)	0.690(11)	0.360(26)	0.758(12)
0011⟩ -  1100⟩	+1	0.978(1)	0.103(2)	0.041(4)	0.035(4)	0.412(47)	0.137(9)	0.476(36)	0.097(7)
	-1	0.022(1)	0.897(2)	0.959(4)	0.965(4)	0.588(47)	0.863(9)	0.524(36)	0.903(7)

Table B.10.: QND probability distributions. Obtained from measurements **without** hiding of the system ions during the measurement of the ancilla.

input state	eigenspace	$p_{out}^m$	$p^{out}$	$p_{m=0}^{out}$	$p_{m=1}^{out}$
0000⟩ +  1111⟩	+1	0.850(3)	0.713(11)	0.789(11)	0.336(30)
	-1	0.150(3)	0.287(11)	0.211(11)	0.664(30)
0000⟩ -  1111⟩	+1	0.188(3)	0.265(12)	0.504(28)	0.220(11)
	-1	0.812(3)	0.735(12)	0.496(28)	0.780(11)
0011⟩ -  1100⟩	+1	0.099(2)	0.073(7)	0.416(35)	0.038(5)
	-1	0.901(2)	0.927(7)	0.584(35)	0.962(5)

Table B.11.: QND figures of merit. Determined from measurements **with** hiding of the system ions during the measurement of the ancilla. Since the state |0011⟩ - |1100⟩ is particularly robust against decoherence, the fidelity  $F_{QSP}$  is higher, as shown for 8 ions in [23].

input state	eigen-space	$p^{in}$	$p^{out}$	$p^m$	$p_{QND=+}^{out}$	$p_{QND=-}^{out}$	$F_M(p^{in}, p^m)$	$F_{QND}(p^{in}, p^{out})$	$F_{QSP}(p^m, p_{QND}^{out})$
0000⟩ +  1111⟩	+1	0.82(1)	0.69(1)	0.85	0.74(1)		0.998(1)	0.978(5)	0.72(1)
	-1	0.18(1)	0.31(1)	0.15		0.64(3)			
0000⟩ -  1111⟩	+1	0.19(1)	0.31(1)	0.17	0.64(3)		0.999(1)	0.980(5)	0.74(1)
	-1	0.81(1)	0.69(1)	0.83		0.76(1)			
0011⟩ -  1100⟩	+1	0.041(4)	0.14(1)	0.10	0.48(4)		0.985(3)	0.969(6)	0.86(1)
	-1	0.959(4)	0.86(1)	0.90		0.90(1)			
1111⟩	+1	0.5	0.47(1)	0.50049	0.70(1)		1	0.9992(6)	0.73(1)
	-1	0.5	0.53(1)	0.49951		0.76(1)			

Table B.12.: QND figures of merit. Determined from measurements **without** hiding of the system ions during the measurement of the ancilla. Since the state  $|0011\rangle - |1100\rangle$  is particularly robust against decoherence, the fidelity  $F_{\text{QSP}}$  is higher, as shown for 8 ions in [23].

input state	eigenspace	$p^{\text{out}}$	$p^{\text{m}}$	$p_{\text{QND}=+}^{\text{out}}$	$p_{\text{QND}=-}^{\text{out}}$	$F_{\text{M}}(p^{\text{in}}, p^{\text{m}})$	$F_{\text{QND}}(p^{\text{in}}, p^{\text{out}})$	$F_{\text{QSP}}(p^{\text{m}}, p_{\text{QND}}^{\text{out}})$
$ 0000\rangle +  1111\rangle$	+1	0.71(1)	0.85	0.79(1)		0.998(1)	0.984(4)	0.77(1)
	-1	0.29(1)	0.15		0.66(3)			
$ 0000\rangle -  1111\rangle$	+1	0.26(1)	0.19	0.50(3)		1.0000(1)	0.992(3)	0.73(1)
	-1	0.74(1)	0.81		0.78(1)			
$ 0011\rangle -  1100\rangle$	+1	0.07(1)	0.10	0.42(3)		0.986(2)	0.996(2)	0.91(1)
	-1	0.93(1)	0.90		0.96(1)			
$ 1111\rangle$	+1	0.52(1)	0.5078	0.75(1)		0.99994	0.9996(5)	0.74(1)
	-1	0.48(1)	0.4922		0.73(1)			

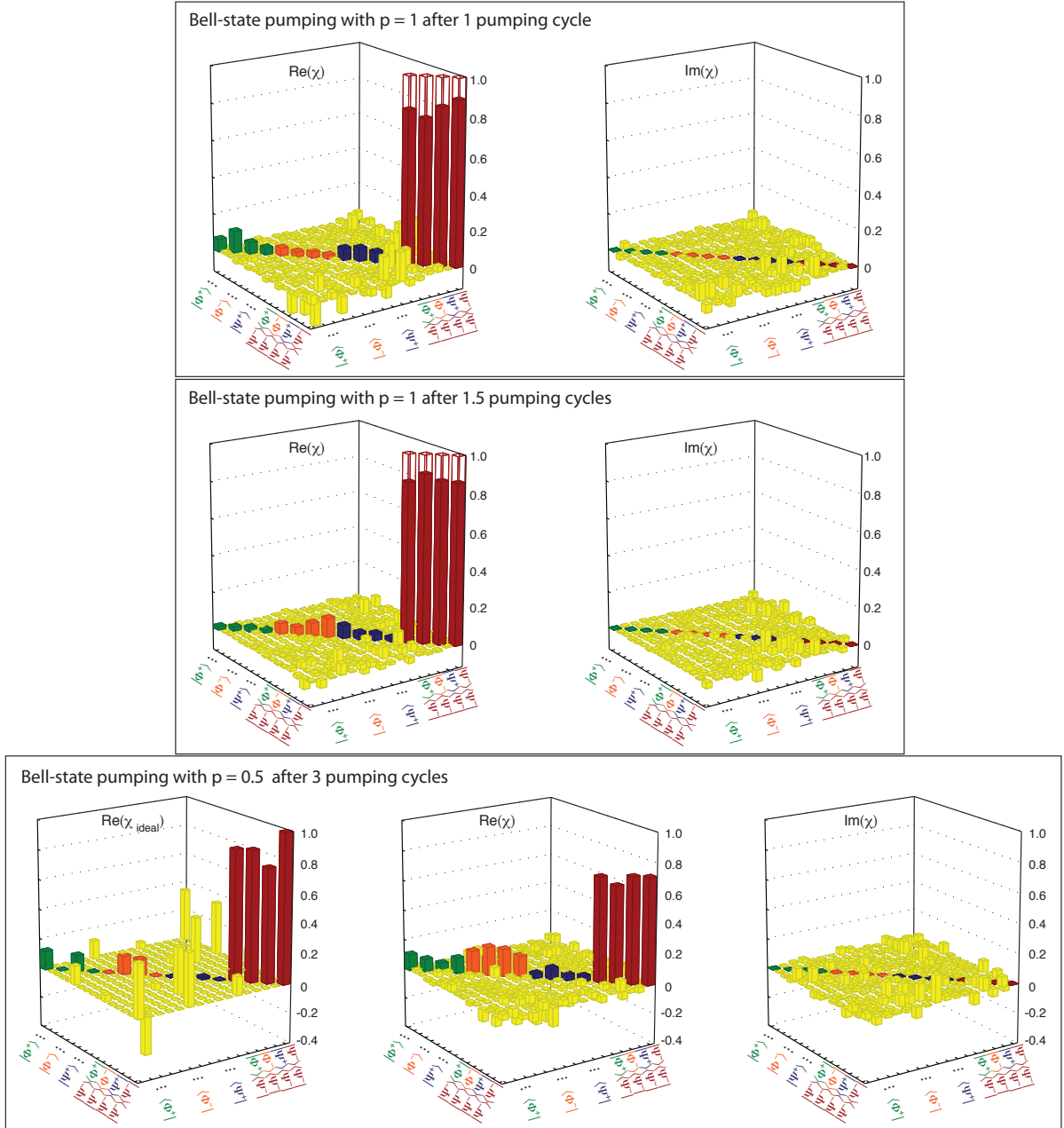


Figure B.13.: **Reconstructed process matrices of experimental Bell-state pumping.** The reconstructed process matrix for  $p = 1$  after 1 (1.5) cycles has a Jamiolkowski process fidelity [37] of 83.4(7)% (87.0(7)%) with the ideal dissipative process  $\rho_S \mapsto |\Psi^-\rangle\langle\Psi^-|$  which maps an arbitrary state of the system into the Bell state  $|\Psi^-\rangle$ . This ideal process has as non-zero elements only the four transparent bars shown. The reconstructed process matrix for  $p = 0.5$  after 3 cycles has a Jamiolkowski process fidelity of 60(1)% with the ideal process  $\chi_{\text{ideal}}$  shown [ $\text{Im}(\chi_{\text{ideal}}) = 0$ ].

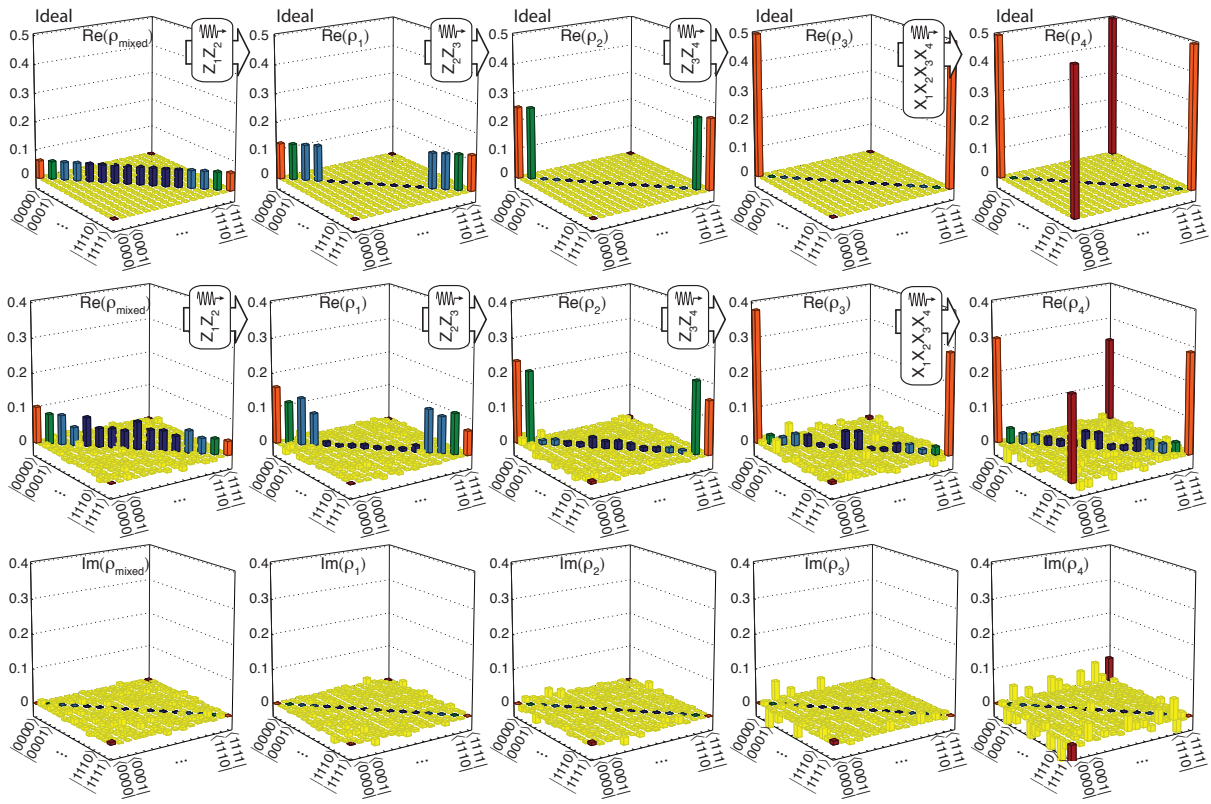


Figure B.14.: **Ideal and reconstructed density matrices of plaquette pumping.** An initial mixed state  $\rho_{\text{mixed}}$  is sequentially pumped by the stabilizers  $Z_1Z_2$ ,  $Z_2Z_3$ ,  $Z_3Z_4$  and  $X_1X_2X_3X_4$  driving the system into the states  $\rho_{1,2,3,4}$ .

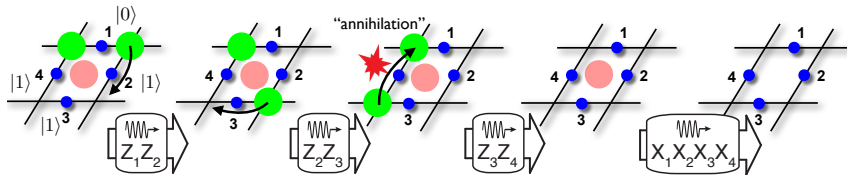


Figure B.15.: **Pushing “anyons”.** Cartoon of the dissipative dynamics. The pumping dynamics can be visualized by dissipative pushing of excitations (green and red dots) between adjacent corners of the plaquette.

Algorithm type	Nr. of MS gates	Nr. of global rotations $R$	Nr. of AC-Stark shifts $S_Z$	Nr. of resets	Total number of operations
Elementary dissipative map	6	7	9	1	23
Hamiltonian competing dynamics with 3+1 ions	2	3	2	0	7
Hamiltonian competing dynamics with 4+1 ions	3	4	4	0	11
QND post-selective error detection	4	8	6	0	18
Mapping for the spin excitation removal	2	9	4	0	15
Mapping for the spin excitation injection	3	12	7	0	22
Excitation injection / removal step (single site)	4	0	2	0	6
Spectroscopic decoupling	0	5	4	0	9
Composite dissipative map (3 spins)	12	26	24	2	64
Composite diss. and coh. dyn. map (3 spins)	14	29	26	2	71
Composite diss. and coh. map + QND (3 spins)	18	40	27	3	88
Composite dissipative map (4 spins)	18	33	35	3	89
Composite diss. and coh. dyn. map (4 spins)	21	44	44	3	112

Table B.13.: Summary of the required resources for the elementary and composite dynamical maps and additional tools used in the quantum simulation. The required operations for the composite maps do not strictly match the sum of the required elementary operations, since in the implementation of composite maps synergy effects in the resources for the spectroscopic decoupling operations can be exploited.

## B.4. Quantum Simulation of Dynamical Maps with Trapped Ions

Table B.13 provides an overview of the algorithmic building blocks required for the implementation of elementary dissipative Kraus maps, the realization of Hamiltonian dynamical maps, spectroscopic decoupling of ions, and elements for the detection and reduction of errors in our ion-trap quantum simulator. The table describes the experimental resources needed for the implementation of these elementary sub-routines as well as for the combination of these building blocks in more complex composite dynamical maps. The details of the underlying Kraus map engineering as well as the detailed quantum circuits used in the experiment are presented in the corresponding subsections below.

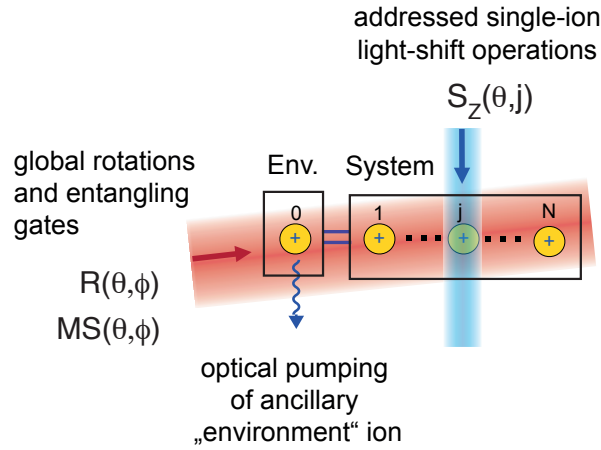


Figure B.16.: Illustration of the geometry of the laser-beams used for qubit manipulation. A global beam illuminating the ion string homogeneously is used to implement collective rotations  $R(\theta, \phi)$  and multi-ion Mølmer-Sørensen-type entangling gates  $MS(\theta, \phi)$ , whereas an addressed beam enables the realization of single-qubit rotations  $S_Z(\theta, j)$ . An addressed optical pumping technique allows one to incoherently reinitialize the state of an ancillary qubit, which plays the role of a tailored environment. See text for more details.

### B.4.1. Experimental system and techniques

In this section we will describe the available operations in our universal ion-trap quantum simulator.

#### Coherent gates

The qubit is encoded in the  $4S_{1/2}(m_j = -1/2)$  and  $3D_{5/2}(m_j = -1/2)$  electronic states of the  $^{40}\text{Ca}^+$  ion and is manipulated by precisely timed light pulses on resonance or near resonant with the optical transition. The laser light can be applied from two different directions as depicted in figure B.16, where one beam illuminates the entire ion string homogeneously and the second beam is able to address each ion individually [46].

The set of coherent gates consists of collective single-qubit rotations, addressed single-qubit gates and collective entangling gates. Collective single-qubit rotations are implemented by the globally applied laser beam, resonant with the qubit transition, realizing the unitary

$$R(\theta, \phi) = \exp\left(-\frac{i\theta\pi}{2}S_\phi\right), \quad (\text{B.19})$$

with  $S_\phi = \sum_{i=0}^N \sigma_i^\phi$  a collective spin operator, and

$$\sigma_i^\phi = \sigma_i^x \cos(\phi \cdot \pi) + \sigma_i^y \sin(\phi \cdot \pi)$$

being a linear combination of the single-qubit Pauli matrices  $\sigma_i^x$  and  $\sigma_i^z$ , acting on qubit  $i$ . The rotation angle  $\theta$  is determined by  $\theta = \Omega \tau / \pi$ , which can be controlled by the Rabi frequency  $\Omega$

and the pulse duration  $\tau$ . In this notation a complete  $\pi$ -flop inverting the electronic population of the logical states corresponds to a rotation angle  $\theta = 1$ . On the other hand, tuning the phase  $\phi$  of the global laser beam allows one to control the rotation axis lying in the  $x$ - $y$ -plane of the Bloch sphere, around which each of the qubits is rotated. Addressed single-qubit operations

$$S_z(\theta, i) = \exp\left(-\frac{i\theta\pi}{2}\sigma_i^z\right) \quad (\text{B.20})$$

around the  $z$ -axis are realized by shining in laser light near resonant with the qubit transition that induces an intensity-dependent AC-Stark shift  $\Delta_{AC}$ . Again, the rotation angle  $\theta$  is determined by the pulse length  $\tau$ ,  $\theta = \Delta_{AC}\tau/\pi$ , and a  $\pi$ -pulse corresponds to  $\theta = 1$ . Finally, collective entangling operations are implemented by a bi-chromatic, globally applied laser field, which effectively realizes two-body Mølmer-Sørensen (MS) type interactions,

$$MS(\theta, \phi) = \exp\left(-\frac{i\theta\pi}{4}S_\phi^2\right) = \exp\left(-\frac{i\theta\pi}{2}\sum_{i>j}\sigma_i^\phi\sigma_j^\phi\right) \quad (\text{B.21})$$

between all pairs  $i$  and  $j$  of the ion chain ( $i, j = 0, 1, \dots, N$ ) [148, 187]. Again, the angle  $\phi$  allows one to control whether  $\sigma_i^x\sigma_j^x$  (for  $\phi = 0$ ),  $\sigma_i^y\sigma_j^y$  (for  $\phi = 1/2$ ) or interactions  $\sigma_i^\phi\sigma_j^\phi$  corresponding to any other axis  $\sigma^\phi$  in the  $x$ - $y$ -plane are realized. In this notation, the angle  $\theta = 1/2$  corresponds to a "fully-entangling" MS gate, i.e. a unitary which maps the computational basis states of  $N+1$  ions onto multi-particle entangled states, which are (up to local rotations) equivalent to  $N+1$ -qubit GHZ states. Altogether, operations (B.19) to (B.21) form a universal set of gates, enabling the implementation of arbitrary unitaries on any subset of ions [33].

## Numerical optimization of gate sequences

Any unitary operation required for the implementation of dissipative and coherent maps, as well the error detection and reduction protocols, needs to be decomposed into a sequence of available operations. As discussed in more detail below, such decompositions can be constructed systematically [55]. However, as such decompositions are in many cases not optimal in terms of the number of required gate operations, it is convenient to resort to a numerical optimal control algorithm [33] to search for optimized sequence decompositions involving less gates. Whereas the numerical optimization algorithm becomes inefficient for general unitary operations acting on a large number of qubits, it is well-suited for the optimization of unitaries which act only on a small subset of ions (such as 2+1 ions in the implementation of an elementary dissipative Kraus map), independently of the total system size.

Numerically optimized pulse sequences may include global AC-Stark pulses and MS gates with negative rotation angles  $\theta < 0$ , which are not directly contained in the available gate set discussed in Sec. B.4.1. However, as any collective rotation around the  $z$ -axis of the Bloch sphere can be interpreted as a re-definition of the  $x$ - and  $y$ -axes, a global AC-Stark pulse can be omitted if the phases  $\phi$  of the following resonant operations are properly adjusted. Regarding MS gates with  $\theta < 0$ , these can be implemented by MS gates with positive rotation angles, as  $MS(-\theta, \phi) \equiv MS(1 - \theta, \phi)$  up to local rotations (see Eq. (9) in Ref. [55]).

Transition	Pulse
$ S\rangle \rightarrow  D'\rangle$	$R(0.5, 0)$
$ S\rangle \rightarrow  D'\rangle$	$S_z(1, i)$
$ S\rangle \rightarrow  D'\rangle$	$S_z(1, j)$
$ S\rangle \rightarrow  D'\rangle$	$R(0.5, 1)$
$ D\rangle \rightarrow  S'\rangle$	$R(0.5, 0)$
$ D\rangle \rightarrow  S'\rangle$	$S_z(1, i)$
$ D\rangle \rightarrow  S'\rangle$	$S_z(1, j)$
$ D\rangle \rightarrow  S'\rangle$	$R(0.5, 1)$
$ S'\rangle \rightarrow  D''\rangle$	$R(1, 0)$

Table B.14.: Pulse sequence for spectroscopic decoupling of ions  $i$  and  $j$  by coherently transferring their quantum information from the qubit states  $|S\rangle$  and  $|D\rangle$  to the states  $|D'\rangle$  and  $|D''\rangle$ . The gates listed in the three blocks of the table realize the pulses (i) - (iii) shown in Fig. 2b of the main text.

### Spectroscopic decoupling of ions

Despite the globally applied beams for the collective rotations and MS gates, operations on subsets of ions can be realized by spectroscopically decoupling ions not involved in the realization of a certain Kraus map from the dynamics. This is realized by coherently transferring ions to electronic states, where they do not couple to the globally applied light fields to a very good approximation. This decoupling technique enables the use of optimized sequences for the realization of Kraus maps on a small number of sites, independently of which subset of ions is currently involved in the map, and independently of the system size, i.e. the total number of sites.

The full decoupling sequence consists of the following parts as also outlined in Fig. 4.8 in the main-text: (i) First, the population is transferred from the qubit state  $|S\rangle = 4S_{1/2}(m_f = -1/2) = |1\rangle = |\uparrow\rangle$  to the  $|D'\rangle = 3D_{5/2}(m_f = -5/2)$  state. (ii) Then, the population from the other qubit state  $|D\rangle = 3D_{5/2}(m_f = -1/2) = |0\rangle = |\downarrow\rangle$  is transferred via  $|S'\rangle = 4S_{1/2}(m_f = +1/2)$  to the  $|D''\rangle = 3D_{5/2}(m_f = -3/2)$  state. The required pulses for decoupling two ions are shown in Table B.14. Bringing the population from the decoupled states back to the original qubit states is realized by implementing the described sequence in reverse order.

The decoupling technique introduces additional errors that are not included in the theoretical error model. A rigorous treatment of these errors is cumbersome since it cannot be modeled in a qubit system anymore, but involves the full electronic substructure of the ion. However, the effect of the decoupling process in the computational basis can be characterized by quantum process tomography. We found a process fidelity of 94(2)% for decoupling a qubit and bringing it back to the original states. Next, we proved that the decoupled qubit is indeed to a high degree not affected by the manipulation pulses. We checked this in a system of 3+1 ions, where we first decoupled a single qubit, then applied the pulses as required for a single elementary dissipative Kraus map on the remaining two system ions and the ancilla ion, and finally transferred the decoupled qubit back to the original qubit state. Due to residual far off-resonant coupling to

Transition	Pulse
$ S'\rangle \rightarrow  D\rangle$	$R(0.5, 0)$
$ S'\rangle \rightarrow  D\rangle$	$S_z(1, j)$
$ S'\rangle \rightarrow  D\rangle$	$R(0.5, 1)$
$ S'\rangle \rightarrow  P\rangle$	$\sigma^-$ repump

Table B.15.: Pulse sequence for the individual reset of qubit  $j$ .

transitions coupling different Zeeman sublevels, the pulses implementing the dissipative Kraus map induce a deterministic AC-Stark shift on the decoupled ion. This Stark shift is measured with a Ramsey-type experiment, and its compensation is performed with the final two pulses in the sequence as shown in Table B.14. Quantum process tomography on the decoupled qubit, where the systematic Stark shift has been compensated, yields a process fidelity of 93(2)%. Thus we can conclude that the pulses corresponding to the Kraus map implementation do not affect the decoupled qubit significantly, and that the dominant errors result from laser intensity fluctuations in the decoupling pulses themselves.

### Incoherent reinitialization of individual ions

The implementation of an elementary dissipative Kraus map is completed by an incoherent reset of the ancillary ion to its initial state  $|S\rangle$ , see step (iii) in Fig. 4.8c in the main text. This reinitialization is realized by an optical pumping technique: First, an addressed pulse is applied to the ancillary ion to transfer the population present in the  $|D\rangle$  state to the  $|S'\rangle$  state. Then  $\sigma^-$  polarized light is applied to the entire ion string performing optical pumping from  $|S'\rangle$  towards  $|S\rangle$  via the short-lived  $4^2P_{1/2}$  state. This procedure does not affect the information in the system ions encoded in the original qubit states  $|S\rangle$  and  $|D\rangle$ , as the light couples only to the  $|S'\rangle$  level [62]. The required operations are shown Table B.15

## B.4.2. Engineering of dissipative and Hamiltonian dynamical maps

In this section we provide details on the engineering and the specifics of the circuit-based experimental implementation of elementary dissipative and Hamiltonian dynamical maps.

### Action of the dissipative Kraus maps

The elementary dissipative Kraus maps

$$\rho \mapsto E_{i,1}\rho E_{i,1}^\dagger + E_{i,2}\rho E_{i,2}^\dagger \quad (\text{B.22})$$

with

$$E_{i,1} = c_i \quad \text{and} \quad E_{i,2} = 1 - c_i^\dagger c_i, \quad (\text{B.23})$$

are generated by the operators  $c_i$  (cf. Eq. (4.5) in the main text), as given by

$$c_i = (\sigma_i^+ + \sigma_{i+1}^+)(\sigma_i^- - \sigma_{i+1}^-). \quad (\text{B.24})$$

These operators act bi-locally, i.e. involve two neighboring spins  $i$  and  $i + 1$ , whereas the other spins are spectators. It is instructive to examine their action on the basis states of the local Hilbert space of the two qubits  $i$  and  $i + 1$ , which is spanned by the singlet and triplet states of the total spin  $S_{i,i+1}^2$  of the two spin-1/2 particles:

$$S_{i,i+1}^2 \frac{1}{\sqrt{2}}(|01\rangle - |10\rangle) = 0$$

and

$$\begin{aligned} & S_{i,i+1}^2(|00\rangle, \frac{1}{\sqrt{2}}(|01\rangle + |10\rangle), |11\rangle) \\ &= 2(|00\rangle, \frac{1}{\sqrt{2}}(|01\rangle + |10\rangle), |11\rangle). \end{aligned}$$

Here,  $\mathbf{S}_{i,i+1} = \mathbf{S}_i + \mathbf{S}_{i+1}$  with  $\mathbf{S}_i = \frac{1}{2}\sigma_i = \frac{1}{2}(\sigma_i^x, \sigma_i^y, \sigma_i^z)^T$  and

$$\mathbf{S}_{i,i+1}^2 = (\mathbf{S}_i + \mathbf{S}_{i+1})^2 = \frac{3}{2} + \frac{1}{2}(\sigma_i^x \sigma_{i+1}^x + \sigma_i^y \sigma_{i+1}^y + \sigma_i^z \sigma_{i+1}^z).$$

For simplicity of the notation, we skip the spin indices  $i$  and  $i + 1$  for the states and use the short-hand notation  $|00\rangle = |0\rangle_i \otimes |0\rangle_{i+1}$ , etc. As illustrated in Fig. B.17, the operators  $c_i$  induce pumping from the singlet into the triplet  $m_S = 0$  state,

$$c_i \frac{1}{\sqrt{2}}(|01\rangle - |10\rangle) = \frac{1}{\sqrt{2}}(|01\rangle + |10\rangle),$$

whereas all triplet states are dark states,

$$c_i|00\rangle = c_i \frac{1}{\sqrt{2}}(|01\rangle + |10\rangle) = c_i|11\rangle = 0.$$

As shown in Fig. 4.3 of the main text, under this dissipative dynamics a single spin excitation (or hardcore boson) is symmetrically delocalized over the two sites, whereas the states of two ( $|11\rangle$ ) or zero ( $|00\rangle$ , "vacuum") spin excitations (or hardcore bosons) are left unchanged.

### Circuit-based implementation of elementary dissipative Kraus maps

Open-system dynamics according to the elementary dissipative Kraus maps (B.22) can be realized in a "digital" way, by using quantum simulation tools for open systems, which have been previously developed and demonstrated experimentally in the context of dissipative preparation of Bell and multi-qubit stabilizer states [62]. The key idea in engineering the two-spin dissipative dynamics according to Eq. (B.22) is to combine the experimentally available gates

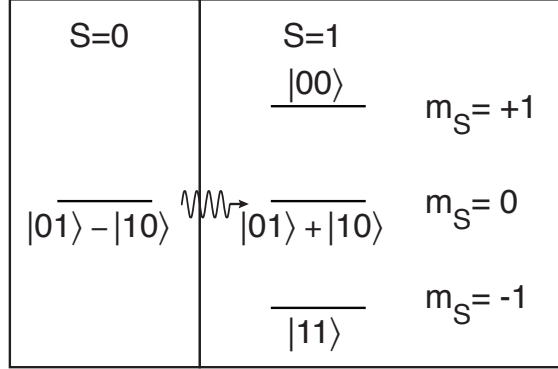


Figure B.17.: Schematics of the action of the two-spin operator (B.24) in the local Hilbert space of the two spins  $i$  and  $i + 1$ , which is spanned by the singlet state (left sector of the Hilbert space) and the triplet states (right sector). The operator  $c_i$  converts the singlet state  $\frac{1}{\sqrt{2}}(|01\rangle - |10\rangle)$  into the triplet  $m_S = 0$  state  $\frac{1}{\sqrt{2}}(|01\rangle + |10\rangle)$ . All triplet states are dark states and left invariant.

(see Sec. B.4.1 below for details) with optical pumping on an additional ancillary qubit (see Sec. B.4.1), which plays the role of a tailored environment.

*General engineering strategy* – The observation that the singlet state is dissipatively converted into the  $m_S = 0$  triplet state suggests the following gate-based implementation via a four-step process (shown in Figure B.18a), which involves a circuit of unitaries applied to the qubits  $i$ ,  $i + 1$  (steps (i) to (iii)), followed by the incoherent reset of the ancilla qubit (step (iv)):

(i) First, a unitary  $M$ , acting on the two system spins  $i$  and  $i+1$  and the ancillary qubit, coherently maps the binary information whether the two system spins are in the singlet or triplet subspace onto the two logical states  $|0\rangle$  and  $|1\rangle$  of the ancillary qubit. This is achieved by the unitary

$$\begin{aligned}
 M(\theta) &= \exp\left(-\frac{i\theta}{2} (\mathbf{S}_{i,i+1}^2 - 2) \otimes \sigma_0^x\right) \\
 &= \exp(i\theta P_{i,i+1} \otimes \sigma_0^x) \\
 &= \cos(\theta P_{i,i+1}) \otimes 1_0 - i \sin(\theta P_{i,i+1}) \otimes \sigma_0^x
 \end{aligned} \tag{B.25}$$

for which we choose  $\theta = \pi/2$  so that the unitary reduces to

$$M(\pi/2) = (1 - P_{i,i+1}) \otimes 1_0 - i P_{i,i+1} \otimes \sigma_0^x. \tag{B.26}$$

The unitary  $M$  is constructed in a way that the state of the ancilla qubit is rotated conditional on the state of the two system spins, and that the angle of this rotation depends on the operator  $(\mathbf{S}_{i,i+1}^2 - 2)$  which acts on the two system spins  $i$  and  $i + 1$ . Here,  $P_{i,i+1} = c_i^\dagger c_i$  is the projector onto the singlet subspace,  $(1 - P_{i,i+1})$  its orthogonal complement, and we have used  $\mathbf{S}_{i,i+1}^2 = 2(1 - P_{i,i+1})$ . Under the unitary  $M(\pi/2)$ , the ancilla qubit is rotated from its initial state  $|1\rangle$  into  $|0\rangle$  if and only if the two systems spins are in the singlet state.

(ii) Next, the transfer of the system qubits from the singlet to the triplet subspace is enabled by

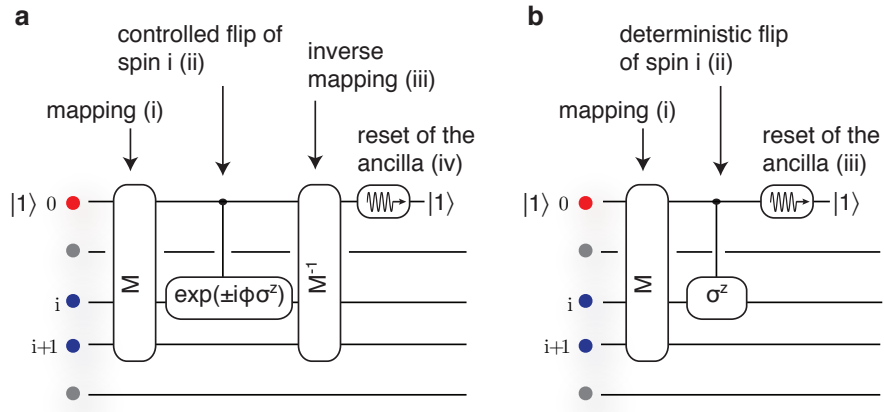


Figure B.18.: Quantum circuits for the realization of elementary dissipative Kraus maps (B.22) on spins  $i$  and  $i + 1$ . **a**, First, the information whether the two system spin-1/2 particles  $i$  and  $i + 1$  are in the singlet or triplet subspace of the two-spin Hilbert space (see Fig. B.17) is coherently mapped onto the logical states  $|0\rangle$  and  $|1\rangle$  of an ancilla qubit which is initially in  $|1\rangle$ . (ii) Next, a two-qubit gate is applied, which realizes an effective spin flip on one of the system spins, and thereby conditionally on the state of the ancilla converts the singlet into the triplet  $m_S = 0$  state:  $\frac{1}{\sqrt{2}}(|01\rangle - |10\rangle) \rightarrow \frac{1}{\sqrt{2}}(|01\rangle + |10\rangle)$ . After inverting the mapping (iii), the ancilla ion is optically pumped backed to its initial state  $|1\rangle$  (iv). This last steps renders the dynamics irreversible and provides the dissipative ingredient to extract entropy from the two system spins. The probability of the conversion from the singlet to the triplet state is controlled by the angle  $\phi$  appearing in the two-qubit gate, and it is given by  $p = \sin^2 \phi$ . In the limit of  $\phi \ll \pi/2$ , the conversion from the singlet into the triplet state takes place only with a small probability, and the general dissipative Kraus map describing the pumping process reduces to the master equation (B.29). **b**, In this work we are interested in deterministic pumping from the singlet into the triplet subspace, i.e. in the case of probability  $p = 1$  for  $\phi = \pi/2$ . In this situation, the circuit simplifies as the inverse mapping to partially disentangle the system spins from the ancilla is not required, and the circuit simplifies to the three-step process, which is also shown in Fig. 4.8 of the main text.

a two-qubit gate, which acts on the ancilla qubit and the system qubit  $i$ . It reads

$$\begin{aligned} C(\phi) &= \exp\left(\pm\frac{1}{2}(1 - \sigma_0^z) \otimes i\phi\sigma_i^z\right) \\ &= |1\rangle\langle 1|_0 \otimes 1_i + |0\rangle\langle 0|_0 \otimes \exp(\pm i\phi\sigma_i^z). \end{aligned} \quad (\text{B.27})$$

This controlled-operation applies  $\sigma^z$  to the  $i$ -th system qubit, and thus with probability  $p = \sin^2 \phi$  converts the singlet into the triplet state:  $\sigma_i^z \frac{1}{\sqrt{2}}(|01\rangle - |10\rangle) = \frac{1}{\sqrt{2}}(|01\rangle + |10\rangle)$ . Here, the ancilla qubit acts as a *quantum controller* [19, 20], which is not observed but controls the coherent feedback which is applied to the system qubits. From Eq. (B.27) it is clear that if the ancilla is in state  $|1\rangle$ , corresponding to the case of the two system spins residing in the triplet subspace, no quantum feedback is applied and the state of the system spins remains unchanged. Due to the previous mapping  $M$ , this assures that the triplet subspace is left invariant.

(iii) The initial mapping (i) is inverted by applying the inverse unitary  $M^\dagger(\pi/2)$ . For the system being in the target triplet space from the outset, this re-installs the conditions before step (i). For the special case of deterministic pumping ( $p = 1$ ), as experimentally realized in this work, the inverse unitary can be omitted (see also Figure B.18b).

(iv) After these unitary steps, the ancillary qubit remains in general entangled with the two system spins  $i$  and  $i + 1$ . It is finally reset to its initial state  $|1\rangle$  by optical pumping: this is the physical dissipative mechanism, which renders the dynamics irreversible and allows to extract entropy from the system spins. This refreshes the ancilla qubit and prepares it in the known pure state  $|1\rangle$ , so that it can be used for the implementation of subsequent dissipative Kraus maps.

For an initially uncorrelated state of the ancilla qubit and the system spins,  $|1\rangle\langle 1|_0 \otimes \rho$ , the resulting dynamics for the system spins (described by the reduced density matrix  $\rho$  of the system spins) is obtained by applying the combined unitary  $U = M^\dagger(\pi/2) C(\phi) M(\pi/2)$  and tracing over the ancilla qubit's degrees of freedom,

$$\rho \mapsto \text{tr}_0 \{U(|1\rangle\langle 1|_0 \otimes \rho)U^\dagger\}. \quad (\text{B.28})$$

Straightforward algebra yields the Kraus map  $\rho \mapsto \sum_{k=1,2} E_{i,k} \rho E_{i,k}^\dagger$  with the operation elements

$$E_{i,1} = \sin \phi c_i \quad \text{and} \quad E_{i,2} = 1 + (\cos \phi - 1) c_i^\dagger c_i.$$

On the one hand, for  $\phi = \pi/2$  the operation elements reduce to Eq. (B.23) and correspond to deterministic pumping ( $p = 1$ ) from the singlet into the triplet states, which is the scenario realized in this work. On the other hand, for  $\phi \ll \pi/2$  one can expand the operation elements of the Kraus map and recovers the master equation limit

$$\rho \mapsto \rho + \phi^2 \left( c_i \rho c_i^\dagger - \frac{1}{2} \{c_i^\dagger c_i, \rho\} \right) + O(\phi^4). \quad (\text{B.29})$$

*Additional remarks* – We note that our implementation corresponds to an *open-loop* control scenario, where the ancillary qubit remains unobserved during the simulation. However, we remark that it is possible to measure the state of the ancillary qubit in the computational basis by an addressed fluorescence measurement, before it is reset to its initial state by optical pumping [62].

Such measurement reveals whether under the application a particular dissipative Kraus map the two system spins have undergone a collective two-spin quantum jump from the singlet into the triplet state or not. This information yields "in-situ" information about the many-body system's dynamics along a particular trajectory. The temporal statistics of quantum jumps in open, driven many-body quantum spin systems contains valuable information about dynamical phase transitions [188, 189]. In the present work we do not further explore this possibility. We remark that the fluorescence measurement of the ancillary ion, which is associated to the scattering of many photons and non-negligible heating of the vibrational modes, can be combined with subsequent laser re-cooling of the relevant vibrational modes via the ancillary ion, as demonstrated by [95]. This allows one to perform such quantum jump measurements and to afterwards re-initialize the *external* degrees of freedom, thereby enabling that in the same experimental run further gate operations required for the implementation of subsequent Kraus maps can be still applied with high fidelity.

*Specific experimental implementation* – For the implementation of the elementary dissipative Kraus maps in the ion-trap simulator, the unitary operations  $M(\pi/2)$  and  $C(\pi/2)$  (see Eqs. (B.25) and (B.27)) have to be decomposed into a quantum circuit of available gates: The mapping  $M$  can be written as a product of three unitaries involving 3-body spin interaction terms,

$$\begin{aligned}
 M(\pi/2) &= \exp\left(-\frac{i\pi}{4}\sigma_0^x(\mathbf{S}_{i,i+1}^2 - 2)\right) \\
 &= \exp\left(+\frac{i\pi}{8}\sigma_0^x\right)\exp\left(-\frac{i\pi}{8}\sigma_0^x\sigma_i^x\sigma_{i+1}^x\right) \\
 &\times \exp\left(-\frac{i\pi}{8}\sigma_0^x\sigma_i^y\sigma_{i+1}^y\right)\exp\left(-\frac{i\pi}{8}\sigma_0^x\sigma_i^z\sigma_{i+1}^z\right).
 \end{aligned}
 \tag{B.30}$$

As discussed in Ref. [55] each of the three-body unitaries can be realized by two "fully-entangling" MS gates in combination with single-qubit rotations, such that  $M$  could be implemented by a quantum circuit involving six MS gates and a number of single-qubit gates to rotate the system spins between the  $x$ ,  $y$  and  $z$ -bases between the different unitaries.

Similarly, the two-qubit controlled operation  $C(\pi/2)$  (see Eq. (B.27)) is up to local unitaries equivalent to one "fully-entangling" two-ion MS gate [55],

$$C(\pi/2) \sim \exp(-i(\pi/4)\sigma_0^x\sigma_i^x),$$

acting on the ancilla qubit and the system spin  $i$ . In the experiment, we did not use such a systematically constructed circuit decomposition, but instead resorted to the numerical optimization algorithm described in Sec. B.4.1 to further reduce the complexity of the quantum circuit: The gates of the experimentally employed sequence decomposition for the implementation of the unitaries of one elementary dissipative Kraus map are listed in Table B.16.

Number	Pulse	Number	Pulse
1	$S_z(1.5, 0)$	11	$MS(0.5, 1.5)$
2	$R(1.5, 1.0)$	12	$S_z(1.75, 2)$
3	$MS(0.25, 1.0)$	13	$MS(0.5, 2.25)$
4	$S_z(1.0, 1)$	14	$R(0.5, 1.75)$
5	$MS(0.875, 1.0)$	15	$R(0.5, 2.25)$
6	$S_z(1.0, 2)$	16	$MS(0.25, 2.25)$
7	$MS(0.125, 1.0)$	17	$S_z(1.5, 2)$
8	$S_z(1.5, 2)$	18	$S_z(1.0, 1)$
9	$R(0.5, 0.5)$	19	$R(0.5, 2.25)$
10	$S_z(0.5, 2)$		

Table B.16.: Pulse sequence for the implementation of a single elementary dissipative map. The necessary operations for the reset step are not shown.

### Engineering Hamiltonian maps for competing coherent interactions

Competing Hamiltonian dynamical maps are realized according to the dimensionless many-body spin Hamiltonian (cf. Eq. 4.8 in the main text)

$$H = \sum_{i=1}^{N-1} H_i := \sum_{i=1}^{N-1} (1 + \sigma_i^z)(1 + \sigma_{i+1}^z)/4, \quad (\text{B.31})$$

where the two-body terms correspond to interactions between spin excitations (or hardcore bosons) located on neighboring sites  $i$  and  $i + 1$ . The Hamiltonian dynamical maps  $U_{i,i+1} = \exp(-i\phi H_i)$  acting on spins  $i$  and  $i + 1$  are up to local rotations equivalent to two-spin MS interactions,  $\exp(-i\phi \sigma_i^x \sigma_{i+1}^x/4)$ . The implementation of the competing Hamiltonian dynamical maps can be realized with two distinct approaches: (i) The elementary two-spin Hamiltonian maps can be implemented sequentially, in analogy to the sequential implementation of the elementary dissipative maps. (ii) Alternatively, since the elementary Hamiltonian maps mutually commute, they can be implemented by a single global unitary operation, acting directly on the entire register of system spins. The unitary according to a sum of pairwise interactions between *neighboring* spins can for instance be built up from MS gates, which involve pairwise interactions between *all* pairs of spins, by means of refocusing techniques [55]. Although one could again try to find numerically optimized sequences of gates for the implementation of the composite Hamiltonian map, we note that such optimization for the unitary acting on the entire register of system spins would have to be done for each system size, and becomes inefficient for increasing system sizes. It is thus advisable to exploit the symmetries of the MS interactions, and to systematically construct sequence decompositions.

*Specific experimental implementation* – For instance, in the case of 3 system spins (with open boundary conditions), this operation can be decomposed into the following unitaries according

to single- and two-body interactions

$$\begin{aligned}
 U_{\text{comp}} = & \exp\left(-\frac{i\phi}{4}(\sigma_1^z\sigma_2^z + \sigma_2^z\sigma_3^z)\right) \\
 & \times \exp\left(-\frac{i\phi}{4}(\sigma_1^z + \sigma_2^z + \sigma_3^z)\right) \exp\left(-\frac{i\phi}{4}\sigma_2^z\right).
 \end{aligned}
 \tag{B.32}$$

As the ancilla qubit is not required to realize the unitary map, and must not be entangled with the system spins during the operation, it is spectroscopically decoupled during the application of the gate sequence. The experimental sequences used for the implementation of competing Hamiltonian maps for 3 system spins (3+1 ions) and 4 system spins (4+1 ions) are shown in Tables B.17 and B.18, respectively.

Number	Pulse
1	$S_z(1.5, 1)$
2	$R(0.5, 0.0)$
3	$MS(1 - 0.25k, 0.5)$
4	$S_z(1.0, 1)$
5	$MS(0.25k, 0.5)$
6	$S_z(1.0, 1)$
7	$R(0.5, 1.0)$

Table B.17.: Pulse sequence for the implementation of a composite Hamiltonian map in a 3-spin system, according to Eq. (B.32). The Hamiltonian strength is controlled by the parameter  $k$ , with experimentally implemented values  $k \in \{1, 0.5\}$ , corresponding to  $\phi \in \{\pi/2, \pi/4\}$ .

Number	Pulse
	Act on qubit 2 and 3
1	$R(0.5, 0.5)$
2	$MS(0.5, 1.0)$
3	$R(0.5, 1.5)$
	Act on qubit 1,2,3,4
4	$R(0.5, 0.5)$
5	$MS(0.25, 1.0)$
6	$S_z(1.0, 3)$
7	$S_z(1.0, 2)$
8	$MS(0.25, 1.0)$
9	$S_z(1.5, 3)$
10	$S_z(1.5, 2)$
11	$R(0.5, 1.5)$

Table B.18.: Pulse sequence for the implementation of a composite Hamiltonian map in a 4-spin system, for strong competing interactions corresponding to an angle  $\phi = \pi/2$ .

### B.4.3. Experimental characterization of an elementary dissipative map and noise model

#### Modeling an imperfect elementary dissipative map

In the following, we will introduce a theoretical model of the elementary pumping step in the presence of experimental noise. A single elementary dissipative map acting on two system ions can be ideally described by the two-qubit process matrix  $\chi_{id}$  which can be straightforwardly calculated from the Kraus map (B.22) with generating operators as defined in Eq. (B.23) [30]. In order to describe the implementation of the elementary dissipative map on the three system qubits (two "active" and one spectroscopically decoupled ion), we will assume a process consisting of the modeled elementary map on the two active system qubits and an identity process on the third qubit. The noise affecting the elementary map is modeled by two independent depolarizing channels acting on each of the two "active" system qubits where the fully depolarizing channel on a single qubit  $i$  can be written as the Kraus map [30]

$$\rho \mapsto \mathcal{E}_{dep}^{(i)}(\rho) = \frac{1}{4} (\rho + \sigma_i^x \rho \sigma_i^x + \sigma_i^y \rho \sigma_i^y + \sigma_i^z \rho \sigma_i^z).$$

The physical noise acting on the register during the individual gates is certainly more complex than this, but the effect of noise on the outcome of any complex algorithm can be approximated by depolarizing noise regardless of the specific characteristics of the noise [30]. We model a noisy elementary dissipative map with the concatenation of two depolarizing channels each acting on one of the system qubits  $\rho \mapsto \Pi(\rho) = \mathcal{E}_{dep}^{(i+1)}(\mathcal{E}_{dep}^{(i)}(\rho))$  with process matrix  $\chi_{\Pi}$  as

$$\chi_{diss}(\epsilon) = (1 - \epsilon)\chi_{id} + \epsilon\chi_{\Pi}.$$

In the limit  $\epsilon \rightarrow 0$ , the imperfect process  $\chi_{diss}$  reduces to the ideal two-qubit process  $\chi_{id}$ , where in the extreme opposite limit of  $\epsilon \rightarrow 1$  depolarizing noise completely dominates and overwrites any effect of the desired engineered dissipative process  $\chi_{id}$ . One can now adjust the parameter  $\epsilon$  of this model to the obtained data by a numerical optimization. For this, we maximized the overlap between the expected output state after a single elementary map  $\rho_{\epsilon}$  with noise strength  $\epsilon$  with the actual measured state  $\rho_{exp}$ ,

$$\arg_{\epsilon} \max \mathcal{F}(\rho_{exp}, \rho_{\epsilon}).$$

where the Uhlmann fidelity  $\mathcal{F}(\rho_1, \rho_2)$  for the comparison of two density matrices  $\rho_1, \rho_2$  is used [37]. We find an optimum for a noise parameter of  $\epsilon = 0.27$ .

#### Implementation and analysis of an elementary dissipative map

Here, we will provide a more detailed analysis of the specific implementation of a single dissipative step. During the realization of an elementary dissipative Kraus map gates act on the two ions encoding the system spins  $i$  and  $i + 1$  and the ancilla ion, while all other ions are spectroscopically decoupled. To quantitatively characterize the implementation of the Kraus map,

Error source	Overlap with $\Psi_+$
All	77 %
Addressing	95%
Dephasing	84 %
Intensity fluctuations	99%
Spectator modes	94%

Table B.19.: Results for the numerical simulation of a quantum simulation algorithm, in order to identify the dominant experimental error source. The simulation is performed multiple times with only a single active error source. From the results one can infer that dephasing is the dominant error source.

as realized by the gate sequence shown in Table B.16 (see also Sec. B.4.2), we performed a quantum process tomography on the two system qubits. A benchmark for the performance is given by the process fidelity with the ideal two-qubit process. Since the ideal process is not a unitary process, the Choi-Jamiolkowsky process fidelity is a suitable measure [37]. We find a mean state fidelity of  $\mathcal{F} = 68(1)\%$ .

In order to identify the leading source of imperfections in the implementation, a numerical analysis of the actual physical system is performed. We performed a Monte Carlo simulation of a single elementary map acting on three ions, including noise originating from: laser frequency and intensity fluctuations, magnetic field fluctuations, imperfect state preparation, motional heating, spontaneous decay and crosstalk of the addressed operations. The noise parameters are independently measured and we find an overlap between the numerically predicted and the measured state of  $\mathcal{F} = 97\%$ . In order to determine the dominant error source, we performed the simulation multiple times where only a single noise source affects the evolution. The results are shown in Table B.19. From this we find that the main error source is dephasing due to fluctuations in the laser frequency and the magnetic field.

## Numerical simulation and long-time dynamics under dissipative maps

### B.4.4. Numerical simulation and long-time dynamics under dissipative maps

Based on the study of experimental errors of an elementary dissipative Kraus map in the previous sections, we have realized a numerical study of the dissipative dynamics driving a mesoscopic spin systems ( $N = 10$ ) with initially three spin excitations present ( $m_0 = 3$ ) towards the Dicke state  $|D(3, 10)\rangle$ . The results are shown and discussed in Figure 4.3.2 of the main text. To take into account the imperfections in the implementation of the elementary maps, as discussed in the previous section, we assumed a depolarizing noise strength of  $\epsilon_{diss} = 0.02$  for each of the two spins  $i$  and  $i+1$  involved in an elementary dissipative map  $D_{i,i+1}$ . Since the implementation of an elementary Hamiltonian dynamical map  $U_{i,i+1}$  on two spins is less complex than the realization of a dissipative map, we assumed a depolarizing noise strength for  $U_{i,i+1}$  of  $\epsilon_{coh} = \epsilon_{diss}/5$ . The error reduction protocol to stabilize the system within the desired  $m_0 = 3$  excitation subspace

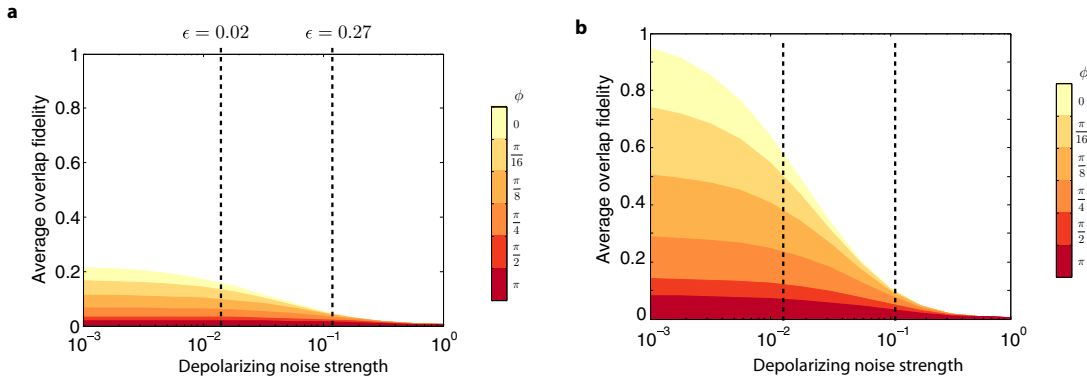


Figure B.19.: **Numerical study of competing Hamiltonian and dissipative dynamics in the presence of depolarizing noise.** The curves corresponding to varying strengths  $\phi$  of competing Hamiltonian dynamics show the overlap with the  $|D(3, 8)\rangle$  Dicke state for a chain of 8 spins with  $m = 3$  excitations, **a**, without and **b**, with active error reduction, as a function of the strength  $\epsilon$  of the depolarizing noise. Under incorporation of the error reduction protocol the dynamical crossover becomes visible for experimental noise levels on the order of  $10^{-2}$  and below. Dashed vertical lines serve as a guide to the eye roughly indicating the current experimental noise level ( $\epsilon = 0.27$ ) as well as the smaller value of  $\epsilon = 0.02$  used for the numerical simulations in the main text. For details see text.

can in practice also be only implemented with a finite accuracy. Here we assumed both for the global operation required for one spin extraction procedure and for one injection procedure that the whole spin register is exposed to a global depolarizing noise channel with a probability  $\epsilon = 0.02$ .

Note that the chosen value of  $\epsilon = 0.02$  for the noise strength is roughly one order magnitude smaller than the current experimental value ( $\epsilon = 0.27$ , see the main text and Sec. B.4.3 above for details). The value of  $\epsilon = 0.02$  for the numerical study is chosen in a way to illustrate how the characteristic physical features of the non-equilibrium dynamics, as generated by competing (imperfect) coherent and dissipative dynamical maps, become more and more visible, under a projected future improvement of the quality of the experimental operations by about a factor of ten. To illustrate this, Fig. B.19 shows the numerically determined dynamics for a system of 8 spins with initially 3 excitations, as a function of the depolarizing noise strength  $\epsilon$ . The different curves display the overlap fidelity with the Dicke state  $|D(3, 8)\rangle$  for different strengths  $\phi$  of competing Hamiltonian dynamics. Whereas without active error reduction the competition between engineered coherent and dissipative dynamics is covered by the dominant effect of the noise. However, as anticipated, under the incorporation of the error reduction protocol the crossover for varying competing Hamiltonian strengths becomes clearly visible as the noise level reaches values on the order of  $10^{-2}$  and below.

*Long-time dynamics and off-diagonal long-range order under imperfect dissipative dynamical maps* – As discussed above and in the main text, under experimental imperfections during the pumping into Dicke states, the system initially residing in the  $m_0$  excitation subspace suffers

population leakage into the subspaces with  $m \neq m_0$ . In the long time limit, the population of the spin system is homogeneously distributed over these  $m$ -subspaces, each subspace populated according to its micro-canonical weight, i.e. the number of computational basis states spanning the corresponding subspace. Within each of the subspaces, not only for  $m = m_0$ , the dissipative maps are active and pump the population within each subspace towards the corresponding Dicke state  $|D(m, N)\rangle$ . As a result, for weak noise and in the long time limit, the system is driven into an incoherent mixture of Dicke states of different excitation numbers  $m = 0, \dots, N$ .

More quantitatively, a normalized Dicke state with  $m$  excitations for  $N$  spins is given by

$$|D(m, N)\rangle = (m!)^{-1} \binom{N}{m}^{-1/2} (S^+)^m |0\rangle^{\otimes N} \quad (\text{B.33})$$

with  $S^+ = \sum_{k=1}^N \sigma_k^+$ . The number of micro-states of  $m$  excitations on  $N$  sites is  $\binom{N}{m}$ . Thus the incoherent mixture of Dicke states is given by

$$\begin{aligned} \rho &= \frac{1}{2^N} \sum_{m=0}^N \binom{N}{m} |D(m, N)\rangle \langle D(m, N)| \\ &= \frac{1}{2^N} \sum_{m=0}^N \frac{1}{(m!)^2} (S^+)^m |0\rangle^{\otimes N} \langle 0|^{\otimes N} (S^-)^m \end{aligned} \quad (\text{B.34})$$

Interestingly, this incoherent mixture of Dicke states is a state with off-diagonal order  $\langle \sigma_i^+ \sigma_j^- \rangle \neq 0$ ,

$$\langle \sigma_i^+ \sigma_j^- \rangle = \frac{1}{N(N-1)} (\langle S^+ S^- \rangle - m), \quad (\text{B.35})$$

as we will show in the following. In Eq. (B.35) we have made use of the symmetry of the Dicke states under permutations of the spin indices. In order to evaluate the global expectation value  $\langle S^+ S^- \rangle$ , we decompose it as  $\langle S^+ S^- \rangle = \langle S^- S^+ \rangle + \langle S^z \rangle$ . Both contributions are easily obtained as  $\langle S^z \rangle = \sum_i \langle \sigma_i^z \rangle = 2m - N$ , and  $\langle S^- S^+ \rangle = (m+1)(N-m)$ . The latter expectation value can be obtained using the normalization factors for the Dicke states  $|D(m, N)\rangle$  and  $|D(m+1, N)\rangle$  with  $m$  and  $m+1$  excitations, respectively. Adding both contributions, we obtain  $\langle S^+ S^- \rangle = m(N+1-m)$ . This allows us to evaluate the expectation value  $\langle \sigma_i^+ \sigma_j^- \rangle$  with respect to a pure Dicke state:

$$\begin{aligned} \langle \sigma_i^+ \sigma_j^- \rangle_{|D(m, N)\rangle} &= \frac{1}{N(N-1)} (\langle S^+ S^- \rangle - m) \\ &= \frac{m}{N} \left(1 - \frac{m}{N}\right) \cdot \frac{1}{1 - \frac{1}{N}}. \end{aligned}$$

In the thermodynamic limit,  $N \rightarrow \infty$ ,  $m/N = \text{const.}$ , we have  $\langle \sigma_i^+ \sigma_j^- \rangle \rightarrow m/N(1 - m/N)$ . This expression reflects the "particle-hole" symmetry and shows that at complete filling ( $m = N$  spin excitations) or in the "vacuum" state ( $m = 0$ ) there is no off-diagonal order because spin excitations or missing spin excitations cannot be delocalized over the spin chain. At half filling  $m = N/2$ , where the number of micro-states is maximal, the effect of delocalization and thus

the off-diagonal order is maximal. The finite-size factor  $1/(1 - 1/N)$  is to be taken into account in small or mesoscopic spin systems, and approaches 1 in the thermodynamic limit.

From this, we can now determine the off-diagonal order of the system in the incoherent mixture of Dicke states as given by the density matrix of Eq.(B.35). Using the identities

$$\sum_{m=0}^N \binom{N}{m} m = N2^{N-1},$$

$$\sum_{m=0}^N \binom{N}{m} m^2 = N(N+1)2^{N-2},$$

one obtains

$$\langle \sigma_i^+ \sigma_j^- \rangle_{\text{mixture}} = \frac{1}{4}.$$

As expected, this value does not depend on the initial number of excitations anymore, since this information is completely lost, once the system has diffused into the incoherent mixture of Dicke states. The off-diagonal order in the incoherent mixture of Dicke states assumes a value which is independent of the system size  $N$ , and remains finite in the thermodynamic limit.

In summary, the experimental imperfections, as described by depolarizing noise and resulting in the non-conservation of the excitation-number during the simulation, lead to a strong decrease of the state overlap between the asymptotically reached many-body state of Eq. (B.35) and the ideal "target" dark state  $|D(m_0, N)\rangle$ . However, from a condensed-matter perspective one can state that the imperfections are not too harmful to the off-diagonal long-range order, measured by the two-spin correlation function  $\langle \sigma_i^+ \sigma_j^- \rangle$  for  $|i - j| \gg 1$  as an *order parameter*. The off-diagonal order is constantly stabilized and re-built by virtue of the repeated application of the engineered (though imperfectly implemented) dissipative dynamical maps.

### B.4.5. Quantum error detection method: Post-selective QND scheme

#### General idea

The post-selective error detection method is based on a quantum non-demolition (QND) measurement of the total number  $m$  of spin excitations present in the system at the end of the sequence of dynamical maps. Simulation outcomes, where due to experimental imperfections the ideally conserved initial spin excitation number  $m_0$  has changed to a final value  $m \neq m_0$  are discarded. This leads to an improvement of the simulation accuracy for longer sequences of dynamical maps, at the expense of an increased number of experimental runs to obtain the same measurement statistics. We remark that in a large system, as typical for post-selective techniques, this method becomes inefficient as the probability of remaining within the subspace of initial excitation number  $m_0$  becomes exponentially small and thus only a vanishingly small number of "successful" runs enter the measurement statistics.

In order to maintain the dissipatively created off-diagonal order in the many-spin system, a crucial property of the excitation number measurement is its QND nature: the spin excitation number  $m$  has to be determined in a way that allows one to only obtain information about the total number of excitations in the system, but no knowledge about the spatial positions of individual excitations along the array. This QND measurement can be realized by a global unitary map, which acts on the entire register of system spins and an ancillary qubit (see Fig. 4.3.2b of the main text). Such a unitary is constructed in a way that it maps the binary information whether the register of system spins is in the correct excitation number subspace with  $m = m_0$  (or not) onto the logical state  $|0\rangle$  ( $|1\rangle$ ) of the ancillary qubit. It involves the projector  $P_{m_0}^{(N)}$  onto the subspace of  $m_0$  spin excitations in an array of  $N$  spins, and reads

$$\begin{aligned} U_{m_0}^{(N)} &= \exp\left(-i\frac{\pi}{2}P_{m_0}^{(N)} \otimes \sigma_0^x\right) \\ &= P_{m_0}^{(N)} \otimes (-i\sigma_0^x) + (1 - P_{m_0}^{(N)}) \otimes 1_0. \end{aligned} \quad (\text{B.36})$$

This equation can be understood as follows: The state of the ancilla qubit, initially prepared in  $|1\rangle$ , is flipped by the  $\sigma_0^x$  operation if the system spins are in a state with exactly  $m = m_0$  excitations, whereas the ancilla qubit is left unchanged otherwise. The QND measurement is then completed by a measurement of the ancilla qubit in the computational basis, providing the desired information on whether  $m = m_0$  or  $m \neq m_0$ , depending on whether the ancilla qubit is measured in  $|0\rangle$  or  $|1\rangle$ .

### Construction of the projectors onto excitation number subspaces

The projector  $P_{m_0}^{(N)}$  required for the unitary (B.36) can be constructed systematically and efficiently for any  $m_0$  and  $N$  as follows: One starts from the ansatz

$$P_{m_0}^{(N)} = \sum_{k=0}^N \alpha_k S_z^k \quad (\text{B.37})$$

with  $S_z = \sum_{i=1}^N \sigma_i^z$ . This ansatz assures that the projector  $P_{m_0}^{(N)}$  (i) is diagonal in the computational basis, (ii) symmetric under any permutation of spin indices, and (iii) does not involve higher powers with  $k > N$  as such terms are already contained in previous terms with  $k \leq N$  due to the property  $(\sigma_i^z)^2 = 1$ . Since the computational basis states are eigenstates of  $S_z$ ,

$$\begin{aligned} S_z|0 \dots 0\rangle &= N|0 \dots 0\rangle, \\ S_z|0 \dots 0, 1\rangle &= (N - 2)|0 \dots 0, 1\rangle, \dots \\ &\vdots \\ S_z|1 \dots 1\rangle &= -N|1 \dots 1\rangle, \end{aligned}$$

and the projector per definition fulfills

$$\begin{aligned}
 P_{m_0}^{(N)}|0 \dots 0\rangle &= 0, \\
 &\vdots \\
 P_{m_0}^{(N)}|\overbrace{0 \dots 0}^{m_0} \overbrace{1 \dots 1}^{N-m_0}\rangle &= |0 \dots 01 \dots 1\rangle, \dots \\
 &\vdots \\
 P_{m_0}^{(N)}|1 \dots 1\rangle &= 0,
 \end{aligned}$$

its form is uniquely determined by the following coupled system of  $N + 1$  linear equations,

$$\begin{pmatrix}
 1 & N & N^2 & \dots & N^N \\
 1 & (N-2) & (N-2)^2 & \dots & (N-2)^N \\
 \vdots & \vdots & \vdots & & \vdots \\
 \vdots & \vdots & \vdots & & \vdots \\
 1 & -N & (-N)^2 & \dots & (-N)^N
 \end{pmatrix}
 \begin{pmatrix}
 \alpha_0 \\
 \alpha_1 \\
 \vdots \\
 \vdots \\
 \alpha_N
 \end{pmatrix}
 =
 \begin{pmatrix}
 0 \\
 \vdots \\
 1 \\
 0 \\
 \vdots
 \end{pmatrix}$$

with the only non-zero entry in the  $(N - m_0 + 1)$ -th row. This matrix equation is readily solved, yielding for the experimentally relevant case of three system spins with one or two spin excitations the projectors

$$\begin{aligned}
 P_1^{(3)} &= |011\rangle\langle 011| + |101\rangle\langle 101| + |110\rangle\langle 110| \\
 &= \frac{1}{16}(9 - 9S_z - S_z^2 + S_z^3) \\
 &= \frac{1}{8}(3 - (\sigma_1^z + \sigma_2^z + \sigma_3^z) \\
 &\quad - (\sigma_1^z\sigma_2^z + \sigma_1^z\sigma_3^z + \sigma_2^z\sigma_3^z) + 3\sigma_1^z\sigma_2^z\sigma_3^z)
 \end{aligned} \tag{B.38}$$

and

$$\begin{aligned}
 P_2^{(3)} &= |001\rangle\langle 001| + |010\rangle\langle 010| + |100\rangle\langle 100| \\
 &= \frac{1}{16}(9 + 9S_z - S_z^2 - S_z^3) \\
 &= \frac{1}{8}(3 + (\sigma_1^z + \sigma_2^z + \sigma_3^z) \\
 &\quad - (\sigma_1^z\sigma_2^z + \sigma_1^z\sigma_3^z + \sigma_2^z\sigma_3^z) - 3\sigma_1^z\sigma_2^z\sigma_3^z),
 \end{aligned} \tag{B.39}$$

where  $S_z = \sum_{i=1}^3 \sigma_i^z$ . Note that the projectors are closely related and can be transformed into each other by the symmetry operation  $S_z \rightarrow -S_z$ , which interchanges the role of up- and down-spins, or occupied and empty sites in the hardcore boson model, respectively.

## Experimental implementation of the QND measurement

As by the total spin excitation number  $m$  a collective property of the entire spin system is measured, the unitary of Eq. (B.36) truly is a many-qubit operation: Equations (B.38) and (B.39)

show that the projectors contains 1, 2 and 3-body spin interaction terms, such that the QND mapping of Eq. (B.36) involves interaction terms with up to 4-body Pauli operators. A decomposition of the unitary for the QND measurement  $U_{m_0=1}^{(3)}$  into experimentally available gates, as obtained using the numerical optimization algorithm, is shown in Table B.20. We note that since the QND measurement involves a *global* unitary, a numerical optimization has to be done separately for any register size and any particular spin excitation number, and furthermore becomes inefficient for increasing register sizes. However, the unitary can be implemented efficiently without resorting to numerical optimization: For a system of  $N$  spins,  $U_{m_0}^{(N)}$  will generally be the product of unitaries corresponding to many-spin interactions, at most  $(N + 1)$ -body Pauli operators. These unitaries can be decomposed into sequences of available gates following the recipes outlined in [55]. Although the implementation of  $U_{m_0}^{(N)}$  becomes experimentally demanding for increasing system sizes  $N$  and in general requires more operations than numerically optimized circuits, the number of required operations for the QND mapping operation still grows polynomially with the number of system spins.

Number	Pulse	Number	Pulse
1	$R(0.5, -0.5)$	11	$R(0.146, -0.895)$
2	$R(0.5, 0.0)$	12	$MS(0.375, -1.054)$
3	$S_z(0.5, 3)$	13	$S_z(0.364, 3)$
4	$MS(0.125, 0.0)$	14	$MS(0.75, -1.054)$
5	$R(0.098, 1.0)$	15	$R(1.0, 0.0)$
6	$S_z(1.636, 3)$	16	$S_z(1.818, 3)$
7	$MS(0.25, 0.0)$	17	$R(0.277, -1.054)$
8	$R(0.136, 0.5)$	18	$S_z(0.152, 3)$
9	$S_z(0.75, 3)$	19	$R(0.5, 0.895)$
10	$R(0.113, -1.054)$		

Table B.20.: Pulse sequence for the QND post-selective measurement of the spin excitation number in a system of 3+1 ions.

Due to the considerable complexity of the mapping operation for the QND measurement, with the optimized circuit involving in total 19 operations (see Table B.20), this method for error detection itself can only be implemented with a certain accuracy and requires a constant resource overhead, independently of the number of dynamical maps applied in the simulation. It can be seen from the data shown in Figs. 3a and b, and Fig. 4a of the main text, that for short sequences such as e.g. only a single elementary dissipative map, where the system without error detection remains with high probability in the desired excitation number subspace, experimental imperfections in the QND measurement itself actually introduce even more errors on the state of the system (red data points) than in the case where it is not applied (blue data points). However, for longer sequences of dynamical maps, where the population loss out of the initial excitation number subspace becomes more and more significant, the application of the QND post-selective method becomes effective and enables a more accurate simulation of the system dynamics for longer times.

## B.4.6. Quantum error reduction scheme - Excitation number stabilization

### General idea

The second error reduction procedure goes beyond the error detection method described in the previous section: it does not only allow one to detect errors, which have changed the ideally conserved spin excitation number  $m$  during the quantum simulation, but performs an active stabilization of the register of system spins in the wanted subspace of spin excitation number  $m_0$ . In the previous post-selective case the ancilla qubit carried the binary information whether the system is in the correct subspace or not. Here, in contrast, it is necessary to distinguish between at least three cases: (i) The excitation number  $m$  is correct, and thus no error correction process is required; the excitation number is (ii) too small or (iii) too large, as illustrated in figure 4.3.2b,c in the main text. This information cannot be stored in a single ancilla qubit with two logical states anymore. Although it is in principle possible to use a higher-dimensional ancillary system, such as multiple ancillary qubits, to store the required information, such an approach would require significantly more complex detection and correction algorithms. Here, we choose an alternative approach, which still allows one to perform the excitation number stabilization with a single ancilla qubit if the stabilization process is implemented as a two-step process: One stabilization step injects a single excitation into the register if there are too few excitations present ( $m < m_0$ ) and a second stabilization step removes an excitation from the system if too many are present ( $m > m_0$ ), as schematically shown in Fig. 4.3.2c of the main text. Similarly to repetitive quantum error correction, the state of the ancilla qubit has to be reset in between the two steps. As the underlying construction of the excitation injection and the extraction step is very similar, we focus in the following on a detailed description of the protocol for the excitation extraction procedure.

Conceptually, the injection protocol consists of two main parts: First, similar to the QND measurement in the previous section, the binary information whether or not there are too many spin excitations in the system is coherently mapped onto the two logical states of an ancillary qubit. Second, conditional on the state of the ancilla qubit, which is acting as a quantum controller, a feedback procedure is applied to the system spins. This quantum feedback procedure extracts one of the (possibly multiple) superfluous spin excitations and stops once this has been achieved.

The first part is realized by a unitary mapping acting on the entire register of system spins and the ancilla qubit. However, in contrast to the QND post-selective method, the ancillary qubit is not measured after this mapping. The unitary for the mapping reads

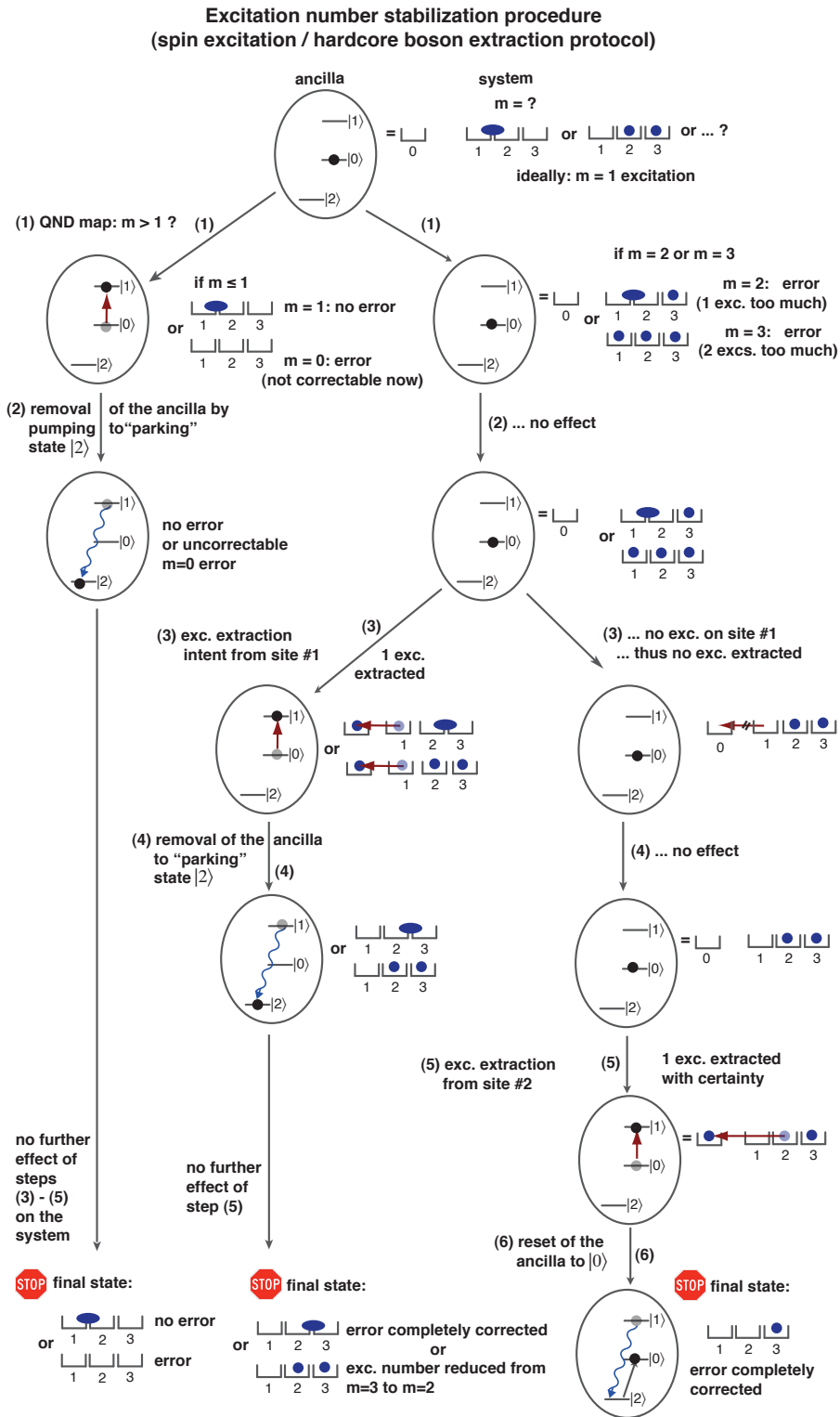
$$U_{m>m_0}^{(N)} = \exp \left( -i \frac{\pi}{2} \left( \sum_{j=m_0+1}^N P_j^{(N)} \right) \otimes \sigma_0^x \right) \quad (\text{B.40})$$

and can be understood as follows: The state of the ancilla qubit prepared in  $|1\rangle$  is flipped if and only if there are *too many* spin excitations present in the system; here the system operator  $\sum_{j=m_0+1}^N P_j^{(N)}$  denotes the projector onto the subspace of states containing strictly more excitations than the desired value  $m_0$ . It is the sum over all projectors  $P_j^{(N)}$  onto subspaces

with  $j > m_0$  excitations in a system of  $N$  spins, and each of these projectors can be readily constructed following the procedure described in Sec. B.4.5.

After the mapping operation between the system spins and the ancilla, the second part of the protocol deals with the actual extraction of a spin excitation from the system. This step faces the difficulty that due to the QND character of the first mapping step, the state of the ancilla qubit only encodes information about whether too many excitations are present in the system, but not on which sites the excitations are located. In order to minimally disturb the state of the system spins it is desirable to devise an extraction scheme with the following properties: (i) An excitation is extracted in a minimally invasive way, i.e. under an extraction of an excitation from a certain site, off-diagonal order among system spins of the rest of the chain is maintained as far as possible. (ii) Second, the scheme should effectively hold and not further alter the state of the system spins once an excitation has been successfully extracted. We have developed and implemented a scheme, which satisfies both criteria, and which exploits a combination of spectroscopic decoupling and optical pumping of the ancillary qubit.

Figure B.20 (following page): Logical tree illustrating the complete excitation extraction procedure for a 3-spin system with ideally a single excitation present, and for various (unknown) initial states of the system spins. Blue circles correspond to spin excitations (hardcore bosons) localized on particular sites, whereas ellipses indicate situations where excitations (hardcore bosons) can be delocalized over several lattice sites. The error reduction takes place in six steps: By a QND map (1) the information whether or not too many excitations are present in the system, is mapped onto an ancilla qubit. (2) In case of the ideal excitation number or too few excitations, the ancilla is removed from the computational space and the protocol effectively halts. In the opposite case, a swap operation (3) is applied to try to extract an excitation from system site # 1. If successful, after the subsequent removal of the ancilla (4) the protocol halts. Otherwise, (5) an extraction by a swap of the ancilla with system site # 2 extracts an excitation. (6) Finally, the ancilla is reset to its initial state  $|0\rangle$  for subsequent error reduction steps. See also text for a more detailed explanation.



## Steps of the excitation extraction procedure

Let us now describe in more detail the steps of the excitation extraction procedure, which is illustrated in Fig. B.4.6 for a system of three spins. In step (1) the mapping introduced above is applied, so that the information whether a correctable error (i.e. too many spin excitations in the system) is present (or not), is encoded in the ancilla state  $|0\rangle$  ( $|1\rangle$ ). If no correctable error is detected ( $m \leq m_0$ ) then the subsequent operations should not affect the system qubits. This can be realized by removing the ancilla qubit incoherently from the computational subspace (step (2)) as will be discussed below. In step (3) an extraction attempt on the first site of the spin register is performed by swapping the ancilla, which is now in the state  $|0\rangle$  corresponding to an empty site (no spin excitation), with the first qubit of the system. In terms of spins this operation corresponds to a swap ("flip-flop") process, under which  $|0\rangle_0|1\rangle_1 \rightarrow |1\rangle_0|0\rangle_1$ , i.e. the spin excitation is coherently exchanged between the ancilla qubit and the first system spin. In the language of hardcore bosons, the process can be interpreted as a tunneling of a boson from the site #1 onto the previously empty ancilla site (see step (3) in Fig. B.4.6). If after this process the ancilla qubit is in the state corresponding to an occupied site (spin excitation present), a single excitation has been successfully extracted from the system and the process should halt. As will be shown below, this can be performed by removing the population of the ancilla qubit from the computational subspace (step (4)). However, if the ancilla is still in the state  $|0\rangle$  corresponding to an empty site after the swap operation, then the first system qubit was in the state corresponding to an unoccupied site and thus no spin excitation (or hardcore boson) could be extracted,  $|0\rangle_0|0\rangle_1 \rightarrow |0\rangle_0|0\rangle_1$ . Thus, this procedure is repeated (step (5)) until the ancilla qubit is found in the state  $|1\rangle$  corresponding to an occupied site. In the case of three sites at most two extraction rounds are required (steps (3), (4), and (5)), before the ancilla is reset to  $|0\rangle$  (step (6)) for subsequent rounds of error reduction.

*Open vs. closed-loop error reduction scheme* – The described extraction (and injection) protocols are realized in an *open-loop* fashion, i.e. the ancilla remains unobserved during the whole procedure. This comes at the cost that all pulses (for steps (1) - (6) in the above example) have to be physically applied in every run of the error reduction procedure, even if the ancilla has been already removed from the computational subspace and in principle no further operations would be required. However, the described protocol could easily be modified into a *closed-loop* control scenario: In this case one would perform individual measurements of the ancilla qubit after the QND map (1) as well as after the coherent swap operations (steps (3) and (5)). The outcomes of these ancilla measurements would then yield the classical information on whether no error correction is required after step (1) or an excitation has already been extracted successfully in steps (3) or (5). This information could then be used for classical feedback on the quantum system in the sense that one can externally decide whether further steps are required in the error reduction protocol, or whether one can stop the current run of the error reduction protocol and no further operations have to be applied. An advantage of this modified scheme is that dissipative removal operations of the ancilla qubit out of the computational subspace are not required. Experimentally, the price to pay in this modified scheme would be a number of fluorescence measurements, which are slow compared to the application of coherent gates, and the requirement to recool the relevant external degrees of freedom of the ion chain after each measurement as recently demonstrated in [95].

## Experimental implementation

In the experiment, the error reduction protocol for a system of three spins, using 3+1 ions was implemented. We considered the case of having ideally  $m_0 = 1$  excitation present on the three sites. For the extraction step, the four-qubit unitary  $U_{m>1}^{(3)}$  (cf. Eq. (B.40)) to detect whether too many excitations (i.e.  $m = 2, 3$ ) are present in the system or not, has been obtained by numerical optimization. The resulting circuit consisting of 15 gates is listed in Table B.21. On the other hand, for the injection part, the unitary

$$U_{m<m_0}^{(N)} = \exp \left( -i \frac{\pi}{2} \left( \sum_{j=0}^{m_0-1} P_j^{(N)} \right) \otimes \sigma_0^x \right) \quad (\text{B.41})$$

which interrogates the system whether too few excitations are present, is required. For the case  $m_0 = 1$  and  $N = 3$ , the unitary  $U_{m<1}^{(3)}$  realizes a spin flip of the ancilla qubit only if the three system spins are in the state  $|000\rangle$ . This operation is equivalent to a triple controlled-NOT operation with the three system spins playing the role of the control qubits and the ancilla the target qubit. As we could not obtain a satisfying circuit decomposition for this unitary by means of the usual numerical optimization algorithm, we did not try to directly optimize  $U_{m<1}^{(3)}$ , but allowed the unitary to add arbitrary phases to states lying outside the desired excitation number subspace  $m_0 = 1$ . Under these relaxed conditions, the numerical optimizer delivered a circuit decomposition of 19 operations as shown in Table B.22.

Number	Pulse	Number	Pulse
1	$R(0.25, 0.5)$	9	$S_z(1.0, 3)$
2	$S_z(1.0, 3)$	10	$R(0.25, 0.5)$
3	$R(0.25, 0.5)$	11	$MS(0.5, 0.5)$
4	$MS(0.25, 0.5)$	12	$R(1.5, 0.5)$
5	$R(1.75, 0.0)$	13	$R(0.125, 0.5)$
6	$S_z(1.0, 3)$	14	$S_z(1.0, 3)$
7	$R(0.25, 0.0)$	15	$R(1.875, 0.5)$
8	$R(1.75, 0.5)$		

Table B.21.: Pulse sequence to implement the QND unitary  $U_{m>1}^{(3)}$  (cf. Eq. (B.40)) as part of the excitation extraction protocol. It maps the information whether there are more than  $m = 1$  spin excitations present in a system of three spins, onto the ancilla qubit.

*Implementation of the actual excitation extraction* – We will now discuss the physical mechanism underlying the implementation of the removal of a spin excitation (or hardcore boson), as described above and illustrated in Fig. B.21. This excitation removal step takes place after the QND mapping (1) and a decoupling operation on the ancilla qubit (2) described below. As mentioned above, the extraction step (3) relies on a swap operation exchanging the excitation of the ancilla qubit with one of the system spins, say #1. This swap operation is realized by applying a  $\pi$ -pulse, according to the "flip-flop" Hamiltonian

$$H_{01} = \sigma_0^+ \sigma_1^- + \sigma_0^- \sigma_1^+ = \frac{1}{2} (\sigma_0^x \sigma_1^x + \sigma_0^y \sigma_1^y).$$

Number	Pulse	Number	Pulse
1	$R(1.75, 0.5)$	12	$R(0.375, 0.0)$
2	$S_z(1.0, 3)$	13	$S_z(1.0, 3)$
3	$R(1.75, 0.5)$	14	$R(1.625, 0.0)$
4	$MS(0.25, 0.0)$	15	$S_z(0.5, 3)$
5	$R(1.875, 0.0)$	16	$MS(0.25, 0.0)$
6	$S_z(1.0, 3)$	17	$R(0.125, 0.0)$
7	$R(0.125, 0.0)$	18	$S_z(1.0, 3)$
8	$R(0.25, 0.5)$	19	$R(1.875, 0.0)$
9	$S_z(1.0, 3)$	20	$R(0.125, 0.5)$
10	$R(1.75, 0.5)$	21	$S_z(1.0, 3)$
11	$MS(0.25, 0.0)$	22	$R(1.875, 0.5)$

Table B.22.: Pulse sequence to implement the QND unitary  $U_{m<1}^{(3)}$  (cf. Eq. (B.41)) as part of the excitation injection protocol. It maps the information whether there are  $m = 0$  instead of ideally  $m = 1$  spin excitations present in a system of three spins, onto the ancilla qubit.

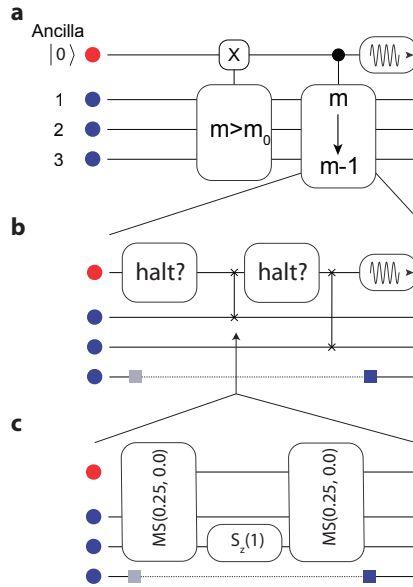


Figure B.21.: **a**, Schematic view of the error detection and excitation removal process (cf. Fig. 4.3.2c of the main text). **b**, The excitation removal process on 3 system qubits can be performed by swap operations and effective halting conditions realized by a dissipative decoupling of the ancilla qubit. **c**, Swap operations (B.42) between the ancilla qubit and one system spin are implemented by two effective two-qubit MS operations, which are build up from 4 MS operations acting on three ions, interspersed with refocusing operations.

The resulting unitary

$$\begin{aligned}
 U_{01} &= \exp\left(-i\frac{\pi}{2}H_{01}\right) \\
 &= \exp\left(-i\frac{\pi}{4}\sigma_0^x\sigma_1^x\right)\exp\left(-i\frac{\pi}{4}\sigma_0^y\sigma_1^y\right)
 \end{aligned}
 \tag{B.42}$$

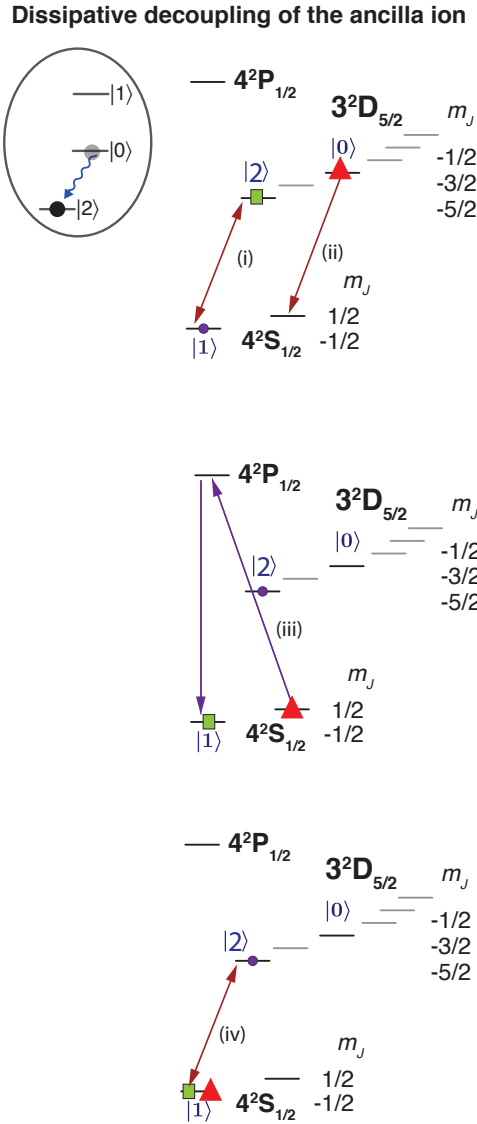


Figure B.22.: The dissipative decoupling process of the ancilla qubit used in the injection/removal processes. The goal is to uni-directionally remove population in the computational state  $|0\rangle$  (red triangular marker) and add it to electronic population that is possibly already present in the "parking" state  $|2\rangle$  (green rectangular marker). Population in the computational state  $|1\rangle$  (blue circle) should be left unchanged. The sequence: (i) First, the population in states  $|1\rangle$  and  $|2\rangle$  is coherently swapped by a  $\pi$ -operation. (ii) Population in  $|0\rangle$  is coherently transferred to the state  $4S_{1/2}(m_j = +1/2)$ . (iii) Optical pumping from this state towards the  $|1\rangle$  state. In this step, the populations that were at the beginning of the sequence present in  $|2\rangle$  and  $|0\rangle$  are added up and temporarily accumulate in state  $|1\rangle$ . (iv) Finally the populations in states  $|1\rangle$  and  $|2\rangle$  are again swapped coherently.

corresponds to the application of two fully-entangling  $x$ - and  $y$ -type MS gates (see Eq. (B.21)) applied to the ancilla ion and the first system ion. This two-ion MS gate can be realized by

Number	Pulse
1	$MS(0.25, 0)$
2	$S_z(1.0, j)$
3	$MS(0.25, 0)$
4	$MS(0.25, 0.5)$
5	$S_z(1.0, j)$
6	$MS(0.25, 0.5)$

Table B.23.: Pulse sequence for a swap operation used for excitation injection or removal, see Fig. B.21c. Ion  $j$  is the spectator ion, which is not spectroscopically decoupled, but is not intended to participate in the swap operation.

the global bi-chromatic light field, if all ions but the ancilla qubit and the system qubit #1 are spectroscopically decoupled. However, since step (3) involves the ancilla qubit and system ion #1, and step (5) the ancilla qubit and system ion #2, it is from an experimental point of view more convenient to spectroscopically decouple only ion #3, but keep *both* ions #1 and #2 in the "active" qubit states during the extraction procedure. Doing so, each of the  $x$ - and  $y$ -type MS-gates required for the operation (B.42) acting on the ancilla (index #0) and system ion #1 can be realized by two MS gates acting on the three ions, interspersed by a  $\pi$ -pulse  $S_z(1, 2)$  applied to the second system ion, as shown in Fig. B.21. The application of the "refocusing" pulse in between the MS gates leads to an effective decoupling of ion #2 that is not supposed to participate in the unitary (B.42) [55]. This technique is also applied to realize the swap operation required in step (5), which acts on the ancilla qubit and the second system. Using this decoupling technique based on refocusing pulses, no additional spectroscopic decoupling operations are required between the two swap operations corresponding to steps (3) and (5). The experimentally employed sequence of 6 gates is listed in Table B.23.

In Sec. B.4.6 we have outlined that the ancilla will be removed from the computational subspace in step (2) if no error is to be corrected in the current error reduction round. In this case, if the ancilla has been removed from the qubit subspace, the two-qubit MS interactions appearing in (B.42) act only on a single qubit. However, in this "pathological" case where the bi-chromatic laser fields used for the generation of the effective spin-spin interactions of the entangling MS gate of Eq.(B.21), are applied to a single ion only, these realize up to negligible corrections the identity operation on this single ion [148, 187]. As a consequence, in this case – despite the fact that the MS gate laser pulses of steps (3) and (5) are physically applied to the ions – they do not alter the state of the systems spins, as desired.

*Dissipative decoupling of the ancillary qubit* – As explained above, the ancilla qubit shall be removed from the computational subspace if either (i) no correctable error is detected in the current round of error reduction, or (ii) a superfluous spin excitation has been successfully extracted from the spin system. In these cases, the removal of the ancilla from the qubit subspace guarantees that the error reduction protocol effectively halts (see the logical tree shown in Fig. B.4.6) and the state of the system spins is no further modified, even though after the removal of the ancilla MS gate laser pulses are applied to the ion string. In steps (2) and (4) of the spin extraction protocol, the ancilla qubit is removed from the computational state  $|1\rangle$  into the "parking" state

$|2\rangle$ , which we encode in the  $3D_{5/2}(m_j = -5/2)$  electronic state (see Fig. B.22). This removal into  $|2\rangle$  takes place if the ancilla ion resides at these instances in  $|1\rangle$ , if it is in  $|0\rangle$  its state remains unaffected.

For this removal it is not possible to use the *coherent* spectroscopic decoupling technique as used for the implementation of the elementary Kraus maps. The reason is that this would lead to errors in the protocol: for instance, imagine no correctable error is present in the system and thus the ancilla is brought to the decoupling state  $|2\rangle$  in step (2). If then another ancilla removal were performed coherently (step (4)), the ancilla would be transferred back from  $|2\rangle$  to the computational state  $|1\rangle$ . This is clearly unwanted as in this case with the ancilla returned to  $|1\rangle$ , the subsequent swap operation (5) would be performed by mistake. This unwanted behavior can be avoided if the transfer of the ancilla from  $|1\rangle$  to  $|2\rangle$  is realized *dissipatively*, by an optical pumping process, which bares similarities with the incoherent reset of the ancilla qubit for the elementary dissipative maps. Such uni-directional, incoherent pumping process from  $|1\rangle$  to  $|2\rangle$  guarantees that once the ancilla has reached the "parking" state  $|2\rangle$ , it will in subsequent steps never return to the computational subspace. This optical pumping process for a removal process of the ancilla qubit from one of the computational basis states into  $|2\rangle$  is illustrated and described in more detail in Fig. B.22.

In the spin excitation protocol the ancilla is removed from  $|1\rangle$  (corresponding to an occupied site) to  $|2\rangle$ , whereas in the spin injection protocol it has to removed from  $|0\rangle$  (empty site) to  $|2\rangle$ . For both scenarios, the pulse sequence outlined in Fig. B.22 can be employed; a  $\pi$ -pulse resonant with the qubit transition of the ancilla, applied before and after the dissipative decoupling sequence, exchanges the roles of the two computational states  $|0\rangle \leftrightarrow |1\rangle$  and thereby allows one to switch between the spin extraction and injection scenario.

## Experimental results for the stabilization

The active excitation number stabilization procedure can be best tested when applying it to a state that has a considerable amount of the population outside the subspace with the correct excitation number  $m_0$ . We applied Hadamard operations on the three system qubits initially in  $|000\rangle$  to prepare the initial state  $|\psi_0\rangle = 1/\sqrt{8}(|0\rangle + |1\rangle)^{\otimes 3}$ , which is an equal-weight superposition of all eight three-qubit computational basis states, each occurring with probability  $1/8$ . The measured and ideal density matrix of this initial state is shown in Fig. B.24a. For  $m_0 = 1$  the states  $|001\rangle, |010\rangle, |100\rangle$  span the subspace with the desired spin excitation number. Thus, the initial fraction of population in this subspace is  $3/8$  as shown in Fig. 4.3.2d of the main text. We then performed the excitation extraction protocol according to the protocol outlined above and summarized in Fig. B.4.6. Ideally this protocol extracts one excitation from the components of the initial state, which contain two or three spin excitations,  $m = 2 \rightarrow m = 1$  and  $m = 3 \rightarrow m = 2$ , thereby pumping the population corresponding to these states into the subspaces with one excitation less. It is a crucial property of the error reduction protocol that the coherences within the subspace of the "correct" excitation number  $m = 1$  are ideally preserved, as the dynamics within the desired simulation subspace should be affected as little as possible. The component  $|000\rangle$  of the initial state corresponds to a state with zero, i.e. too few spin excitations, and thus to an error which is not corrected by the spin excitation procedure.

In Fig. 4.3.2d in the main text, the ideal and the measured populations in all four excitation number subspaces at the end of the extraction protocol are shown. From this information one can deduce that the protocol within experimental accuracy realizes the pumping of populations between the different excitation number subspaces as expected. To infer whether the coherences are preserved, we measured the three-qubit density matrices after the first excitation extraction attempt from the first site (step (3) in Fig. B.4.6) and after the second extraction attempt from the second site (step (5)). The measured and the ideal density matrices are shown in Fig. B.24b and c, where the relevant coherences within the  $m_0 = 1$  subspace are highlighted in red color. From the comparison of measured and ideal density matrices it can be seen that the coherences in the  $m_0$  excitation subspace are well-preserved.

The complete error correction protocol consists of the excitation extraction and injection procedures. For the same initial state  $|\psi_0\rangle$ , we implemented the injection procedure, which ideally only acts on the  $|000\rangle$  state, and pumps the population from the  $m = 0$  into the  $m = 1$  subspace. Again, the coherences within the  $m = 1$  subspace should be preserved under this procedure, yielding as a result of the injection protocol the ideal density matrix shown in the right part of Fig. B.24d. Comparison with the measured density matrix shows that most of the population is pumped out of the  $m = 0$  subspace, and that the initially present coherences within the  $m = 1$  subspace are reasonably well conserved.

The ultimate goal of any error reduction protocol is certainly to increase the performance of a complex algorithm. As a step in this direction, we integrated the excitation removal protocol into the simulation sequence for dynamics according to composite dissipative maps with 3+1 ions. In Fig. B.23 we compare the probabilities for all excitation numbers  $m$  when (i) no error reduction technique is used (blue data points), (ii) with the post-selective QND measurement applied (red), and (iii) with the excitation removal procedure included in the simulation (green). It can be seen that the removal procedure has a higher overhead due to its considerable complexity. Nevertheless, as an indication of its usefulness, a slower decay of the probability of finding the population in the desired subspace for  $m = 1$  can be observed, for the case in which the stabilization procedure is applied, compared to the case without any error correction. This indicates that the stabilization procedure indeed works qualitatively as intended, when it is incorporated into the actual simulation.

### B.4.7. Additional experiments and data analysis for competing dissipative and coherent dynamics

In Figs. 4.9 and 4.10 of the main text, the experimental results for systems of 3+1 and 4+1 ions are depicted. The attentive reader noticed that in Fig. 4.10 in the main text the data point for 5 maps is missing. This is due to the fact that in view of the length of the algorithm, the memory of the current experimental control system is not sufficient to generate the required pulse sequence for 4 elementary dissipative maps and one composite Hamiltonian dynamical map. It is however possible to generate the sequence for two elementary maps and one Hamiltonian dynamical map, and to repeat this sequence twice (data point for 6 maps).

Here, we extend the experimental analysis that was omitted from the main text due to space

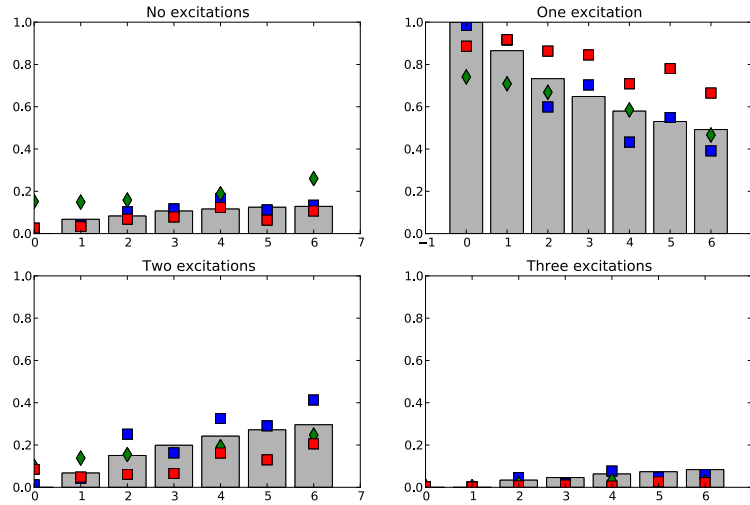


Figure B.23.: Experimental study of the error reduction protocol, incorporated into the actual quantum simulation of composite dynamical maps with 3+1 ions, with an initial and ideal excitation number of  $m = 1$ . The four plots show the fraction of the population in the subspaces with zero, one, two and three spin excitations, as a function of the number of elementary dissipative dynamical maps applied. For comparison, blue data points corresponds to the population under dissipative maps, without error detection or reduction technique applied. Red data points correspond to the case where after the final elementary dissipative map the QND post-selective measurement was applied. Green data points corresponds to the case where the extraction protocol has been applied at the end of the simulation. Bars are the theory, where depolarizing noise in the elementary dissipative maps is taken into account (cf. Sec. B.4.3).

restrictions by showing different measures for the already presented data and also additional datasets: In Figs. B.26 and B.25 we add the measures purity and off-diagonal order for the data already presented in Figs. 4.9 and 4.10 of the main text. The purity  $\text{Tr}\rho^2$  is a measure for how close the measured state is to a pure state. Off-diagonal order measures the coherences between neighboring sites as the expectation value of the operator  $\sum_j \sigma_-^{(j)} \sigma_+^{(j+1)}$  evaluated within the  $m_0$ -excitation subspace. This parameter emphasizes the effect of the competing Hamiltonian dynamics as it changes the sign from positive to negative after the application of a Hamiltonian map, as shown in figure B.26.

Figure B.27 shows an alternative dataset which demonstrates that the coherent competing Hamiltonian dynamical map in a system of three sites has - as physically expected - no effect if only a single excitation is present in the system. Comparison with the data of Fig. 4.10 in the main text, underlies the significance of the decrease in the overlap with the target Dicke state  $|D(2, 3)\rangle$ , and this effect is indeed caused by the competing Hamiltonian dynamics.

Figure B.28 shows a dataset with competition and two spin excitations present in the system. Compared to the analysis in the main text, the competition strength is now set to  $\phi = \pi/4$  instead of  $\pi/2$ . As expected, this leads to a reduced effect of the competing Hamiltonian maps

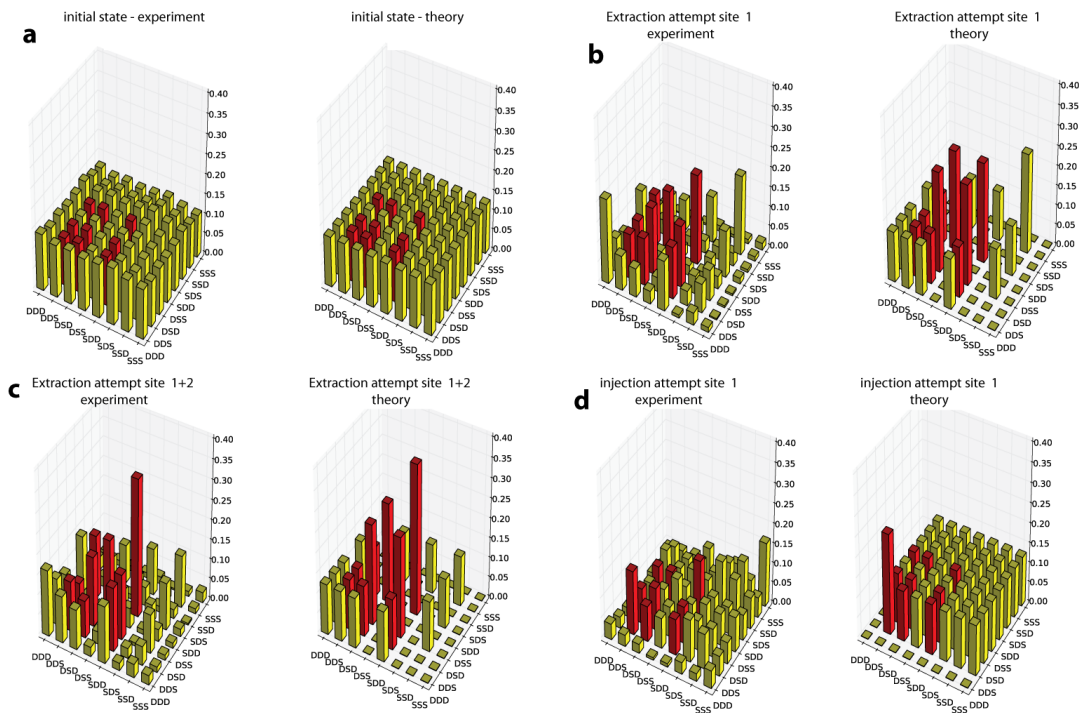


Figure B.24.: Reconstructed (left) and ideal (right) density matrices of the removal and injection process in a 3+1 ion experiment. Populations and coherences within the desired excitation number subspace with  $m = 1$  are high-lighted by red bars. **a**, The initial state is an equal-weight superposition of all eight computational basis states. **b**, The state after the system after a spin excitation removal attempt from the first site. **c**, The state of the system after the second swap operation to remove an excitation from the second site. After both steps, the coherences shown in red are well-preserved. **d**, The state of the system after a spin excitation injection attempt, starting again in the equal-weight superposition state shown in a. The population from the  $|DDD\rangle = |000\rangle$  state is depleted, and coherences within the  $m = 1$  subspace are reasonably well preserved.

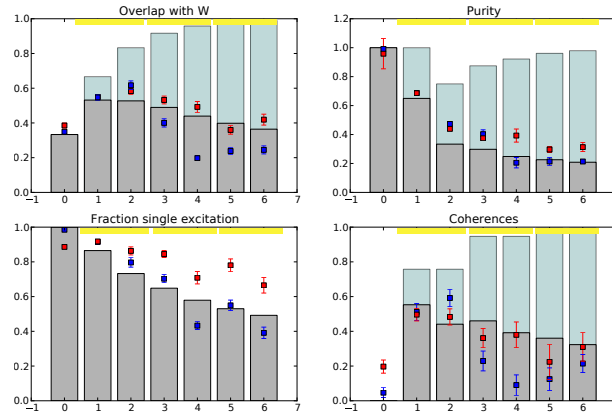


Figure B.25.: **Experimental results of dissipatively induced delocalization through composite dynamical maps with 3+1 ions.** The results from an ideal model are shown in light-blue bars whereas those from a model including depolarization noise are indicated by dark-grey bars. Blue rectangles indicate the experimentally observed dynamics without any correction scheme whereas red rectangles include a post-selective error detection scheme (error bars,  $1\sigma$ ). Overlap fidelity, purity, population in the  $m = 2$  subspace, and off-diagonal order in a 4-spin quantum simulation with 4+1 ions, studying purely dissipative dynamics that induces pumping towards the Dicke state  $|D(2, 4)\rangle$  as shown in figure 4.9 in the main text.

on the dissipatively created order.

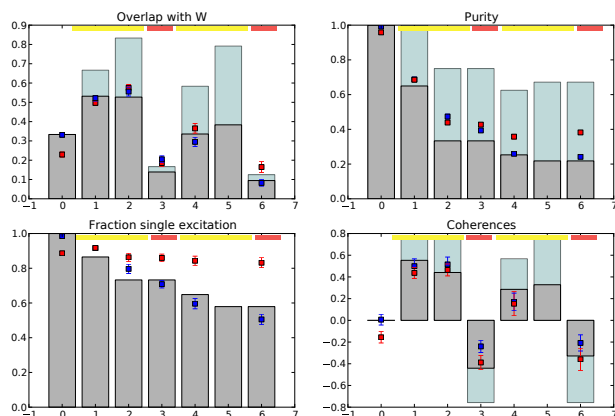


Figure B.26.: **Experimental results for competing dissipative and coherent dynamics with 3+1 ions** The results from an ideal model are shown in light-blue bars whereas those from a model including depolarization noise are indicated by dark-grey bars. Blue rectangles indicate the experimentally observed dynamics without any correction scheme whereas red rectangles include a post-selective error detection scheme (error bars,  $1\sigma$ ). Overlap fidelity, purity, population in the  $m = 2$  subspace, and off-diagonal order in a 3-spin quantum simulation with 3+1 ions. The dynamics corresponds to dissipative maps and coherent Hamiltonian competition as shown in figure 4.10 in the main text.

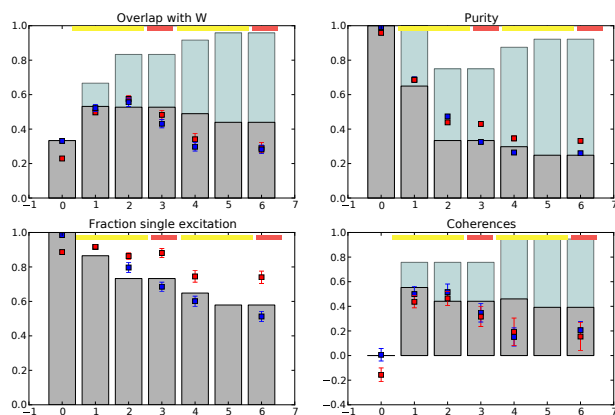


Figure B.27.: **Experimental results for competing dissipative and coherent dynamics with 3+1 ions with a single excitation.** The results from an ideal model are shown in light-blue bars whereas those from a model including depolarization noise are indicated by dark-grey bars. Blue rectangles indicate the experimentally observed dynamics without any correction scheme whereas red rectangles include a post-selective error detection scheme (error bars,  $1\sigma$ ). Data from simulated dynamics with Hamiltonian competition for 3 spins (3+1 ions), but only a single spin excitation present. As physically expected, the data confirms that in this case the Hamiltonian dynamical map has no effect.

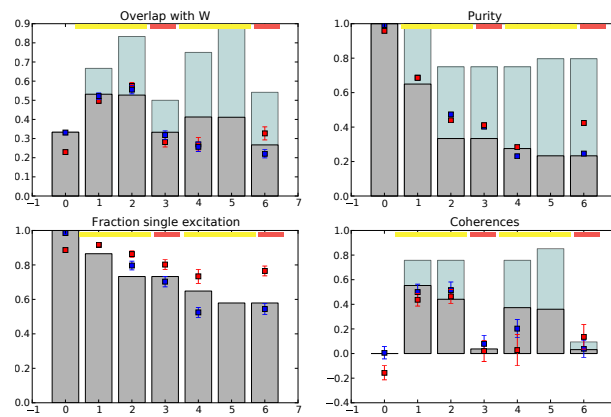


Figure B.28.: **Experimental results for competing dissipative and coherent dynamics with 3+1 ions with weak interaction** The results from an ideal model are shown in light-blue bars whereas those from a model including depolarization noise are indicated by dark-grey bars. Blue rectangles indicate the experimentally observed dynamics without any correction scheme whereas red rectangles include a post-selective error detection scheme (error bars,  $1\sigma$ ). Data from simulated dynamics with weaker competing Hamiltonian dynamics ( $\phi = \pi/4$ ) in a 3-spin system with two spin excitations present in the system (3+1 ions).

# Bibliography

- [1] P. Benioff, *Quantum Mechanical Models of Turing Machines That Dissipate No Energy*, Physical Review Letters **48**, 1581 (1982).
- [2] R. Feynman, *Simulating Physics with Computers*, International Journal of Theoretical Physics **21**, 467 (1982).
- [3] D. Deutsch, *Quantum Theory, the Church-Turing Principle and the Universal Quantum Computer*, Proceedings of the Royal Society of London. Series A, Mathematical and Physical Sciences: **400** (1985).
- [4] P. W. Shor, *Algorithms for quantum computation: discrete logarithms and factoring*, Foundations of Computer Science, 1994 Proceedings., 35th Annual Symposium on pp. 124–134 (1994).
- [5] R. L. Rivest, A. Shamir, and L. Adleman, *A method for obtaining digital signatures and public-key cryptosystems*, Communications of the ACM **21**, 120 (1978).
- [6] J. I. Cirac and P. Zoller, *Quantum Computations with Cold Trapped Ions*, Physical Review Letters **74**, 4091 (1995).
- [7] D. P. Divincenzo, *The Physical Implementation of Quantum Computation*, Fortschritte der Physik **48**, 771 (2000).
- [8] R. Blatt and D. Wineland, *Entangled states of trapped atomic ions*, Nature **453**, 1008 (2008).
- [9] J. Clarke and F. K. Wilhelm, *Superconducting quantum bits*, Nature **453**, 1031 (2008).
- [10] I. Bloch, *Quantum coherence and entanglement with ultracold atoms in optical lattices*, Nature **453**, 1016 (2008).
- [11] L. M. K. Vandersypen and I. L. Chuang, *NMR techniques for quantum control and computation*, Review of Modern Physics **76** (2004).
- [12] B. Joshi, D. Pradhan, and J. Stiffler, *Fault-Tolerant Computing*, Wiley Encyclopedia of Computer Science and Engineering (2007).
- [13] A. R. Calderbank and P. W. Shor, *Good quantum error-correcting codes exist*, Physical Review A **54**, 1098 (1996).

- [14] A. M. Steane, *Error Correcting Codes in Quantum Theory*, Physical Review Letters **77**, 793 (1996).
- [15] S. Lloyd, *Universal Quantum Simulators*, Science **273**, 1073 (1996).
- [16] J. I. Cirac and P. Zoller, *Goals and opportunities in quantum simulation*, Nature Physics **8**, 264 (2012).
- [17] I. Kassal, *et al.*, *Simulating Chemistry Using Quantum Computers*, Annual Review of Physical Chemistry **62**, 185 (2011).
- [18] N. Lambert, *et al.*, *Quantum biology*, Nature Physics **9**, 10 (2013).
- [19] S. Lloyd and L. Viola, *Engineering quantum dynamics*, Physical Review A **65**, 010101 (2001).
- [20] G. Baggio, F. Ticozzi, and L. Viola, *Quantum state preparation by controlled dissipation in finite time: From classical to quantum controllers*, in *Decision and Control (CDC), 2012 IEEE 51st Annual Conference on*, pp. 1072–1077, IEEE (2012).
- [21] F. Verstraete, M. M. Wolf, and J. Ignacio Cirac, *Quantum computation and quantum-state engineering driven by dissipation*, Nature Physics **5**, 633 (2009).
- [22] W. Paul and H. Steinwedel, *Ein neues Massenspektrometer ohne Magnetfeld*, Zeitschrift für Naturforschung A **8**, 448 (1953).
- [23] T. Monz, *et al.*, *14-Qubit Entanglement: Creation and Coherence*, Physical Review Letters **106**, 130506 (2011).
- [24] B. P. Lanyon, *et al.*, *Universal Digital Quantum Simulation with Trapped Ions*, Science **334**, 57 (2011).
- [25] T. Monz, *et al.*, *Realization of Universal Ion-Trap Quantum Computation with Decoherence-Free Qubits*, Physical Review Letters **103**, 200503 (2009).
- [26] T. Monz, *et al.*, *Realization of the Quantum Toffoli Gate with Trapped Ions*, Physical Review Letters **102**, 040501 (2009).
- [27] J. Benhelm, G. Kirchmair, C. F. Roos, and R. Blatt, *Towards fault-tolerant quantum computing with trapped ions*, Nature Physics **4**, 463 (2008).
- [28] M. Riebe, *et al.*, *Quantum teleportation with atoms: quantum process tomography*, New Journal of Physics **9**, 211 (2007).
- [29] H. Haffner, *et al.*, *Scalable multiparticle entanglement of trapped ions*, Nature **438**, 643 (2005).
- [30] M. A. Nielsen and I. L. Chuang, *Quantum Computation and Quantum Information (Cambridge Series on Information and the Natural Sciences)*, Cambridge University Press, 1 edn. (2004).

- 
- [31] O. Gühne and G. Tóth, *Entanglement detection*, Physics Reports **474**, 1 (2009).
- [32] A. Sørensen and K. Mølmer, *Quantum Computation with Ions in Thermal Motion*, Physical Review Letters **82**, 1971 (1999).
- [33] V. Nebendahl, H. Häffner, and C. F. Roos, *Optimal control of entangling operations for trapped-ion quantum computing*, Physical Review A **79**, 012312 (2009).
- [34] M. Ježek, J. Fiurášek, and Z. Hradil, *Quantum inference of states and processes*, Physical Review A **68**, 012305 (2003).
- [35] G. Tóth, *et al.*, *Permutationally Invariant Quantum Tomography*, Physical Review Letters **105**, 250403 (2010).
- [36] M. Cramer, *et al.*, *Efficient quantum state tomography*, Nature Communication **1**, 149 (2010).
- [37] A. Gilchrist, N. K. Langford, and M. A. Nielsen, *Distance measures to compare real and ideal quantum processes*, Physical Review A **71**, 062310 (2009).
- [38] I. Chuang and M. A. Nielsen, *Prescription for experimental determination of the dynamics of a quantum black box*, Journal of Modern Optics **44**, 2455 (1997).
- [39] D. Wineland, P. Ekstrom, and H. Dehmelt, *Monoelectron Oscillator*, Physical Review Letters **31**, 1279 (1973).
- [40] E. Schrödinger, *Are there quantum jumps? Part II*, The British Journal for the Philosophy of Science **III**, 233 (1952).
- [41] D. Wineland, *Experimental Issues in Coherent Quantum-State Manipulation of Trapped Atomic Ions*, Journal of Research of the National Institute of Standards and Technology **103** (1997).
- [42] C. F. Roos, *Controlling the quantum state of trapped ions*, Ph.D. thesis, Universität Innsbruck (2000).
- [43] E. T. Jaynes and F. W. Cummings, *Comparison of quantum and semiclassical radiation theories with application to the beam maser*, Proceedings of the IEEE **51**, 89 (1963).
- [44] H. C. Naegerl, *Ion Strings for Quantum Computing*, Ph.D. thesis, Universität Innsbruck (1998).
- [45] P. W. Shor, *Fault-tolerant quantum computation*, Foundations of Computer Science **96** (1996).
- [46] F. Schmidt-Kaler, *et al.*, *The coherence of qubits based on single  $\text{Ca}^+$  ions*, Journal of Physics B: Atomic, Molecular and Optical Physics **36**, 623 (2003).
- [47] C. Roos, *et al.*, *Quantum State Engineering on an Optical Transition and Decoherence in a Paul Trap*, Physical Review Letters **83**, 4713 (1999).

- [48] W. M. Itano, *et al.*, *Quantum projection noise: Population fluctuations in two-level systems*, *Physical Review A* **47**, 3554 (1993).
- [49] J. Eschner, G. Morigi, F. Schmidt-Kaler, and R. Blatt, *Laser cooling of trapped ions*, *Journal of the Optical Society of America B* **20**, 1003 (2003).
- [50] H. Rohde, *et al.*, *Sympathetic ground-state cooling and coherent manipulation with two-ion crystals*, *Journal of Optics B: Quantum and Semiclassical Optics* **3**, S34 (2001).
- [51] I. Marzoli, J. I. Cirac, R. Blatt, and P. Zoller, *Laser cooling of trapped three-level ions: Designing two-level systems for sideband cooling*, *Physical Review A* **49**, 2771 (1994).
- [52] A. Sørensen and K. Mølmer, *Entanglement and quantum computation with ions in thermal motion*, *Physical Review A* **62**, 022311 (2000).
- [53] H. Häffner, *et al.*, *Precision Measurement and Compensation of Optical Stark Shifts for an Ion-Trap Quantum Processor*, *Physical Review Letters* **90**, 143602 (2003).
- [54] G. Kirchmair, *et al.*, *Deterministic entanglement of ions in thermal states of motion*, *New Journal of Physics* **11**, 023002 (2009).
- [55] M. Müller, *et al.*, *Simulating open quantum systems: from many-body interactions to stabilizer pumping*, *New Journal of Physics* **13**, 085007 (2011).
- [56] N. Khaneja, *et al.*, *Optimal control of coupled spin dynamics: design of NMR pulse sequences by gradient ascent algorithms*, *Journal of Magnetic Resonance* **172**, 296 (2005).
- [57] D. Kielpinski, C. Monroe, and D. J. Wineland, *Architecture for a large-scale ion-trap quantum computer*, *Nature* **417**, 709 (2002).
- [58] J. T. Barreiro, *et al.*, *Experimental multiparticle entanglement dynamics induced by decoherence*, *Nature Physics* **6**, 943 (2010).
- [59] S. Diehl, *et al.*, *Quantum states and phases in driven open quantum systems with cold atoms*, *Nature Physics* **4**, 878 (2008).
- [60] D. Nigg, *et al.*, *Experimental Characterization of Quantum Dynamics Through Many-Body Interactions*, *Physical Review Letters* **110**, 060403 (2013).
- [61] P. Schindler, *et al.*, *Experimental Repetitive Quantum Error Correction*, *Science* **332**, 1059 (2011).
- [62] J. T. Barreiro, *et al.*, *An open-system quantum simulator with trapped ions*, *Nature* **470**, 486 (2011).
- [63] D. J. Berkeland, *et al.*, *Minimization of ion micromotion in a Paul trap*, *Journal of Applied Physics* **83**, 5025 (1998).
- [64] M. Chwalla, *et al.*, *Absolute Frequency Measurement of the  $^{40}\text{Ca}$   $4s^2S_{1/2} - 3d^2D_{5/2}$  Clock Transition*, *Physical Review Letters* **102**, 023002 (2009).

- 
- [65] M. Chwalla, *Precision spectroscopy with  $^{40}\text{Ca}^+$  ions in a Paul trap*, Ph.D. thesis, Universität Innsbruck (2009).
- [66] S. Gulde, *Experimental Realization of Quantum Gates and the Deutsch-Josza Algorithm with Trapped Ca Atoms*, Ph.D. thesis, Universität Innsbruck (2003).
- [67] P. Pham, *A general-purpose pulse sequencer for quantum computing*, Master's thesis, Massachusetts institute of technology (2005).
- [68] J. Alnis, *et al.*, *Subhertz linewidth diode lasers by stabilization to vibrationally and thermally compensated ultralow-expansion glass Fabry-Pérot cavities*, *Physical Review A* **77**, 053809 (2008).
- [69] A. H. Burrell, D. J. Szwer, S. C. Webster, and D. M. Lucas, *Scalable simultaneous multi-qubit readout with 99.99% single-shot fidelity*, *Physical Review A* **81**, 040302 (2010).
- [70] P. A. Barton, *et al.*, *Measurement of the lifetime of the  $3d^2 D_{5/2}$  state in  $^{40}\text{Ca}^+$* , *Physical Review A* **62**, 032503 (2000).
- [71] G. Tommaseo, *et al.*, *The  $g_J$  -factor in the ground state of Ca*, *The European Physical Journal D - Atomic, Molecular, Optical and Plasma Physics* **25**, 113 (2003).
- [72] D. J. Szwer, S. C. Webster, A. M. Steane, and D. M. Lucas, *Keeping a single qubit alive by experimental dynamic decoupling*, *Journal of Physics B: Atomic, Molecular and Optical Physics* **44**, 025501 (2011).
- [73] Y. Sagi, I. Almog, and N. Davidson, *Process Tomography of Dynamical Decoupling in a Dense Cold Atomic Ensemble*, *Physical Review Letters* **105**, 053201 (2010).
- [74] C. Barthel, *et al.*, *Interlaced Dynamical Decoupling and Coherent Operation of a Singlet-Triplet Qubit*, *Physical Review Letters* **105**, 266808 (2010).
- [75] G. de Lange, *et al.*, *Universal Dynamical Decoupling of a Single Solid-State Spin from a Spin Bath*, *Science* **330**, 60 (2010).
- [76] C. A. Ryan, J. S. Hodges, and D. G. Cory, *Robust Decoupling Techniques to Extend Quantum Coherence in Diamond*, *Physical Review Letters* **105**, 200402 (2010).
- [77] J. Du, *et al.*, *Preserving electron spin coherence in solids by optimal dynamical decoupling*, *Nature* **461**, 1265 (2009).
- [78] M. J. Biercuk, *et al.*, *Optimized dynamical decoupling in a model quantum memory*, *Nature* **458**, 996 (2009).
- [79] S. Kotler, *et al.*, *Single-ion quantum lock-in amplifier*, *Nature* **473**, 61 (2011).
- [80] J. Bylander, *et al.*, *Noise spectroscopy through dynamical decoupling with a superconducting flux qubit*, *Nature Physics* **7**, 565 (2011).

- [81] H. Häffner, *et al.*, *Robust entanglement*, Applied Physics B: Lasers and Optics **81**, 151 (2005).
- [82] T. Monz, *Quantum information processing beyond ten ion-qubits*, Ph.D. thesis, Universität Innsbruck (2011).
- [83] C. F. Roos, *et al.*, '*Designer atoms*' for quantum metrology, Nature **443**, 316 (2006).
- [84] U. Poschinger, *et al.*, *Interaction of a laser with a qubit in thermal motion and its application to robust and efficient readout*, Applied Physics B: Lasers and Optics **107**, 1159 (2012).
- [85] C. F. Roos, *et al.*, *Nonlinear coupling of continuous variables at the single quantum level*, Physical Review A **77**, 040302 (2008).
- [86] M. Riebe, *Preparation of entangled states and quantum teleportation with atomic qubits*, Ph.D. thesis, Universität Innsbruck (2005).
- [87] S. X. Wang, *Quantum Gates, Sensors, and Systems with Trapped Ions*, Ph.D. thesis, Massachusetts institute of technology (2012).
- [88] J. Dalibard, Y. Castin, and K. Mølmer, *Wave-function approach to dissipative processes in quantum optics*, Physical Review Letters **68**, 580 (1992).
- [89] K. Mølmer, Y. Castin, and J. Dalibard, *Monte Carlo wave-function method in quantum optics*, Journal of the Optical Society of America B **10**, 524 (1993).
- [90] P. Schindler, *et al.*, *Quantum simulation of open-system dynamical maps with trapped ions*, Nature Physics in press arXiv:1212.2418 (2012).
- [91] R. B. Griffiths and C. S. Niu, *Semiclassical Fourier Transform for Quantum Computation*, Physical Review Letters **76**, 3228 (1996).
- [92] C. A. Fuchs, *Distinguishability and Accessible Information in Quantum Theory*, arxiv:quant-ph/9601020 (1996).
- [93] J. Chiaverini, *et al.*, *Implementation of the Semiclassical Quantum Fourier Transform in a Scalable System*, Science **308**, 997 (2005).
- [94] E. Martin-Lopez, *et al.*, *Experimental realization of Shor's quantum factoring algorithm using qubit recycling*, Nature Photonics **6**, 773 (2012).
- [95] P. Schindler, *et al.*, *Undoing a Quantum Measurement*, Physical Review Letters **110**, 070403 (2013).
- [96] S. J. Devitt, K. Nemoto, and W. J. Munro, *The idiots guide to Quantum Error Correction*, arxiv:0905.2794 (2011).
- [97] A. Steane, *Quantum computing*, Reports on Progress in Physics **61**, 117 (1999).

- 
- [98] W. K. Wootters and W. H. Zurek, *A single quantum cannot be cloned*, Nature **299**, 802 (1982).
- [99] A. Steane, *Multiple-Particle Interference and Quantum Error Correction*, Proceedings of the Royal Society of London. Series A: Mathematical, Physical and Engineering Sciences **452**, 2551 (1996).
- [100] J. Preskill, *Reliable quantum computers*, Proceedings of the Royal Society of London. Series A: Mathematical, Physical and Engineering Sciences **454**, 385 (1998).
- [101] P. Aliferis and A. W. Cross, *Subsystem Fault Tolerance with the Bacon-Shor Code*, Physical Review Letters **98**, 220502 (2007).
- [102] K. Khodjasteh, D. A. Lidar, and L. Viola, *Arbitrarily Accurate Dynamical Control in Open Quantum Systems*, Physical Review Letters **104**, 090501 (2010).
- [103] D. G. Cory, *et al.*, *Experimental Quantum Error Correction*, Physical Review Letters **81**, 2152 (1998).
- [104] E. Knill, R. Laflamme, R. Martinez, and C. Negrevergne, *Benchmarking Quantum Computers: The Five-Qubit Error Correcting Code*, Physical Review Letters **86**, 5811 (2001).
- [105] N. Boulant, L. Viola, E. M. Fortunato, and D. G. Cory, *Experimental Implementation of a Concatenated Quantum Error-Correcting Code*, Physical Review Letters **94**, 130501 (2005).
- [106] J. Chiaverini, *et al.*, *Realization of quantum error correction*, Nature **432**, 602 (2004).
- [107] T. Aoki, *et al.*, *Quantum error correction beyond qubits*, Nature Physics **5**, 541 (2009).
- [108] T. B. Pittman, B. C. Jacobs, and J. D. Franson, *Demonstration of quantum error correction using linear optics*, Physical Review A **71**, 052332 (2005).
- [109] G. A. Paz-Silva, G. K. Brennen, and J. Twamley, *Fault Tolerance with Noisy and Slow Measurements and Preparation*, Physical Review Letters **105**, 100501 (2010).
- [110] M. Riebe, *et al.*, *Process Tomography of Ion Trap Quantum Gates*, Physical Review Letters **97** (2006).
- [111] P. Zanardi and M. Rasetti, *Noiseless Quantum Codes*, Physical Review Letters **79**, 3306 (1997).
- [112] D. A. Lidar, I. L. Chuang, and K. B. Whaley, *Decoherence-Free Subspaces for Quantum Computation*, Physical Review Letters **81**, 2594 (1998).
- [113] Y.-S. Kim, Y.-W. Cho, Y.-S. Ra, and Y.-H. Kim, *Reversing the weak quantum measurement for a photonic qubit*, Optics Express **17**, 11978 (2009).
- [114] Y.-S. Kim, J.-C. Lee, O. Kwon, and Y.-H. Kim, *Protecting entanglement from decoherence using weak measurement and quantum measurement reversal*, Nature Physics **8**, 117 (2011).
-

- [115] N. Katz, *et al.*, *Reversal of the Weak Measurement of a Quantum State in a Superconducting Phase Qubit*, Physical Review Letters **101**, 200401 (2008).
- [116] N. Katz, *et al.*, *Coherent State Evolution in a Superconducting Qubit from Partial-Collapse Measurement*, Science **312**, 1498 (2006).
- [117] R. Jozsa, *Fidelity for Mixed Quantum States*, Journal of Modern Optics **41**, 2315 (1994).
- [118] R. Blatt and C. F. Roos, *Quantum simulations with trapped ions*, Nature Physics **8**, 277 (2012).
- [119] P. Hauke, *et al.*, *Can one trust quantum simulators?*, Reports on Progress in Physics **75**, 082401 (2012).
- [120] H. F. Trotter, *On the product of semi-groups of operators*, Proceedings of the American Mathematical Society **10**, 545 (1959).
- [121] S. Diehl, *et al.*, *Dynamical Phase Transitions and Instabilities in Open Atomic Many-Body Systems*, Physical Review Letters **105**, 015702 (2010).
- [122] T. D. Ladd, *et al.*, *Quantum computers*, Nature **464**, 45 (2010).
- [123] H. J. Kimble, *The quantum internet*, Nature **453**, 1023 (2008).
- [124] R. J. Schoelkopf and S. M. Girvin, *Wiring up quantum systems*, Nature **451**, 664 (2008).
- [125] M. Neeley, *et al.*, *Generation of three-qubit entangled states using superconducting phase qubits*, Nature **467**, 570 (2010).
- [126] M. Saffman, T. G. Walker, and K. Mølmer, *Quantum information with Rydberg atoms*, Review of Modern Physics **82**, 2313 (2010).
- [127] I. Bloch, J. Dalibard, and W. Zwerger, *Many-body physics with ultracold gases*, Review of Modern Physics **80**, 885 (2008).
- [128] J. L. O'Brien, *Optical Quantum Computing*, Science **318**, 1567 (2007).
- [129] J. A. Jones, *Quantum Computing with NMR*, arXiv:1011.1382 (2010).
- [130] R. Hanson, *et al.*, *Spins in few-electron quantum dots*, Review of Modern Physics **79**, 1217 (2007).
- [131] J. Wrachtrup and F. Jelezko, *Processing quantum information in diamond*, Journal of Physics: Condensed Matter **18**, 807 (2006).
- [132] I. Buluta and F. Nori, *Quantum Simulators*, Science **326**, 108 (2009).
- [133] C. J. Myatt *et al.*, *Decoherence of quantum superpositions through coupling to engineered reservoirs*, Nature **403**, 269 (2000).

- 
- [134] L. Viola, *et al.*, *Experimental Realization of Noiseless Subsystems for Quantum Information Processing*, *Science* **293**, 2059 (2001).
- [135] S. Deleglise, *et al.*, *Reconstruction of non-classical cavity field states with snapshots of their decoherence*, *Nature* **455**, 510 (2008).
- [136] H. Krauter, *et al.*, *Entanglement Generated by Dissipation and Steady State Entanglement of Two Macroscopic Objects*, *Physical Review Letters* **107**, 080503 (2011).
- [137] J. Cho, S. Bose, and M. S. Kim, *Optical Pumping into Many-Body Entanglement*, *Physical Review Letters* **106**, 020504 (2011).
- [138] F. Pastawski, L. Clemente, and J. I. Cirac, *Quantum memories based on engineered dissipation*, *Physical Review A* **83**, 012304 (2011).
- [139] G. Goldstein, *et al.*, *Environment-Assisted Precision Measurement*, arXiv:1001.0089 (2010).
- [140] H. Häffner, C. F. Roos, and R. Blatt, *Quantum computing with trapped ions*, *Physics Reports* **469**, 155 (2008).
- [141] J. P. Home, *et al.*, *Complete Methods Set for Scalable Ion Trap Quantum Information Processing*, *Science* **325**, 1227 (2009).
- [142] H. Weimer, *et al.*, *A Rydberg quantum simulator*, *Nature Physics* **6**, 382 (2010).
- [143] D. Bacon, *et al.*, *Universal simulation of Markovian quantum dynamics*, *Physical Review A* **64**, 062302 (2001).
- [144] A. Y. Kitaev, *Fault-tolerant quantum computation by anyons*, *Annals of Physics* **303**, 2 (2003).
- [145] A. M. Steane, *Efficient fault-tolerant quantum computing*, *Nature* **399**, 124 (1999).
- [146] W. Dür, M. J. Bremner, and H. J. Briegel, *Quantum simulation of interacting high-dimensional systems: The influence of noise*, *Physical Review A* **78**, 052325 (2008).
- [147] H. M. Wiseman and G. J. Milburn, *Quantum Measurement and Control*, Cambridge University Press (2009).
- [148] K. Mølmer and A. Sørensen, *Multiparticle Entanglement of Hot Trapped Ions*, *Physical Review Letters* **82**, 1835 (1999).
- [149] C. F. Roos *et al.*, *Control and Measurement of Three-Qubit Entangled States*, *Science* **304**, 1478 (2004).
- [150] O. Gühne and M. Seevinck, *Separability criteria for genuine multiparticle entanglement*, *New Journal of Physics* **12**, 053002 (2010).
- [151] A. Friedenauer, *et al.*, *Simulating a quantum magnet with trapped ions*, *Nature Physics* **4**, 757 (2008).

- [152] K. Kim, *et al.*, *Quantum simulation of frustrated Ising spins with trapped ions*, *Nature* **465**, 590 (2010).
- [153] D. Porras and J. I. Cirac, *Effective Quantum Spin Systems with Trapped Ions*, *Physical Review Letters* **92**, 207901 (2004).
- [154] C. Nayak, *et al.*, *Non-Abelian anyons and topological quantum computation*, *Review of Modern Physics* **80**, 1083 (2008).
- [155] T. C. Ralph, *et al.*, *Quantum nondemolition measurements for quantum information*, *Physical Review A* **73**, 012113 (2006).
- [156] M. Riebe, *et al.*, *Deterministic entanglement swapping with an ion-trap quantum computer*, *Nature Physics* **4**, 839 (2008).
- [157] G. R. Fleming, S. Huelga, and M. Plenio, eds., *Focus on Quantum Effects and Noise in Biomolecules*, *New Journal of Physics*, vol. 12, Institute of Physics (2010).
- [158] J. R. Maze, *et al.*, *Nanoscale magnetic sensing with an individual electronic spin in diamond*, *Nature* **455**, 644 (2008).
- [159] C. Schneider, D. Porras, and T. Schätz, *Experimental quantum simulations of many-body physics with trapped ions*, *Reports on Progress in Physics* **75**, 024401 (2012).
- [160] I. Bloch, J. Dalibard, and S. Nascimbène, *Quantum simulations with ultracold quantum gases*, *Nature Physics* **8**, 267 (2012).
- [161] A. Aspuru-Guzik and P. Walther, *Photonic quantum simulators*, *Nature Physics* **8**, 285 (2012).
- [162] A. A. Houck, H. E. Türeci, and J. Koch, *On-chip quantum simulation with superconducting circuits*, *Nature Physics* **8**, 292 (2012).
- [163] J. Zhang, *et al.*, *Digital quantum simulation of the statistical mechanics of a frustrated magnet*, *Nature Communications* **3**, 880 (2012).
- [164] J. F. Poyatos, J. I. Cirac, and P. Zoller, *Quantum Reservoir Engineering with Laser Cooled Trapped Ions*, *Physical Review Letters* **77**, 4728 (1996).
- [165] M. J. Kastoryano, F. Reiter, and A. S. Sørensen, *Dissipative Preparation of Entanglement in Optical Cavities*, *Physical Review Letters* **106**, 090502 (2011).
- [166] M. Kliesch, *et al.*, *Dissipative Quantum Church-Turing Theorem*, *Physical Review Letters* **107**, 120501 (2011).
- [167] S. Diehl, E. Rico, M. A. Baranov, and P. Zoller, *Topology by dissipation in atomic quantum wires*, *Nature Physics* **7**, 971 (2011).
- [168] C. W. Gardiner and P. Zoller, *Quantum Noise*, Springer Verlag, Berlin (1999).

- 
- [169] L. E. Reichl, *The Transition to Chaos In Conservative Classical Systems: Quantum Manifestations*, Springer-Verlag, New York (1992).
- [170] B. V. Chirikov, *A universal instability of many-dimensional oscillator systems*, Physics Reports **52**, 263 (1979).
- [171] F. M. Izrailev, *Simple models of quantum chaos: spectrum and eigenfunctions*, Physics Reports **196**, 299 (1990).
- [172] F. Haake, *Quantum Signatures of Chaos*, Springer Series in Synergetics (2010).
- [173] F. L. Moore, *et al.*, *Atom Optics Realization of the Quantum Delta-Kicked Rotor*, Physical Review Letters **75**, 4598 (1995).
- [174] H. Ammann, R. Gray, I. Shvarchuck, and N. Christensen, *Quantum Delta-Kicked Rotor: Experimental Observation of Decoherence*, Physical Review Letters **80**, 4111 (1998).
- [175] M. B. d’Arcy, *et al.*, *Quantum Enhancement of Momentum Diffusion in the Delta-Kicked Rotor*, Physical Review Letters **87**, 074102 (2001).
- [176] K. Henderson, *et al.*, *Bose-Einstein Condensate Driven by a Kicked Rotor in a Finite Box*, Europhysical Lett. **75**, 392 (2006).
- [177] R. Islam, *et al.*, *Onset of a quantum phase transition with a trapped ion quantum simulator*, Nature Communications **2**, 377 (2011).
- [178] J. W. Britton, *et al.*, *Engineered two-dimensional Ising interactions in a trapped-ion quantum simulator with hundreds of spins*, Nature **484**, 489 (2012).
- [179] S. Sachdev, *Quantum Phase Transitions*, Cambridge University Press (1999).
- [180] C. Sayrin, *et al.*, *Real-time quantum feedback prepares and stabilizes photon number states*, Nature **477**, 73 (2011).
- [181] M. D. Reed, *et al.*, *Realization of three-qubit quantum error correction with superconducting circuits*, Nature **482**, 382 (2012).
- [182] C.-Y. Lu, *et al.*, *Demonstrating Anyonic Fractional Statistics with a Six-Qubit Quantum Simulator*, Physical Review Letters **102**, 030502 (2009).
- [183] J. K. Pachos, *et al.*, *Revealing anyonic features in a toric code quantum simulation*, New Journal of Physics **11**, 083010 (2009).
- [184] D. Bouwmeester *et al.*, *Experimental quantum teleportation*, Nature **390**, 575 (1997).
- [185] M. Riebe, *et al.*, *Deterministic quantum teleportation with atoms*, Nature **429**, 734 (2004).
- [186] M. D. Barrett, *et al.*, *Deterministic quantum teleportation of atomic qubits*, Nature **429**, 737 (2004).

- [187] C. F. Roos, *Ion trap quantum gates with amplitude-modulated laser beams*, New Journal of Physics **10**, 013002 (2008).
- [188] J. P. Garrahan and I. Lesanovsky, *Thermodynamics of Quantum Jump Trajectories*, Physical Review Letters **104**, 160601 (2010).
- [189] C. Ates, B. Olmos, J. P. Garrahan, and I. Lesanovsky, *Dynamical phases and intermittency of the dissipative quantum Ising model*, Physical Review A **85**, 043620 (2012).

# Danksagung

Diese Arbeit wäre ohne die Hilfe und Unterstützung der gesamten Arbeitsgruppe nicht zustande gekommen. Daher möchte ich mich an dieser Stelle bei ihnen für bedanken.

Mein Dank gebührt zuallererst Professor Rainer Blatt der mir die Möglichkeit gab in dieser einzigartigen Umgebung zu arbeiten.

Der Alltag im Labor wurde mithilfe meiner Mitstreiter Thomas Monz, Daniel Nigg, Julio Barreiro, Michael Chwalla, Mark Riebe und Esteban Martinez aufgeheitert. Die Tage und Nächte im Labor wurden dadurch zu einem besonderen Erlebnis. Das Experiment würde es ohne die Arbeit der Assistenten Markus Henrich, Wolfgang Hänsel, Hartmut Häffner, Christian Roos und Piet Schmidt nicht geben - Danke für die hervorragende Arbeit. Für weitere Unterstützung am Experiment danke ich Allesandro Villar, Khiwan Kim, Matthias Brandl, Stephan Quint und Shannon Wang.

Ein Dank geht auch an die theoretischen Physiker, ohne die ein großer Teil dieser Arbeit nicht entstanden wäre. Markus Müller stand uns im Kampf mit den verdammten Vorzeichen nächteweise im Labor bei. Madalin Guta, Matthias Kleinmann und Tobias Moroder halfen mir, mich im Dschungel der Quantenstatistik zurechtzufinden. Volckmar Nebendahl bändigte die Pulssequenzen und Sebastian Diehl wurde nicht müde den Phasenübergang noch einmal zu erklären.

Ein herzliches "Vergelt's Gott" geht an alle Nichtwissenschaftlichen Mitarbeiter in den Sekretariaten und Werkstätten, ohne die unser Leben um ein vielfaches Mühsamer wäre. Besonders möchte ich mich bei Patricia Moser bedanken, die immer ein offenes Ohr für unsere Anliegen hat.

Abseits des Labors möchte ich vor allem meiner Familie danken, die immer ein sicherer Hafen für mich war. Ganz besonders bedanke ich mich bei Tanja und allen anderen Freunden, die mich des öfteren aus meiner eigenen Welt herausholten und einfach da waren, wenn ich sie brauchte.